INVESTIGATION OF NOVEL TOPOLOGICAL PROPERTIES IN KAGOME METALS $A_2T_3S_4$ (WHERE A ARE K, Rb & Cs AND T ARE 3d & 4d TRANSITION METALS)

A THESIS SUBMITTED TO THE

CENTRAL DEPARTMENT OF PHYSICS

INSTITUTE OF SCIENCE AND TECHNOLOGY

TRIBHUVAN UNIVERSITY

NEPAL

FOR THE AWARD OF

DOCTOR OF PHILOSOPHY

IN PHYSICS

By

GANG BAHADUR ACHARYA

JULY 2024

INVESTIGATION OF NOVEL TOPOLOGICAL PROPERTIES IN KAGOME METALS $A_2T_3S_4$ (WHERE A ARE K, Rb & Cs AND T ARE 3d & 4d TRANSITION METALS)

A THESIS SUBMITTED TO THE

CENTRAL DEPARTMENT OF PHYSICS

INSTITUTE OF SCIENCE AND TECHNOLOGY

TRIBHUVAN UNIVERSITY

NEPAL

FOR THE AWARD OF

DOCTOR OF PHILOSOPHY

IN PHYSICS

By

GANG BAHADUR ACHARYA

JULY 2024

TRIBHUVAN UNIVERSITY

Institute of Science and Technology

DEAN'S OFFICE

Kirtipur, Kathmandu, Nepal

Reference No.:

EXAMINERS

Institute of Science & Technology
Dean's Office
Kirtipur 2045

The Title of Ph.D. Thesis: " Investigation of Novel Topological Properties in Kagome Metals $A_2T_3S_4$ (Where A are K, Rb & Cs and T are 3d & 4d Transition Metals"

Name of Candidate: Gang Bahadur Acharya

Internal Examiner :

Prof. Dr. Rajendra Parajuli
Amrit Campus
Tribhuvan University
Kathmandu, NEPAL

External Examiners:

(1) Dr. Suresh Kumar Dhungel
Nepal Academy of Science and Technology
Lalitpur, NEPAL

(2) Prof. Dr. Surendra Prasad
Banaras Hindu University
Varanasi, INDIA

(3) Prof. Dr. Parashu Ram Kharel
South Dakota State University
Brookings, USA

17 July 2024

(Dr. Surendra Kumar Gautam)
Asst. Dean

DECLARATION

Thesis entitled **"INVESTIGATION OF NOVEL TOPOLOGICAL PROPERTIES IN KAGOME METALS $A_2T_3S_4$ (WHERE A ARE K, Rb & Cs AND T ARE 3d & 4d TRANSITION METALS)"** which is being submitted to the Central Department of Physics, Institute of Science and Technology (IoST), Tribhuvan University, Nepal for the award of the degree of Doctor of Philosophy (Ph.D.), is a research work carried out by me under the supervision of Associate Professor Dr. Madhav Prasad Ghimire of Central Department of Physics, Tribhuvan University co-supervised by PD Dr. Manuel Richter of Leibniz Institute for Solid State and Materials Research, IFW-Dresden, Germany.

This research is original and has not been submitted earlier in part or full in this or any other form to any university or institute, here or elsewhere, for the award of any degree.

.....

Gang Bahadur Acharya

July 2024

RECOMMENDATION

This is to recommend that **GANG BAHADUR ACHARYA** has carried out research entitled **"INVESTIGATION OF NOVEL TOPOLOGICAL PROPERTIES IN KAGOME METALS $A_2T_3S_4$ (WHERE A ARE K, Rb & Cs AND T ARE 3d & 4d TRANSITION METALS)"** for the award of Doctor of Philosophy (Ph.D.) in **Physics** under our supervision. To our knowledge, this work has not been submitted for any other degree.

He has fulfilled all the requirements laid down by the Institute of Science and Technology (IoST), Tribhuvan University, Kirtipur for the submission of the thesis for the award of Ph.D. degree.

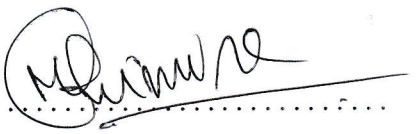

Dr. Madhav Prasad Ghimire
Supervisor
(Associate Professor)
Central Department of Physics
Tribhuvan University, Kirtipur
Kathmandu, Nepal

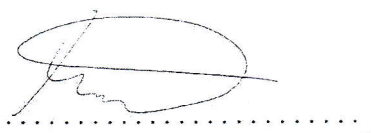

PD Dr. Manuel Richter
Co-Supervisor
Leibniz Institute for Solid State and Materials Research
IFW-Dresden, Germany

JULY 2024

TRIBHUVAN UNIVERSITY
CENTRAL DEPARTMENT OF PHYSICS
Kirtipur, Kathmandu, Nepal

☎ 4331054
www.tucdp.edu.np

Tribhuvan University Central Department of Physics Kirtipur

Ref. No.: (F.No .....) CDP .....

Date: 24 July 2024

LETTER OF APPROVAL

Date:

On the recommendation of Associate Professor Dr. **Madhav Prasad Ghimire** and PD. Dr. **Manuel Richter**, this Ph.D. thesis submitted by **GANG BAHADUR ACHARYA**, entitled **"INVESTIGATION OF NOVEL TOPOLOGICAL PROPERTIES IN KAGOME METALS $A_2T_3S_4$ (WHERE A ARE K, Rb & Cs AND T ARE 3d & 4d TRANSITION METALS)"** is forwarded by Central Department Research Committee (CDRC) to the Dean, IoST, T.U..

OP Niraula

.....

Dr. Om Prakash Niraula
(Professor)
Head
Central Department of Physics
Tribhuvan Universit
Kirtipur, Kathmandu, Nepal

ACKNOWLEDGEMENTS

First and foremost, I wish to express my sincere appreciation to my advisors, Associate Professor Dr. Madhav Prasad Ghimire from the Central Department of Physics, Tribhuvan University, Kirtipur, Nepal, and PD Dr. Manuel Richter from the Leibniz Institute for Solid State and Materials Research, IFW-Dresden, Germany. Their unwavering supervision, guidance, constant inspiration, and incredible assistance have been invaluable throughout my research. I thank Prof. Dr. Om Prakash Niraula, Head of the Central Department of Physics, TU, for his support. Special thanks to Prof. Dr. Binil Aryal, Dean of IoST, for his valuable suggestions and encouragement during my Ph.D. work. I am grateful to all the CDRC members, especially Prof. Dr. Narayan Prasad Adhikari, Prof. Dr. Raju Khanal, and the staff of CDP, TU, for their support and interactions. Thanks to Mrs. Ulrike Nitzsche from IFW-Dresden, Germany, for her technical assistance throughout my research. Moreover, I thank the Nepal Academy of Science and Technology (NAST) for the generous three-year Ph.D. fellowship awarded under grant number Ph.D./076-77. Additionally, my heartfelt thanks go to the Department of Science and Technology (DST), India, for the India Science Research Fellowship (ISRF) for the years 2023-24. I thank Assistant Professor Dr. Bhuvanesh Srinivasan for hosting me at IIT Madras during this fellowship. In addition, I would like to convey my sincere thanks to my research collaborators, Assistant Professor Dr. Sobhit Singh (University of Rochester), Bishnu Prasad Belbase, Ph.D. scholar (Purdue University), and Bishnu Karki, Ph.D. scholar (University of Houston) from the USA. I reserve special acknowledgment for Bishnu Karki, whose invaluable support in calculations and discussions on Berry curvature and the Fermi arc surface state. The Advanced Material Research Laboratory (AMRL) at CDP, TU, deserves recognition for providing computational and technical assistance. My family and friends' unwavering support, encouragement, and motivation have been crucial in completing this thesis. Significantly, my thanks extend to my friends Mr. Resham Babu Regmi, Mr. Shyam Sundar Sharma, Mr. Arjun Subedi, Mr. Kamal Khanal, Mr. Pawan Joshi, Mr. Dipak Bhattarai, Mr. Deergh Bahadur Sahi, Dr. Suresh Basnet, Dr. Salika Ram Bhandari, and Mr. Dipak Kumar Subedi for their technical and moral supports. I sincerely appreciate my beloved spouse, Mrs. Pratibha Paudel, for her enduring love and steadfast support throughout this journey. At every step, she has been a wellspring of motivation. With heartfelt dedication, I present this thesis to my son, Mr. Madhav Weyl Acharya.

Gang Bahadur Acharya
July 2024

शोध सार

आधारभूत रुपले निकै नयाँ र विशिष्ट गुणहरू प्रदर्शन गरेकाले हालका केही समयमा topological material हरूको अनुसन्धानमा महत्वपूर्ण अभिरुचि देखापरेको छ। विना कुनै energy gap यस्ता पदार्थहरूको विशिष्ट गुणसंरक्षित surface states को उपस्थिति non-trivial topology को bulk wave functions बाट प्रकट हुन्छ। यी material हरू अनौठो quantum सूचना प्रविधिका उपकरण सृजना तथा उपयोग गर्नका लागि प्रयोग गरिन्छन्। Topological semimetal मा Dirac, Weyl र nodal line सहितको विशेषताहरूको अन्वेषण गर्न kagome lattice crystal संरचना सम्भाव्य उम्मेदवार हो। Kagome lattice को electronic स्वरुप भित्र स्वाभाविक रुपले Dirac fermions, flat bands र van Hove singularities आउँछन्। विगतका दशकमा topological Weyl semimetals क्षेत्रको लोकप्रियता सटिक सैद्धान्तिक भविष्यवाणी, नियन्त्रित material संश्लेषण तथा उन्नत characterization प्रविधिहरू सहितको अनुसन्धान कार्यमा बढेको छ। यसभित्र angle-resolved photoemission spectroscopy, scanning tunneling microscopy, magneto-transport मापन, optical spectroscopy तथा अन्य पर्दछन्। यो थेसिसमा हामीले प्रस्तावित यौगिकको electronic, optical, magnetic र topological गुणहरूको अनुसन्धान density functional theory (DFT) प्रयोग गरी गरेका छौं। शुरुमा, $Cs_2Co_3S_4$ र $Li_3Fe_3S_4$ gapless system हरूको electronic, magnetic र topological गिुणहरू जाँच गरियो। Topological विशेषताहरूको सन्दर्भमा, खासगरी Weyl semimetallic र त्यसँग सम्बन्धित विशेषताहरू जस्तै Berry curvature, anomalous Hall conductivity र Fermi arc surface मा हाम्रो रुचि थियो। हामीले $Cs_2Co_3S_4$ मा करिब $3\mu_B$ प्रति formula यूनिट total spin magnetic moment सहित half-metallic ferrimagnetism रहेको पायौं। यसले majority spin channel को Fermi level मा 0.36 eV को energy band gap र minority spin channel मा pseudo-gap देखाउँदछ। हामीले low-energy Weyl points का धेरै समूहहरूको पहिचान गर्यौं र तिनीहरूको चुम्बकीकरणको दिशाको निर्भरता पत्ता लगायौं। Intrinsic anomalous Hall conductivity अधिकतम 500 $\Omega^{-1}cm^{-1}$ पुगेको पाइयो जुन चाहिँ प्रसिद्ध Weyl semimetal हरूको value सँग तुलनायोग्य छ।

यसका अतिरिक्त हामीले Fermi arc surface states जुन विपरीत chirality सहितका Weyl points लाई जोड्दछन्, त्यसको पनि खोजी गर्यौं। $Li_3Fe_3S_4$ मा पनि Weyl semi-metallic गुणहरू छन् जस्मा Fermi level को नजिक low-energy Weyl point हरु प्राप्त भए। Gapped system हरूमा हामीले $Rb_2Ni_3S_4$, $Cs_2Ni_3S_4$, $Rb_2Pd_3S_4$ र $Cs_2Pd_3S_4$ ले non-magnetic (गैरचुम्बकीय) ground state प्रदर्शन गरेको पायौं। Ni र Pd परमाणुहरूले two-dimensional plane मा kagome lattice निर्माण गर्दछन् र semi-conducting गुण धारण गर्दछन्। चाखलाग्दो त के छ भने, यी यौगिकहरूमा Fermi level को तल flat band देखियो जसले kagome lattice को एक महत्वपूर्ण लक्षण दर्शाउँदछ। यसको विपरीत $K_2Mn_3S_4$ र $Rb_2Mn_3S_4$ ले semi-conducting गुण कायम गर्दै magnetic ground state प्रदर्शन गर्दछन्। हामीले kagome संरचना भएका material हरूमा तिनीहरूको optical गुणको थप अध्ययन गर्यौं जसले visible र lower UV energy दायरा optical गतिविधिको पुष्टि भयो। यी उपरोक्त परिणामहरूको आधारमा high mobility उपकरणहरू, spintronics र quantum computing को लागि gapless topological Weyl semimetal हरू उपयुक्त हुन्छन् भन्ने निष्कर्ष निकाल्न सकिन्छ। साथै, kagome gapped materials चाहिँ optoelectronic उपकरणहरको लागि उपयुक्त र आदर्श हुन्छन् भन्ने पनि निष्कर्ष निकाल्न सकिन्छ।

ABSTRACT

There has been significant research interest in topological materials in recent years due to their demonstration of fundamentally novel physical phenomena. A distinguishing feature of topological materials is the presence of protected surface states without energy gaps, a characteristic that emerges from the nontrivial topology of bulk wave functions. These materials could create novel quantum information technology devices and applications. Kagome lattice crystal structures are promising for exploring topological properties, including features such as Dirac, Weyl, and Nodal line characteristics in topological semimetals. The electronic structure of a kagome lattice inherently includes Dirac fermions, flat bands, and van Hove singularities. Over the past decade, the topological Weyl semimetals (WSMs) have experienced an increase in popularity in research, leading to precise theoretical predictions, controlled material synthesis, and advanced characterization techniques. These techniques include angle-resolved photoemission spectroscopy, scanning tunneling microscopy, magnetotransport measurements, and optical spectroscopy. In this thesis, we used density functional theory (DFT) simulations to investigate a series of proposed compounds' electronic, optical, magnetic, and topological properties. Initially, we examined the electronic, magnetic, and topological properties of the gapless systems $Cs_2Co_3S_4$ and $Li_2Fe_3S_4$. Regarding topological features, we were especially interested in exploring Weyl semimetallic characteristics and related properties, including Berry curvature, anomalous Hall conductivity, and Fermi arc surface states. We found $Cs_2Co_3S_4$ to be a ferrimagnetic half-metal with a total spin magnetic moment of about 3 μ_B per formula unit. It shows an energy band gap of 0.36 eV in the majority-spin channel and a pseudo-gap at the Fermi level in the minority-spin channel. We identified several sets of low-energy Weyl points and traced their dependence on the direction of magnetization. The intrinsic anomalous Hall conductivity is predicted to reach a magnitude of 500 $\Omega^{-1}cm^{-1}$, comparable to values obtained in other celebrated Weyl semimetals. In addition, we calculate the Fermi arc surface states that connect the Weyl points with opposing chirality. $Li_2Fe_3S_4$ also has Weyl semimetallic characteristics with low energy Weyl points near the Fermi level. For gapped systems, we found that $Rb_2Ni_3S_4$, $Cs_2Ni_3S_4$, $Rb_2Pd_3S_4$, and $Cs_2Pd_3S_4$ exhibit nonmagnetic ground state. Ni and Pd atoms constitute a kagome lattice in a two-dimensional plane. These materials possess a semiconducting nature. Interestingly, a flat band was noticed below the Fermi level, demonstrating one significant feature of the kagome lattice. Conversely, $K_2Mn_3S_4$ and $Rb_2Mn_3S_4$ display a magnetic ground state while maintaining a similar semiconducting character. In the case of materials with a kagome structure, we con-

ducted further studies on their optical properties, revealing optical activity in both the visible and lower ultraviolet energy ranges. Based on these findings, gapless topological Weyl semimetals may be suitable for use in high-mobility devices, spintronics, and quantum computing. Kagome-gapped materials, on the other hand, may be possible for optoelectronic device applications.

Keywords: kagome, electronic properties, magnetic properties, optical properties, Wannier mapping, topology, Weyl semimetal, Weyl point, Berry curvature, anomalous Hall conductivity, Fermi arc surface states

LIST OF ACRONYMS AND ABBREVIATIONS

FM	: Ferromagnetic
AFM	: Antiferromagnetic
FIM	: Ferrimagnetic
BO	: Born-Oppenheimer
BZ	: Brillouin Zone
CB	: Conduction Band
DFT	: Density Functional Theory
HK	: Hohenberg Kohn
KS	: Kohn Sham
DOS	: Density of States
GGA	: Generalized Gradient Approximation
LDA	: Local Density Approximation
DFT+U	: Desnsity Functional Thory with Hubbard potential
GGA+mBJ	: Desnsity Functional Theory with modified Becke–Johnson Functional
PBE	: Perdue, Burke, and Ernzerhof
SCF	: Self Consistent Field
SWE	: Schrödinger Wave Equation
TF	: Thomas Fermi
eV	: electron Volt
XC	: Exchange Correlation
SOC	: Spin-Orbit Coupling
TRS	: Time Reversal Symmetry
IS	: Inversion Symmetry
WSMs	: Weyl Semimetals
WPs	: Weyl Points
DSMs	: Dirac Semimetals
TNLSMs	: Topological Nodal Line Semimetals
TI	: Topological Insulators
2D	: Two Dimension
3D	: Three Dimension
QHE	: Quantum Hall Effect
QSHE	: Quantum Spin Hall Effect
STIs	: Strong topological Insulators
WTIs	: Weak topological Insulators
ARPES	: Angle-Resolved Photoemission Spectroscopy
STM/STS	: Scanning Tunneling Microscopy/Spectroscopy
XRD	: X-ray Diffraction
ND	: Neutron Diffraction

LIST OF SYMBOLS

σ_{xy}	:	Hall Conductivity
σ_{xy}^{an}	:	Anomalous Hall Conductivity
$\sigma^{\text{an,in}}$	:	Intrinsic Contribution to the Anomalous Hall Conductivity
$\sigma^{\text{an,sj}}$	:	Side Jump Contribution to the Anomalous Hall Conductivity
$\sigma^{\text{an,sk}}$	:	Skew Scattering Contribution to the Anomalous Hall Conductivity
E_{F}	:	Fermi Level
χ	:	Chern Number/Chirality
Ω	:	Berry Curvature
Ω_x and Ω_y	:	x and y Component of the Berry Curvature
$\epsilon(\omega)$	:	Complex Dielectric Function
ϵ_1 and ϵ_2	:	Real and Imaginary Part of the Dielectric Function
$\sigma(\omega)$	:	Optical Conductivity
L(ω)	:	Loss Function

LIST OF TABLES

Page No.

LIST OF FIGURES

Page No.

TABLE OF CONTENTS

CHAPTER 1

INTRODUCTION

1.1 Basics of the Topology in Quantum Mechanics

1.1.1 Classical and Quantum Hall Effects

The classical Hall effect, discovered by Edwin Hall in 1879, is caused by charged particle motion in the presence of a magnetic field. When electrons in an x-direction that has current (I_{xx}) flowing along it and sample are subjected to a perpendicular magnetic field (B_z) along the z-direction, they experience a Lorentz force that deflects them. As a result, charge accumulates on one side of the sample, producing a voltage drop (V_{xy}) across the sample known as the Hall voltage, as shown in Fig. 1 (a) (Klitzing *et al.*, 2020). Understanding the Hall effect provides the foundation for understanding the quantum Hall effect (QHE) (Tong, 2016). The QHE was first discovered in two-dimensional (2D) electron gases subjected to high magnetic fields at extremely low temperatures (Klitzing *et al.*, 1980). These experiments proved that electrons in closed circular cyclotron orbits create an energy gap, a phenomenon termed Landau quantization. As a result, the quantum Hall system's inside existed as an insulator. Charges, however, were able to flow along the system's edges in a single direction, indicating the quantized conductance characteristic of one-dimensional transport (Hasan and Kane, 2010). The quantum Hall system's edge states were discovered to have an unusual feature called chirality, which

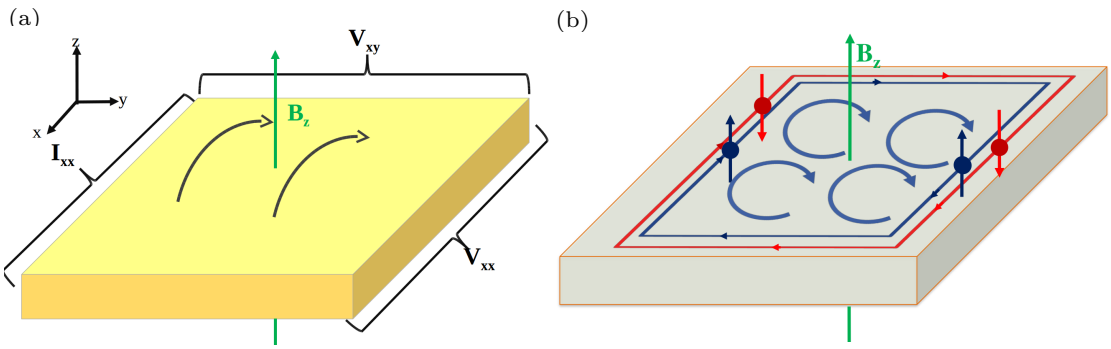

Figure 1: Schematic diagram: (a) Classical Hall effect and (b) Quantum Hall effect. This Fig.is based on Ref. (Klitzing *et al.*, 2020).

was dictated by the direction of the applied magnetic field. Because charge carriers on the edge states can only travel in one direction, back-scattering events are effectively suppressed. As a result, charge carriers in the edge states not only resist scattering but may also be produced without wasting energy (Lee, 2017). Klitzing and his group made an important finding about the quantum Hall conductance (σ_{xy}) (Klitzing *et al.*, 1980). In contrast to the classical Hall experiment, in which V_{xy} is linearly proportional to the applied magnetic field (B), they discovered a series of large plateaus at quantized values, producing a staircase-like sequence. The quantum Hall conductance can be mathematically represented as

$$\sigma_{xy} = \upsilon \frac{e^2}{h}, \tag{1.1}$$

where υ is an integer, e represents the electron charge, and h denotes Planck's constant. Equation (1.1) shows that the Hall conductance is a product of an integer and a fundamental constant of nature, $\frac{e^2}{h} = \frac{1}{25812.80759}$ A/V, irrespective of the system's dimension or imperfections. This behavior can be explained by the work of Thouless, Kohmoto, Nightingale, and den Nijs (TKNN), which establishes a connection between Hall conductivity and the topology of Bloch wave functions, we will discuss in the next section (Thouless *et al.*, 1982). The quantum Hall effect exhibits distinctive edge states. It can only be observed in the presence of a strong external magnetic field that breaks time-reversal symmetry (TRS).

1.1.2 Quantum Spin Hall Effect

Unlike quantum Hall systems, there is a new phenomenon called the quantum spin Hall effect (QSHE), which maintains TRS and can be considered analogous to the QHE (Kane and Mele, 2005a; Bernevig and Zhang, 2006). Given that a quantum spin Hall state is made up of two copies of a quantum Hall state, the latter must have gapless edge states (Hasan and Kane, 2010), as shown in Fig. 2. In the QSHE, electrons with different spin orientations, travel in opposite directions along the edge states, resulting in the generation of spin-polarized currents. This occurs due to the presence of spin-orbit coupling (SOC) (Liu *et al.*, 2016). These spin-polarized currents remain unaffected by the presence of disorders and exhibit edge modes without a energy gap, as indicated in Fig. 2 (b), in accordance with the principle of bulk-boundary correspondence. Initially, it was proposed that graphene could exhibit the QSHE; however, the weak SOC of carbon is too small to be measurable and thus prevented this from occurring. To achieve a significant SOC effect, it is necessary to use heavy elements because SOC is a relativistic phenomenon (Kane and Mele, 2005b). An experimental approach suggested to detect the QSHE by creating 2D quantum well structures by sandwiching a thin layer of HgTe, a semiconductor material with a robust SOC, between two CdTe barriers (Bernevig

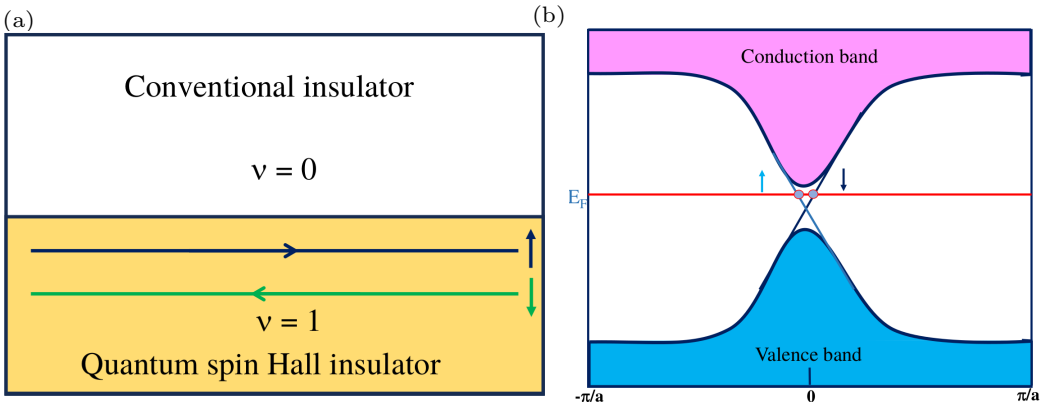

Figure 2: (a) The interface between an ordinary insulator and a Quantum spin Hall insulator. (b) The graphene model's edge state dispersion, where the propagation of up and down spins is opposite. This Fig. is based on Ref. (Hasan and Kane, 2010)

and Zhang, 2006). This configuration provided a distinct method for manipulating the electronic properties of the material. Shortly thereafter, an experiment validated this prediction by observing the quantized conductance of $2e^2/h$ even in the absence of a magnetic field (Konig *et al.*, 2007).

1.1.3 The TKNN Invariant

The TKNN formula proposed by Thouless, Kohmoto, Nightingale, and den Nijs, states that the quantum Hall conductivity of a system is a topological invariant (Thouless *et al.*, 1982). This formula is significant because it helps to explain the robustness of the integer QHE. The quantum Hall conductivity, represented by an integer value known as the Chern number, cannot change continuously during deformations of the system. Consequently, if the system is deformed, the quantum Hall conductivity remains fixed at its integer value. Also, the TKNN formula demonstrated that the QHE is not only a quantum mechanical phenomenon but also has a topological nature (Tong, 2016). The TKNN invariant is also referred to as the first Chern number or the winding number. It can be calculated by evaluating the Berry phase of the Bloch wave function around the boundary of the Brillouin zone (BZ) and dividing it by 2π. The QHE can be regarded as one of topological effects recognized by physicists. During quantization, the energy spectrum becomes gapped due to Landau quantization, and the chemical potential resides within this energy gap, resembling an insulator-like situation. In this scenario, the TKNN invariant specifies the nontrivial topology of a 2D system with TRS. The eigenfunctions of an electron in a periodic potential, satisfying the Schrödinger equation $H\psi_{kn}(r) = E_{kn}(r)\psi_{kn}(r)$, can be represented as a product of a plane wave and a periodic Bloch function, $u_{kn}(r)$. These eigenfunctions can be written as $\psi_{kn}(r)=e^{ik.r}u_{kn}(r)$, where n is the band index and k is the wave vector. The function $u_{kn}(r)$ possesses the same periodicity as the underlying lattice. Using the Kubo formula, TKNN demonstrated

that the Hall conductivity of a 2D electron gas system can be expressed in terms of the Bloch wave functions, is given by the following equation. The TKNN invariant or Chern number (C) plays a crucial role in this expression (Lee, 2017):

$$C = \frac{i}{2\pi} \sum_n \oint_{BZ} d^2k \left(\frac{\partial u_{n,y}}{\partial k_x} - \frac{\partial u_{n,x}}{\partial k_y}\right) = \frac{h}{e^2}\sigma_{xy} \tag{1.2}$$

Above equation expresses the relationship between C, the Hall conductivity, and the BZ integration. The summation is taken over the electron bands that are occupied, while the integral is performed across the entire BZ. u_n is the periodic part of the Bloch wave function. The BZ periodicity gives it a topological representation as a torus. Importantly, C is solely determined by the Bloch wave functions and the integral always results in an integer value when computed over the BZ. Thus, under the condition that there are no partially filled bands, C must be an integer (Simon, 1983). The topological characteristics of electronic states in a material are largely described by the Berry connection and the corresponding Berry curvature; the quantized Hall conductance is connected to these topological characteristics by the Chern number.

1.1.4 Berry Phase and Berry Curvature

The concept of Berry phase is important in the field of topological phases. In the following discussion, I will give a brief explanation of what Berry phase is and why it is important. Michael Berry developed the first concept in 1985 (Berry, 1985).

Mathematical Formulation: Mathematical formulation taken one-to-one from the (Ando, 2013) paper. Assuming a collection of time-varying parameters denoted by R(t), which can be viewed as a vector in the parameter space, we can represent the Hamiltonian of a system determined by H(R(t)), and its n^{th} eigenstate as $|n, R(t)\rangle$. The Schrödinger equation for this system is

$$H(R(t))|n, R(t)\rangle = E_n(R(t))|n, R(t)\rangle \tag{1.3}$$

Let's consider a scenario where the parameter R undergoes an adiabatic change starting from its initial value at t = 0, denoted as R_0. The time evolution of the state can be described as follows

$$H(R(t))|n, t\rangle = i\hbar\frac{\partial}{\partial t}|n, t\rangle \tag{1.4}$$

The state at time t is given by:

$$|n,t\rangle = exp(\frac{i}{\hbar}\int_0^t L_n(R(t'))dt')|n,R(t)\rangle \tag{1.5}$$

where,

$$L_n(R(t)) = i\hbar\dot{R}(t).\langle n,R(t)|\nabla_R|n,R(t)\rangle - E_n(R(t)). \tag{1.6}$$

This can be confirmed through putting equation 1.5 into the right hand side of equation 1.4 and then using L_n(R(t)) in equation 1.6, one may write the time-dependent state as,

$$|n,t\rangle = exp(-\int_0^t (\dot{R}(t'))dt'.\langle n,R(t')|\nabla_R|n,R(t'))\rangle)|n,R(t)\rangle \times exp(\frac{i}{\hbar}\int_0^t dt' E_n(R(t')) \tag{1.7}$$

The initial exponential term in the expression represents the nontrivial impact of the quantum-mechanical phase that accumulates during the time evolution. On the other hand, the final exponential term is considered trivial and is referred to as the dynamical term. When the parameter R undergoes a closed loop C, starting from t = 0 and returning to its original position at t = T, denoted as R(T) = R_0, the Berry phase denoted as $\gamma_n(C)$ for this loop C is defined as follows:

$$\gamma_n(C) = \int_0^T dt\dot{R}(t).i\langle n,R(t)|\nabla_R|n,R(t)\rangle \tag{1.8}$$

$$= \oint_C dR.i\langle n,R|\nabla_R|n,R\rangle \tag{1.9}$$

$$= -\oint_C dR.A_n(R) \tag{1.10}$$

$$= -\oint_S dS.B_n(R). \tag{1.11}$$

The final equivalence is a result of applying Stokes' theorem. In this context, we introduce the Berry connection as follows:

$$A_n(R) = -i\langle n,R|\nabla_R|n,R\rangle, \tag{1.12}$$

and its rotation is the Berry curvature

$$\Omega_n(R) = \nabla_R \times A_n(R). \tag{1.13}$$

By examining equations 1.7 and 1.8, we can understand that the Berry phase represents the accumulated phase factor experienced by a quantum-mechanical system upon completing a closed trajectory in the parameter space. Analogously, the Berry connection can be seen as a gauge field defined on this parameter space, much like the vector potential for electromagnetic fields in physical space.

1.2 Topological Materials

Topological materials form a new class of quantum materials, characterized by their unique properties derived from the principles of topology, a mathematical field concerned with properties that remain constant during smooth deformations. These materials possess properties that are invariant under topological transformations, making them highly interesting and significant for scientific exploration. Notable examples of topological materials include topological insulators, Dirac semimetals, Weyl semimetals, sodal line semimetals, and topological superconductors. These materials are formed by combining Dirac, Weyl, and Majorana fermionic electron states with the intrinsic magnetism of the materials. Topological Insulators are unique in that they are insulating in their bulk but exhibit conductivity on their surface (Bhardwaj and Chatterjee, 2020). In contrast, another class of topological materials is comprised of semimetals, where the valence and conduction bands intersect near the Fermi level. Depending on whether these bands are singly or doubly degenerate, these materials are referred to as Topological Weyl semimetals or topological Dirac semimetals, respectively. Due to their property of dissipationless transport, topological materials show great potential for practical applications in quantum computing and spintronics devices, making them an exciting field of research with promising technological implications (Kumar *et al.*, 2020). For the detailed discussion of the topological materials see in later subsection. Recently, topological properties are observed in a material that have 2D kagome structure. The word “kagome" is made up of “kago" and “me": “kago", means bamboo basket, and “me,” means woven pattern, comes from Japanese community (Mekata, 2003). This pattern has gained popularity in the magnetism community; the kagome structure is attractive due to its peculiar magnetic ground states of, e.g., the related Heisenberg model. It is also interesting due to its geometrical frustration that produces peculiar band structures. It has been found that some kagome materials having special topological states, mainly caused by magnetism and SOC. For instance, it has been discovered that the kagome ferromagnet Fe_3Sn_2 displays a spin-polarized Dirac cone with a gap generated by SOC (Ye *et al.*, 2018). $Co_3Sn_2S_2$, a ferromagnetic Weyl semimetal, the antiferromagnets

Mn_3Sn and Mn_3Ge have also shown a significant intrinsic anomalous Hall effect as a result of their large Berry curvature (Wang *et al.*, 2018; Liu *et al.*, 2018; Kübler and Felser, 2014; Nakatsuji *et al.*, 2015). Additionally, the kagome material is a potential candidate to study the interaction between lattice geometry, electron correlation, and band topology, according to these interesting experimental advances. A new type of kagome RMn_6Sn_6 family (where R is a trivalent rare earth element) has recently gained significant interest (Yin *et al.*, 2020; Wang *et al.*, 2021; Asaba *et al.*, 2020; Ma *et al.*, 2021). Particularly, Chern gapped Dirac fermions were discovered in the ferrimagnetic order of $TbMn_6Sn_6$ (Yin *et al.*, 2020).

1.2.1 Topological Insulators

In condensed matter physics, "Topological Insulators" (TIs) describes materials that have metallic boundary states but insulating bulk. The bulk band structure ensures that these boundaries are composed of 1D electronic edge or 2D surface states containing electrons with spin polarization. Taking into account spin orbit coupling, the spin and momentum of these boundary state electrons are locked together (Eschbach *et al.*, 2017; Hasan and Kane, 2010). Due to these features, TI is highly desirable for use in spintronics (Hsieh *et al.*, 2009). The presence of metallic surface states is an advantageous feature of 3D TIs because their surface always possesses these states as long as the topological indices are preserved (Eschbach *et al.*, 2017). Furthermore, the nontrivial Z_2 topology of bulk electronic wave functions in TIs gives rise to topologically protected Dirac surface states (Breunig and Ando, 2022). The characterization of 3D TIs as strong or weak is determined by four Z_2 invariants (ν_0;ν_1, ν_2, ν_3). A material is classified as a strong TI if ν_0 equals 1, while a weak TI has ν_0 equal to 0 and at least one of the indices (ν_1, ν_2, ν_3) equal to 1 (Fu *et al.*, 2007; Moore and Balents, 2007; Ghimire and Richter, 2017). (Eschbach *et al.*, 2017). From the experimental view, transport measurements, angle-resolved photoemission spectroscopy (ARPES), scanning tunneling microscopy/spectroscopy (STM/STS), magneto-optical spectroscopy, and ultra-fast optics measurements are a few of the experimental methods that have been utilized to characterize TIs. The prediction of Bi_2Te_3 being both a STI and a Topological Chern insulator (TCI) was a first, and this material was termed a dual TI due to its exhibition of two topological properties (Rauch *et al.*, 2014). KHgSb is an another 3D WTI with honeycomb lattice, reported on the basis of ab initio calculations (Yan *et al.*, 2012). Fig. 3 shows the schematic diagram of edge and surface states of TIs with Dirac dispersions (Ando, 2013).

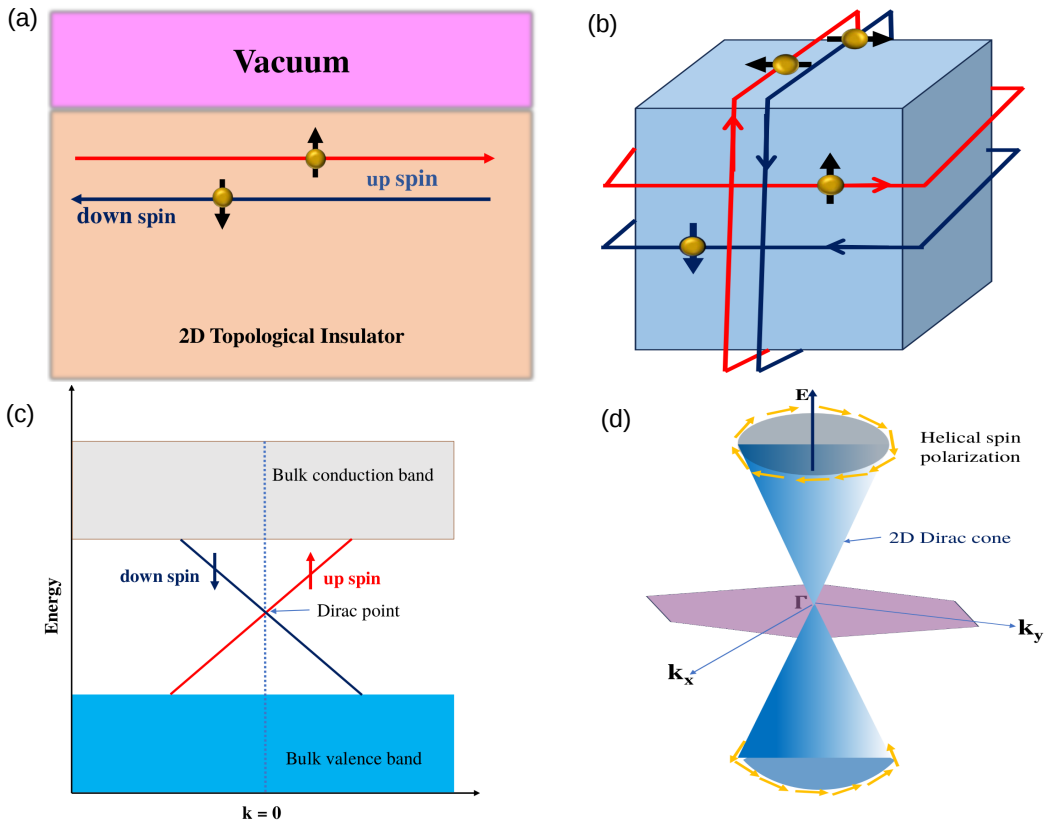

Figure 3: (a) A 1D helical edge state in a 2D TI. (b) The energy dispersion of the spin non-degenerate edge state in a 2D TI, forming a 1D Dirac cone. (c) A real-space picture of the 2D helical surface state in a 3D TI. (d) The energy dispersion of a spin non-degenerate surface state in a 3D TI, forming a 2D Dirac cone. This Dirac cone arises from the helical spin polarization, and it prevents back-scattering from occurring between momentum states k and -k. This Fig. is based on Ref. (Ando, 2013).

1.2.2 Dirac Semimetals

In 3D solid materials with both time reversal (T) and inversion (I) symmetry, the topological phase boundary between a normal insulating phase and a topological insulator phase gives rise to Dirac semimetals (DSMs) (Murakami, 2007). For this, Dirac Hamiltonian can be represented in the following form (Gao *et al.*, 2019).

$$E = H(k) = \begin{pmatrix} m & vk.\sigma \\ vk.\sigma & -m \end{pmatrix} = vk.\sigma\tau_x + m\tau_z, \tag{1.14}$$

where $k = (k_x, k_y, k_z)$ is momentum, v is velocity (considered as a Fermi velocity), and m is mass. The sets of Pauli matrices, $\sigma = (\sigma_x, \sigma_y, \sigma_z)$ and $\tau = (\tau_x, \tau_y, \tau_z)$, can be interpreted as representing spin and orbital degrees of freedom, respectively. The topological properties of the system are determined by the mass parameter, m. A change in the sign of m results in a change in the topology of the system's ground state, indicating a transition from a normal insulator to a TI at a T symmetry-invariant momentum. This

transition is marked by a band inversion in above equation. At the critical point of the transition (when m = 0), the system's energy spectrum becomes gapless at k = 0, leading to the formation of a fourfold-degenerate point node with linear dispersion. This critical point is characterized by low-energy electronic excitation that are described by a massless Dirac equation. There are two mechanisms for generating stable Dirac points. The first type is called nonsymmorphic DSMs, related to the nonsymmorphic nature of the crystal space group; Dirac points appear at high-symmetry points on the boundary of the BZ (Young *et al.*, 2012). The second type is referred to as topological DSMs, which depend on a band inversion in the presence of an n-fold rotational symmetry axis with n = 3, 4, and 6. In this case, the Dirac points occur in pairs on the rotation symmetry axis, but away from a high-symmetry point. It is worth noting that the stable Dirac points responsible for defining 3D DSMs remain stable even in the presence of SOC. This is in contrast to 2D graphene, which is TI once the effects of SOC are considered (Young and Kane, 2015). The realization of nonsymmorphic DSMs in real materials requires that the four fold-degenerate Dirac point is situated at or near the Fermi level, with low-energy electrons originating solely from the Dirac nodes. Identified β-cristobalite BiO_2 as a symmetry-enforce DSM that satisfies these requirements, with fourfold-degenerate band crossings exhibiting linear dispersion at the X points shown in the first-principles band structure of β-cristobalite BiO_2 (Young *et al.*, 2012). However, confirming the DSM phase experimentally in BiO_2 has proven challenging due to its chemical instability. Several other material candidates, including $BiZnSiO_4$, $BiCaSiO_4$, $BiAlInO_4$, and $BiMgSiO_4$, a cluster compound family AMo_3X_3 with A = (Na, K, Rb, In, Tl) and X = (Se, Te), and HfI_3 have been proposed, but no experimental evidence has been achieved yet (Steinberg *et al.*, 2014; Gibson *et al.*, 2015). A group of compounds called alkali pnictides A_3Bi (where A can be Na, K, or Rb) and Cd_3As_2 suggested as potential topological DSMs (Wang *et al.*, 2013a). ZrBeSi and BaAgBi have also been identified as potential topological DSMs, with band inversions that produce Dirac points in a similar manner to Na_3Bi (Du *et al.*, 2015). While the materials mentioned so far are centrosymmetric, noncentrosymmetric crystals without I symmetry can also exhibit topological DSMs. By analyzing these semimetals and found that rotation axes with little groups isomorphic to the C_{4v} and C_{6v} point groups can lead to stable four fold degenerate crossings (Gao *et al.*, 2018). Hexagonal ABC materials with LiGaGe-type structure and polar space group 186, such as SrHgPb and LiZnBi, were proposed as material realizations of noncentrosymmetric DSMs (Cao *et al.*, 2017). The previously mentioned DSMs are all nonmagnetic and maintain T symmetry. However, progress has been made in studying magnetic systems. Investigated the possibility of stable Dirac points in magnetic systems by demonstrating that an antiferromagnetic spin arrangement that preserves both TR and I symmetry (Tang *et al.*, 2016). Magnetic CuMnAs was predicted by first-principles calculations to be an antiferromagnetic DSM.

Other materials have since been discovered, such as $EuCd_2As_2$, which is protected by C_3 rotation symmetry, and CeSbTe, which is believed to have both Dirac and Weyl states (Hua *et al.*, 2018; Schoop *et al.*, 2018).

1.2.3 Weyl Semimetals

If two non-degenerate bands cross or touch in a single, separated point in k-space, this is called a Weyl point (WP). WPs are topologically protected and are robust against small perturbations and they exist in pairs with opposing chiral charges (Zheng *et al.*, 2019). Non-degenerate bands, which are required for the existence of WPs, are present if IS or TRS or both are broken (Hosur and Qi, 2013).

Quasiparticles near the WPs demonstrate characteristics similar to massless relativistic Weyl fermions. Materials possessing WPs in the 3D BZ are termed as topological Weyl semimetals (WSMs)

Now the Hamiltonian in the case of low energy expansion around a generic degeneracy point k_o can be expanded to linear order in momentum space is given by,

$$H_{Weyl}(\delta k) = \epsilon_o(k_o) + v_o.\delta k + \sum_{i=xyz} v_i.\delta k \sigma_i \tag{1.15}$$

The parameters v_o and $v_i = (v_x, v_y, v_z)$ describe the linear dispersion near the degeneracy point, while σ_x, σ_y, and σ_z are the Pauli matrices. The second term $v_o.\delta k$ controlling the transition between the two semimetallic phase, type-I and type-II. The third term encodes the topological properties of the Weyl point (Gao *et al.*, 2019). Nielsen and Ninomiya established a no-go theorem in 1981, implies that on a lattice, the number of charges of monopoles is equivalent to the number of anti-monopoles (Nielsen and Ninomiya, 1981). This can be explained in terms of Berry curvature near the degenerate point. In general, Weyl points behaves as either source or sink of Berry curvature, which is

$$\oint_{\partial v} \Omega_n(k).dS = 2\pi C, \tag{1.16}$$

over a closed volume (V) surrounding the node, gives the Chern number of the Weyl node. Periodicity requires that the Berry curvature flux via opposite surfaces should be identical when such a closed surface is expanded to completely occupy the BZ, which implies that the total enclosed chiral charge has to be zero (Ivanov, 2021). Each Weyl node needs a partner with the opposing chirality in order to cancel the entire amount of chiral charge in the BZ. Unlike Dirac point, Weyl point can not remove through a mass perturbation, they can only create and annihilate with opposite chirality (Burkov and Balents, 2011; Wan *et al.*, 2011). Moreover, Berry curvature is odd under TRS, T$\Omega_n(k)$=-

$\Omega_n(-k)$ and even under IS, $I\Omega_n(k)=\Omega_n(-k)$. Total number of Weyl points in a TRS and IS broken symmetry system has multiples of two and four, respectively (Gao *et al.*, 2019). In non-magnetic WSMs, only IS is broken, important and extensively investigated examples are TaAs family, layered transition metal dichalcogenides WTe_2, $MoTe_2$, $TaIrTe_4$ and the alloy $Mo_xW_{1-x}Te_2$ (Weng *et al.*, 2015b; Lv *et al.*, 2015; Soluyanov *et al.*, 2015; Haubold *et al.*, 2017; Sun *et al.*, 2015; Deng *et al.*, 2016; Chang *et al.*, 2016; Karki *et al.*, 2022). In

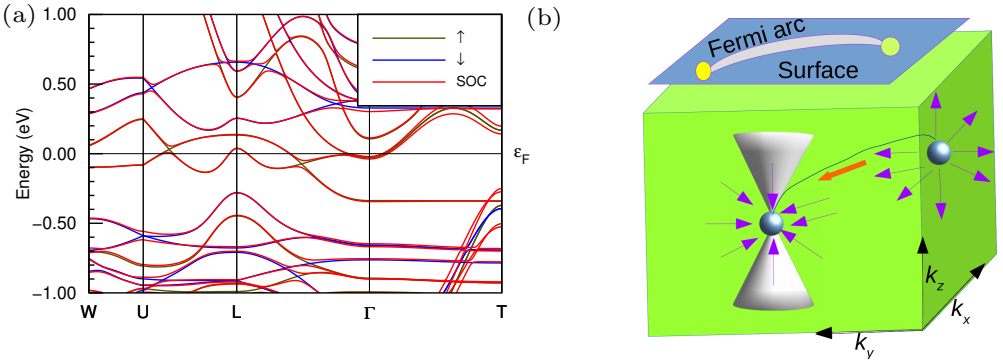

Figure 4: (a) Energy dispersion of electronic bands along high symmetry paths without and with the SOC of $Co_3Sn_2S_2$ in a hexagonal setting. (b) Schematic diagram of Weyl nodes connected by Fermi arc in the bulk band structure. This Fig. is based on Ref. (Bernevig, 2015)

.

magnetic WSMs, either TRS or both TRS and IS are broken due to the intrinsic magnetic characteristics of the system. A pyrochlore iridate ($Y_2Ir_2O_7$) is the first theoretically predicted magnetic WSM (Wan *et al.*, 2011). After that $HgCr_2Se_4$, Ti_2MnAl, $Co_3Sn_2S_2$, $YbMnBi_2$, Co_2MnGa, Mn_3Sn/Mn_3Ge and GdPtBi as well as certain Co-based Heusler compounds predicted to host the TRS-breaking Weyl phase (Xu *et al.*, 2011; Shi *et al.*, 2018; Morali *et al.*, 2019; Ghimire *et al.*, 2019; Borisenko *et al.*, 2019; Kübler and Felser, 2016; Kuroda *et al.*, 2017; Hirschberger *et al.*, 2016; Kübler and Felser, 2016; Wang *et al.*, 2016b). In recent years, magnetic WSMs are receiving more and more attention. Because they have several advantages over nonmagnetic WSMs. For example, the position of WPs in the reciprocal space and their energy can be tuned by rotating the magnetization of a ferromagnet in an external magnetic field. In this way, the related intrinsic anomalous Hall conductivity and the anomalous Nernst conductivity are also tuned. Further, systems with both TRS and IS broken can by application of an external magnetic field be prepared in a state where the Shubnikov group contains only the identity element. In such a case, pairs of WPs become energy-split and give access to chiral electromagnetic responses (Ray *et al.*, 2022). $Co_3Sn_2S_2$ with TRS breaking, which has six WPs at 60 meV above the Fermi level, is a magnetic WSM that has been extensively examined and investigated both experimentally and theoretically (Liu *et al.*, 2018). Fig. 4 (a) Electronic band structure of $Co_3Sn_2S_2$ showing that spin up spin down channel without SOC and single channel for SOC. (b) Schematic diagram as shown in Fig. 4 denote the two Weyl nodes which are connected by Fermi arc in 3D momentum

space (Bernevig, 2015). One node behave as a source while another node as a sink of Berry curvature.

1.2.4 Topological Nodal Line Semimetals

Topological nodal-line semimetals (TNLSMs) are materials that possess linearly touching conduction and valence bands, forming 1D loops or line in 3D momentum space (Burkov *et al.*, 2011). Topological materials exhibit nontrivial topological properties, and various topological invariants can be associated with them. For instance, each nodal line can be linked to a specific topological invariant, which depends on the symmetry group responsible for preserving the nodal-line structure. The presence of various symmetry groups that protect nodal lines leads to the emergence of distinct types of topological invariants. The Z_2 Berry phase, monopole charge, topological charge for nodal lines protected by both TI symmetries, a Z-invariant for nodal lines protected by mirror-reflection symmetry, and a Z-invariant for nodal lines enforced by nonsymmorphic symmetries are all included in this group of invariants (Chiu and Schnyder, 2014; Yu *et al.*, 2015; Fang *et al.*, 2016). TNLSMs exhibit distinctive surface states, when projected onto the surface, can be found in the energy region between the conduction and valence bands. These surface states are known as "drumhead" surface states because of a distinctive property they have: a flat dispersion (Weng *et al.*, 2015a). These drumhead surface states contribute to a high surface density of states at the E_{F}, making them potential candidates for the realization of phenomena like high-temperature superconductivity or surface magnetism, as well as other intriguing correlated effects on the surface of TNLSMs (Heikkilä *et al.*, 2011; Heikkilä and Volovik, 2011). It is important to note that these drumhead surface states are not inherently topologically protected. The flatness of the surface bands can be broken by even small surface perturbations. Both in the bulk and at the surface, TNLSMs unique electronic structures give rise to exciting phenomena in the areas of transport and optics. Some predicted effects include a non-dispersive Landau-level spectrum, unique collective modes, and a quasi-topological electromagnetic response (Rhim and Kim, 2015; Yan *et al.*, 2016; Ramamurthy and Hughes, 2017). These phenomena are a consequence of the specific properties of TNLSMs and offer opportunities for exploring novel transport and optical behaviors in these materials. In recent times, there has been an increasing recognition of different types of TNLSMs that can be distinguished based on various characteristics of their nodal lines. These characteristics include the crystal symmetry or the mechanisms responsible for their generation. Additionally, distinctions can be made based on factors such as the degeneracy of the band crossing, the slope and order of band dispersion, as well as the linking structure of multiple nodal lines. In the absence of SOC, NLSMs can generally be classified into two main categories based on their characteristics. These categories are: (i) TI-symmetry protected NLSMs: Several materials have been theoret-

ically proposed. These materials include Cu_3PdN, graphene networks, CaTe, the CaP_3 family, LaX (X=N, P, As, Sb, Bi), WHM (W=Zr, Hf, or La; H= Si, Ge, Sn, or Sb; M=O, S, Se, and Te), and Mg_3Bi_2 (Kim *et al.*, 2015; Weng *et al.*, 2015a; Du *et al.*, 2017; Quan *et al.*, 2017; Zeng *et al.*, 2015; Schoop *et al.*, 2016; Zhang *et al.*, 2017). Taking Cu_3PdN as an example, without considering SOC, band inversion occurs at the R point, resulting in the formation of three nodal rings that are perpendicular to each other (see Ref. (Yu *et al.*, 2015)). On the [0 0 1] surface of Cu_3PdN, there are nearly flat surface bands known as drumhead surface states. (ii) Mirror Symmetry protected NLSMs: In this category, the presence of mirror symmetry, which encompasses mirror reflection and mirror glide, helps to stabilize nodal lines on the mirror plane. TaAs is an example of this type of NLSMs. In this case, the band inversion phenomenon gives rise to the formation of twelve nodal rings located within the two mirror planes. These nodal rings enable the two intersecting bands to possess distinct irreducible representations, emphasizing the unique electronic structure and properties of TaAs as a mirror symmetry-protected NLSMs. Other materials that exhibit similar characteristics include Ca_3P_2, CaAgAs, and HfC (Xie *et al.*, 2015; Yamakage *et al.*, 2016; Yu *et al.*, 2017). When considering the effect of SOC, two distinct types of nodal lines can be identified in TNLSMs. These types are mirror-symmetry-protected WNLSMs and nonsymmorphic symmetry-enforced DNLSMs. Materials such as $HgCr_2Se_4$, KCu_2EuTe_4 and $InNbS_2$ exhibit the characteristics of mirror-symmetry-protected WNLSMs (Xu *et al.*, 2011; Bian *et al.*, 2016; Yang *et al.*, 2018). In these materials, the presence of mirror symmetry plays a crucial role in stabilizing Weyl nodal lines. On the other hand, materials such as $SrIrO_3$, $BaMX_3$ (M=V, Nb, or Ta; X=S or Se), IrF_4, and InBi belong to the category of nonsymmorphic symmetry-enforced DNLSMs (Chen *et al.*, 2015; Liang *et al.*, 2016; Bzdušek *et al.*, 2016; Ekahana *et al.*, 2017). In these materials, the nodal lines are protected by nonsymmorphic symmetries, which involve a combination of lattice translations and rotations. These symmetries enforce the presence of Dirac nodal lines in the electronic band structure.

1.2.5 Topological Superconductor

Majorana fermions were initially proposed by Ettore Majorana in 1937 as a concept in elementary particle physics (Majorana, 1937). In condensed matter physics, the idea of Majorana fermions has been extended to quasiparticles, which are superpositions of electron and hole excitations. If the creation operator $\gamma+$ and annihilation operator $\gamma-$ of a quasiparticle are identical, the particle can be considered a Majorana fermion. Topological superconductors (TSCs) have gained significant attention in recent years because they possess protected Majorana surface states (Yupeng and Xu, 2019). The Read-Green model proposes that the Bogoliubov quasiparticles, which are neutral excitations found in superconductors, can be identified as Majorana fermions with a dispersive nature in

the bulk (Read and Green, 2000). These Majorana fermions can form bound states with defects at zero energy, known as Majorana bound states or Majorana zero modes (MZMs) (Wilczek, 2009; Beenakker, 2013). Theoretical predictions suggest that MZMs localized at defects exhibit exotic exchange statistics, similar to non-Abelian anyons. This means that interchanging the positions of MZMs can cause a change in their quantum states. This property of MZMs is particularly appealing as it enables nontrivial transformations within a degenerate ground-state manifold, representing a noncommutative operation that is topologically protected. The specific method or execution details of the exchange do not matter; the outcome remains the same. This topologically protected operation has potential applications in quantum gates and topological quantum computing, as it relies solely on the exchange statistics of quasiparticles. In general, TSCs can be categorized into two types: time-reversal breaking TSCs and time-reversal-invariant TSCs (Ando and Fu, 2015). An example of a time-reversal breaking TSC is Sr_2RuO_4, which is often considered a representative case. Experimental evidence supporting the presence of an internal magnetic field in the superconducting state, which breaks TRS, has been obtained through nuclear magnetic resonance measurements and muon spin rotation experiments (Ishida *et al.*, 1998; Luke *et al.*, 1993). Another approach to realizing time-reversal breaking TSCs involves constructing semiconductor/superconductor heterostructures. In such heterostructures, Majorana zero modes (MZMs) can be localized at the ends of semiconductor nanowires, leading to the emergence of time-reversal breaking TSCs (Mourik *et al.*, 2012). On the other hand, time-reversal-invariant TSCs require strong SOC to induce odd-parity pairing. $Cu_xBi_2Se_3$ has been proposed as a promising candidate for this type of TSC (Fu and Berg, 2010).

1.3 Rational of the Study

In kagome $A_2T_3S_4$, most of the compounds have been experimentally synthesized, and their crystal information data, including lattice parameters and Wyckoff positions, are available. Additionally, electronic and magnetic properties have been predicted (using DFT calculations) and measured (experimentally) for some of them. However, to the best of our knowledge, no reports on its topological properties have been explored to date. Thus, based on the density functional theory approach, we have systematically investigated the electronic, magnetic, and topological Weyl properties of $A_2T_3S_4$.

1.4 Objectives of the Study

1.4.1 General Objective

The general aim and objective of my research work is to explore the kagome $A_2T_3S_4$, and also find its possible application to the modern science and technology.

1.4.2 Specific Objectives

The specific objectives of my research work are:

(a) to investigate the structural stability of proposed system.

(b) to study the electronic, magnetic and optical properties.

(c) to compute the Wannier band mapping.

(d) identification of Weyl points.

(e) calculation of Chern number to confirm the Weyl points.

(f) calculation of topological Fermi arc surface states.

(g) to study the Berry curvature properties.

(h) calculation of intrinsic anomalous Hall conductivity.

CHAPTER 2

LITERATURE REVIEW

2.1 Theoretical/Computational Based Literature Review

Dirac introduced the Dirac equation, initially used to describe spin-1/2 particles in the context of relativistic quantum mechanics (Dirac, 1928). Weyl presented his equation, a simplified version of the Dirac equation. However, due to its violation of parity, Wolfgang Pauli challenged Weyl's equation in 1933 (Weyl, 1929). It's interesting to note that Pauli himself had proposed the neutrino as a new elementary fermion to explain beta decay three years earlier. Later, the neutrino was finally described using the Weyl equation. Herring proposed that Weyl fermions might exist as quasiparticles in condensed matter (Herring, 1937). In 1956, neutrinos were experimentally discovered, demonstrating their extremely low mass (Bilenky, 2005). In the same year, provided experimental proof that weak interaction violated parity, effectively challenging Pauli's earlier criticism (Wu *et al.*, 1957). Neutrino's helicity was determined in 1958. The Weyl equation regained interest after later experiments revealed no proof of neutrino mass. As a result, it was assumed that neutrinos were Weyl fermions while developing the Standard model (Goldhaber *et al.*, 1958). An Italian physicist Pontecorvo, first suggested that neutrinos might have masses and oscillations, but it wasn't until 1998 that the Super-Kamiokande experiment verified the existence of neutrino mass, proving that neutrinos cannot be entirely explained by the Weyl equation since it can only account for massless particles. After this confirmation, research on topological properties in condensed matter has been initiated (Pontecorvo, 1957; Fukuda *et al.*, 1998). Fang *et al.* shows that magnetic monopoles can appear in the crystal momentum space of a solid in the accessible low-energy range (-0.1 to 1 eV) in the context of the anomalous Hall effect. They provide experimental evidence in the ferromagnetic crystal $SrRu_3$ along with first-principle calculations. This study provides the basic evidence that Weyl nodes might exist as magnetic monopoles (Fang *et al.*, 2003). Avron *et al.* provide a comprehensive analysis of the quantum Hall effect from a topological perspective. Their research highlights that the remarkably accurate quantization of Hall conductance in a 2D electron gas can be comprehended by considering a topological property referred to as the Chern number (Avron *et al.*, 2003).

Kane and Mele investigated the influence of spin-orbit interactions on the low-energy electronic structure of a single plane of graphene. They discovered that the edge states in graphene are nonchiral. The study also delves into the calculation of spin and charge conductances within these edge states (Kane and Mele, 2005a). Bernevig and Zhang made a prediction about the quantized spin Hall effect in the absence of a magnetic field. They proposed that the intrinsic spin Hall conductance could be quantized in units of $2\frac{e^2}{h}$. This phenomenon could be achieved through the creation of degenerate quantum Landau levels (Bernevig and Zhang, 2006). Roy demonstrated the presence of topological phases in 3D Bloch insulators with time-reversal symmetry. These phases are distinguished by topological Z_2 invariants, and their stability is analyzed through band-touching arguments (Roy, 2009). Wan *et al.* theoretically proposed that pyrochlore iridates $A_2Ir_2O_7$, specifically $Y_2Ir_2O_7$, can be classified as a WSM with a total of 24 WPs. This material showcases notable topological properties through surface states in the form of Fermi arcs, highlighting the unique nature of pyrochlore iridates in terms of their topological characteristics (Wan *et al.*, 2011). Xu *et al.* based on DFT calculations, proposed that a ferromagnetic compound $HgCr_2Se_4$ has the potential to exhibit a unique quantum state. This quantum state is characterized by the presence of a single pair of Weyl fermions that are spatially separated in momentum space. Notably, they realize the quantum Hall effect even without the application of an external magnetic field (Xu *et al.*, 2011). Young and Kene present a new class of 2D Dirac semimetals that are protected by symmetry. These semimetals possess Dirac cones located at specific high-symmetry points in their electronic band structure. Notably, these Dirac cones remain ungapped even in the presence of spin-orbit interactions. These 2D Dirac semimetals are distinct from that of both graphene and 3D Dirac semimetals (Young and Kane, 2015). Yan and Felser reviewed topological materials and WSMs. In their review article, they discuss the basic concept of topological materials and WSMs as topological materials. They also provide a refined concept of types of semimetals and their properties. This article can provide the strong foundation to start research on WSMs (Yan and Felser, 2017). Shi *et al.* predicted a magnetic WSMs in the inverse Heusler Ti_2MnAl. Despite the vanishing net magnetic moment, they calculate a large intrinsic anomalous Hall effect (Shi *et al.*, 2018). Ghimire *et al.* demonstrated, via density functional electronic structure calculations $Co_3Sn_2S_2$, that Weyl nodes can be created and annihilated through magnetization rotation. In this study they further calculated the anomalous Hall conductivity and Nernst conductivity (Ghimire *et al.*, 2019). Lv *et al.* provided an overview of the recent advancements in 3D TSMs. They discussed the presence of different topological semimetal phases, highlighting the significance of nontrivial surface states, including Fermi arcs observed in Dirac and WSMs. Additionally, the authors explored the unique transport and optical responses exhibited by these materials, such as the chiral anomaly-induced negative magnetoresistance in both Dirac and WSMs (Lv *et al.*, 2021). Karki *et*

al. by means of density-functional theory calculations to explore the influence of hydrostatic pressure on the electronic structure of two phases, namely the *Td* and $1T^{''}$ phases, of the WSM $Mo_{0.5}W_{0.5}Te_2$. The authors suggest that $Mo_{0.5}W_{0.5}Te_2$ holds great potential as a material for two significant technological applications: phase-change memory technology and superconductivity (Karki *et al.*, 2022). Sun *et al.* investigated the properties of the ferromagnetic WSM in $BaCrSe_2$, specifically focusing on the distribution of WPs. Through their research, they confirmed the presence of a long-distance distribution of WPs in the material. Also Chern number and analysis of Fermi arc surface states were conducted. They found only 2 pairs of WPs (Sun *et al.*, 2023).

2.2 Experimental Based Literature Review

Till date several experimental studies have investigated the topological characteristics of materials, including Dirac and Weyl fermions, as well as their surface properties. Klitzing *et al.* conducted measurements on a 2D electron gas using a silicon metal-oxide-semiconductor field-effect transistor. They observed specific values of the Hall voltage at well-defined surface carrier concentrations. Importantly, these values were independent of the device's geometry and solely dependent on fundamental constants (Klitzing *et al.*, 1980). Zhang *et al.* conducted an experimental study on magneto-transport in a single layer of high-mobility graphene. They manipulated the chemical potential using the electric field effect and made a notable observation. This led to the discovery of an atypical phenomenon known as the half-integer quantum Hall effect (Zhang *et al.*, 2005). Lv *et al.* presented experimental evidence for the existence of a Weyl semimetal in the material TaAs. They employed ARPES to observe the formation of Fermi arcs in the surface states of TaAs. These experimental findings were in excellent agreement with their first-principles calculations (Lv *et al.*, 2015). Deng *et al.* presented experimental findings supporting the existence of topological Fermi arcs in the predicted type-II Weyl semimetal $MoTe_2$. They provided evidence for these topological surface states by directly observing them using both bulk and surface-sensitive ARPES (Deng *et al.*, 2016). Haubold *et al.* presents experimental evidence for a type-II noncentrosymmetric Weyl state in $TaIrTe_4$, as recently predicted theoretically. They found direct correspondence between ARPES data and calculated electronic structure both in the bulk and the surface. They clearly observed exotic surface states supporting quasi-one-dimensional Fermi arcs that connect only four WPs (Haubold *et al.*, 2017). Ye *et al.* studied the d-electron kagome metal Fe_3Sn_2. They observed a temperature-independent intrinsic anomalous Hall conductivity that persists above room temperature, suggesting the presence of Berry curvature from time-reversal symmetry-breaking electronic bands in the kagome lattice (Ye *et al.*, 2018). Borisenko *et al.* used a combination of ARPES, magnetization measurements, and magneto-optical microscopy to investi-

gate the electronic properties of the time-reversal symmetry-breaking type-II Weyl state in the material $YbMnBi_2$. They observed WPs and a Fermi arc on the Fermi surface through both experimental and theoretical calculations using semi-infinite-slab models (Borisenko *et al.*, 2019). Kang*et al.* conducted a study on the kagome metal CoSn using a combination of ARPES and band structure calculations. Their investigation revealed the existence of topological flat bands in CoSn, providing evidence that flat bands derived from the kagome lattice have the potential to serve as a promising platform for the emergence of novel phases of matter, combining strong correlation effects and topological properties (Kang *et al.*, 2020). Li *et al.* studied on kagome YMn_6Sn_6, combining ARPES measurements with theoretical calculations. They observed the presence of a Dirac point and a flat band near the Fermi level. These features were found to arise from a spin-polarized band with intrinsic Berry curvature, potentially explaining the anomalous Hall effect observed in transport measurements (Li *et al.*, 2021). Wu *et al.* provided spectroscopic evidence revealing a distinctive interplay between topology and correlation effects in the kagome superconductor CsV_3Sb_5. They observed the presence of topologically nontrivial surface states near the Fermi energy, indicating that the system's topological physics may become active upon entering the superconducting state. Additionally detected flat bands (Wu *et al.*, 2022). Sakhya *et al.* utilized ARPES in combination with density functional theory calculations to identify CeAlSi as a novel noncentrosymmetric magnetic WSM. Additionally, surface-sensitive vacuum ultraviolet ARPES measurements provided conclusive evidence of the presence of surface Fermi arcs in CeAlSi (Sakhya *et al.*, 2023).

2.3 Research Gap

The study of topological Weyl properties has attracted many physicists in the present day due to extensive applications and its potential as a foundation for future technologies. One interesting aspect is the interplay between magnetism and topology in magnetic materials, giving rise to unusual quantum phenomena. Based on a review of the literature, it is evident that there has been a significant time gap between the discovery of the Weyl equation in 1929 and the theoretical/experimental prediction of WSMs. From 2011 until now, only a limited number of Weyl materials have been discovered both experimentally and theoretically. Among these discoveries, the prediction and observation of kagome WSMs are particularly rare. This has sparked our interest in exploring the Weyl semimetallic properties in the kagome $A_2T_3S_4$ series, as we believe they may exhibit such properties.

CHAPTER 3

MATERIALS AND METHODS

3.1 Theoretical Background

Investigation of the fundamental properties of quantum mechanical systems at their lowest energy state is a formidable challenge. While the Hydrogen atom, which involves two interacting particles, can be mathematically solved, the same is not true for Helium. Solving the Helium atom problem analytically is not possible. Alternatively, small quantum systems can be solved numerically using methods such as matrix diagonalization. However, the difficulty arises from the fact that the dimension of the parameter space increases exponentially with the size of the system. Consequently, computational limitations are quickly encountered. Walter Kohn, a prominent figure in the development of density functional theory (DFT), addressed this issue in his Nobel prize lecture. He estimated that the parameter space required to describe a system comprising 100 interacting particles would surpass the number of baryons (subatomic particles like protons and neutrons) in the entire universe. He referred to this limitation as the “exponential wall" (Kohn, 1999). Hence, intricate many-body systems, such as solids, necessitate alternative approaches for their solution. Among these approaches, DFT is widely recognized. In this section, we provide a straightforward overview of DFT. We follow Refs. [(Tsuneda, 2014) and (Martin, 2020),] to develop the concepts of Hartree method, Hartree-Fock method and Thomas-Fermi-Dirac approximation.

3.1.1 Hartree and Hartree-Fock Method

In 1928, just two years after the publication of the Schrödinger equation, Hartree proposed the Hartree method-a technique for solving this equation for multiple-electron systems, based on fundamental physical principles, the Hartree method (Hartree, 1928).

Before discussing the Hartree method, let us know the charge density and the equations determining the one-particle wave functions. Charge density, measures the electric charge per unit volume at a given point in space. It describe how charge is distributed in a region of space. It can be expressed in terms of the wave functions of the electrons in

a material. For a single electron in a potential V(r), the time-independent Schrödinger equation is:

$$\hat{H}\Psi(r) = E\Psi(r) \tag{3.1}$$

$$\hat{H} = \frac{-h^2}{2m}\nabla^2 + V(r) \tag{3.2}$$

where $\hbar$ is the planck constant, ∇^2 is the Laplacian operator and E is the energy eigenvalue associated with the wave function Ψ(r).

Hartree postulated that electrons move within the averaged potential resulting from electrostatic interactions with neighboring electrons. He proposed the independent electron approximation, wherein the averaged potential is approximated as an effective potential. So, the wavefunction can be represented as the product of two one-particle electronic wavefunctions,

$$\psi(r_1, r_2) = \phi_1(r_1)\phi_2(r_2) \tag{3.3}$$

Hartree developed the self-consistent field (SCF) method. In this method, the average field is calculated iteratively until it converges to a self constant solution. The self interaction energy is,

$$E_{Hartree} = \frac{1}{2}\int d^3r d^3r' \frac{n(r)n(r')}{|r - r'|} \tag{3.4}$$

However, as time went on, it became apparent that the energies obtained using this method were inaccurate to be useful in analyzing chemical processes and characteristics. It has been found that the primary reason of the inaccuracies was missing the presence of electron-electron exchange interactions (Tsuneda, 2014). The Hartree-Fock method, established in 1930 by Fock (Fock, 1930), is a commonly used technique in many-particle theory. It involves constructing an appropriately antisymmetrized determinant wavefunction for a specified number (N) of electrons. Finding the unique determinant that reduces the total energy related to the full interacting Hamiltonian is the aim. In the absence of spin orbit coupling, a Slater determinant (Slater, 1929) can be used to express the determinant wavefunction as follows:

$$\phi = \frac{1}{(N!)^{1/2}} = \begin{vmatrix} \phi_1(r_1,\sigma_1) & \phi_1(r_2,\sigma_2) & \phi_1(r_3,\sigma_3) & .... \\ \phi_2(r_1,\sigma_1) & \phi_2(r_2,\sigma_2) & \phi_2(r_3,\sigma_3) & .... \\ \phi_3(r_1,\sigma_1) & \phi_3(r_2,\sigma_2) & \phi_3(r_3,\sigma_3) & .... \\ . & . & . & .... \\ . & . & . & .... \end{vmatrix} \tag{3.5}$$

where, the $\phi_i(r_j,\sigma_j)$ are single particle spin-orbitals. Without spin orbit interaction case, $\phi_i(r_j,\sigma_j)$ can be expressed as a product of function of position, $\psi_i^{\sigma}(r_j)$ and a function of the spin variable, $\alpha_i(\sigma_j)$. Note that in closed-shell cases, $\phi_i(r_j,\sigma_j)$ is independent of spin σ. This assumption is corresponding to the spin-restricted Hartree–Fock approximation in open-shell systems. When the spin functions are quantized on an axis, the Hartree-Fock equations are obtained by varying $\psi_i^{\sigma_i^*}(r)$ for each spin
$\Big[-\frac{1}{2}\nabla^2 + V_{ext}(r) \sum_{j,\sigma_j} \int dr' \psi_j^{\sigma_j^*}(r')\psi_j^{\sigma_j}(r') \frac{1}{|r-r'|} \Big] \psi_i^{\sigma}(r)$

$$- \sum_j \int dr' \psi_j^{\sigma^*}(r')\psi_i^{\sigma}(r') \frac{1}{|r-r'|} \psi_j^{\sigma}(r) = \epsilon_i^{\sigma} \psi_i^{\sigma}(r) \tag{3.6}$$

the equation adds up the exchange term for all similar spin orbitals, including when i = j. This eliminates an unwanted self-term present in the direct term. By adjusting the exchange term using a multiplication and division involving $\psi_i^{\sigma}(r)$, equation (3.6) can be written in a way similar to the non-interacting (Hartree-like) electron approximation. The key difference is that the effective Hamiltonian is an operator that relies on the specific state.

$$\hat{H}^i_{eff} \psi_i^{\sigma}(r) = \Big[-\frac{\hbar^2}{2m_e}\nabla^2 + \hat{V}^{i,\sigma}_{eff}(r) \Big] \psi_i^{\sigma}(r) = \epsilon_i^{\sigma} \psi_i^{\sigma}(r), \tag{3.7}$$

with

$$\hat{V}^{i,\sigma}_{eff}(r) = V_{ext}(r) + V_{Hartree}(r) + \hat{V}^{i,\sigma}_{x}(r), \tag{3.8}$$

the exchange operator term is given by

$$\hat{V}^{i,\sigma}_{x}(r) = -\sum_j \int dr' \psi_j^{\sigma^*}(r')\psi_i^{\sigma}(r') \frac{1}{|r-r'|} \frac{\psi_j^{\sigma}(r)}{\psi_i^{\sigma}(r)}. \tag{3.9}$$

Thus, for each orbital ψ_i^{σ}, the equation is expressed in relation to the exchange operator $V_{ext}(r)$, which includes an integral incorporating ψ_i^{σ} and all other ψ_j^{σ} of the same

spin. Unlike independent Hartree-like equations, HF equations are routinely solved in all available quantum chemical codes for large molecules or clusters. Ignorance of electron correlation is one of the main drawbacks of the Hartree-Fock approximation. Additionally, the basis set selection has a significant impact on the accuracy of HF predictions. Results from different basis sets can differ significantly, and large computationally expensive basis sets are frequently needed to achieve high accuracy.

3.2 Density Functional Theory

3.2.1 Thomas-Fermi-Dirac Approximation

The Hartree-Fock technique was the first attempt in condensed matter physics to improve the incorporation of electron correlation in models defining electronic motion states. However, until the 1980s, the huge amount of processing time needed to perform quantum-mechanical calculations restricted their practical applicability to theorists' trial usage. These computational difficulties were overcome with the advent of DFT in the 1990s, which was a groundbreaking development. Since then, DFT has become widely accepted and is now the most commonly used theory in condensed matter physics research publications (Tsuneda, 2014). The core concept of DFT is to describe the potential by looking at the electron density instead of the orbital wave function. This approach enables quick calculations for systems with many electrons. The idea emerged just a year after the development of the Schrödinger equation and the introduction of the Hartree method in 1927. Thomas established this fundamental idea of DFT to address the electronic motion states of solid crystals within the context of the Schrödinger equation (Thomas, 1927). According to his theory, the Schrödinger equation can be solved based on the electron density in the electronic state of a uniform electron gas. It also states that the external potential, which is the same as the nuclear-electron interaction potential in the absence of an electromagnetic field, depends only on the distances, which are defined by nuclear charge and electron density, from the nuclei. Next, the electron density n(r) kinetic energy functional is developed, expanding upon these suppositions, which is given by following equation,

$$T^{TF} = C_F \int d^3 r n^{5/3}(r), \tag{3.10}$$

$$C_F = \frac{3}{10}(3\pi^2)^{2/3} \tag{3.11}$$

Using Fermi statistics at zero temperature, Fermi independently developed the same kinetic energy functional as Thomas in the next year (1928). After this was finished, the Hartree approach was extended and became known as the Thomas-Fermi method (Fermi, 1928). The Thomas-Fermi method, while interesting in its representation of the Hamiltonian operator as a functional of the electron density, is not very useful for electronic state computations in practice, even when used for qualitative considerations. Dirac ascribed this constraint to the lack of exchange energy, a theory put forth by Fock in the same year (Fock, 1930). Also, presenting the first exchange functional of electron density n(r) (Dirac, 1930), which is described as follows:

$$E_x^{LDA} = -\frac{3}{4}\left(\frac{3}{\pi}\right)^{1/3} \int d^3r n^{4/3}(r). \tag{3.12}$$

This functional has been identified as the precise exchange functional within the framework of Local Density Approximation (LDA). Additionally, von Weizsäcker (Weizsäcker, 1935) introduced a correction term that incorporates the gradient of electron density for the Thomas Fermi kinetic energy functional.

$$T^W = \frac{1}{8}\int d^3r \frac{|\nabla n(r)|^2}{n(r)} \tag{3.13}$$

Parr and Yang (1994) proved that the 1/9 th value for this term is accurate and serves as the exact correction term for the Thomas-Fermi kinetic energy functional (Parr and Weitao, 1994). This correction term is recognized as the first example of a generalized gradient approximation (GGA) since it involves the gradient of the electron density n(r). The Thomas-Fermi approach has been refined many times, but none of these attempts have been effective in proving the reliability of the system. The method was widely ignored until the mid-1960s due to its inability to replicate structures of atoms and binding of molecules qualitatively and the lack of a physical basis for the existence of density functional and the uniqueness of solutions.

3.2.2 The Hohenberg-Kohn Theorems

Density functional theory is framed by Hohenberg and Kohn as an accurate representation of many-body systems (Hohenberg and Kohn, 1964). This formulation is applicable to any system of interacting particles within an external potential $V_{ext}(r)$, including electron and fixed-nuclei problems, where the Hamiltonian can be expressed as,

$$\hat{H} = -\frac{\hbar^2}{2m_e}\sum_i \nabla_i^2 + \sum_i V_{ext}(r_i) + \frac{1}{2}\sum_{i\neq j}\frac{e^2}{|r_i - r_j|}. \tag{3.14}$$

Theorem I

In any system of interacting particles within an external potential $V_{ext}(r)$, the potential $V_{ext}(r)$ is uniquely determined, with the exception of a constant term, based on the ground-state particle density $n_0(r)$. This unique determination of the potential allows for the determination of the many-electron wave functions. Consequently, all characteristics and features of the system can be fully determined solely based on the ground state density $n_0(r)$. Suppose we have two different external potentials $V^1_{ext}(r)$ and $V^2_{ext}(r)$ that differ by more than a constant, but lead to the same density n(r). Here, two external potential belong to two distinct Hamiltonian $H_1(r)$ and $H_2(r)$, which gives rise to distinct ground state wave-functions ψ_1 and ψ_2 respectively. Also that are hypothesized to have the same ground state density $n_0(r)$.

Since ψ_2 is not the ground state of $H_1(r)$, it follows that

$$E_1 = \langle \psi_1 | H_1 | \psi_1 \rangle < \langle \psi_2 | H_1 | \psi_2 \rangle \tag{3.15}$$

The strict in-equality follows if the ground state is non-degenerate. Because of the identical ground state density for the two Hamiltonian, the last term of above equation can be written as

$$\langle \psi_2 | H_1 | \psi_2 \rangle = \langle \psi_2 | H_2 | \psi_2 \rangle + \langle \psi_2 | H_1 - H_2 | \psi_2 \rangle \tag{3.16}$$

$$= \int d^3r [V^1{}_{ext}(r) - V^2{}_{ext}(r)] n_0(r) \tag{3.17}$$

so that

$$E_1 < E_2 + \int d^3r [V^1{}_{ext}(r) - V^2{}_{ext}(r)] n_0(r) \tag{3.18}$$

By considering the E_2 in exactly the same way,

$$E_2 < E_1 + \int d^3r [V^2{}_{ext}(r) - V^1{}_{ext}(r)] n_0(r) \tag{3.19}$$

Now if we add equation 3.16 and 3.17 we get,

$$E_1 + E_2 < E_2 + E_1 \tag{3.20}$$

Which is obviously a contradiction. so our initial assumption must be wrong that means two different potential can not yield the same ground state density. This means that the external potential is uniquely determined by the density within a constant.

Theorem II

The universal functional for the energy, denoted by E[n], can be defined in terms of the density $n(r)$, which is valid for any external potential $V_{ext}(r)$. For a given $V_{ext}(r)$, the exact ground state energy of the system is the minimum value of this functional, and the density $n(r)$ that minimizes the functional is the exact ground state density $n_0(r)$. Therefore, the functional $E[n]$ alone is enough to determine both the exact ground state energy and density of the system.

First we define the functional from the Hamiltonian:

$$E_{HK}[n] = T[n] + E_{int}[n] + \int V_{ext}(r)n(r)d^3r + E_{II} \tag{3.21}$$

$$= F_{HK}[n] + \int V_{ext}(r)n(r)d^3r + E_{II}, \tag{3.22}$$

where $T[n] + E_{int}[n] = F_{HK}[n]$ encompasses all internal energies, such as kinetic and potential energies of electrons within the interacting system. Furthermore, it is inherently universal in design, as the kinetic and interaction energies of electrons are solely dependent on the density. Last term E_{II} denote the interaction energy between the nuclei.

Suppose $n_1(r)$ is the ground state density of the system and corresponding potential is $V^1_{ext}(r)$. The Hohenberg-Kohn functional is equal to the expectation value of the Hamiltonian in the unique ground state having wave function ψ_1

$$E_1 = E_{HK}[n_1] = \langle \psi_1 | H | \Psi_1 \rangle \tag{3.23}$$

and $n_2(r)$ is the another density of $V^2_{ext}(r)$ correspond to ψ_2

$$E_1 = E_{HK}[n_1] = \langle \psi_1 | H | \Psi_1 \rangle < \langle \psi_2 | H | \Psi_2 \rangle = E_{HK}[n_2] = E_2. \tag{3.24}$$

Consequently, if the functional $F_{HK}[n]$ were identified, minimizing the system's total energy, as per equation (3.22), with respect to variations in the density function n(r), would lead to the determination of the precise ground-state density and energy.

3.2.3 Constrained Search Formulation of Density Functionals

Levy and Lieb provide a more comprehensive and intuitive explanation of the functional (Levy, 1979,9; Lieb, 2002). They formalize the functionals definition and give clarity to its physical relevance. This modification enables an in-principle method for exactly calculating the functional, resulting in the same ground-state density and energy as the Hohenberg-Kohn analysis at the minimum. Furthermore, their technique is appropriate even in the presence of degenerate ground states. Levy and Lieb propose a two-step minimization process that starts with the general expression for energy in relation to the many-body wavefunction ψ. The concept involves initially minimizing the energy with respect to all variables in the wavefunction ψ to find the ground state. However, they suggest an alternative approach by first examining the energy for a specific set of many-body wavefunctions ψ that have the same density n(r). For any wavefunction total energy can be express as

$$E = \left\langle \psi | \hat{T} | \Psi \right\rangle + \left\langle \psi | \hat{V}_{int} | \Psi \right\rangle + \int d^3 r V_{ext}(r) n(r). \tag{3.25}$$

If one minimizes the above energy equation over the class of wavefunctions with the same density n(r), one can define the unique lowest energy for that density,

$$E_{LL}(n) = \lim_{\psi \to (n(r)} [\left\langle \psi | \hat{T} | \Psi \right\rangle + \left\langle \psi | \hat{V}_{int} | \Psi \right\rangle] + \int d^3 r V_{ext}(r) n(r) + E_{II} \tag{3.26}$$

$$\equiv F_{LL}[n] + \int d^3 r V_{ext}(r) n(r) + E_{II}, \tag{3.27}$$

where Levy-Lieb functional of the density defined by

$$F_{LL}[n] = \lim_{\psi \to (n(r))} \left\langle \psi | \hat{T} + \hat{V}_{int} | \Psi \right\rangle \tag{3.28}$$

3.2.4 The Kohn-Sham Ansatz

Hohenberg and Kohn's formulation of DFT has two main limitations. Firstly, the specific form of the functional F_{HK}[n] is generally unknown, making it impossible to use a simple variational approach to directly find the ground state density. Secondly, while there exists a unique relationship between the ground state density and the properties of a solid, there is currently no known method to extract these properties directly from the density. In 1965, Kohn and Sham proposed a method to simplify the full interacting many-body problem by introducing a non-interacting auxiliary problem (Kohn and Sham, 1965). Their approach is based on the assumption that the ground state density of the

interacting system can be described using the ground state density of a carefully chosen non-interacting system. The crucial idea is to reintroduce orbitals for non-interacting electrons and reformulate the many-body problem in terms of an exchange-correlation functional that depends on the density. By doing so, the Hohenberg-Kohn functional F_{HK}[n] is reduced to the kinetic energy of these non-interacting fictitious electrons. The auxiliary Kohn-Sham Hamiltonian for the independent-particle system, replacing equation 3.23, is defined as follows

$$H_{KS}^{\sigma} = -\frac{1}{2}\nabla^2 + V_{KS}^{\sigma}(r) \tag{3.29}$$

where σ indicates the spin-index.

The N = N↑ + N↓ electrons occupy orbitals ψ_i^{σ}(r), where i represent the orbital index. These orbitals are determined by solving the Schrödinger-like Kohn-Sham equations to obtain the lowest eigenvalues:

$$(H_{KS}^{\sigma} - \epsilon_i^{\sigma})\psi_i^{\sigma}(r) = 0 \tag{3.30}$$

where ϵ_i are the corresponding Kohn-Sham eigenvalues. The density of the Kohn-Sham system is given by the sums of squares of the orbitals for each spin

$$n(r) = \sum_{\sigma} n(r,\sigma) = \sum_{\sigma}\sum_{i=1}^{N^{\sigma}} |\psi_i^{\sigma}(r)|^2 \tag{3.31}$$

and the Kohn-Sham independent particles kinetic energy is given by

$$T_s = \frac{-1}{2}\sum_{\sigma}\sum_{i=1}^{N^{\sigma}} \left\langle \psi_i^{\sigma}|\nabla^2|\psi_i^{\sigma}\right\rangle^2 = \frac{1}{2}\sum_{\sigma}\sum_{i=1}^{N^{\sigma}} \int d^3r|\nabla\psi_i^{\sigma}(r)|^2 \tag{3.32}$$

The energy associated with the classical Coulomb interaction of the electron density with itself is given by the Hartree energy

$$E_{Hartree}[n] = \frac{1}{2}\int \frac{n(r)n(r')}{|r-r'|} d^3r d^3r' \tag{3.33}$$

Kohn and Sham chose to write the total energy of full interacting many-body problem with the Hohenberg-Kohn expression for the ground-state energy functional in the form

$$E_{KS} = T_s[n] + E_{Hartree}[n] + \int V_{ext}(r)n(r)dr + E_{II} + E_{xc}[n] \tag{3.34}$$

where, $V_{ext}(r)$ represents the external potential arising from the nuclei and other external fields, while E_{II} denotes the interaction among the nuclei.

3.3 Exchange-Correlation Functional

To summarize, the Kohn-Sham ansatz provides an exact method for determining the ground-state density and total energy without any initial approximations. However, the exchange-correlation functional, which is necessary for the calculation, is not known precisely. The Kohn-Sham equations have been introduced as a way to overcome the challenges associated with solving the full many-body problem. These equations enable the accurate calculation of most of the electron system's total energy. Only a small portion, known as the exchange-correlation energy, needs to be approximated. Two different approaches can be distinguished for developing these approximations: empirical and non-empirical. Empirical functions are constructed to closely match experimental data, while non-empirical functions are based on established physical constraints that the functional must adhere to.

3.3.1 The Local Spin Density Approximation (LSDA)

In their influential paper, Kohn and Sham highlighted the notion that solids can be viewed as approaching the limit of a homogeneous electron gas. At this limit, the influence of exchange and correlation is recognized to be locally defined. Consequently, they introduced the concept of the local density approximation (LDA) or, more broadly, the local spin density approximation (LSDA). In these approximations, the exchange-correlation energy is represented as an integral across all space, with the assumption that the exchange-correlation energy density at each point is similar to that of a homogeneous electron gas with the corresponding density,

$$E_{xc}^{LSDA}[n^{\uparrow}, n^{\downarrow}] = \int d^3(r)(n(r))\epsilon_{xc}^{hom} n^{\uparrow}(r), n^{\downarrow}(r) \tag{3.35}$$

$$E_{xc}^{LSDA}[n^{\uparrow}, n^{\downarrow}] = \int d^3(r)(n(r))[\epsilon_{x}^{hom} n^{\uparrow}(r), n^{\downarrow}(r) + \epsilon_{c}^{hom} n^{\uparrow}(r), n^{\downarrow}(r)]. \tag{3.36}$$

The exact form of the correlation component is currently unknown and thus requires an approximation. Initially, approximations based on perturbation theory were developed (Gunnarsson and Lundqvist, 1976; von Barth and Hedin, 1972). However, modern approaches parameterize the correlation part using data obtained from quantum Monte

Carlo simulations of the homogeneous electron gas (Ceperley and Alder, 1980). Since the homogeneous electron gas resembles a perfect metal, the LDA is particularly well-suited for metallic solids. Surprisingly, LDA also yields satisfactory results for other systems like molecules due to systematic error cancellation (Capelle, 2006). However, LDA tends to overestimate binding energies, leading to shorter bond lengths. Examples of LDA exchange-correlation functionals include the Vosko, Wilk, and Nusair (VWN) or Perdew and Wang (PW) implementations (Vosko *et al.*, 1980; Perdew *et al.*, 1996).

3.3.2 Generalized Gradient Approximation (GGA)

In actual systems, the distribution of electrons is typically non-uniform, resulting in the presence of density gradients. The LDA can be viewed as a basic estimate based solely on the local electron density value, without accounting for its derivatives. Therefore, to improve on the LDA, additional functions are needed that consider not only the local electron density value but also its gradients. Attempts to incorporate higher-order corrections, such as $|\nabla n(r)|$ and $|\nabla^2 n(r)|$, through gradient expansion approximations have generally been unsuccessful in improving the accuracy of results. However, a significant breakthrough occurred when a more comprehensive functional, known as the generalized gradient approximations was introduced. Unlike the previous power series expansions, the GGA considers a broader range of terms involving both $n(r)$ and its gradient $\nabla n(r)$. Mathematically this can be written as $E_{xc}^{GGA}[n^{\uparrow}, n^{\downarrow}] = \int d^3(r)(n(r))\epsilon_{xc}(n^{\uparrow}, n^{\downarrow}, |\nabla n^{\uparrow}|, |\nabla n^{\downarrow}|, ..)$

$$\equiv \int d^3(r)(n(r))\epsilon_x^{hom} F_{xc}(n^{\uparrow}, n^{\downarrow}, |\nabla n^{\uparrow}|, |\nabla n^{\downarrow}|, ..) \tag{3.37}$$

where F_{xc} is dimensionless, ϵ_x^{hom} is the exchange energy of the unpolarized gas GGA functions are particularly beneficial when dealing with systems characterized by a non-uniform electron density. One widely employed GGA function in the field of solid-state physics is the Perdew, Burke, and Ernzerhof (PBE) implementation (Perdew *et al.*, 1996). The PBE function addresses the issue of overestimating binding energies found in the LDA, but it tends to slightly overestimate bond lengths in a systematic manner. Several functions, including the PBE function, are considered non-empirical in nature, meaning they are not derived from experimental measurements.

3.3.3 Hubbard-Corrected DFT Energy Functionals: DFT+*U*

The Hubbard model is one of the simplest models developed to provide a semi-quantitative explanation for the physics of correlated materials (Hubbard, 1964). This model is especially suitable to describe systems in which electrons are confined on atomic orbitals, according to its real-space second-quantization formalism (Hubbard,

1965). It includes the “on-site repulsion," which results from electrons within the same atomic orbitals repulsion toward each other via Coulomb forces. As a result, the Hubbard model can explain how the conducting and insulating characteristics seen in these systems change. With this model, an additive Hubbard term that takes electronic interactions into account directly can be included, creating a new Hamiltonian. The additive Hubbard Hamiltonian can be represented in its simplest form as follows (Cococcioni, 2012):

$$H_{Hub} = t \sum_{\langle i,j\rangle,\sigma} (C^{\dagger}_{i,\sigma} C_{j,\sigma} + h.c.) + U \sum_{i} n_i, \uparrow n_i, \downarrow \tag{3.38}$$

The two terms, t and U, are where the Hubbard Hamiltonian depends, as expected. The nearest-neighbor atomic sites are denoted by $\langle i, j\rangle$, and the electronic creation, annihilation, and number operators, which correspond to the spin electrons on site i, are denoted by $c^{\dagger}_{i}$, c_j, and n_i, respectively. The hopping amplitude, t, has a direct proportionality to the valence electrons' bandwidth, or dispersion. At the same time, the product of the occupation numbers of atomic states on the same site determines the on-site Coulomb repulsion term, U. The insulating nature of the system emerges when electrons lack the necessary energy to overcome the repulsive potential posed by electrons on neighboring sites, specifically when the hopping amplitude (t) is much smaller than the on-site (U). The accuracy of the DFT in predicting electronic properties is reliable when t is much larger than U. However, for substantial U values, DFT notably falls short compared to the HF method. The HF method describes the electronic ground state using a variationally optimized single determinant, but it fails to capture the physics of Mott insulators in such instances (Pavarini *et al.*, 2012; Austin and Mott, 1970). One of the most straightforward corrective techniques developed to increase the accuracy of DFT functionals in defining the ground state of correlated systems is the LDA+U or GGA+U. Its basic idea is to represent “strongly correlated" electronic states (usually localized d or f orbitals) using the Hubbard Hamiltonian, while treating the remaining valence electrons at the "standard" level of approximation (Anisimov and Gunnarsson, 1991; Anisimov *et al.*, 1997). The main reasons for the DFT+U method's success are its simplicity of use, its relatively low computing cost, and having the capacity to predict the accurate magnetic ground state of Mott insulators (Anisimov *et al.*, 1997; Tancogne-Dejean *et al.*, 2017). The total energy of a system within DFT+U can be expressed as follows (Pavarini *et al.*, 2012):

$$E_{DFT+U}[n(r)] = E_{DFT}[n(r)] + E_{Hub}[n^{I\sigma}_{mm'}] - E_{dc}[n^{I\sigma}] \tag{3.39}$$

In this formula, the term E_{Hub} denotes the Hubbard Hamiltonian component that includes electron-electron interactions. Because this correction is additive, it becomes necessary to eliminate the part of interaction energy that is already included in E_Hub from the (approximate) DFT energy functional, E_{LDA}, in order to avoid double-counting. This is achieved by subtracting the "double-counting" (dc) term, E_{dc}, which simulates the contribution to the DFT energy arising from correlated electrons in a mean-field approximation to E_{Hub}. The dc term is not uniquely defined because there isn't an exact diagrammatic expansion of the DFT total energy, hence several formulations and implementations will be used (Anisimov *et al.*, 1997). It should be noted that the Hubbard correction only affects the system's localized states. As projections of occupied Kohn-Sham orbitals (ψ^{σ}_{kv}) onto the states of a localized basis set (ϕ^{I}_{m}), it is essentially a functional dependent on occupation numbers:

$$n^{I\sigma}_{mm'} = \sum_{k,v} f^{\sigma}_{kv} \left\langle \psi^{\sigma}_{kv} | \phi^{I}_{m'} \right\rangle \left\langle \psi^{\sigma}_{kv} | \phi^{I}_{m} \right\rangle \tag{3.40}$$

The Fermi-Dirac occupations of the KS states, denoted as f_{kv}, are crucial in this context (where k and v represent the k-point and band indexes, respectively). When these occupations, as defined in equation (3.40), are applied to the functional in equation (3.38), it involves replacing the number operators from equation (3.39) with their mean-field averages over the occupied manifold of the system. While this substitution is essential for implementing the Hubbard model in current DFT implementations, it's worth noting that the choice of the localized basis set is not unique. Popular options include atomic orbitals or maximally localized Wannier functions (Pavarini *et al.*, 2012).

3.3.4 Modified Becke–Johnson Functional: GGA+mBJ

Becke and Johnson (BJ) introduced a notably simple effective local potential for exchange, and its value at a specific point, denoted as r, depends only on densities evaluated at that same point (Becke and Johnson, 2006). Despite its simplicity, this local potential provides a good approximation to the potential derived from the nonlocal Fock operator. In 2007, an exchange potential proposed by Becke and Johnson, designed to mimic the shape of the exact exchange optimized effective potential of atoms. Their findings indicated that this potential outperforms LDA and GGA potentials in describing band gaps. However, when the BJ potential is used in conjunction with LDA correlation, it still significantly underestimates band gaps, indicating a need for improvement (Tran *et al.*, 2007). In addressing this, Tran and Blaha in 2009 introduced a simple modification by incorporating the parameter 'c' to the original BJ exchange potential, termed the mBJ potential. This modification aims to enhance the accuracy of the potential in predicting

band gaps (Martin, 2020). The mathematical expression as

$$V_x^{MBJ}(r) = cV_x^{BR}(r) + (3c-2)\frac{1}{\pi}\sqrt{\frac{5}{12}}\sqrt{\frac{2t(r)}{n(r)}}, \tag{3.41}$$

where, V_x^{BR}(r) represents the local potential as defined by Becke and Roussel (Becke and Roussel, 1989), closely related to the Slater potential, and when c=1, it corresponds to the original BJ potential. Moreover, V_x^{BR}(r) stands as a semilocal potential, making it significantly more computationally efficient compared to hybrid functionals. By selecting a value for c within the range of 1.1 to 1.3, it has been observed that the resulting band gaps exhibit remarkable agreement with experimental data (Waroquiers *et al.*, 2013).

3.4 Wannier Function

We strictly follow the Refs. [(Vanderbilt, 2018; Taherinejad *et al.*, 2014)] to develop concepts of Wannier function.

We define Wannier function for the isolated band and relate for the multi band system. For this we have isolated band $E_n(k)$ which is smooth and periodic function of k in 3D reciprocal space. The Fourier transform of $E_n(k)$ to real space is ,

$$E_{nR} = \frac{V_{cell}}{(2\pi)^3}\int e^{-i\vec{k}.\vec{R}}E_{nk}d^3k \tag{3.42}$$

where,

$E_{nk} = \Sigma_R e^{i\vec{k}.\vec{R}}E_{nR}$

The two orthogonal identities supports the consistency between these two pair of equations,

$$\int_{BZ} e^{ik.(\vec{R}-\vec{R'})}d^3k = \frac{(2\pi)^3}{V_{cell}}\delta_{R,R'} \tag{3.43}$$

and

$$\Sigma_R e^{i(\vec{k}-\vec{k'}).\vec{R}} = \frac{(2\pi)^3}{V_{cell}}\delta^3(k-k') \tag{3.44}$$

Here we can say $E_n(k)$ is smooth in k-space and E_{nR} to be large only for few lattice vector R near the origin otherwise decays rapidly with increasing $|\vec{R}|$. Now we choose a smooth and periodic gauge for the Bloch function $|\psi_{nk}\rangle$ associated with this band. Then

the Fourier transform of this becomes,

$$|w_{nR}\rangle = \frac{V_{cell}}{(2\pi)^3}\int_{BZ} e^{-i\vec{k}.\vec{R}}|\psi_{nk}\rangle d^3k \tag{3.45}$$

where,

$|\psi_{nk}\rangle = \Sigma_R e^{i\vec{k}.\vec{R}}|w_{nR}\rangle$

The Fourier-transform partner of the Bloch wave function in above two equation are called the Wannier function associated with band n.

3.5 Computational Tool

3.5.1 Full Potential Local Orbital Code

Full potential local orbital (FPLO) code is a computational code based on density functional theory that is widely used for electronic structure calculations. It is known for its high accuracy, ease of use, and stable numerics. The code is built upon the framework of the Kohn-Sham (KS) and Kohn-Sham-Dirac equations, and offers both non-relativistic and relativistic versions, including a four-component Dirac version (Koepernik and Eschrig, 1999). In the non-relativistic version of FPLO, extended states are represented as a linear combination of local orbitals. These orbitals are solutions to an atom-like Schrödinger equation with a spherically averaged potential. The orbitals are classified as either core states or valence states, depending on whether they are treated to be overlapping or non-overlapping between different sites. FPLO also features four modes of treating relativistic effects: non-relativistic, two categories of scalar relativistic, and full relativistic. It offers two exchange-correlation potential functionals: the Perdew-Burke-Ernzerhof functional (GGA) and the Local Spin Density Approximation (LSDA). For highly correlated systems, FPLO implements the LSDA+U and GGA+U functionals. In FPLO, atomic position optimization can be performed via force calculation, which is implemented in the scalar relativistic modes. Fixed spin moment calculations are available for all four relativistic modes, making FPLO a comprehensive tool for electronic structure studies. Wannierization of the FPLO band structure enables post-processing and model extraction, specifically the computation of topological characteristics, topological surface states, dHvA spectra, and more through the use of the built-in PYTHON interface (pyfplo). To make the most of the FPLO code, it is important to be familiar with its various features and options. These are explained in more detail below.

1. FEDIT

It is input file editor which generates =.in file as input file.

2. XFPLO

It is used for the visualization of structures and Fermi surface and the Brillouin zone. It also helps for the splitting of structure, generation of supercell, structure, and symmetry manipulation.

3. FPLO

It performs the Kohn-sham calculation. Final output provides information on the system such as energy, charge density, magnetic moment, energy band gap, etc.

4. XFBP

It is the graph plotting tool. It helps to plot graph of different calculations such as: band structure, DOS, dielectric function, optical conductivity, loss function etc.

3.6 Calculation Scheme

In the results and discussion section, we employed a rigorous methodology to analyze the electronic, magnetic, and topological characteristics of $A_2T_3S_4$. Our approach involved utilizing the full-potential local-orbital code (Koepernik and Eschrig, 1999) along with a localized basis and full potential treatment. By conducting calculations based on density functional theory, we accurately determined the electronic structure of the material.

3.6.1 Electronic and Magnetic Properties Calculation

To perform the DFT calculations, we used the FPLO, version 18.00-52. The standard GGA based on the parameterization by Perdew, Burke, and Ernzerhof (PBE) was used for the exchange-correlation potential. A linear tetrahedron method with a k-mesh of $12 \times 12 \times 12$ points in the Brillouin zone was applied for the integration in reciprocal space. Self-consistent calculations were conducted in both scalar relativistic and four component full relativistic modes of FPLO. In the full relativistic mode that includes spin-orbit coupling in all orders, the direction of magnetization was fixed by a global setting of the spin quantization axis. To ensure accuracy, the convergence criteria for self-consistency were set to 10^{-8} Hartree for energy and 10^{-6} e/(Bohr radii)^3 for the charge density. During the structural optimization, a force convergence of 10^{-3} eV/Å was applied. The flowchart in Fig. 5 illustrates the step-by-step process for calculating the electronic and magnetic properties in detail. For the optical property calculations, we have used the FOPTICS module of FPLO. A finer k-mesh subdivision of $32\times32\times32$ was employed.

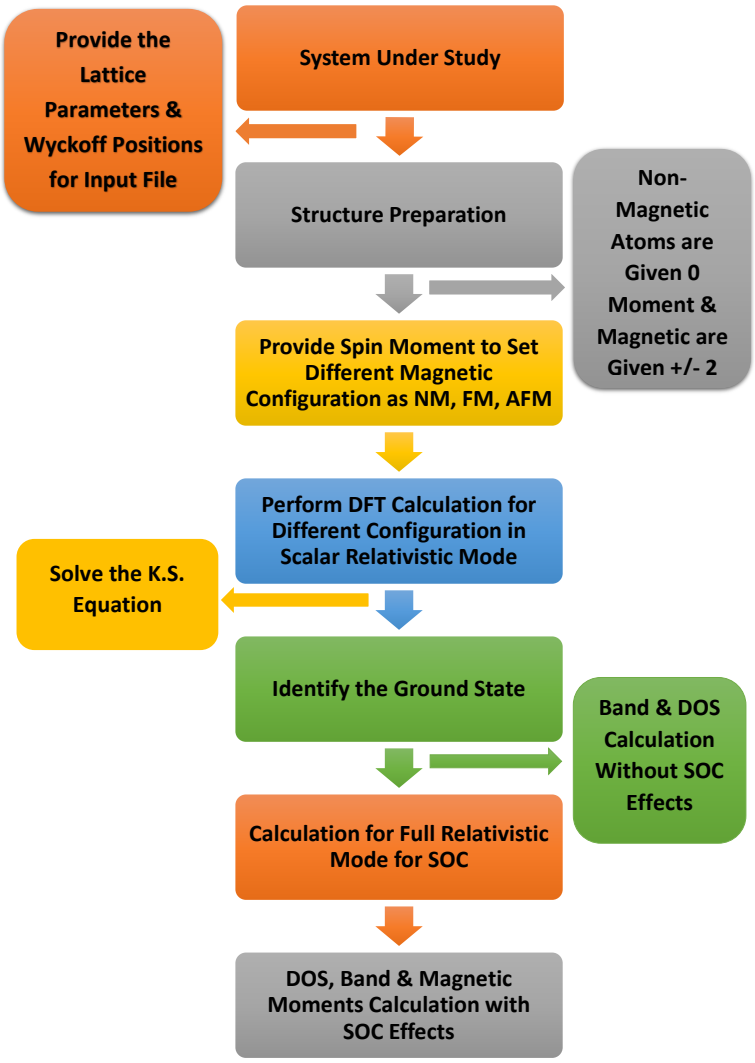

Figure 5: Flowchart for the electronic and magnetic properties calculations.

3.6.2 Topological Properties Calculation

We apply Wannier fitting to examine the topological features of the system. The flowchart in Fig. 6 illustrates the step-by-step process for calculating the topological properties in detail. Utilizing Wannier functions produced from a basis set of local orbitals allows for this transformation. We specifically carry out the Wannier fitting using the local orbitals of each atom. We then derive the Wannier Hamiltonian, which enables us to determine the Weyl points, Chern number, Berry curvature, Fermi surface and anomalous Hall conductivity. Weyl points are found by using a modified algorithm developed by Takahiro Fukui and colleagues (Fukui *et al.*, 2005). The algorithm can be summarised through the following bullets:

- At first we define a box which defines grid where the Weyl points are to be computed.

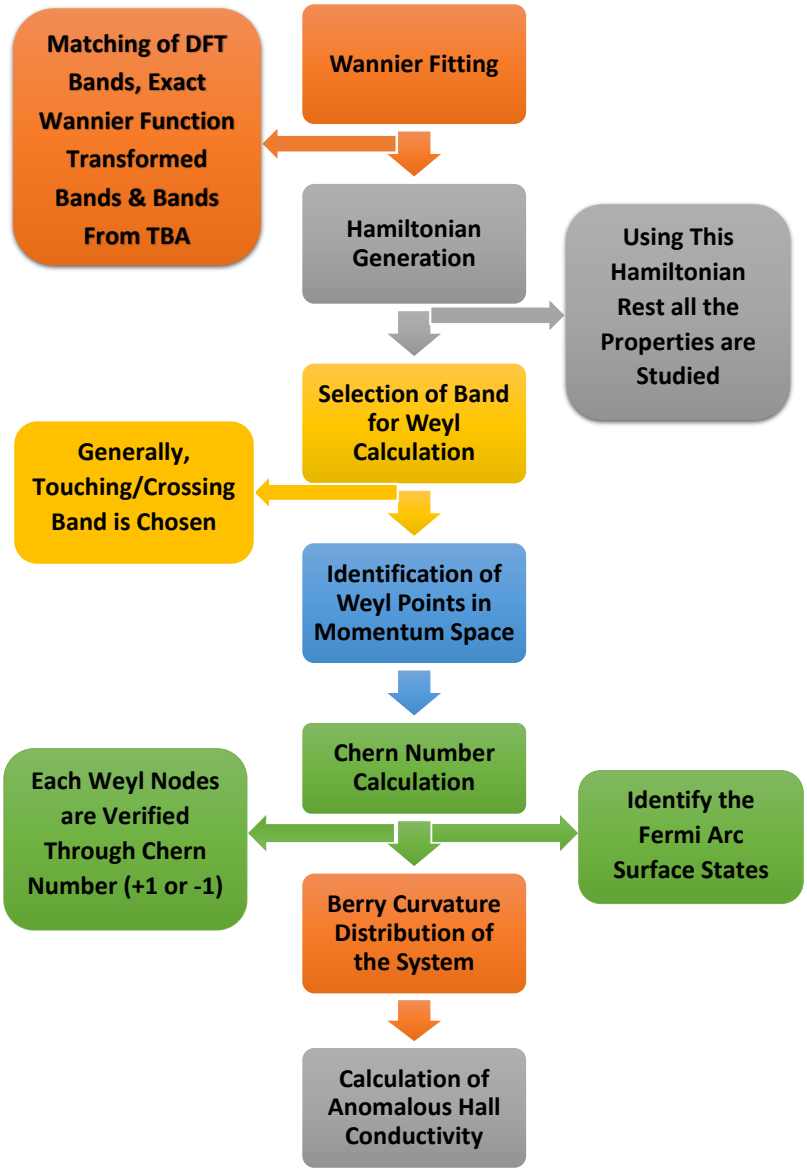

Figure 6: Flowchart for the topological properties calculations.

- On all the grid points the Hamiltonian is diagonalized.
- For each micro cell of the grid the berry curvature is integrated over the surface of the cell.
- The integration gives the chirality of the Weyl points if the box contains the Weyl points.
- For all cells which has non zero result subsequent bisections is performed until the finest value is reached. All the resulting boxes with non-zero chirality are written to be weyl points.
- For the calculation of the AHC the berry curvature is integrated over the torus

multiplied by the occupation number. $300 \times 300 \times 300$ k- grid was used for the integral of AHC. For the calculation of surface property, we used the pyfplo model of FPLO. The script fs.py, which calculates the surface spectral function for E=0 in the surface Brillouin zone (the Fermi surface equivalent). We set up a semi-infinite slab with a (0 0 -1) surface. We set the anchor slightly above 0. The cell whose semi-infinite repetition will make up the semi-slab. Note that the c-axis points downwards. Hence, the surface is the lower face of the cell, while the infinite side grows on the upper cell face (not shown). If we had chosen the (0 0 1) surface, the c-axis would have pointed upwards. Number of layers to be constructed from the layered cell. For semislab, the smallest possible number should be chosen. Note that the number of layers is set to 7. We set up the surface BZ and a mesh which represents the upper right quadrant of the surface BZ. We set the Fermi surface values -6 meV, 0 meV, and +6 meV. After the calculation finishes, we execute xfbp fs.xpy. It read the 'slabifyres/+fssf.spin1'. We separately picked this file and plot from Python and got those three states (Fermi arc surface states).

CHAPTER 4

RESULTS AND DISCUSSION

4.1 Structural, Electronic, Magnetic and Topological Properties of $Cs_2Co_3S_4$

4.1.1 Structural Properties

$Cs_2Co_3S_4$ is a compound synthesized in 1988 (Bronger *et al.*, 1988a). Though synthesized, there are no reports yet on its electronic and related properties studied to our knowledge. Thus, on the basis of DFT approach we have systematically investigated the electronic, magnetic and topological Weyl properties. $Cs_2Co_3S_4$ crystallizes in a body centered orthorhombic Bravais lattice with the centrosymmetric space group *Ibam* (SG 72) and two formula units per primitive unit cell. Experimental lattice parameters and atomic positions were determined both by XRD and by ND. While the ND data were obtained at a temperature of 4.2 K, XRD was presumably performed at room temperature. The experimental lattice parameters obtained by room-temperature XRD are a = 5.712 Å, b = 11.231 Å, and c = 13.879 Å. According to the same experiment, Cs and S atoms occupy the 8j and 16k sites at (0.234, 0.121, 0) and at (0.223, 0.367, 0.159), respectively, while the Co atoms occupy the 8g sites, denoted as Co(I), at (0, 0.232, 0.250) and the 4b sites, denoted as Co(II), at (0.500, 0, 0.250). The structure is shown in Fig. 7. The Cs atoms are centered within distorted cubes of S atoms, and the Co atoms are surrounded by S tetrahedra. The related shortest bond lengths amount to 3.54 Å for Cs - S, 2.31 Å for Co(I) - S, and 2.34 Å for Co(II) - S. The experimental lattice parameters obtained by low-temperature ND amount to a = 5.663 Å, b = 11.160 Å and c = 13.708 Å. They are somewhat smaller than the related room-temperature parameters, in accordance with a positive thermal expansion coefficient. Atomic site positions obtained by ND are Cs-8j (0.234, 0.115, 0), S-16k (0.814, 0.369, 0.140), Co(I)-8g (0, 0.235, 0.250), and Co(II)-4b (0.500, 0, 0.250). These positions agree well with those determined by XRD with the exception of the sulfur position. The latter results in a Cs-S interatomic distance of 1.98 Å, which is only somewhat more than half of the expected value of about 3.60 Å. Thus, we consider the ND-value of the S-16k atomic position as incorrect and use the XRD atomic positions in all DFT calculations.

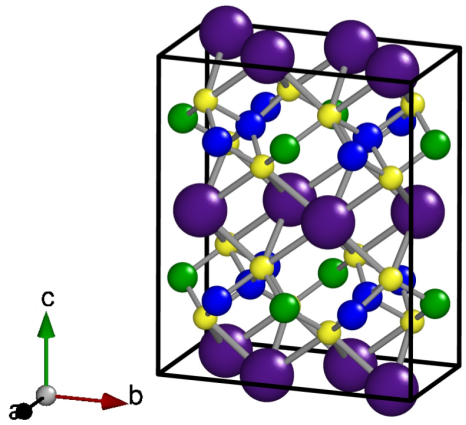

Figure 7: Crystal structure of $Cs_2Co_3S_4$ in the conventional elementary cell. Violet (blue, green, yellow) balls denote Cs (Co(I), Co(II), S) atoms.

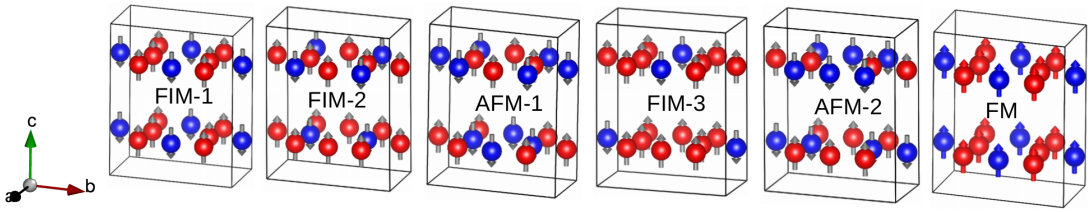

Figure 8: Considered spin configurations. From left to right, different ferrimagnetic (FIM), antiferromagnetic (AFM), and ferromagnetic (FM) arrangements are depicted in ascending order of their energy according to our calculations using experimental room-temperature lattice parameters. Only Co atoms are shown. Different colors denote different spin orientations.

4.1.2 Electronic and Magnetic Properties

We started our calculations with a search for the stable magnetic ground state of $Cs_2Co_3S_4$. Based on ND data, a collinear antiferromagnetic (AFM) order was suggested to be the stable magnetic state at 4.2 Kelvin. In this state, four of the Co(I) sites show a spin orientation opposite to the spin orientation of the four other Co(I) sites and two of the Co(II) sites show a spin orientation opposite to the spin orientation of the two other Co(II) sites (see Fig. 8). Permutation of the spin orientations of these four groups of sites yields eight different combinations. Two of the combinations are equivalent by symmetry to other combinations. We investigated the six remaining combinations, shown in Fig. 8. They include ferromagnetic (FM), two different AFM, and three ferrimagnetic (FIM) arrangements. Tab. 1 compiles the relative total energies and spin magnetic moments, obtained by means of calculations in a scalar relativistic mode and using both low-temperature ND and room-temperature XRD lattice parameters. Different from the experimental result, the arrangement FIM-1 is found to be the lowest-energy state. However, both FIM-2 and the experimental ground state AFM-1 are further low-energy solutions with energies of 2 meV per atom or less above the computed ground state. All other considered arrangements have much higher total energies. In order to make sure that the obtained solutions with atomic spin moments of about 2 μ_B

are the only stable solutions of the given arrangements, we performed two tests. First, FSM calculations were done for the case of FM order. They showed that there is no other (meta)stable FM state in the possible range of local moments. Second, calculations for the AFM-1 order were performed with larger than usual initial spin splittings of 4 and 5 μ_B. Both calculations converged to the same state as obtained with default initial splitting of 2 μ_B and shown in Tab. 1. The question arises why the experimental ground state AFM-1 is found higher in energy than the state FIM-1 in the calculations. To get an idea about a possible reason, we performed additional calculations for the states FIM-1 and AFM-1 with slight doping of 0.1 electrons (holes) per unit cell of 18 atoms. As a result, the original energy difference between FIM-1 and AFM-1 of 36.5 meV (ND lattice parameters) was reduced by 1.3 meV (enhanced by 1.4 meV). This means, a strong electron doping would be needed to change the order of the two states, which would only be possible by significant modification of the stoichiometry in the order of a few percent. We cannot rule out this possibility, nor can we rule out the applied approximation to the exchange-correlation functional GGA to be responsible for the disagreement between calculated and experimental ground states. In any case, the two discussed states are relatively close in energy. Thus, it should be possible to prepare FIM-1 either by appropriate modification of the stoichiometry (improved preparation or intentional electron doping) or by application of a moderate external magnetic field. The latter option would be very interesting, since also the state FIM-2 is close to AFM-1. Thus, a competition between three different phases could occur. Next, we carried out full relativistic calculations including spin-orbit coupling. Here, we focus on the calculated ground state FIM-1 and on the experimental ground state AFM-1. The results are presented in the upper part of Tab. 2. By spin-orbit coupling, the total energy depends on the direction of magnetization. Here, we consider the three in-equivalent orthorhombic directions [1 0 0], [0 1 0], and [0 0 1]. Among these, the lowest energy is found for the configuration FIM-1 with [1 0 0] orientation of the magnetization. In the configuration AFM-1, the lowest energy is achieved if the magnetization is oriented along [0 0 1]. This is in agreement with the easy axis measured by ND. The maximum value of the magnetic anisotropy energy (MAE), which is the energy difference between unlike orientations of the magnetization, amounts to about 2.50 meV per unit cell in both configurations. The total magnetic moments per Co atom are not much enhanced in comparison with the scalar relativistic results, due to the relatively small orbital moments that do not exceed 10% of the spin moments. This finding is at variance with the experimental magnetic moments of about 3.7 μ_B, obtained by ND. We note, however, two important caveats. First, the title system is a (half)metal with a relatively broad Co-d band of about 3 eV. As such, it is expected that the Co orbital moment is ruled by itinerant behavior and, thus, much smaller than the large-moment limit of the d^7 atomic configuration, 3 μ_B. Second, there exists a generic problem to define the local

moment of atoms in an AFM configuration, since the total moment of the unit cell has to be zero. In the present AFM-1 configuration, Co atoms with antiparallel magnetic moments are less than 2.9 Å away from each other, which is only 15% more than the distance in densely packed metallic Co. Thus, it is possible to define very different local projections of the magnetization density which add up to the same total magnetization density. Further, we applied so-called orbital polarization corrections (OPC) to GGA. These corrections improve the compliance of GGA and similar approximations to the exchange-correlation functional of DFT with Hund's second rule. (Eschrig *et al.*, 2005) Related results are compiled in the lower part of Tab. 2. We note that the spin magnetic moments are merely unchanged in comparison with those obtained by scalar relativistic or full relativistic calculations without OPC. The orbital magnetic moments, however, are enhanced with respect to the data of the latter calculations by factors between two and four. As a result, the total moments amount up to about 2.7 μ_B. This value is still significantly below the numbers reported in Tab. 1, but much larger than cobalt moments commonly known from other metallic systems. Further, the lowest-energy directions of magnetization remain unchanged by OPC for the two considered configurations: [1 0 0] for the configuration FIM-1 and [0 0 1] for AFM-1. This fact is reassuring since AFM-1 [0 0 1] is the experimental ground state. Here, by applying GGA+OPC, this state is found to be only less than 1 meV per atom higher in energy than the state FIM-1 [1 0 0]. We conclude this section by stating that we identify the state FIM-1 [1 0 0] as the ground state of the title compound, treated in relativistic GGA without or with OPC, with exact stoichiometry and free of defects. Since this state is very close in energy to the experimental ground state AFM-1 [0 0 1], we think that it can be obtained either directly by refined sample preparation or by application of a moderate external magnetic field. Thus, our further investigations will be focused on FIM-1.

Table 1: Scalar relativistic energies and spin moments. Calculated relative total energies E, given per primitive unit cell with 18 atoms and local and total spin magnetic moments M_s for the six considered configurations depicted in Fig. 8. ND and XRD indicate the results obtained by using low-temperature ND and room-temperature XRD lattice parameters, respectively.

	E [meV/unit cell]		M_s(Co(I)) [μ_B]		M_s(Co(II)) [μ_B]		M_s(unit cell) [μ_B]	
Configuration	ND	XRD	ND	XRD	ND	XRD	ND	XRD
FIM-1	0	0	2.01	2.11	-1.77	-1.91	5.94	5.99
FIM-2	19.6	20.4	1.98, -1.67	2.09, -1.82	2.03, 2.05	2.13, 2.16	5.96	6.00
AFM-1	36.5	23.1	1.87, -1.87	2.00, -2.00	2.00, -2.00	2.14, -2.14	0	0
FIM-3	171	161	2.01, 2.04	2.17, -2.20	-1.71, 2.13	-1.80, 2.28	10.87	11.58
AFM-2	157	165	1.81, -1.81	1.97, -1.97	1.95, -1.95	2.09, -2.09	0	0
FM	367	388	1.92	2.04	1.92	2.04	14.26	14.79

All results of this and the following sections were obtained by using room-temperature XRD structure data. Fig. 9 (a) shows the total and partial densities of states (PDOS) for the ground state FIM-1 configuration in scalar relativistic mode. Majority and minority spin channels are indicated with up- and down-arrows, respectively. The related scalar relativistic band structure on high-symmetry lines is depicted in Fig. 9

Table 2: Full relativistic energies, spin and orbital moments. Calculated relative total energies E, given per primitive unit cell with 18 atoms, and local spin, orbital, and total magnetic moments (M_s, M_l, and M_{tot}, resp.) of the Co atoms. The two numbers in each column refer to Co(I) and Co(II). The upper part shows results of full relativistic calculations with different orientations of the magnetization for the configurations FIM-1 and AFM-1, the lower part shows results of full relativistic calculations with orbital polarization correction. Low-temperature ND lattice parameters were used for all calculations.

With s-o					
Configuration	Direction of magnetization	E [meV/unit cell]	M_s(Co) [μ_{B}]	M_l(Co) [μ_{B}]	M_{tot}(Co) [μ_{B}]
FIM-1	[1 0 0]	0	2.00, -1.76	0.17, -0.14	2.17, -1.90
	[0 1 0]	2.7	2.00, -1.77	0.15, -0.15	2.15, -1.92
	[0 0 1]	2.5	2.00, -1.76	0.16, -0.15	2.16, -1.92
AFM-1	[1 0 0]	37.4	± 1.86, ± 1.99	± 0.15, ± 0.16	± 2.01, ± 2.15
	[0 1 0]	37.7	± 1.86, ± 1.99	± 0.14, ± 0.16	± 2.00, ± 2.15
	[0 0 1]	35.1	± 1.86, ± 1.99	± 0.18, ± 0.18	± 2.04, ± 2.17
With s-o and OPC					
FIM-1	[1 0 0]	0	1.99, -1.76	0.70, -0.47	2.69, -2.23
	[0 1 0]	17.9	2.01, -1.77	0.40, -0.56	2.41, -2.33
	[0 0 1]	11.7	2.01, -1.77	0.46, -0.58	2.47, -2.35
AFM-1	[1 0 0]	46.3	± 1.88, ± 2.01	± 0.50, ± 0.57	± 2.38, ± 2.58
	[0 1 0]	51.7	± 1.86, ± 1.99	± 0.44, ± 0.48	± 2.30, ± 2.47
	[0 0 1]	12.6	± 1.85, ± 1.96	± 0.71, ± 0.80	± 2.56, ± 2.76

(b). The positions of the symmetry points are compiled in Tab. 3. The DOS shows an interesting combination of semi-metallic and covalent features. Sulphur states (green color in the upper panel of Fig. 9 (a)) dominate the DOS between about -5 eV and about -3 eV (bonding region), while Co states (lower panel of Fig. 9 (a)) dominate between -2 eV and +1 eV (anti-bonding region). Both regions are separated by a covalency gap in the minority spin channel. In the majority spin channel, however, this energy range is occupied by states localized almost exclusively at Co(I) sites. There is a narrow, separated band with a width of only 0.5 eV in the majority spin channel above the Fermi level. However, the widths of the occupied majority spin band and of the minority spin band around the Fermi level in the Co-dominated anti-bonding region amount to about 3 eV. Thus, the title compound is expected to show itinerant magnetism. Within the majority spin band, there is a 0.36 eV gap only 14 meV above the Fermi level, see Fig. 9 (a, b). Thus, the system is very close to a half metallic state. This finding is in accordance with the calculated spin moment of 5.99 μ_{B}, which is almost an integer value that would indicate half metallicity in a scalar relativistic approximation. Moreover, a narrow pseudogap of about 80 meV width is present in the minority spin band at E_{F}, qualifying $Cs_2Co_3S_4$ as a semi-metal. The majority spin band has a small hole pocket at point Γ, see Fig. 9 (b), and only two minority spin bands cross the Fermi level. Those bands which feature as highest occupied band in certain regions of the k-space are indicated in Fig. 9 (b) with their band number (129, 130, or 131). Note that these numbers do not include the 120 semi-core states. The electronic band structure with spin-orbit coupling is shown in Fig. 9 (c) for the case of magnetization along [1 0 0] (ground state). Due to broken time reversal symmetry, all bands are non-degenerate almost everywhere in the k-space. Exceptions are bands on the line W-R, which are at least two-fold degenerate by symmetry, and accidental band degeneracies. The latter

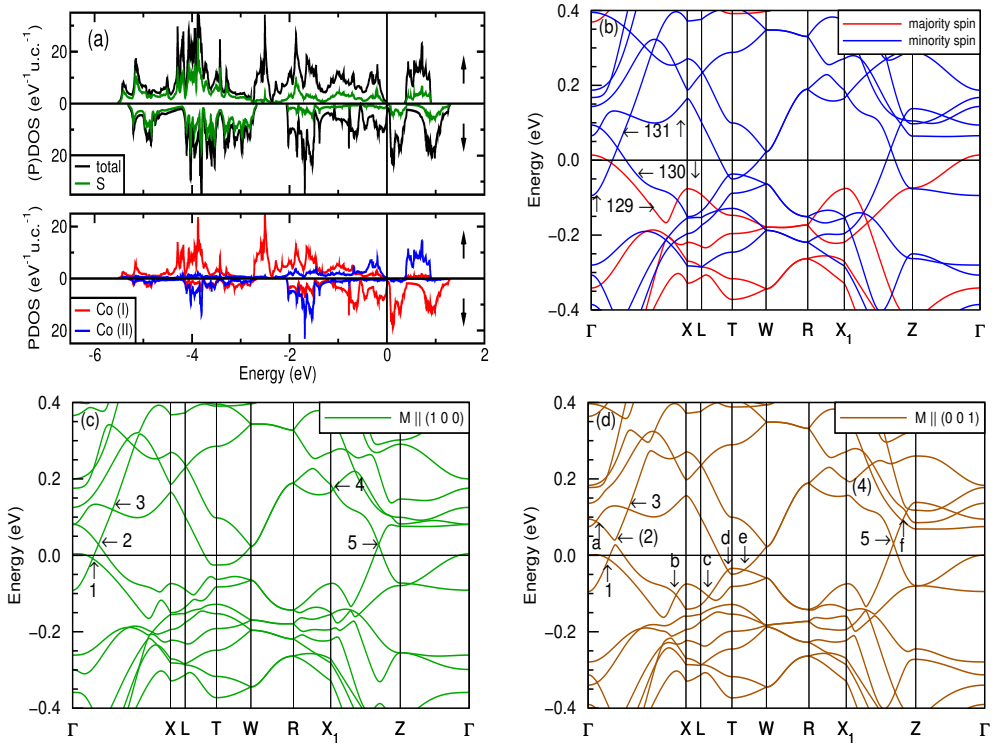

Figure 9: Electronic structure of the ground state magnetic configuration. The Fermi level is set to zero energy in all sub-figures and indicated with solid lines. (a) Total and partial DOS obtained in scalar relativistic mode. The majority and minority spin channels are indicated by up- and down-arrows, respectively. The total DOS is shown with black lines, the partial sulphur, Cobalt(I), and Cobalt(II) contributions with green, red, and blue lines, respectively. (b) Electronic band structure obtained in scalar relativistic mode. The majority and minority spin contributions are shown with red and blue lines, respectively. Several numbers of bands close to the Fermi level are given together with arrows pointing to the related bands. Note, the numbering is in the order of the band energy at each k-point. (c) Electronic band structure obtained in full relativistic mode with magnetization M parallel to [1 0 0] (ground state). Apparent band crossings involving bands n and $n+1$, $n = \{129, 130, 131\}$, are indicated with arrows and numbered. (d) Electronic band structure obtained in full relativistic mode with magnetization M parallel to [0 0 1]. Crossings already present for M parallel to [1 0 0] are numbered as before; former crossings that are obviously gapped are numbered with parentheses; new crossings are distinguished by letters.

may form so-called nodal lines or are isolated Weyl points, which are of special interest for their impact on transport behavior, see below. Inspection of Fig. 9 (c-d) shows a number of apparent band crossings. We call these degeneracies "apparent", as the information provided by Fig. 9 (c) does not allow a final categorization into Weyl points, nodal lines, or gapped states. Those apparent crossings that take place between bands n and $n+1$ close to the Fermi level, $n = \{129, 130, 131\}$, are marked in Fig. 9 (c) by numbers 1 to 5 and will be investigated in the following section. If the magnetization is rotated by, e.g., application of an external magnetic field, the band structure changes due to spin-orbit coupling. This means that also the positions and energies of Weyl points depend on the direction of magnetization, and pairs of Weyl points may even annihilate or emerge. This effect becomes obvious by comparing Fig. 9 (c) with Fig. 9 (d). The

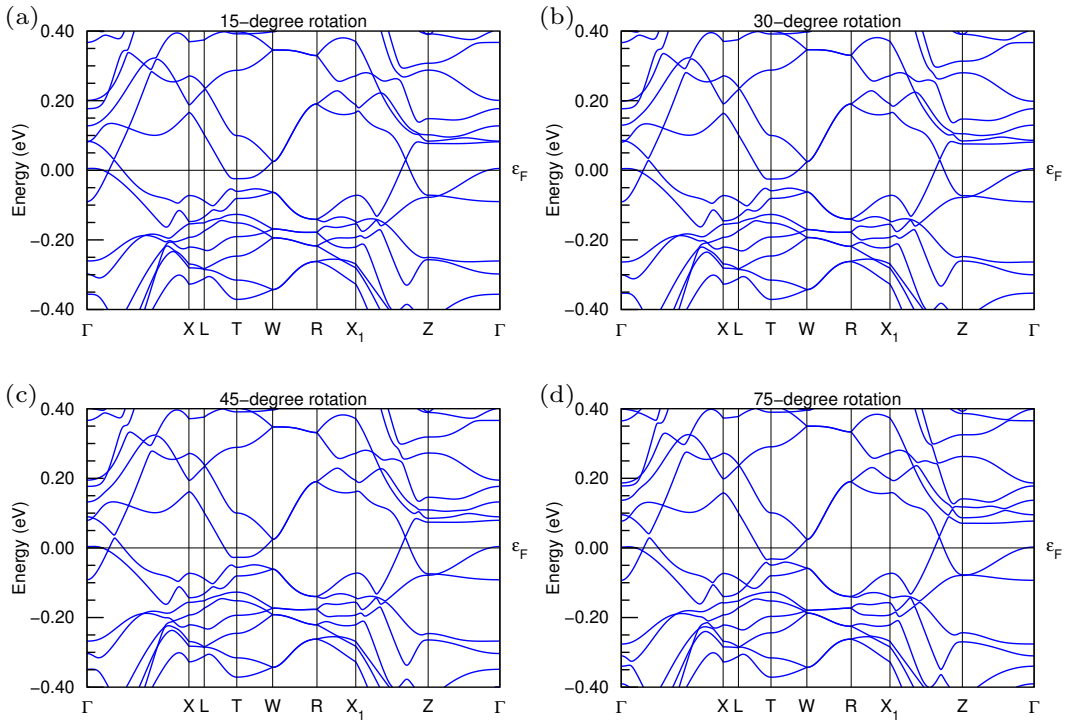

Figure 10: Change in electronic band structure of $Cs_2Co_3S_4$ for orientation of the magnetization away from [1 0 0].

latter figure shows the band structure for magnetization along [0 0 1]. Out of the five apparent band crossings marked in Fig. 9 (c), two are now visibly split. Those, (2) and (4), are marked in parentheses in Fig. 9 (d). Moreover, six new apparent crossings manifest themselves, marked with letters a to f.

4.1.3 Weyl Points

Maximally localized Wannier functions were produced from self-consistent full relativistic DFT band structures using the PYFPLO module of the FPLO code, version 18.00-52. The localized Wannier basis consists of Cs [5p, 6s], Co [3d, 4s], and S [3p, 3s] orbitals, i.e., a total of 168 orbitals. To map the Wannier model, the same k-mesh

Table 3: Location of the symmetry points used in Fig. 9.

point	$k_x[2\pi/a]$	$k_y[2\pi/b]$	$k_z[2\pi/c]$
Γ	0	0	0
X	0.58469	0	0
L	0.58469	0.17259	0
T	1/2	1/2	0
W	1/2	1/2	1/2
R	1/2	0	1/2
X_1	0.41531	0	1
Z	0	0	1

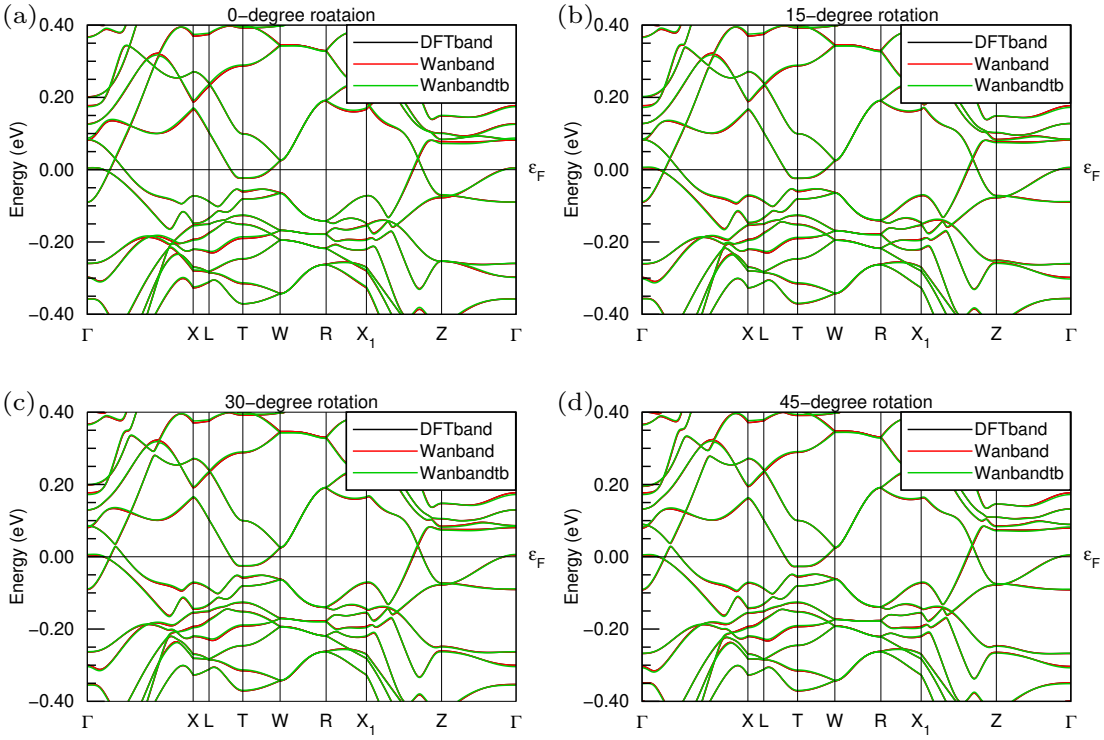

Figure 11: Wannier mapping of electronic band structure of $Cs_2Co_3S_4$ for orientation of the magnetization away from [1 0 0]. The two different Wannier mappings are both almost on top of the DFT band structure.

as in the self-consistent calculations was chosen. The generated Wannier Hamiltonians were used to interpolate the band structure and to search the Weyl points with the help of the abovementioned PYFPLO module. The search was limited to the Wannier bands 129-131, counted in ascending order, as lower bands at the Weyl node, see Fig. 9(b). For the Chern number calculation, we used nsubdiv=100 which results non-zero values close to +1 or -1. The k-space integrations to evaluate the anomalous Hall conductivity were carried out with a mesh of $200 \times 200 \times 200$ points. We are now going to scrutinize the character of the apparent band crossings found in the band structure and to investigate their dependence on the direction of magnetization. For this aim, sets of Weyl points were searched using the Wannier presentation (see Fig. 11) of the DFT band structure among all bands n and $n+1$, $n = \{129, 130, 131\}$. For comparison, or if the visible crossing was not detected as a Weyl point while using the search algorithm, additional checks using the DFT band structure were performed. Tab. 4 shows the results for the ground state with M|| [1 0 0]. For this orientation of M, the magnetic point group includes a simple (i.e., without time reversal) $C_2(x)$ rotation axis. All five apparent crossings lie on this axis, including points 4 and 5 which can be shifted to a position with $k_y = k_z = 0$ by subtracting a reciprocal lattice vector. Along any simple C_2 axis, crossings between bands belonging to the two different irreps are always WPs (Gosálbez-Martínez *et al.*, 2015; Fang *et al.*, 2012). Points 1, 2, and 5 are indeed confirmed as WPs with chiralities χ of 1 or -1. Their energies and k_x-positions obtained from the Wannier Hamiltonian

are close to the related DFT results. Points 3 and 4 are not detected as Weyl points by the Wannier-based search. Using the DFT band structure, they seem to be linear crossings with gaps below 10^{-6} eV. Thus, we denote them as likely WPs.

Table 4: Characteristics of points in the low-energy electronic structure of $Cs_2Co_3S_4$, if the magnetization points along the [1 0 0] direction. "P" denotes the specific points as defined in Fig. 9 (c); E is the energy relative to the Fermi level; k_i, $(i = x, y, z)$ are the coordinates of one representative position of the point set; "M" is the symmetry-determined multiplicity of the positions; "T" is the type of the node (WP: confirmed Weyl point); χ is the chirality. Energies and positions obtained from the DFT calculation are given in parentheses.

P	E[meV]	$k_x[2\pi/a]$	$k_y[2\pi/b]$	$k_z[2\pi/c]$	M	T	χ
1	-6	0.118	0	0	2	WP	1
	(-8)	(0.119)	(0)	(0)			
2	32	0.153	0	0	2	WP	-1
	(28)	(0.154)	(0)	(0)			
3	123	0.236	0	0	2	WP	1
	(120)	(0.238)	(0)	(0)	2	WP	
4	179	0.399	0	1	2	WP	-1
	(173)	(0.400)	(0)	(1)	2	WP	
5	33	0.132	0	1	2	WP	1
	(28)	(0.129)	(0)	(1)			

If the magnetization is rotated away from the easy [1 0 0] axis, the electronic structure changes, as shown in Fig. 10. As a consequence, the Weyl points move both in energy and position (Gosálbez-Martínez *et al.*, 2015). Tab. 5 and Tab. 6 show, how the angle ϕ of magnetization, varied in steps of 15 degrees from [1 0 0] toward [0 0 1], affects point 2 and point 5, respectively. We note, that the band energy E and k_x are only marginally shifted. However, the WPs move strongly in the direction of k_z in both cases. For $M||$ [M_x 0 M_z], $M_z \neq 0$, the m'_z plane (mirror plane with time reversal) is not contained in the magnetic point group, in distinction to $M||$ [1 0 0]. Thus, for $\phi \neq 0$, the multiplicity of the WPs does not depend on k_z. Especially, $k_z = 0$ is not a plane with a symmetry different from $k_z \neq 0$. Vice versa, a set of WPs with multiplicity 2 and coordinates (k_x, 0, $k_z \neq 0$) for the case of $M||$ [M_x 0 M_z], $M_z \neq 0$, has to move toward the plane $k_z = 0$ if M rotates toward [1 0 0] in order to keep its multiplicity. If ϕ exceeds 45 degrees, none of the WP pairs can be detected. Obviously, they are annihilated before ϕ reaches the value of 60 degrees.

The magnetic point group changes again, if the magnetization direction reaches [0 0 1]. In this case, $m(z)$ becomes a simple mirror plane. Such a plane cannot host WPs, since the chiral charge is odd under reflection, and the generic degeneracies are nodal lines (Gosálbez-Martínez *et al.*, 2015). Indeed, we found only one WP among the apparent degeneracies (point e), see Tab. 7. Another WP (point g) was found during the general search. This point is not situated on a symmetry line. As required by symmetry, these two WPs have coordinates $k_z \neq 0$. All other apparent degeneracies are situated on

Table 5: Impact of magnetization direction on the WP number 2. ϕ denotes the deflection of the magnetization direction from [1 0 0] toward [0 0 1], in degree; E is the energy relative to the Fermi level; k_i, $(i = x, y, z)$ are the coordinates of one representative position of the WP set; "M" is the symmetry-determined multiplicity of the positions. Note, the data for $\phi = 0$ are the same as given in Tab. 4.

ϕ	E[meV]	$k_x[2\pi/a]$	$k_y[2\pi/b]$	$k_z[2\pi/c]$	M
0	32	0.153	0	0	2
15	31	0.153	0	0.076	2
30	31	0.154	0	0.179	2
45	30	0.155	0	0.339	2

Table 6: Impact of magnetization direction on the WP number 5. ϕ denotes the deflection of the magnetization direction from [1 0 0] toward [0 0 1], in degree; E is the energy relative to the Fermi level; k_i, $(i = x, y, z)$ are the coordinates of one representative position of the WP set; "M" is the symmetry-determined multiplicity of the positions. Note, the data for $\phi = 0$ are the same as given in Tab. 4

ϕ	E[meV]	$k_x[2\pi/a]$	$k_y[2\pi/b]$	$k_z[2\pi/c]$	M
0	33	0.132	0	1	2
15	31	0.134	0	0.898	2
30	31	0.135	0	0.851	2
45	30	0.142	0	0.691	2

Table 7: Characteristics of points in the low-energy electronic structure of $Cs_2Co_3S_4$, if the magnetization points along the [0 0 1] direction. "P" denotes the specific points as defined in Fig. 9 (d) and one more point, g, which is not situated on a symmetry line; E is the energy relative to the Fermi level; k_i, $(i = x, y, z)$ are the coordinates of one representative position of the point set; "M" is the symmetry-determined multiplicity of the positions; "T" is the type of the point (WP: confirmed Weyl point; NL: a point on a nodal line; G: gapped); χ is the chirality in case of a confirmed Weyl point. Energies and positions obtained from the DFT calculation are given in parentheses.

P	E[meV]	$k_x[2\pi/a]$	$k_y[2\pi/b]$	$k_z[2\pi/c]$	M	T	χ
a	(89)	(0.047)	(0.001)	(0)	4	NL	
1	(-10)	(0.121)	(0)	(0)	2	NL	
3	(121)	(0.239)	(0)	(0)	2	G	
b	(-104)	(0.526)	(0.003)	(0)	4	NL	
c	(-108)	(0.563)	(0.255)	(0)	4	NL	
d	(-39)	(0.511)	(0.456)	(0)	4	NL	
e	-36	0.5	0.5	0.140	4	WP	-1
	(-38)	(0.5)	(0.5)	(0.176)			
5	(31)	(0.133)	(0)	(1)	2	G	
f	(90)	(0.080)	(0)	(1)	2	NL	
g	35	0.863	0	0.112	4	WP	-1
	(35)	(0.865)	(0)	(0.141)			

the plane $k_z = 0$ or can be moved to that plane by subtracting a reciprocal lattice vector. Two of them are found to be gapped (point 3, point 5). The others are not gapped but do not carry any chiral charge. Therefore, we denote them to be likely points on nodal lines. A comparison between the Wannier data and the DFT results for the two WPs shows, that the related band energies almost agree. This holds as well for the k_x coordinates,

while the values for k_z deviate somewhat stronger from each other.

4.1.4 Berry Curvature and Anomalous Hall Conductivity

We used the approach to calculate the Berry curvature, as implemented in FPLO to determine the topology of the electronic structure (Wang *et al.*, 2006). Based on this method, we established that the flux of the Berry curvature for all bands, up to and including band N, through a closed surface enclosing the Weyl point is equal to the Chern number. In this context, we applied the strategy of selecting a small sphere surrounding the Weyl point, characterized by a gap between bands N and $N+1$ (Soluyanov *et al.*, 2015; Wang *et al.*, 2016a). The Berry curvature components Ω_x and Ω_z are shown in Fig. 12 (a) and (b), respectively. It is evident that Ω_z exhibits a higher amount of curvature than Ω_x. Berry curvature's source and sink characteristics are indicated by the colors red and blue, respectively. In Fig. 13 (a), within the energy range encompassing bands from -0.4 eV to 0.4 eV, along [1 0 0] magnetization direction, the averaged Berry curvature is projected onto the k_x and k_y plane. Different color spots denote either source or sink of the Berry curvature of opposite chiralities of the Weyl points and nodal line crossings. The anomalous Hall effect (AHE) is a another notable

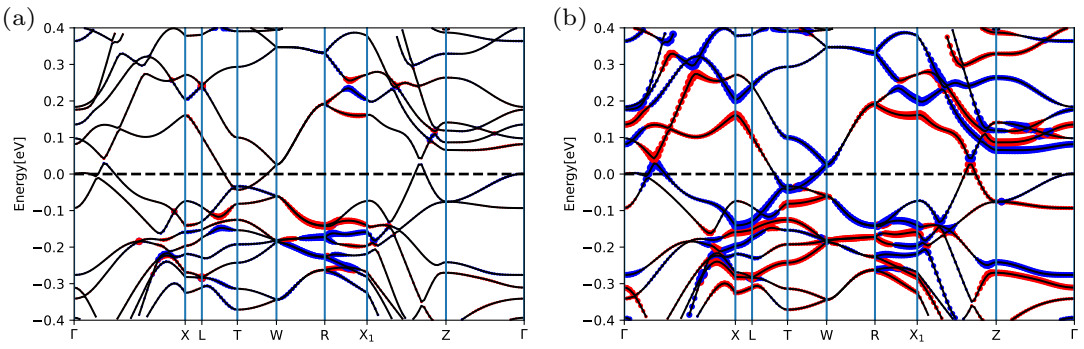

Figure 12: The Berry curvature components (a) Ω_x and (b) Ω_z of $Cs_2Co_3S_4$ for orientation of the magnetization along [1 0 0]. Blue and red color denote the Berry curvature's source and sink, respectively.

characteristic of topological magnetic Weyl materials. Three particular contributions to the anomalous Hall conductivity (AHC), $\sigma_{xy}^{\mathrm{an}}$ are commonly distinguished: the intrinsic contribution, $\sigma^{\mathrm{an,in}}$, which arises solely from the material's band structure, the skew scattering contribution $\sigma^{\mathrm{an,sk}}$, and the side jump contribution $\sigma^{\mathrm{an,sj}}$. The latter two arise from extrinsic mechanisms (Nagaosa *et al.*, 2010). All three contributions are additive, $\sigma^{\mathrm{an}} = \sigma^{\mathrm{an,in}} + \sigma^{\mathrm{an,sk}} + \sigma^{\mathrm{an,sj}}$. Here, we consider only the intrinsic contribution to the AHC, which is known to reach large values in magnetic WSMs (Liu *et al.*, 2018; Manna *et al.*, 2018; Li *et al.*, 2020b). This behavior is considered to be due to the non-trivial band topology at WPs with related large Berry curvature $\Omega(k)$. As $k-$space analogy to magnetic dipoles, pairs of WPs act as sources and drains of Berry curvature which, in turn, generates the AHC. The Kubo-formula linear-response approach was

used to evaluate the AHC from the Berry curvature, based on the available tight-binding Hamiltonian:

$$\sigma_{ab}^{\text{an,in}} = -\frac{e^2}{\hbar}\Sigma_{n,c}\epsilon_{abc}\int_{BZ}\frac{d^3k}{(2\pi)^3}f_0(E_n(k))\Omega_n^c(k), \tag{4.1}$$

where ϵ_{abc} is the Levi-Civita tensor, $f_0(E_n(k))$ is the equilibrium Fermi-Dirac distribution function, n is the band index, $E_n(k)$ is the related eigenvalue at k, and Ω_n^c is the c-component of the Berry curvature. Fig. 13 (b) shows the band-intrinsic contribution to the AHC as a function of the chemical potential and the magnetization direction, obtained with a zero-temperature Fermi-Dirac distribution function. For the two considered magnetization directions [1 0 0] and [0 0 1], $\sigma_{yz}^{\text{an,in}}$ and $\sigma_{xy}^{\text{an,in}}$, respectively, were evaluated.

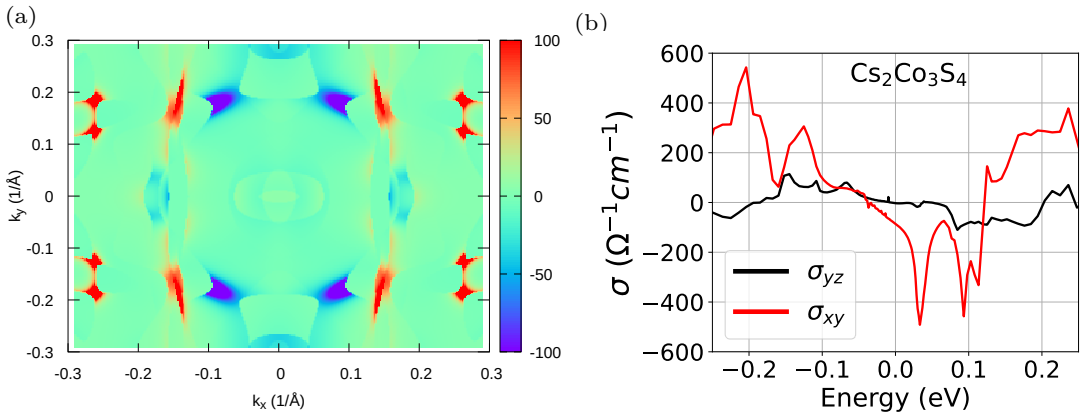

Figure 13: (a) Berry curvature distribution in the $k_z = 0$ plane. Hot spots are represent the significant Berry curvature of Weyl points and nodal line crossing in $Cs_2Co_3S_4$ for magnetization directions along [1 0 0]. Color bars are arbitrary units. (b) Intrinsic anomalous Hall conductivity of as a function of the chemical potential. The AHC σ_{yz} and σ_{xy} were obtained for orientation of the magnetization along [1 0 0] and [0 0 1], respectively.

In the ground state with easy magnetization axis [1 0 0], the calculated AHC is found to be nearly zero at E_F, but finite with ~ -15 Ω^{-1}cm^{-1} around 30 meV above E_F, where four WPs were found. However, this feature is much less prominent than the extended regions of large $|\sigma_{yz}^{\text{an,in}}|$ farther away from the Fermi level. These regions may originate from WPs that were not found in our limited search described in the previous section. However, it is known that in general the combination of broken time reversal symmetry with spin-orbit coupling generates contributions to the AHC also for bands with zero Chern number (Xiao *et al.*, 2010). Thus, the relation between AHC and Weyl points can be relatively weak (Ghimire *et al.*, 2019). As reported by Shi *et al.*, AHC is noted to be raised significantly in presence of WPs, agreeing with our calculation (Shi *et al.*, 2018). For the [0 0 1] direction of magnetization, on the other hand, the calculated AHC

at E_F amounts to -86 $\Omega^{-1}cm^{-1}$. At around 30 meV above E_F, a prominent AHC peak is observed with a magnitude of $\sim$ 500 $\Omega^{-1}cm^{-1}$, appearing at the position of the observed WP (point g). It is worth noting that, with a small amount of electron doping, a large value of AHC can be attained at E_F.

4.1.5 Fermi Arc Surface States

Properties of surface states are commonly associated with insulators and semiconductors. These surface states are well-defined and can exist within the bulk band gap, concentrated near the surface in an exponential manner. When dealing with a gapless semimetal, we assume translational invariance and identify surface states based on crystal momenta in the two-dimensional surface Brillouin zone (sBZ) (Armitage *et al.*, 2018). The key requirement is that there are regions in the sBZ where bulk states are absent at the same energy.

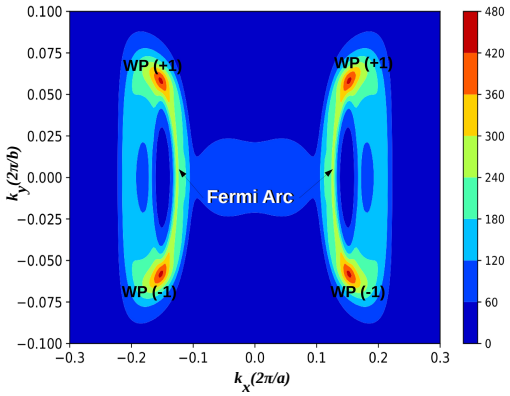

Figure 14: Fermi arc surface states of $Cs_2Co_3S_4$ of (0 0 -1) surface E_F = 0 meV for orientation of the magnetization along [1 0 0]. Color bars are arbitrary units.

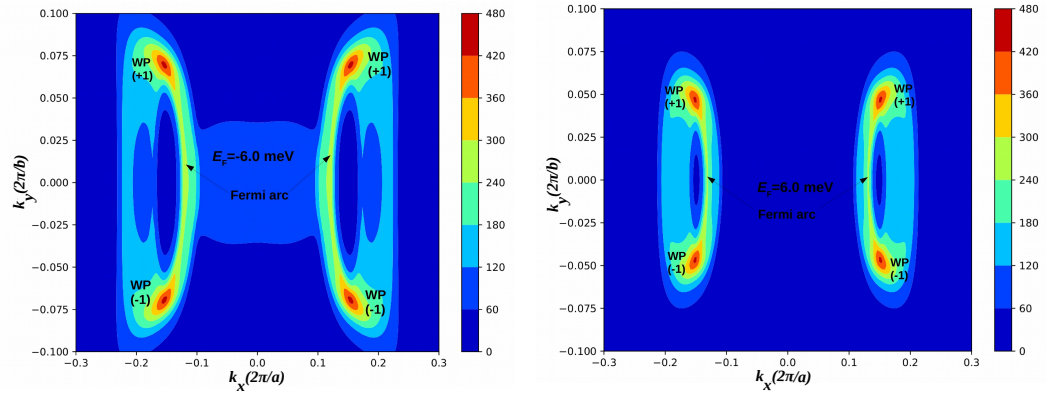

Figure 15: Fermi arc surface states of $Cs_2Co_3S_4$ of (0 0 -1) surface of (left) E_F = -6 meV and (right) E_F = 6 meV for orientation of the magnetization along [1 0 0]. Color bars are arbitrary units.

To investigate potential Fermi arc states at the E_F and around it, we also examined the energy dispersion of states related to Fermi arcs. The Fig. 14 and 15 indicate that these Fermi-arc-related bands can stretch from E_F to ±6 meV around the energy of

Weyl points, providing a promising opportunity to detect Fermi arcs in the low-energy range. We noticed that Weyl points lead to topologically protected surface states known as Fermi arc surface states. We projected Weyl points onto the (0 0 -1) direction and mapped individual Weyl points to spots in the sBZ to identify these states. The presence of topologically protected Fermi arcs is suggested by this mapping. The (0 0 -1) surface Fermi surface (spectral function) of an ideal semi-infinite slab is displayed in Fig. 15 and Fig. 14. Green's function recursion was used to obtain the spectral function by fitting the bulk Weyl fermion Hamiltonian to the slab form, while removing any surface or relaxation-induced Hamiltonian alterations (Koepernik *et al.*, 2016; Wang *et al.*, 2006; Sancho *et al.*, 1985). The shown portion of the sBZ is constrained in order to highlight the most important information.

4.2 Structural, Electronic, Magnetic and Topological Properties of $Li_2Fe_3S_4$

4.2.1 Structural Properties

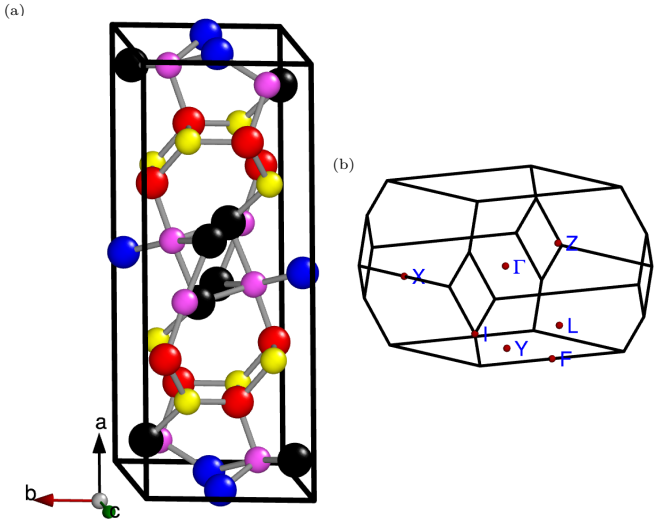

Figure 16: (a) Crystal structure of $Li_2Fe_3S_4$. Black (red, blue, pink, yellow) balls denote Li (Fe(I), Fe(II), S(I), S(II)) atoms. (b) Bulk Brillouin zone (BZ). The red dots indicate the high-symmetry point in the BZ.

Table 8: Total number of in-equivalent atoms and their Wyckoff positions in $Li_2Fe_3S_4$

Atom	Point location	x	y	z
Li	8f	0.087	0.102	-0.055
Fe(I)	4e	0	0.487	-1/4
Fe(II)	8f	0.186	0.371	-0.442
S(I)	8f	0.054	0.253	-0.444
S(II)	8f	0.198	0.302	0.204

$Li_2Fe_3S_4$ is Spinel-like structured and crystallizes in the monoclinic with nonsymmorphic space group C2/c (SG 15) and two formula units per primitive unit cell [structural lattice parametar and Wyckoff positions are taken from material project (Materials, 2020)]. Lattice parameters are a = 16.714 Å, b = 6.529 Å, c = 6.207 Å, and Angles $\alpha = \gamma = 90°$ and β =108°. In this system, the number of chemical formula units per structural unit cell is Z=2 shown in Fig. 16. It means total 18 atoms in the unit cell. G = $\{g, t\}$, combination of a point-group symmetry g with a fractional Bravais lattice vector translation t, represent a nonsymmorphic symmetry. Nonsymmorphic symmetries generate enforced band crossings. Symmetry-enforced band crossings are defined by a global topological charge, which measure the winding of the eigenvalue of G as we pass through BZ (Schnyder, 2020). There are 4 full group operations in crystal structure which includes Identity E, rotation C_{2y}, inversion I and mirror reflection M_y. In order to examine the thermodynamical stability of $Li_2Fe_3S_4$, the formation energy is calculated

by using equation

$$E_{for} = E^{Tot}_{Li_2Fe_3S_4} - [2E^{bulk}_{Li} + 3E^{bulk}_{Fe} + 4E^{bulk}_{S}]. \tag{4.2}$$

where $E^{Tot}_{Li_2Fe_3S_4}$ is the total energy of the crystal and E^{bulk}_{Li}, E^{bulk}_{Fe}, E^{bulk}_{S} are the energies of Lithium, Iron and Sulphur respectively obtained from bulk calculation. The formation energy per atom is -0.53 eV. The negative value of formation energy shows thermodynamical stability of the $Li_2Fe_3S_4$.

4.2.2 Electronic and Magnetic Properties

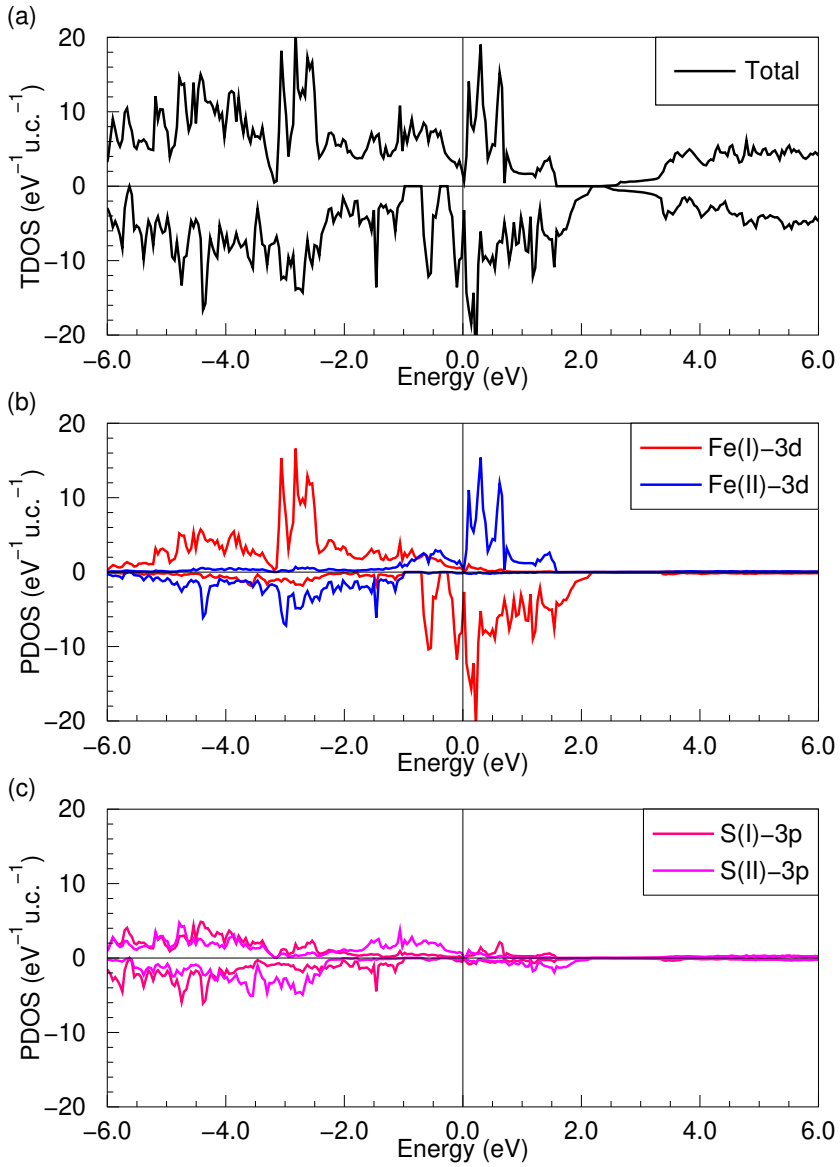

Figure 17: (a) Total DOS and (b-c) partial DOS of Fe, and S atoms calculated without SOC for ferrimagnetic $Li_2Fe_3S_4$. The Fermi level set to zero.

The results of the first principle calculation indicate the metallic feature of $Li_2Fe_3S_4$. We performed non-magnetic, FM and AFM coupling calculations for the identification of

the ground state of the system. We found the ferrimagnetic ground state with remaining magnetic moment 7.98 μ_B per unit cell (in scalar relativistic case). The total energies along the orientation of the magnetization [0 0 1], [0 1 0], and [1 0 0] directions were compared to obtain the magnetic ground state (in full relativistic). 7.95 μ_B, 7.96 μ_B and 7.96 μ_B for the fully relativistic mode with ferrimagnetic state along [0 0 1], [0 1 0] and [1 0 0] orientations respectively. The orbital magnetic moments are included in these values. The [0 0 1] magnetization direction found to be the lowest ferrimagnetic state. Magnetic anisotropic energy equal to 1.5 meV per unit cell in [0 0 1] to [1 0 0] direction and 3.0 meV per unit cell in [0 0 1] to [0 1 0] direction. The 3-d orbitals of Fe atoms exhibit large contributions at the (E_F), according to the computed density of states (see Fig. 17). In comparison to the Fe-3d, the S-3p and Li-1s orbitals have a small contribution to the E_F. From the analysis of the orbital character as shown in Fig. 18 (c) for the Wyckoff position of Fe(I) considering all four sites and (d) for the Wyckoff position of Fe(II) considering all two sites. We see clearly, for Fe(I), the conduction and valence bands near the E_F, $d_{x^2-y^2}$, d_{xy}, d_{yz} has major contribution but d_{z^2} and d_{zx} has minor contribution near the E_F. For the Fe(II), only d_{xy} has contribution bellow E_F. It is worth noting that the system contains four Fe atoms in the Fe(I) Wyckoff position and two in the Fe(II) Wyckoff position. We initially calculated the electronic band structure of $Li_2Fe_3S_4$ without SOC and plotted it along high-symmetry directions as shown in Fig. 18 (a). Near the E_F, we identify clear band inversion and several band crossing characteristics along the YX and UΓ lines. Besides, the band structure around the Fermi level changes when SOC is included shown in Fig. 18 (b).

4.2.3 Wannier Mapping and Weyl Properties

Fig. 18 (a) shows the electronic band structure of $Li_2Fe_3S_4$ for scalar and full relativistic case (with orientation of the magnetization along z-direction). After the consideration of SOC along 001 orientation of the magnetization, there is a gap open between the Y to X region by 19 meV, while 100 is not influence by SOC see Fig. 18 (b). We found, the electronic band structure is significantly influenced by the effect of SOC. We clearly see the band degeneracy near the Fermi level and which are possible for Weyl points. For this aim, in the search for Weyl points, we consider band numbers those making degeneracy, at the Y-X regions just above the Fermi level. The localized Wannier basis consists of Li [1s, 2s], Fe [3d, 4s], and S [3p, 3s] orbitals. To map the Wannier model, the same k-mesh as in the self-consistent calculations was chosen. The generated Wannier Hamiltonians were used to search Weyl points with the help of the PYFPLO module of FPLO. The search was limited to the Wannier bands 84 and 85. For the Chern number calculation, we used nsubdiv=100 which results in non-zero values close to +1 or -1. For orientation of the magnetization along [0 0 1], there are total of 8 Weyl points having either +1 or -1 chirality. Energies and their positions are shown in Tab. 9. Magnetization directions can

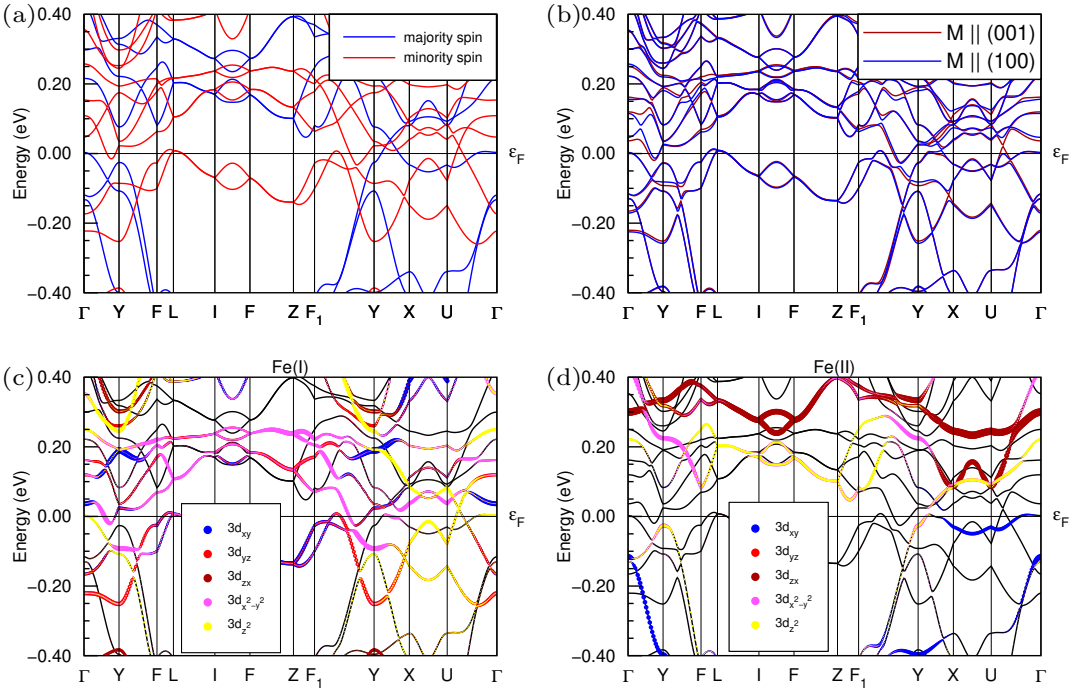

Figure 18: (a) Electronic band structure of $Li_2Fe_3S_4$ without SOC. The majority and minority spin contributions are shwon with red and blue color lines, respectively. (b) Electronic band structure obtained in SOC mode with magnetization M parallel to easy orientation of the magnetization along [0 0 1] and hard orientation of the magnetization along [1 0 0]. (c) Analysis of orbital contribution by Fe(I) site and Fe(II) site in the band structure for orientation of the magnetization along [0 0 1].

modify the Weyl characteristics of magnetic materials, changing the number of Weyl points and their energies in the momentum space (Zheng *et al.*, 2019). Additionally performed the Weyl calculation for orientation of the magnetization along [0 1 0] and [1 0 0]. 8 Weyl points are found in both orientation of the magnetization. Energies and their positions are shown in Tab. 10 and 11, respectively. This system has possibilities for large intrinsic anomalous Hall conductivity due to the large Berry curvature. Because large Berry curvature comes from monopole of Weyl points. Fig. 19) shows the Wannier fitting of $Li_2Fe_3S_4$ for orientation of the magnetization along [0 0 1] and [1 0 0].

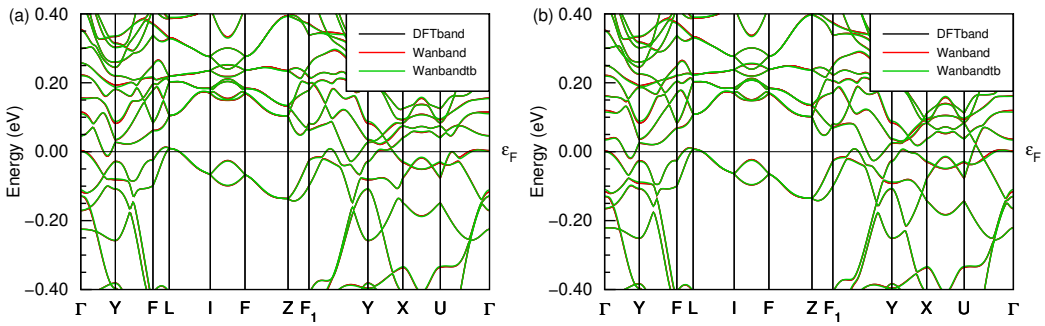

Figure 19: Wannier fitting of $Li_2Fe_3S_4$ for orientation of the magnetization along (a) [0 0 1], and (b) [1 0 0] magnetization directions.

Table 9: Characteristics of Weyl points in the $Li_2Fe_3S_4$ electronic structure for orientation of the magnetization along [0 0 1]. WP denotes the sets of Weyl points. There are three sets of Weyl nodes denoted by W_1, W_2, and W_3. 'M' denotes the multiplicity of the Weyl nodes.

WP	Energy (meV)	M	k_x (2π/a)	k_y(2π/b)	k_z(2π/c)	χ
W_1	2	4	-0.143	-0.572	0.130	-1
W_2	10	2	-0.854	0	-0.121	1
W_3	39	2	0.745	0	-0.155	-1

Table 10: Characteristics of Weyl points in the $Li_2Fe_3S_4$ electronic structure for orientation of the magnetization along [0 1 0]. WP denotes the sets of Weyl points. There are three sets of Weyl nodes denoted by W_1, W_2, and W_3. 'M' denotes the multiplicity of the Weyl nodes.

WP	Energy (meV)	M	k_x (2π/a)	k_y(2π/b)	k_z(2π/c)	χ
W_1	12	2	0	0.858	0	-1
W_2	18	2	0	-0.449	0	-1
W_3	19	4	-0.160	-0.449	-0.044	-1

Table 11: Characteristics of Weyl points in the $Li_2Fe_3S_4$ electronic structure for the orientation of the magnetization along [1 0 0]. WP denotes the sets of Weyl points. There are three sets of Weyl nodes denoted by W_1, W_2, and W_3. 'M' denotes the multiplicity of the Weyl nodes.

WP	Energy (meV)	M	k_x (2π/a)	k_y(2π/b)	k_z(2π/c)	χ
W_1	8	4	-0.100	0.594	0.136	1
W_2	29	2	-0.762	0	-0.131	1
W_3	35	2	-0.781	0	0.153	-1

4.3 Structural, Electronic and Magnetic Properties of $Cs_2Mn_3S_4$

4.3.1 Structural Properties

Similar to $Cs_2Co_3S_4$, $Cs_2Mn_3S_4$ is another material discovered by (Bronger *et al.*, 1988a). Despite its synthesis, there is no available information on its electronic and related properties as per our knowledge. $Cs_2Mn_3S_4$ has a crystalline structure in a body-centered orthorhombic Bravais lattice with the centrosymmetric space group *Ibam* (SG 72), featuring two formula units per primitive unit cell. The XRD results, presumably obtained at room temperature, revealed lattice parameters a = 5.940 Å, b = 11.490 Å, and c = 14.169 Å. According to the same experiment, Cs and S atoms occupy the 8j and 16k sites at (0.232, 0.119, 0) and at (0.221, 0.366, 0.153), respectively, while the Mn atoms occupy the 8g sites, denoted as Mn(I), at (0, 0.230, 0.250) and the 4b sites, denoted as Mn(II), at (0.500, 0, 0.250). Cs atoms were positioned at the center of distorted cubes of S atoms, while Mn atoms were surrounded by S tetrahedra. The relevant bond lengths were measured as 3.62 Å for Cs - S, 2.42 Å for Mn(I) - S, and 2.44 Å for Mn(II) - S. The overall structure is depicted in Fig. 20.

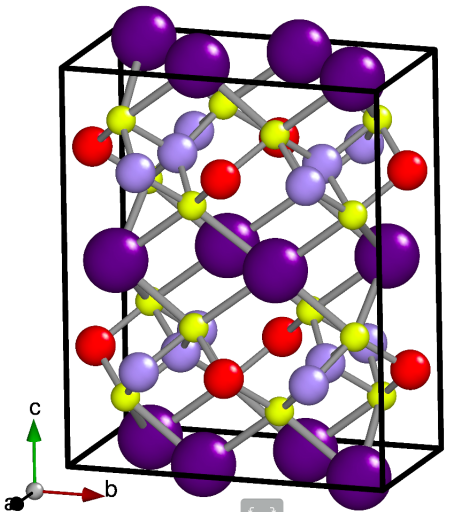

Figure 20: Crystal structure of $Cs_2Mn_3S_4$ in the conventional elementary cell. Violet (blue, red, yellow) balls denote Cs (Mn(I), Mn(II), S) atoms.

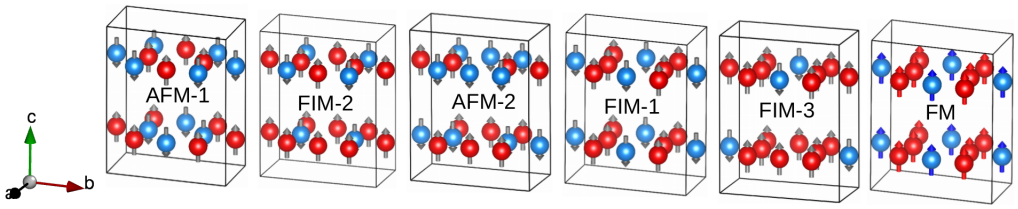

Figure 21: Considered spin configurations. the same Wyckoff position were considered to carry magnetic moments with different orientation were performed in space group *I222* (SG 23). From left to right, different AFM, FIM and FM arrangements are depicted in ascending order of their energy according to our calculations using experimental room-temperature lattice parameters. Only Mn atoms are shown. Different colors denote different spin orientations.

4.3.2 Electronic and Magnetic Properties

Table 12: Scalar relativistic energies and spin moments. Calculated relative total energies E, given per primitive unit cell with 18 atoms and local and total spin magnetic moments M_s for the six considered configurations depicted in Fig. 21.

Configuration	E [meV/unit cell]	M_s(Mn(I)) [μ_B]	M_s(Mn(II)) [μ_B]	M_s(unit cell) [μ_B]
AFM-1	0	4.40, -4.40	4.56, -4.56	0
FIM-2	180.7	4.51, -4.30	4.57, -4.56	10
AFM-2	344.8	4.40, -4.40	4.55, -4.55	0
FIM-1	543.7	4.53	-4.35	10
FIM-3	1466.8	4.62, -4.33	4.75	20
FM	2434.2	4.72	4.75	30

We started our calculations with a search for the stable magnetic ground state of $Cs_2Mn_3S_4$. Based on ND data, a collinear AFM order was suggested to be the stable magnetic state at 4.2 Kelvin. In this state, four of the Mn(I) sites show a spin orientation opposite to the spin orientation of the four other Mn(I) sites and two of the Mn(II) sites show a spin orientation opposite to the spin orientation of the two other Mn(II) sites (AFM-1 in Fig. 20). Permutation of the spin orientations of these four groups

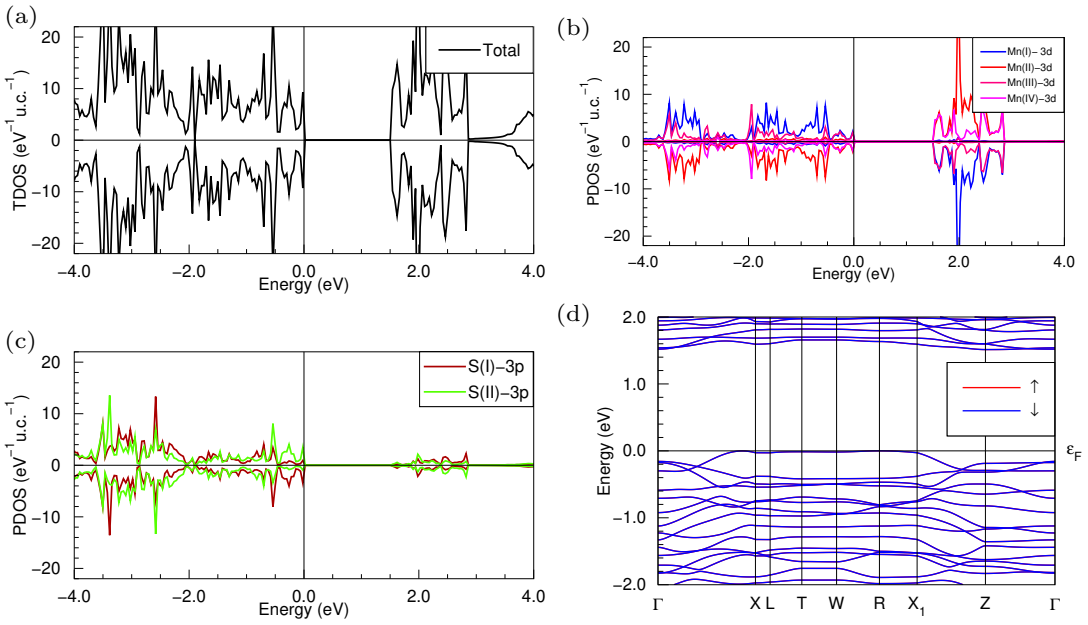

Figure 22: (a) Total DOS. (b-c) Partial DOS. (d) Electronic band structure of $Cs_2Mn_3S_4$ in scalar relativistic case for AFM-1 spin configuration.

of sites yields eight different combinations. Two of the combinations are equivalent by symmetry to other combinations. We investigated the six remaining combinations, shown in Fig. 21. They include FM, two different AFM, and three FIM arrangements. Tab. 12 compiles the relative total energies and spin magnetic moments, obtained by means of calculations in a scalar relativistic mode and using room-temperature XRD lattice parameters (Bronger *et al.*, 1988a). Agreement with the experimental result, the arrangement AFM-1 is found to be the lowest-energy state. All other considered arrangements have much higher total energies. The three in-equivalent orthorhombic directions [1 0 0], [0 1 0], and [0 0 1] are taken into consideration here. Experimental observed magnetic moment per atom for Mn(I)=4.65 μ_B and Mn(II)=5.04 μ_B (Bronger *et al.*, 1988a). The configuration AFM-1 with the magnetization oriented in the [0 0 1] direction has the lowest energy among them. The value of the magnetic anisotropy energy (MAE), which is the energy difference between unlike orientations of the magnetization (from 001 to 010), amounts to about 0.2 meV per unit cell. We also performed full relativistic calculations using spin-orbit coupling. In electronic band structure, SOC has a negligible effect. Thus, we confine our discussion focused only on to the scalar relativistic calculations findings. Fig. 22 (a-c) shows the total and PDOS for the ground state AFM-1 configuration in scalar relativistic mode. A band gap of 1.5 eV is observed between the valence band and the conduction band. The main contributions to the total DOS are seen from the Mn-3d orbitals around E_F. Focusing now on the electronic band structure (see Fig. 22 (d)), both the valence band maximum (VBM) and the conduction band minimum (CBM) lies at the different high-symmetry point in the momentum space

dictating that the material $Cs_2Mn_3S_4$ is an indirect band gap semiconductor. Identifying new magnetic semiconductors opens the door for additional experimental research for this group of materials that could be used to fabricate valuable devices, including semiconductor lasers, solar cells, and light-emitting diodes, etc.

4.4 Structural, Electronic and Magnetic Properties of $Rb_2Mn_3S_4$

4.4.1 Structural Properties

$Rb_2Mn_3S_4$ (Fig. 23) has been reported to be a body-centered orthorhombic structure with space group *Ibam* (SG 72), featuring two formula units per primitive unit cell. Eight equivalent S^{2-} atoms form a body-centered cubic geometry connection with Rb^{1+}. There exist two different sites of Mn^{2+}. Mn^{2+} is linked to four equivalent S^{2-} atoms in the Mn^{2+} site, creating a mixture of edge and corner-sharing MnS_4 tetrahedra. The experimental lattice parameter of $Rb_2Mn_3S_4$ are a = 5.842 Å, b = 11.211 Å, c = 13.660 Å. The atomic Wyckoff positions are [0.268, 0.119, 0] for Rb, [0, 0.276, 0.250] for Mn(I), [0, 0, 0.250] for Mn(II), [0.218, 0.133, 0.344] for S (Bronger and Böttcher, 1972).

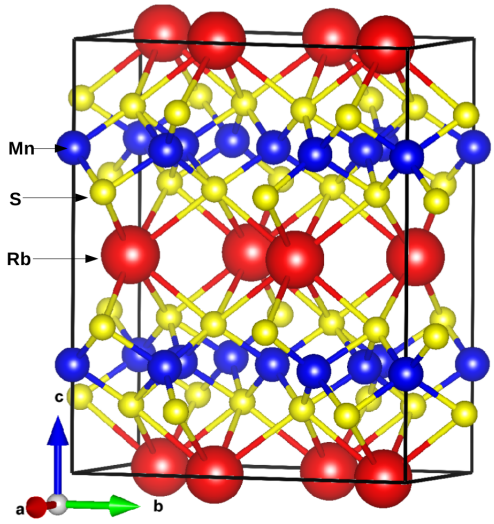

Figure 23: Crystal structure of $Rb_2Mn_3S_4$.

4.4.2 Electronic and Magnetic Properties

We performed nonmagnetic and magnetic calculations to identify the ground state of the system. In the magnetic calculations, we considered FM and AFM interactions of Fe(I) and Fe(II). These calculations revealed a ferrimagnetic ground state with a remaining magnetic moment of 10 μ_B per unit cell (in the scalar relativistic case). An individual magnetic moment of 4.4 μ_B for Mn(I) and 4.1 μ_B for Mn(II), with polarized moment transfer to S (0.07 μ_B) atoms. However, the total ordered magnetic moment within GGA+U remains the same (10 μ_B/unit cell) as that of GGA; the individual moment rises

slightly to 4.8 μ_B and 4.7 μ_B for Mn(I) and Mn(II), due to reduced Mn-S hybridization. We further consider the relativistic effect (spin-orbit coupling) to identify the magnetic easy axis along [0 0 1], [0 1 0], and [1 0 0] directions. The magnetic easy axis was found along [0 1 0], while the [1 0 0] is a hard axis orientation of the magnetization direction. The calculated magnetic anisotropic energy is ~ 0.4 meV per unit cell in $Rb_2Mn_3S_4$.

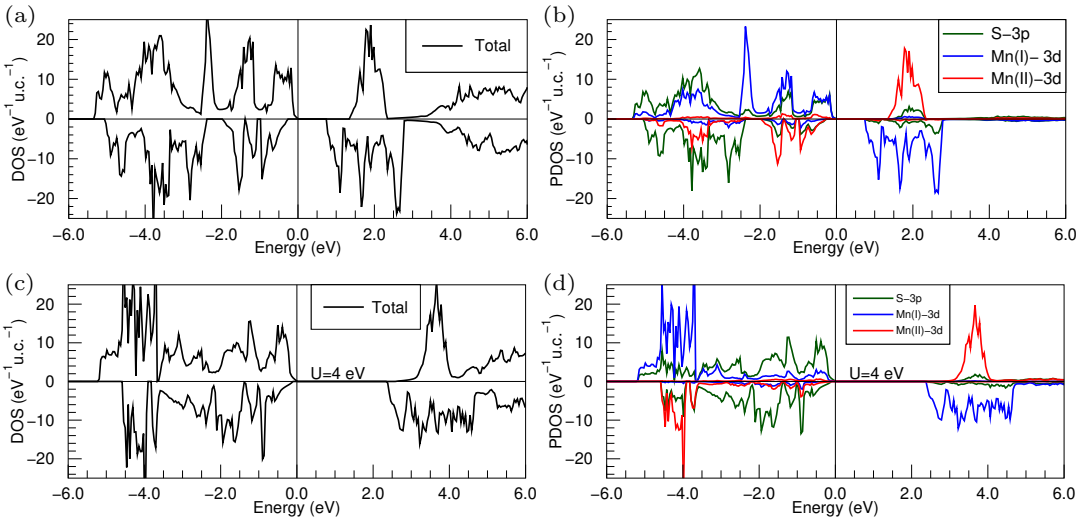

Figure 24: Total and partial DOS of $Rb_2Mn_3S_4$ in scalar relativistic mode within (a-b) GGA and (c-d) GGA+U (with U=4 eV for Mn).

From the total and partial density of states (DOS) within GGA for the ferrimagnetic ground state (see Fig. 24 (a-b)), band gap of 0.75 eV is found. The main contributions to the total DOS are seen from the Mn(I)-3d, Mn(II)-3d and S-3p orbitals around E_F. In the conduction region, S-3p and Mn(II)-3d dominate above E_F in spin-up channels, while in spin-down, Mn(I)-3d has significant contributions. On the other hand, below E_F, Mn(I)-3d states significantly contribute to spin-up, while the spin-down channel is contributed by Mn(II)-3d hybridizing with the S-3p states. Generally, the DFT technique underestimates the size of the electronic band gap. We apply the Hubbard parameter *(U)*, which plays a significant role in handling the delocalized d-bands resulting in the prediction of the experimental band gap. This was done following the literature's (Pak *et al.*, 2019; Boukhvalov and Solovyev, 2010; Tolba *et al.*, 2018; Tran *et al.*, 2006), which suggests that the appropriate value of U for Mn is between 3 eV and 4 eV in most cases. We used the full-localized limit of the double counting scheme with F^0 =4.0 eV, F^2 = 5.5 eV, and F^4 = 8.5 eV, leading to U = 4.0 eV and J = 1 eV. The total and partial DOS within GGA+U is shown in Fig. 24 (c-d). Interestingly, the Mn-3d states below E_F shift far below, with some minor states around E_F hybridizing significantly with the S-3p states. The band gap so formed is of charge-type between the Mn(I) and S-3p states. Focusing now on the electronic band structure of $Rb_2Mn_3S_4$ in scalar relativistic mode (see Fig. 25), both the VBM and CBM lies at the high-symmetry

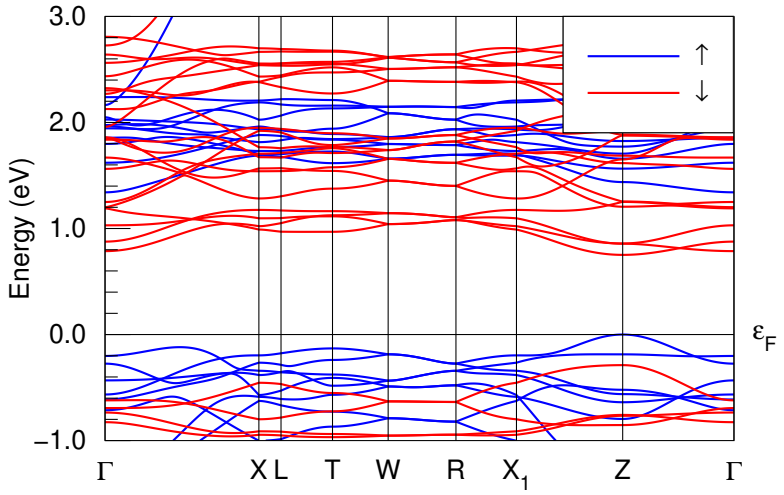

Figure 25: Electronic band structure of $Rb_2Mn_3S_4$ in scalar relativistic mode for GGA. The Fermi level is set to zero.

point Z in the momentum space dictating that the material $Rb_2Mn_3S_4$ is a direct band semiconductor. This suggests that electrons can transfer directly from the VBM to the CBM. In particular, the band gap makes $Rb_2Mn_3S_4$ an attractive choice for photovoltaic and opto-electronic devices due to the finite gap size within the visible range (Li *et al.*, 2020a). The calculated energy gap within GGA and GGA+U are 0.75 eV and 2.34 eV, respectively. Semiconducting materials, especially with a direct band gap, are helpful for modern photovoltaic and opto-electronic device fabrication.

4.5 Structural, Electronic and Magnetic Properties of $K_2Mn_3S_4$

4.5.1 Structural Properties

$K_2Mn_3S_4$ has been reported to be a monoclinic structure with space group *P2/c* (SG 13), having two formula units per primitive unit cell. By fusing potassium carbonate and manganese in a stream of hydrogen sulfide at 900 °C, $K_2Mn_3S_4$ has been synthesized (Bronger *et al.*, 2000). There are two in-equivalent K^{1+} sites, Mn^{2+} sites and S^{2-} sites denoted by K (I), K (II), Mn (I), Mn (II), respectively. In order to create a mixture of corner and edge-sharing MnS_4 tetrahedra, Mn^{2+} is bound to four S^{2-} atoms at both Mn^{2+} sites. S^{2-} is linked to four K^{1+} and three Mn^{2+} atoms in the first S^{2-} site. S^{2-} is linked to four K^{1+} and three Mn^{2+} atoms in the second S^{2-} site in a 7-coordinate geometry as shown in Fig. 26 (a). The respective Brillouin zone (BZ) for the crystal is shown in Fig. 26 (b). $K_2Mn_3S_4$ has a non-symmorphic with centrosymmetric system. The experimental lattice parameter that we used for our calculations are a = 7.244 Å, b = 5.822 Å, and c = 11.018 Å. And angles are $\alpha = 90°$, $\gamma = 90°$ and β =112.33° (Bronger

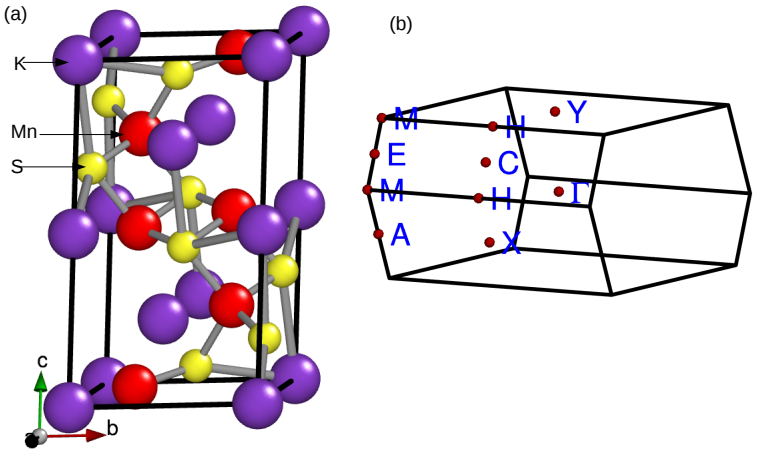

Figure 26: (a) Crystal structure of $K_2Mn_3S_4$. (b) 3-D Brillouin zone. The red dot indicates the high symmetry point in the momentum space.

et al., 2000).

4.5.2 Electronic and Magnetic Properties

To identify the ground state of the $K_2Mn_3S_4$, we performed nonmagnetic and magnetic calculations. In the magnetic calculations, we considered FM and AFM interactions of Fe(I) and Fe(II). These calculations revealed a ferrimagnetic ground state with a total remaining magnetic moments found to be 10 μ_B per unit cell (in the scalar relativistic case). The individual moments calculated are 4.2 μ_B for Mn(I) and 4.1 μ_B for Mn(II), respectively. Total and partial DOS within GGA calculation as shown in Fig. 27 (a-c), wherein the main contributions above the E_F in spin-up channels are from Mn(II)-3d and spin-down channels from Mn(I)-3d orbitals. Below E_F, the contributions are from Mn(I)-3d in spin-up channel and in spin-down channel contributions are from Mn(II)-3d states hybridizing with the S-3p states. Exchange coupling between the spin-up and spin-down DOS close to E_F are prominently contributed by Mn(II)-3d with an exchange splitting of $\sim$ 2 eV, while for Mn(I) found to be approximately 3 eV, respectively. The electronic band structure of $K_2Mn_3S_4$ in scalar relativistic is shown in Fig. 27 (d), the valence VBM lies in MA while the CBM lies at ΓY line in the momentum space resulting in an indirect band gap between VBM and CBM (see Fig. 27 (d)). $K_2Mn_3S_4$ is thus a semiconductor with an indirect band gap of 1.1 eV. The effect of SOC is minimal and retains the similar size of band gap. So, we only focus on scalar relativistic case for the discussion. In particular, the band gap value of 1.1 eV. The magnetic easy axis is found to be [0 0 1] with hard axis along [0 1 0] direction in full relativistic case calculation (i.e. within the consideration of SOC).

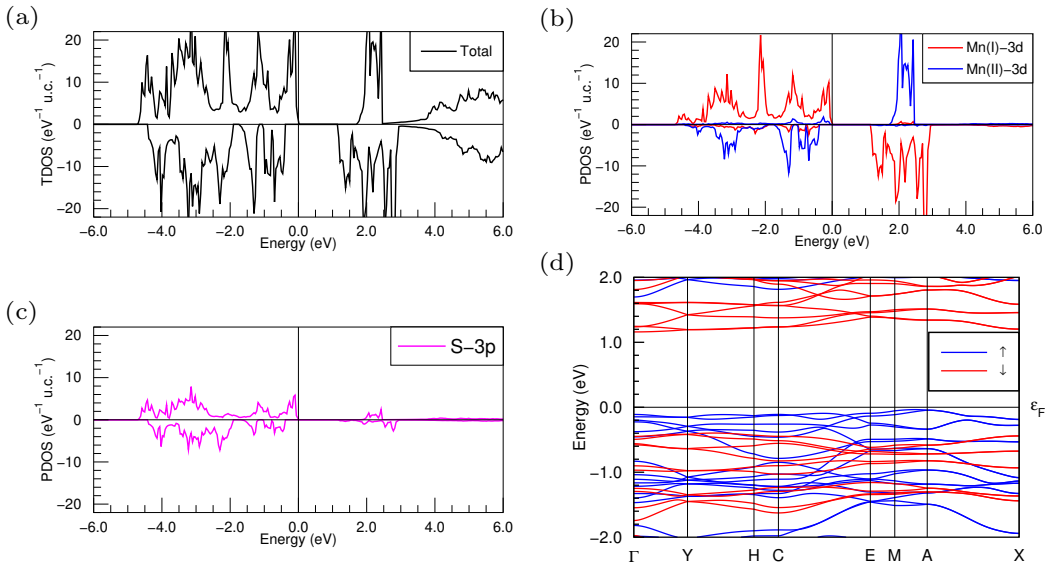

Figure 27: (a) Total DOS and (b-c) partial DOS for both in-equivalent S and Mn atoms without SOC of $K_2Mn_3S_4$. The Fermi level is set to zero. (d) Electronic band structure in scalar relativistic case. Horizontal solid line indicates the Fermi level.

4.6 Structural, Electronic and Optical Properties of Kagome $Rb_2Ni_3S_4$

4.6.1 Structural and Electronic Properties

$Rb_2Ni_3S_4$ crystallizes in an orthorhombic crystal structure with space group *Fmmm* (SG 69), having one formula units per primitive unit cell. The experimental lattice parameters used in this study are a = 5.862 Å, b= 9.937 Å and c = 13.758 Å (Bronger *et al.*, 1991). The system consists of four in-equivalent atoms labeled as Rb, Ni(I), Ni(II), and S, respectively. In $Rb_2Ni_3S_4$, Rb^{1+} ions are surrounded by eight equivalent S^{2-} ions in an 8-coordinate geometry. All Ni^{2+} ions are coordinated by four equivalent S^{2-} ions, adopting a square co-planar arrangement (see Fig. 28 (a)). At the first and second Ni^{2+} site, the Ni–S bond length measured are 2.22 Å. Furthermore, $Rb_2Ni_3S_4$ exhibits symmorphic crystal symmetry, and due to the presence of a center of inversion, they are considered centrosymmetric crystal. Tab. 13 presents the in-equivalent atoms and their coordinates for $Rb_2Ni_3S_4$.

Table 13: Total number of in-equivalent atoms and their Wyckoff positions in $Rb_2Ni_3S_4$.

Atom	Point location	x	y	z
Rb	8i	0	0	0.343
Ni(I)	8e	-1/4	-1/4	0
Ni(II)	4a	0	0	0
S	16m	0	0.168	0.106

We performed the total energy calculations for non-magnetic and ferromagnetic configuration. The total energy is found to be lowest for nonmagnetic dictating the ground state

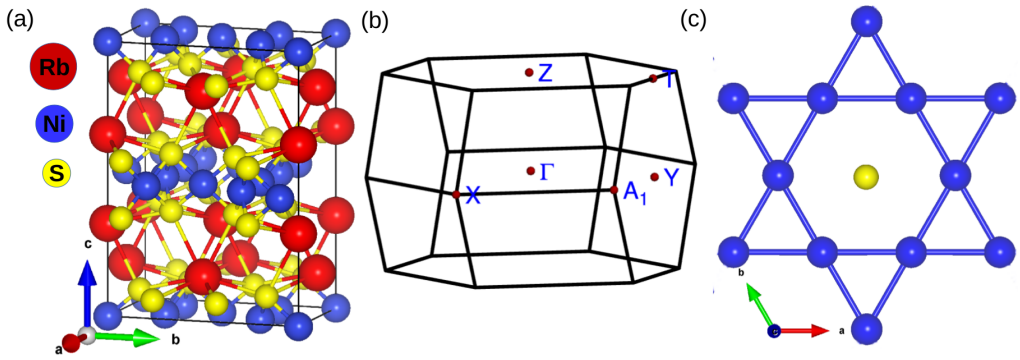

Figure 28: (a) Crystal structure of $Rb_2Ni_3S_4$. (b) Three dimensional Brillouin zone. Red dots are indicates the high symmetry points in momentum space. (c) Ni-ions constitute a kagome lattice in *ab* plane.

of the material, agreement with experimental ground state (Bronger *et al.*, 1991). To understand the electronic properties, we performed the density of states (DOS) and band structure calculation. Based on the total and partial DOS analysis, as shown in Fig. 29, it is evident that 3d orbital of Ni and 3p orbital of S atoms contribute significantly to the DOS, while Rb has minor contributions (see Fig. 29 (b)). This difference is due to the presence of only one electron in the outermost 5s orbital of Rb atom. To enhance clarity, we display the local DOS projections individually, focusing on Ni(I)-3d as depicted in Fig. 29 (c), and of Ni(II)-3d as shown in Fig. 29 (d).

The analysis of the local DOS (LDOS) projection (see Fig. 29 (c-e)) reveals that the insulating behavior originates from the splitting of energy bands due to the ligand field effect. It is well-established that each nickel (Ni) ion is surrounded by four S ions, forming a square planar coordination arrangement Fig. 28 (a). In this situation, the S^{2-} ions strongly bind with the central Ni^{2+} metal, causing a separation of energy levels known as ligand field splitting. As a result, metal ions with a d^8 configuration tend to adopt a square planar geometry when exposed to a strong ligand field. This arrangement forms low spin complexes where the eight d electrons fill the lower-energy d_{xz}, d_{yz}, d_z^2, and d_{xy} orbitals, while the high-energy $d_{x^2-y^2}$ orbital remains unoccupied. Furthermore, below the E_F, a pronounced hybridization occurs between the S-3p_x and S-3p_y orbitals with the Ni-3d_{xy}, $d_{x^2-y^2}$, and d_z^2 orbitals in the energy range spanning from 0 to -0.035 eV. Conversely, above E_F, S-3p_x and S-3p_y orbitals exhibit significant hybridization with the Ni-3d_{xz} and Ni-3d_{yz} orbitals within the energy range from 0.7 to 1.2 eV (see Fig. 29 (c-e). Additionally, the kagome lattice of Ni^{2+} leads to the formation of flat bands below E_F, which is mainly contributed by 3d_{xy} orbital of Ni atom. Theoretical studies have suggested that such flat band systems in a kagome lattice can give rise to various exotic many-body phenomena (Li *et al.*, 2022; Hondou and Chikazawa, 2007; Hondou *et al.*, 2002; Kang *et al.*, 2020; Wang *et al.*, 2013b; Yu and Li, 2012). Based on the analysis of the electronic band structure, $Rb_2Ni_3S_4$ exhibit semiconducting behavior

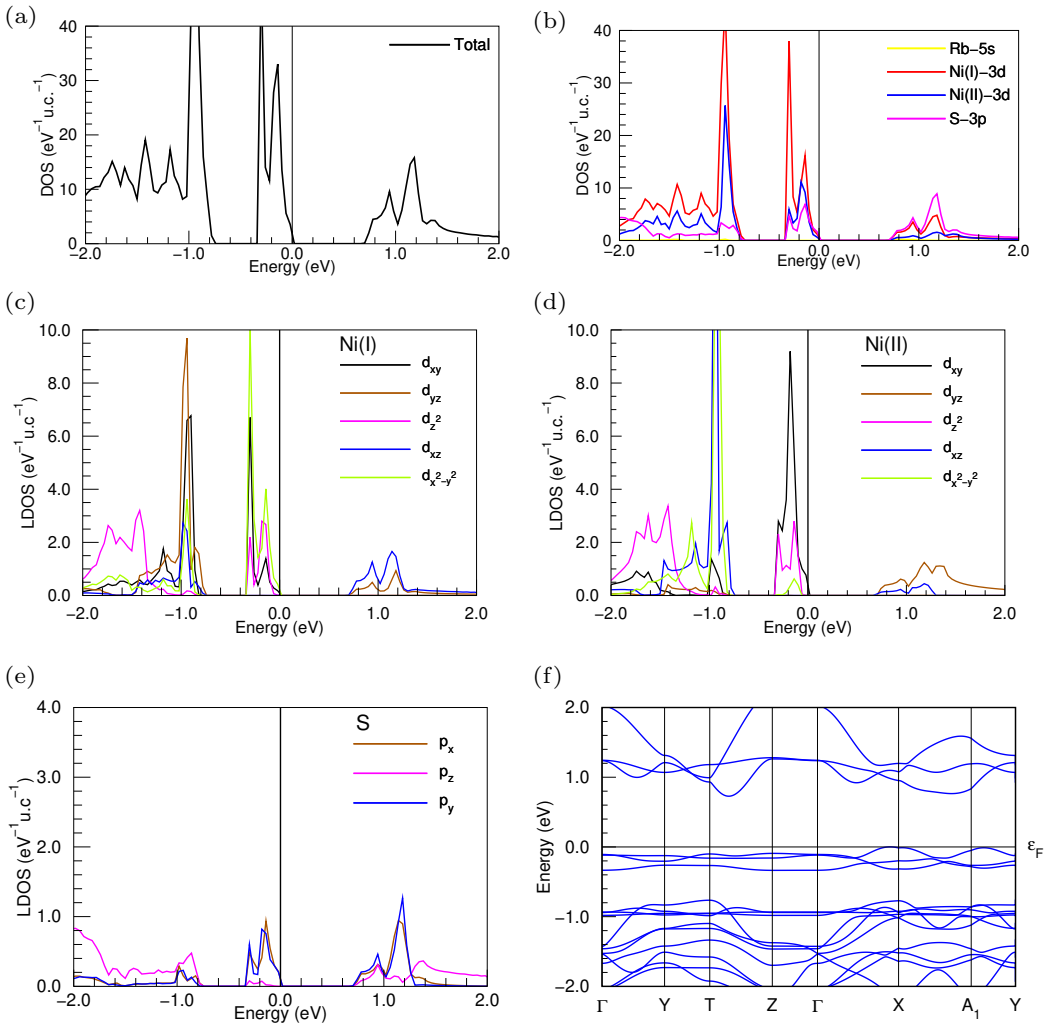

Figure 29: Total, partial and local DOS of $Rb_2Ni_3S_4$. (a) Total DOS. (b) partial DOS. (c) Projected local DOS for Ni(I)-3d, (d) Ni(II)-3d and (e) S-3p. The vertical solid line at zero energy denotes E_F. (f) Electronic band structure of $Rb_2Ni_3S_4$. The horizontal solid line at zero energy denotes E_F.

with an energy band gap of ~0.67 eV. These findings are consistent with the previously reported DFT value of 0.66 eV (Nawai *et al.*, 2004) and the experimental value of 0.80 eV deduced from a transport study (Hondou *et al.*, 2002). The nature of the band gap is indirect. This is attributed to the occurrence of the VBM at the high symmetry point X and the CBM at the T-Z line in the momentum space (see Fig. 29) (f).

4.6.2 Optical Properties

The linear response of the system to electromagnetic radiation, which is associated to the interaction of photons with electrons, can be defined using the complex dielectric function, $\epsilon(\omega)$.

$$\epsilon(\omega) = \epsilon_1(\omega) + i\epsilon_2(\omega) \tag{4.3}$$

where, ϵ_1 and ϵ_2 are the real and imaginary part of the dielectric function, respectively (He *et al.*, 2006; Ghosh and Thangavel, 2017). In accordance with the selection criteria, the momentum matrix elements between the occupied and unoccupied state are used to calculate the imaginary component of the dielectric function, which is given by the following equation (Ambrosch-Draxl *et al.*, 1995; Launay *et al.*, 2004),

$$\epsilon_2(\omega) = \frac{4\pi^2 e^2}{m^2\omega^2 V} \sum_{g,g'} | < kg|p|kg' > |^2 \delta(E_{kg} - E_{kg'} - \hbar\omega) \tag{4.4}$$

where e, p, V, and $\hbar\omega$ is the electronic charge, momentum operator, unit cell volume, and the energy of the incident photon. The Fermi distribution function is indicated by *f(kg)*, and E_{kg} is the eigenvalue associated with eigenfunction $|kg >$. The real part is given by Kramers-Kronig relationship (Toll, 1956),

$$\epsilon_1(\omega) = 1 + \frac{2}{\pi} \int \frac{\epsilon_2(\omega')\omega'}{(\omega')^2 - \omega^2} d\omega' \tag{4.5}$$

The optical conductivity and electron loss function are given by the following equation,

$$\sigma(\omega) = \frac{-i\omega(\epsilon(\omega) - 1)}{4\pi} \tag{4.6}$$

$$L(\omega) = \frac{\epsilon_2}{\epsilon_1^2(\omega) + \epsilon_2^2(\omega)} \tag{4.7}$$

As already observed from electronic structure calculations, $Rb_2Ni_3S_4$ exhibits semiconducting properties with a band gap of approximately ~0.67 eV. Therefore, when exposed to incident photons, electronic transitions can occur if the photon energy is equal to or greater than the band gap energy. In such transitions, photons excite electrons from occupied states in the valence band region to unoccupied states in the conduction band region known as interband transition (Stepanjuga *et al.*, 2022). To understand these phenomena, to study the underlying optical properties, we consider the polarization components along the x, y, and z directions due to an orthorhombic crystal structure. To understand the electronic polarizability of the material under an applied electric field, we analyze the real part of the dielectric function $\epsilon_1(\omega)$ as depicted in Fig. 30 (a). $\epsilon_1(\omega)$ along x, y and z direction denoted by ϵ_{1xx}, ϵ_{1yy}, and ϵ_{1zz}, respectively. The real part of the dielectric function at zero frequency, (which is connected to the material's band gap is known as static dielectric constants $\epsilon_1(0)$) are found to be ~7.5 along both the x and y directions, while it is ~6.2 along the z direction. Correspondingly, the refractive index was determined using the established Penn Relation n(0) = $\sqrt{\epsilon_1(0)}$ (Penn, 1962) gives

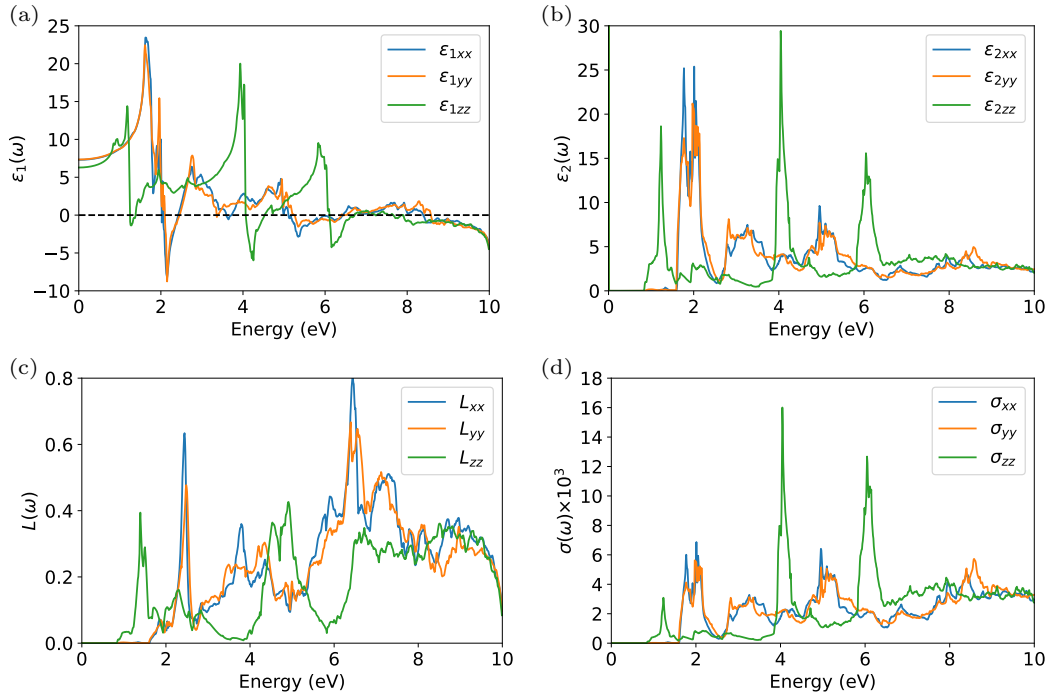

Figure 30: Optical properties of $Rb_2Ni_3S_4$. (a) real part of the dielectric function $\epsilon_1(\omega)$. (b) Imaginary part of the dielectric function $\epsilon_2(\omega)$. (c) Energy loss spectrum L(ω). (d) Optical conductivity $\sigma(\omega)$ [in $Ohm^{-1}cm^{-1}$].

the static refractive index as 2.74 along x and y direction while 2.49 along z direction. The obtained value shows that the material has optical anisotropy. In the energy range 0 to 1.3 eV for the x, y direction, and 0 to 1 eV for the z direction, we observe a gradual increase in $\epsilon_1(\omega)$, which indicates that the material interacts effectively with photons. Notably, at 1.63 eV, 1.60 eV, and 1.16 eV for ϵ_{1xx}, ϵ_{1yy}, and ϵ_{1zz}, respectively, sharp peaks are observed. These peaks correspond to the inter-band transition, indicating the photon-induced electron transitions from occupied valence bands to the unoccupied conduction bands. This means that the material can absorb light particularly well at that specific energy. Within the photon energy range exceeding 1.16 eV, the real part of the dielectric function $\epsilon_1(\omega)$ exhibits a remarkable characteristic: it adopts a negative value. This phenomenon is indicative of incident light being reflected by the medium. Consequently, the material demonstrates metallic attributes in this specific energy range (Shore, 2019; Kumar *et al.*, 2021). Furthermore, we also observe sharp peaks at approximately 2.01 eV, 1.96 eV, and 3.93 eV for x, y and z direction, respectively. $\epsilon_2(\omega)$, the imaginary part of the dielectric function, reveals details about optical absorption in crystal. The absorption begins at 0.84 eV for the imaginary part of the dielectric function, which act as the threshold energy associated with the occurrence of an optical band gap (see Fig. 30 (b)). Beyond the threshold point, curve increases rapidly. Notably, sharp peaks are seen along the x, y, and z directions, respectively, at 2.02 eV, 1.97 eV, and 1.22 eV. These absorption peaks may clearly be associated with transitions from the Ni(3d) valence band to the S(3p) conduction band based on the predicted PDOS (see Fig. 30

(b)). Additionally, within the energy range of 2.83 eV to 6.05 eV, various significant peaks are observed. These peaks correspond to inter-band transitions from the valence band to the conduction band (Kumar and Ahluwalia, 2012; Belbase *et al.*, 2023). However, beyond the energy of 6.05 eV, the peaks begin to diminish, eventually disappearing at higher energy ranges. Another important optical property calculated in this work is the electron energy loss function L(ω). Fig. 30 (c) shows the variation of L(ω) with photon energy. The L(ω) provides the information about the energy loss of a fast-moving electron traversing in the material (Wang and Klein, 1981; Zhang *et al.*, 2007a). The visible area of the loss spectrum exhibits a slight energy loss, which rises as photon energy increases. The identified peaks in the L(ω) spectra provide information about the material's plasma frequency. The nature of the material, i.e., whether it exhibits metallic properties or dielectric behavior, is known to be described by the plasma frequency. It is well known that materials exhibit metallic [$\epsilon_1(\omega) < 0$] behavior below the plasma resonance frequency and dielectric [$\epsilon_1(\omega) > 0$] behavior above this frequency (Kumar *et al.*, 2021; Hu *et al.*, 2007; Sun *et al.*, 2006). The maximal peaks for L_{xx}, L_{yy}, and L_{zz} are clearly visible in the energy loss spectra at approximately 6.44 eV, 6.41 eV, and 4.91 eV, respectively. The resonant energy loss is seen at 6.44 eV along x direction with a maximum value of 0.8. After these peaks, the spectrum starts to decline. In Fig. 30 (d), show the optical conductivity which depend on photon energy. This indicate that the $Rb_2Ni_3S_4$ exhibits optical activity in the range from 1.25 eV to 8.60 eV. The $\sigma(\omega)$ edge starts 0.84 eV, which corresponds to the calculated optical band gap of the material, and numerous peaks are observed in the spectrum. Maximum optical conductivity, σ_{xx}, σ_{yy} and σ_{zz} was found to be 6.5×10^3 $Ohm^{-1}cm^{-1}$, 16×10^3 $Ohm^{-1}cm^{-1}$ and 5.9×10^3 $Ohm^{-1}cm^{-1}$, respectively at photon energy of 2.02 eV to 4.05 eV. These findings are consistent with the imaginary part of the dielectric function, results obtained in Fig. 30 (b).

4.7 Structural, Electronic and Optical Properties of Kagome $Cs_2Ni_3S_4$

4.7.1 Structural and Electronic Properties

$Cs_2Ni_3S_4$ crystallizes in the hexagonal structure with space group $P6_3/mmc$ (SG 194), having two formula units per primitive unit cell. A total of four in-equivalent atoms such as Cs, Ni, S(I) and S(II) are present. Cs^{1+} ions bonded to seven S^{2-} ions, forming distorted edge-sharing CsS_7 hexagonal pyramids. Among these bonds, there are six shorter Cs-S bond lengths measuring 3.53 Å, while one bond is longer, measuring 3.74 Å. The Ni^{2+} ions are bonded in a square co-planar arrangement to four S^{2-} ions. Two of the Ni-S bond lengths are shorter, measuring 2.20 Å, while the other two bonds are longer, measuring 2.21 Å. The experimental lattice parameters used in this study are $a = b = 5.841$ Å, and $c = 15.109$ Å (Bronger *et al.*, 1988b). Tab. 14 illustrates

the atomic coordinates of the in-equivalent atoms in $Cs_2Ni_3S_4$. Because fractional Bravais lattice vector translation and point group symmetry are combined, $Cs_2Ni_3S_4$ has a nonsymmorphic crystal symmetry. Due to the center of inversion, it is also a centrosymmetric crystal material.

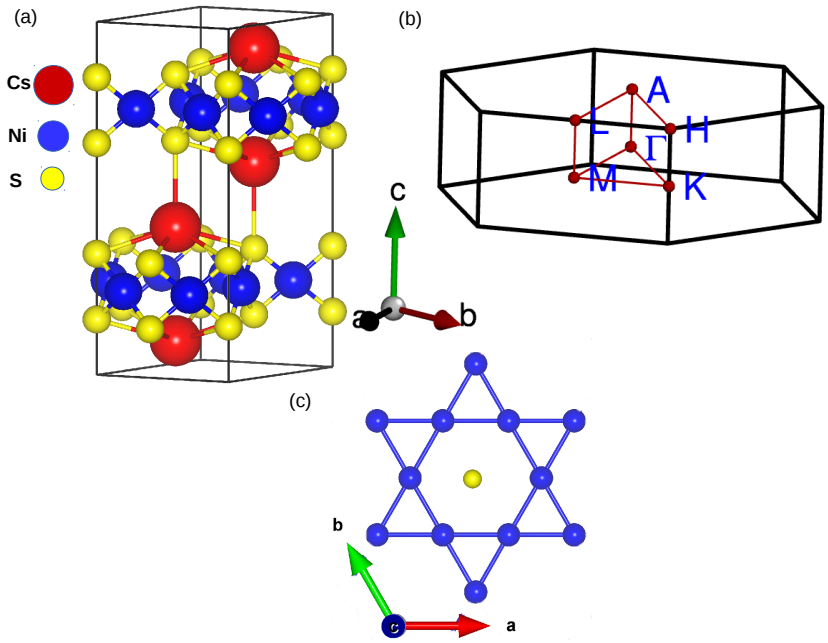

Figure 31: (a) Crystal structure of $Cs_2Ni_3S_4$. (b) 3D bulk Brillouin zone, the red dots and red lines indicate the high-symmetry point and high-symmetry line, respectively. (c) Ni-ions constitute a kagome lattice in *ab* plane.

We performed the total energy calculations for non-magnetic and ferromagnetic configuration. The total energy is found to be lowest for nonmagnetic dictating the ground state of the material, agreement with experimental ground state (Bronger *et al.*, 1988b). The presence of sulfur as a strong field ligand influences the electronic structure of the system, resulting in the compound adopting a low spin state (Hondou and Chikazawa, 2007).

Table 14: Total number of in-equivalent atoms and their Wyckoff positions in $Cs_2Ni_3S_4$.

Atom	Point location	x	y	z
Cs	4f	1/3	-1/3	-0.409
Ni	6h	1/6	1/3	1/4
S(I)	4e	0	0	0.154
S(II)	4f	1/3	-1/3	0.154

From the total and partial DOS shown in Fig. 32 (a-b), $Cs_2Ni_3S_4$ is found to be semiconducting with a band gap of ~0.8 eV (~1.4 eV) between the top of the valence band and bottom of the conduction band within GGA (GGA+mBJ). As mBJ functional is reported to appropriately describe the semiconducting behaviour of non-magnetic systems (Tran

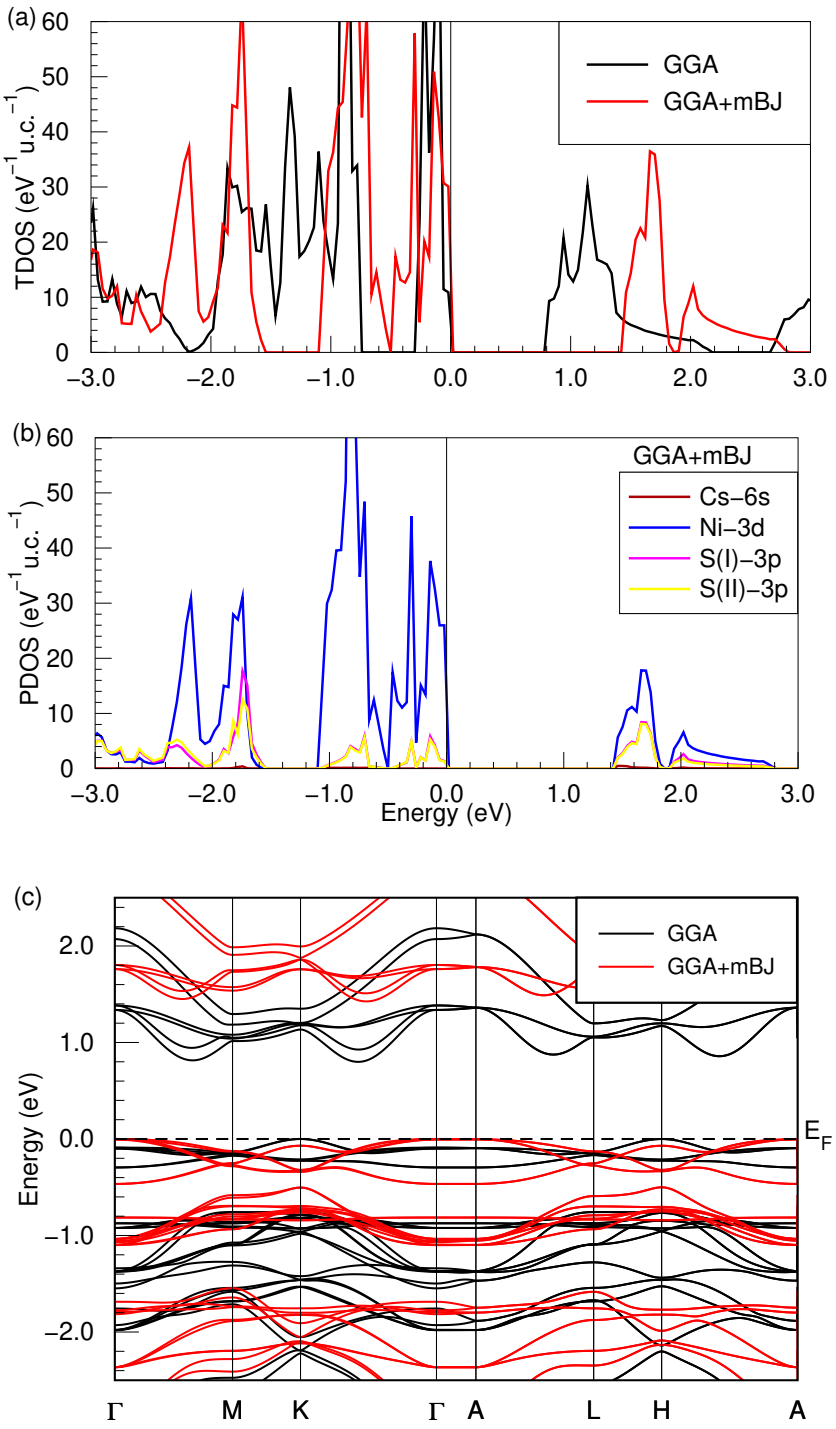

Figure 32: The DOS and electronic band structure of $Cs_2Ni_3S_4$: (a) Total DOS within GGA and GGA+mBJ; (b) Partial DOS within GGA+mBJ. The vertical solid line represents E_F; (c) Electronic band structure in scalar relativistic mode within GGA and GGA+mBJ calculations. The horizontal dashed line at zero energy denotes E_F.

and Blaha, 2009). We will thus focus discussing our results obtained with the mBJ. From the partial DOS contributions from Cs-6s, Ni-3d, and S-3p orbitals shown in Fig. 32 (b), the Ni-3d states have a significant contribution in the valence and conduction region hybridizing with the S-3p states. Two in-equivalent S atoms are found to exhibit similar features overlapping with each other. For a detailed study on the electronic

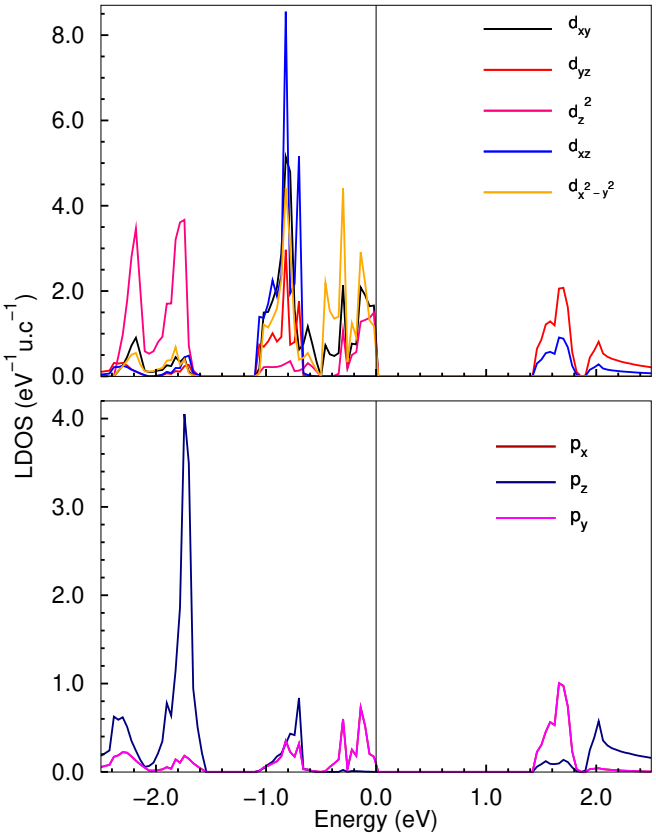

Figure 33: The projection of local DOS of Ni-3d and S-3p orbitals in $Cs_2Ni_3S_4$ within GGA+mBJ calculation

properties, the projection of local DOS has been considered which clearly depicts the hybridization between Ni-3d and S-3p states (see Fig. 33). As discussed earlier, each Ni ion is surrounded by four S ions, constituting a square planar coordination (see Fig. 31 (a)). In this situation S^{2-} acts as a strong ligand to central metal Ni^{2+}, resulting in the ligand field splitting. This leads to the low spin complexes where the eight d electrons fill the lower-energy d_{xz}, d_{yz}, d_z^2 , and d_{xy} orbitals, while the high-energy $d_{x^2-y^2}$ orbital remains unoccupied. Furthermore, a strong hybridization between the S-3p_x, S-3p_y, S-p_z is noticed with the Ni-d_{yz}, d_{xz} orbitals above E_F within an energy range of 1.4 to 1.8 eV, while below E_F, S-3p_x, S-3p_y hybridize with the Ni-3d_{xy}, $d_{x^2-y^2}$ and d_z^2 orbitals within 0 to 0.45 eV. Additionally, the kagome lattice of Ni^{2+} leads to the formation of flat bands below E_F, which is mainly contributed by the 3d-orbitals of $d_{x^2-y^2}$ and d_{xy} of Ni atom. Theoretical studies have suggested that such flat band systems in a kagome lattice can give rise to various exotic many-body phenomena (Li *et al.*, 2022; Hondou and Chikazawa, 2007; Hondou *et al.*, 2002; Kang *et al.*, 2020; Wang *et al.*, 2013b; Yu and Li, 2012). From the electronic band structure calculation shown in Fig. 32 (c), $Cs_2Ni_3S_4$ is found to be an indirect band gap semiconductor. The indirect band gap

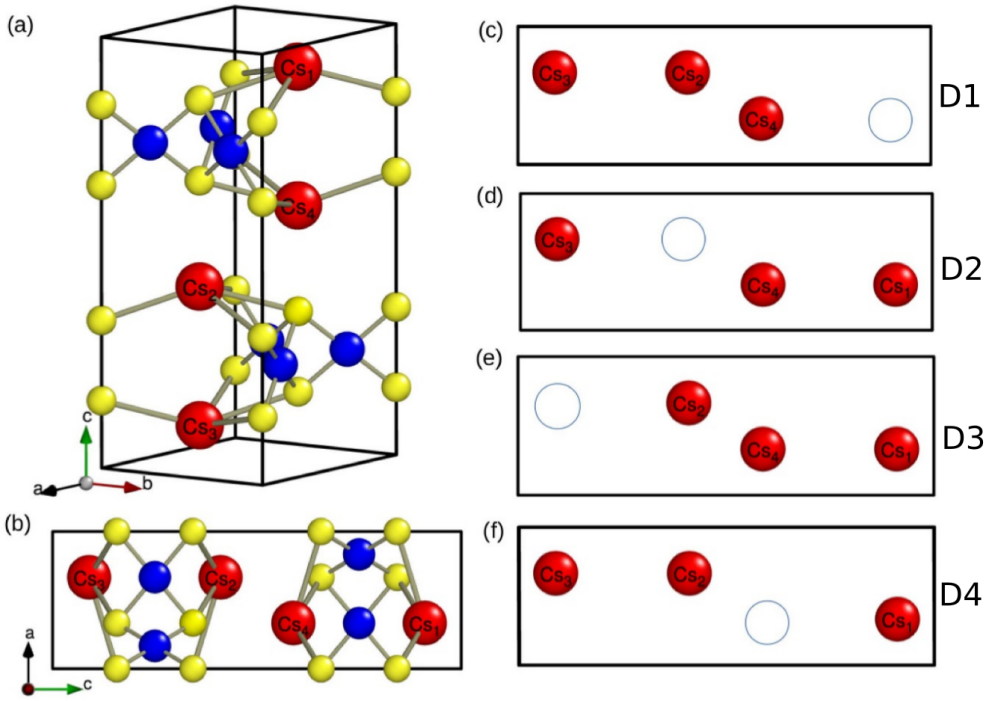

Figure 34: (a) Crystal structure of $Cs_2Ni_3S_4$ in 3D view. (b) 2D view. (c-f) Creation of vacancy defect by removing the Cs atoms. Different locations of the circle indicate that from where Cs atoms are removed.

arises between the top of the valence band at the high symmetry point K, and the bottom of the conduction band along the K-Γ in the momentum space. With GGA+mBJ taken into account, the electronic band gap rises to ∼ 1.4 eV (Tran and Blaha, 2009). Another important feature we observed is the presence of a dispersionless band (commonly referred to as a flat band) below E_F (see Fig. 32 (c)) which exist usually in a kagome lattice layers (Hondou and Chikazawa, 2007; Hondou *et al.*, 2002; Kang *et al.*, 2020).

Vacancy defects play significant role in materials science. They provide a systematic approach to change the physical characteristics of materials, which significantly influence their ability for practical applications (Freysoldt *et al.*, 2014; Zhang *et al.*, 2007b). We have considered vacancy defect in $Cs_2Ni_3S_4$ at the Cs-site. $Cs_2Ni_3S_4$ consists of two-formula unit with a total of 18 atoms in a unit cell out of which four are Cs atoms (see Fig. 34 (a)). By removing one Cs atom from the Cs-site we create a vacancy defect in the system. This corresponds to 25% vacancy at the Cs-site and 5.56% vacancy defect in $Cs_2Ni_3S_4$. Vacancy has been created by removing one Cs atom at different sites (see Fig. 34 (c-f)). We performed DFT calculations for defect-created structures in nonmagnetic and ferromagnetic configurations. The total energy was found to be lowest for the optimized structure with ferromagnetic ground state. The total energy of non-magnetic configuration was found to be 23.9 meV higher than the ferromagnetic state. Our calculation demonstrates that introducing a vacancy opens the possibility of adjusting magnetization leading to an total ordered magnetic moment of 1 μ_B per unit cell. From the electronic DOS and band structure calculation, as shown in Fig. 35, the

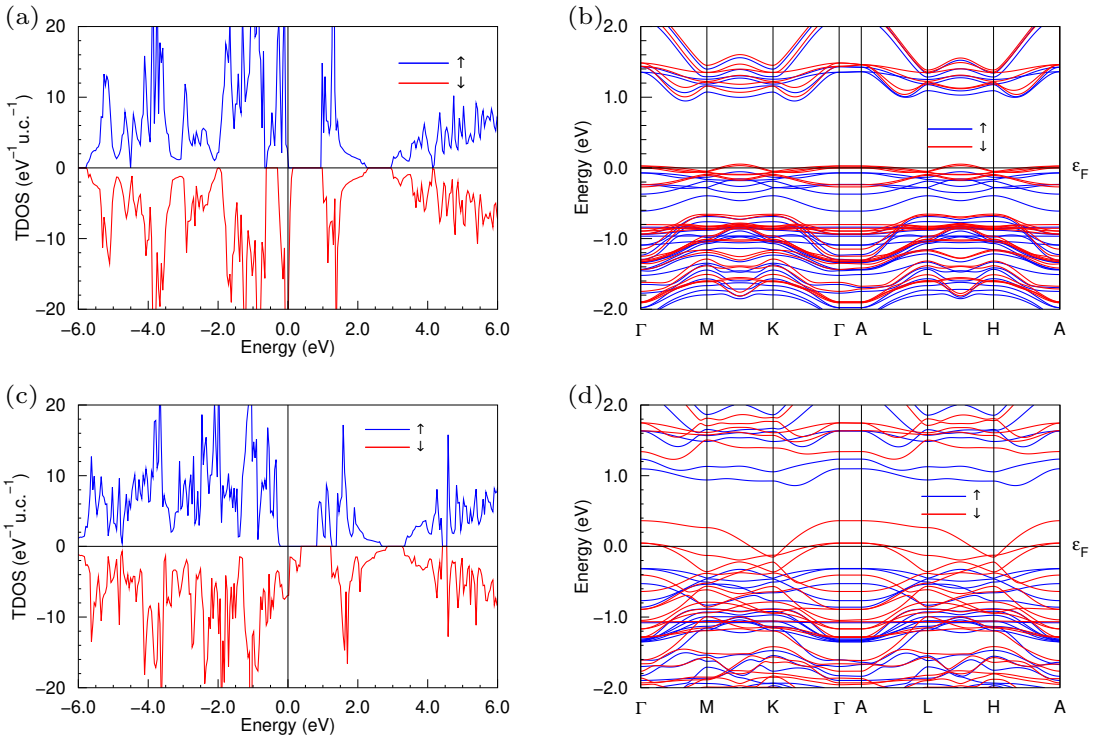

Figure 35: (a) Total DOS and (b) electronic band structure within GGA calculation. (c) Total DOS and (d) electronic band structure of $Cs_2Ni_3S_4$ within GGA+mBJ calculation.

vacancy defect $Cs_2Ni_3S_4$ is found to exhibit half-metallic ferromagnetism with insulating in spin-up and metallic in spin-down channels.

4.7.2 Optical Properties

Since there is a significant change in the band gap after considering the mBJ potential, we discuss optical calculations within mBJ. Given the hexagonal symmetry of $Cs_2Ni_3S_4$, we limited our investigation of optical anisotropy to the x and z directions. Fig. 36 illustrates the energy-dependent optical properties of the material, showing how these properties vary with direction within the energy range of 0-10 eV. Fig. 36 (a) shows the real part of the dielectric function ($\varepsilon_1(\omega)$), which is related to the ability of the material to refract or transmit radiation. The x and z components are denoted by ε_{1xx} and ε_{1zz} respectively. The $\varepsilon_1(\omega)$ also plays an important role in determining the other optical properties of materials, such as refractive index, reflectivity, and transmission of light. The computed static dielectric functions, represented by $\varepsilon_{1xx}(0)$ and $\varepsilon_{1zz}(0)$, have respective values of 4.79 and 4.00, respectively. Correspondingly, $n(0) = \sqrt{\varepsilon_1(0)}$ gives static refractive index as 2.19 and 2.00 along x and z direction, indicating clear optical anisotropy. In the energy range of 0-1.8 eV and 0-1.4 eV, we observe a slow rise of $\varepsilon_1(\omega)$ in the x and z directions, respectively. Sharp peaks at $\approx$ 2.2 eV and 1.8 eV in $\varepsilon_{1xx}(\omega)$ and $\varepsilon_{1zz}(\omega)$, respectively, correspond to the first interband transition in the system. The

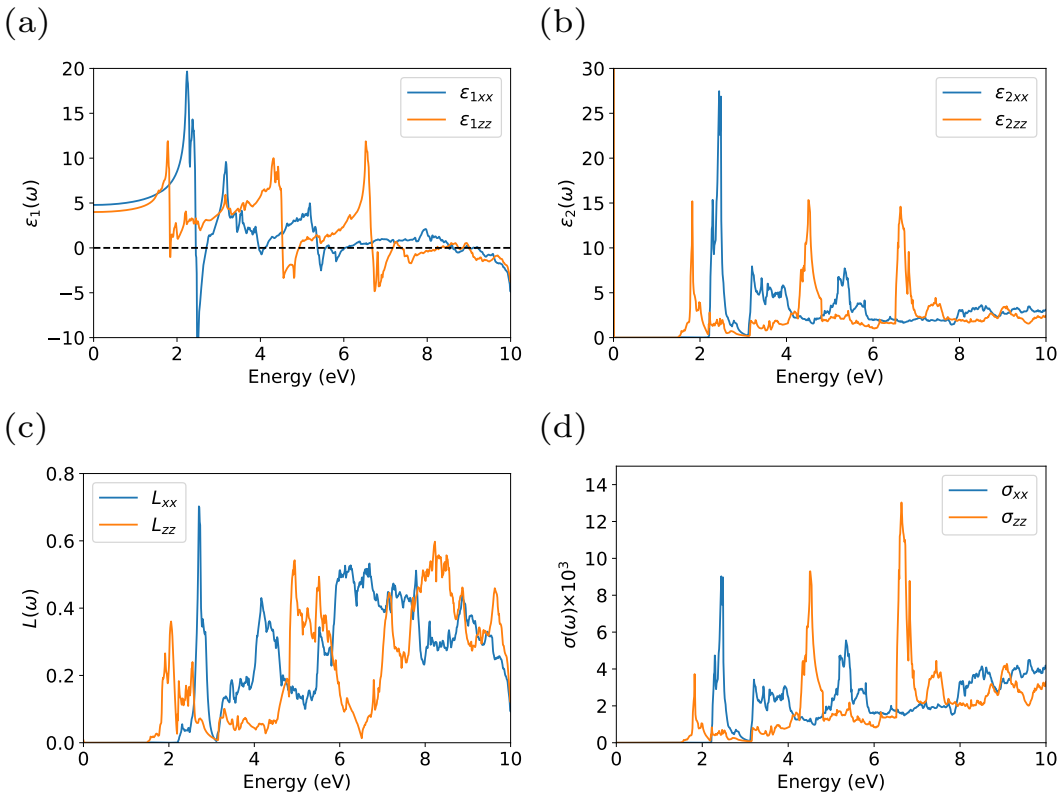

Figure 36: Optical properties of $Cs_2Ni_3S_4$ calculated within GGA+mBJ. (a) real part of the dielectric function ϵ_1 (ω). (b) Imaginary part of the dielectric function ϵ_2 (ω). (c) Energy loss spectrum L(ω). (d) Optical conductivity σ (ω) [in Ohm^{-1}cm^{-1}.]

features exhibited by the real part of the dielectric function (Fig. 36 (a)), including the negative values, are the typical signatures of interband transitions that can be related to the maxima in the imaginary part and, to some extent, in the loss function. Additionally, we observe sharp peaks at $\approx$ 3.2 eV and 5.2 eV in $\varepsilon_{1xx}(\omega)$, and at $\approx$ 4.3 eV and 6.5 eV in $\varepsilon_{1zz}(\omega)$, which correspond to interband transitions. In Fig. 36 (b), the imaginary part of the dielectric function $(\varepsilon_2(\omega))$ is displayed, which characterizes the material's absorption or dissipation of radiation in response to an external electromagnetic field at a given frequency ω. It is a measure of the electronic transition strength and is closely linked to the band structure. The spectrum starts to emerge beyond 1.5 eV, resulting in an optical gap. We observe a sharp increase in $\varepsilon_2(\omega)$ at $\approx$ 2.4 eV and 1.8 eV along x and z directions, respectively, where optical response occurs and represents the energy of the initial inter-band transition between the valence band maximum and conduction band minimum. In the z direction, other significant peaks are observed at $\approx$ 4.5 eV and 6.6 eV, with smaller peaks appearing around 3.2 eV and 5.3 eV in x direction. These multiple peaks correspond to the interband transitions from the Ni-3d valence band to the S-3p conduction band and are consistent with the result obtained in Fig. 36 (a). Beyond 6.6 eV, the peaks begin to decrease, eventually disappearing at higher energy ranges. Fig. 36 (c) depicts the electron energy loss in correlation to photon energy. It

characterizes the energy-dependent attenuation of the electric field of light as it passes through the material. Peaks begin to appear after approximately 2.2 eV and 1.8 eV along the x and z axes, respectively, suggesting photoelectron energy loss beyond that point. It is generally prominent around the plasmon energy. The most notable peak in the $L(\omega)$ spectra corresponds to the characteristic associated with the plasmon resonance, and such a peak is observed at 2.5 eV in the x-direction. Fig. 36 (d) displays the optical conductivity ($\sigma(\omega)$) as a function of energy. Peaks are noticeable around 2.5 eV, 3.2 eV, and 5.3 eV along the x direction, while sharp peaks can be seen around 1.8 eV, 4.5 eV, and 6.6 eV along the z direction. These outcomes are in agreement with the $\varepsilon_2(\omega)$ results we obtained in Fig. 36 (b). In general, $Cs_2Ni_3S_4$ is optically active in the visible and lower ultraviolet energy ranges. Therefore, this material may be a promising candidate for opto-electronic applications. Nonetheless, it is crucial to note that precise predictions necessitate careful consideration of factors such as electron-phonon interactions, many-body effects, and disorder.

4.8 Structural and Electronic Properties of Kagome $Rb_2Pd_3S_4$ and $Cs_2Pd_3S_4$

4.8.1 Structural Properties

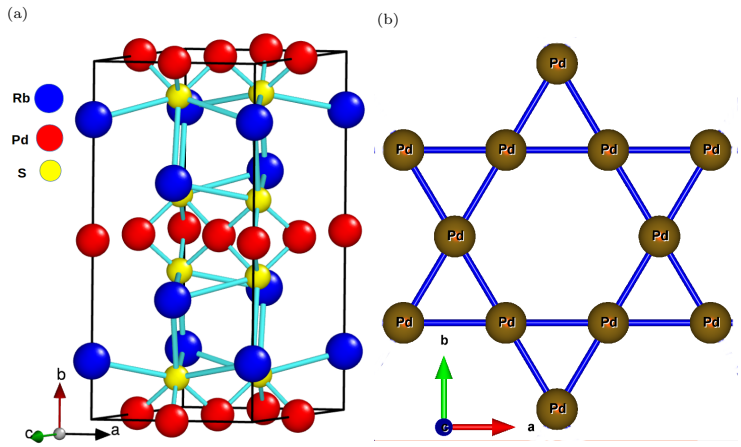

Figure 37: (a) Crystal structure of $Rb_2Pd_3S_4$. (b) Pd-ions constitute a kagome lattice in *ab* plane.

Both $Rb_2Pd_3S_4$ and $Cs_2Pd_3S_4$ crystallize in a monoclinic crystal structure with space group *C2/m* (SG 12) and belong to the point group C_{2h}. It consists of five in-equivalent atoms labeled as Cs, Pd(I), Pd(II), Pd(III), and S. In $Rb_2Pd_3S_4$, Rb^{1+} ions are surrounded by eight equivalent S^{2-} ions in an 8-coordinate geometry. The Rb–S bond distances exhibit a range from 3.53 Å to 3.61 Å. All Pd^{2+} ions are coordinated by four equivalent S^{2-} ions, adopting a square co-planar arrangement (see Fig. 37 (a)). At the first Pd^{2+} site, the Pd–S bond length measures 2.37 Å, while at the second and third Pd^{2+} sites, the Pd–S bond lengths are similar, measuring 2.38 Å. For $Cs_2Pd_3S_4$, the Cs–S bond distances range from 3.61 Åto 3.65 Å, and all three Pd^{2+} sites display similar Pd–S bond

lengths of 2.38 Å. Furthermore, both systems exhibit symmorphic crystal symmetry, and due to the presence of a center of inversion, they are considered centrosymmetric crystal materials. Tab. 15 and Tab. 16 presents the inequivalent atoms and their coordinates for $Rb_2Pd_3S_4$ and $Cs_2Pd_3S_4$, respectively.

Table 15: Total number of in-equivalent atoms and their Wyckoff positions in $Rb_2Pd_3S_4$.

Atom	Point location	x	y	z
Rb	4g	0	0.156	0
Pd(I)	2b	0	-1/2	0
Pd(II)	2c	0	0	-1/2
Pd(III)	2d	0	-1/2	-1/2
S	8j	-0.332	-0.119	0.337

Table 16: Total number of in-equivalent atoms and their Wyckoff positions in $Cs_2Pd_3S_4$.

Atom	Point location	x	y	z
Cs	4g	0	0.159	0
Pd(I)	2b	0	-1/2	0
Pd(II)	2c	0	0	-1/2
Pd(III)	2d	0	-1/2	-1/2
S	8j	-0.331	-0.111	0.336

4.8.2 Electronic Properties

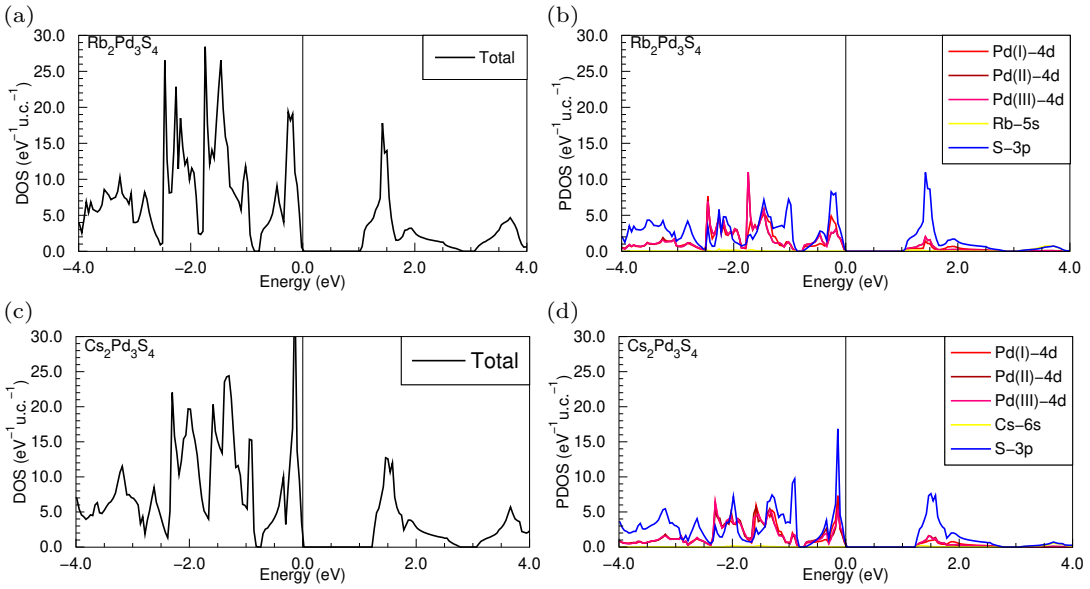

Figure 38: (a-d) Total and partial DOS of $Rb_2Pd_3S_4$ and $Cs_2Pd_3S_4$ for scalar relativistic calculation. The vertical solid line at zero energy denotes E_F.

To understand the electronic properties, we performed their electronic energy band structure calculation along the high-symmetry directions within the Brillouin zone,

as illustrated in Fig. 39. Additionally, we plotted the total DOS and partial DOS shown in Fig. 38 (a-d) to further analyze their electronic nature. Based on the analysis of the electronic band structure, both compounds, $Rb_2Pd_3S_4$ and $Cs_2Pd_3S_4$, exhibit semiconductor behavior with energy band gaps of approximately 1.1 eV and 1.2 eV, respectively. This is attributed to the occurrence of the valence band maximum at the high symmetry point I and the conduction band minimum at the F-H line in the momentum space, as illustrated in Fig. 39 (a & b).

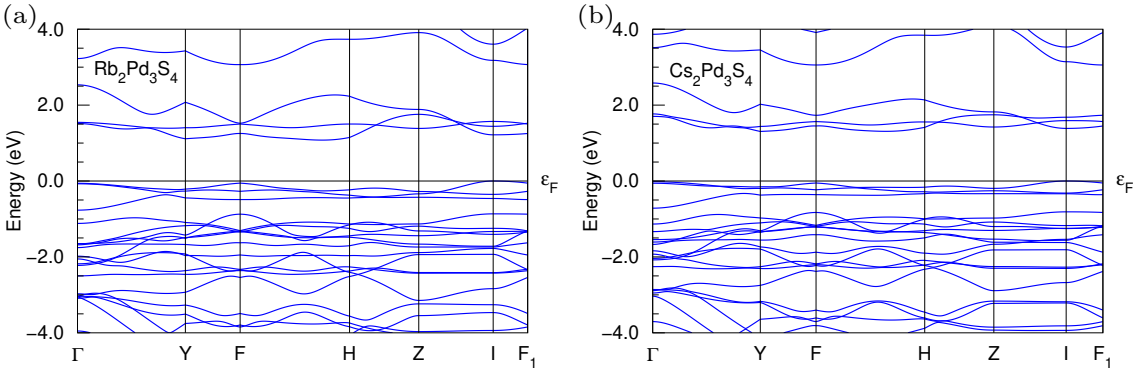

Figure 39: Electronic band structure of (a) $Rb_2Pd_3S_4$ and (b) $Cs_2Pd_3S_4$ for scalar relativistic calculation. The horizontal solid line at zero energy denotes E_F.

The total DOS distributions show similar characteristics for both compounds. It is evident that S and Pd orbitals contribute significantly to the DOS, while Rb and Cs make only minor contributions. This difference is attributed to the presence of only one electron in the outermost orbitals of these atoms (refer to Fig. 38 (b & d). In the square

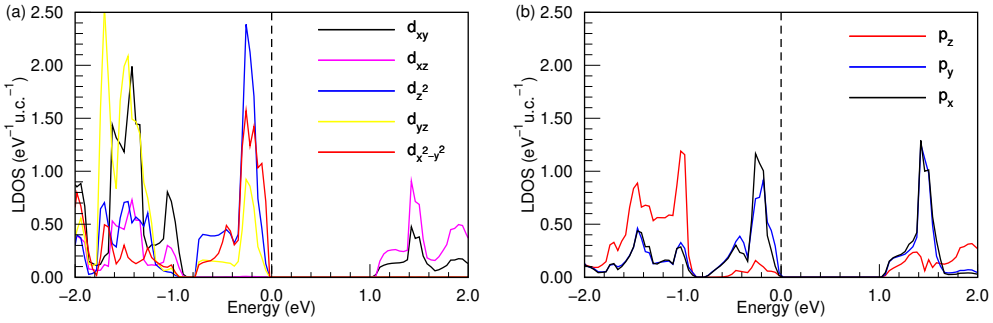

Figure 40: Projected local DOS for (a) Pd(I) site and (b) S site in $Rb_2Pd_3S_4$ within scalar relativistic calculation.

planar configuration shown in Fig. 37 (a), each Pd ion is surrounded by four S ions. The ligand field of planar $(S^{2-})_4$ exhibits strong covalency between Pd^{2+} and S^{2-}, leading to certain d-orbitals lower-energy d_{xz}, d_{yz}, d_z^2, and d_{xy} orbitals, while the high-energy $d_{x^2-y^2}$ orbital remains unoccupied. Below the E_F, there is a strong hybridization between the S-3p_x and S-3p_y orbitals with the Pd-4d_{yz} orbitals. On the other hand, above the

Fermi level, the S-$3p_x$ and S-$3p_y$ orbitals are strongly hybridized with the Pd-$4d_{xz}$ orbitals. Additionally, the kagome lattice of Pd^{2+} in the system leads to the presence of flat bands from the d-orbitals below the Fermi level. These flat bands contribute to a sharp density of states just below the Fermi level. Theoretical studies have suggested that such flat band systems in a kagome lattice can give rise to various exotic many-body phenomena (Hondou and Chikazawa, 2007; Hondou *et al.*, 2002; Kang *et al.*, 2020).

CHAPTER 5

CONCLUSION AND RECOMMENDATIONS

5.1 Conclusion

In conclusion, we investigated the electronic structure, the magnetic properties, Weyl properties, Berry curvature, intrinsic contributions to the anomalous Hall effect, and Fermi arc surface states of $Cs_2Co_3S_4$ using density functional theory calculations. We found a ferrimagnetic ground state of $Cs_2Co_3S_4$ at variance with the original experimental results that report an antiferromagnetic low-temperature state. The energy difference between the two states is in the order of meV/atom. Thus, a very small stoichiometry of the samples could have influenced the experimental result; likewise, one should remember the limitations of the chosen approximations to the density functional. We characterized the theoretical ground state as a semimetal close to a half-metallic state. Several Weyl points are situated close to the Fermi level for the lowest-energy orientation of magnetization along [1 0 0]. They move both in k and energy if the magnetization is rotated and are eventually annihilated. Relatedly, we found the intrinsic anomalous Hall conductivity to be very sensitive to the orientation of the magnetization. It is relatively small for the easy-axis orientation. However, it reaches magnitudes up to 500 $\Omega^{-1}cm^{-1}$ if the magnetization is oriented along [0 0 1]. Based on the thermodynamical stability of the system through the calculation of formation energy, we investigated the $Li_2Fe_3S_4$, a ferrimagnetic topological Weyl semimetal state with four pairs of Weyl points slightly above the Fermi level. The orientation of the magnetization direction of $Li_2Fe_3S_4$ breaks the specified mirror symmetries, resulting in the gap opening of the corresponding band crossing. We noticed that SOC had a significant influence on the [0 0 1] magnetization direction compared to the [0 1 0] and [1 0 0] magnetization directions. However, the total number of Weyl points is similar in all the magnetization as mentioned above directions. Our findings suggest that $Li_2Fe_3S_4$ could be a viable platform for studying the interaction between topological properties and magnetism. For the other compound of this series, $Cs_2Ni_3S_4$ is found to be an indirect band gap semiconductor. With the band gap value ($\sim$1.4 eV) found suitable for optical applications, we considered optical properties by calculating dielectric function, loss function, and

optical conductivity. Our findings demonstrate that the material exhibits optical activity within the visible and lower ultraviolet energy range. In addition, we considered the Cs-vacancy defect in $Cs_2Ni_3S_4$. Removing one Cs atom from the system gives rise to half-metallic ferromagnetism, making the material a suitable candidate for spintronic device applications. $Rb_2Ni_3S_4$ is found to be a nonmagnetic semiconductor with an indirect band gap of ~0.67 eV. The Ni atoms form a kagome lattice in a two-dimensional plane, resulting in a flat band below the Fermi energy. We found the material optically active in the visible and lower ultraviolet regions. These results suggest that the potential of the $Cs_2Ni_3S_4$ and $Rb_2Ni_3S_4$ are promising candidates for optoelectronic applications. Similarly, $Rb_2Pd_3S_4$ and $Cs_2Pd_3S_4$ exhibit a nonmagnetic ground state. Ni and Pd atoms form a kagome lattice in a two-dimensional plane. These materials possess a semiconducting nature. Interestingly, a flat band was noticed below the Fermi level, demonstrating one significant feature of the kagome lattice. But $K_2Mn_3S_4$ has a ferrimagnetic ground state with the total magnetic moment of 10 μB per unit cell shows indirect band gap semiconductor nature. This magnetic moment mainly was created by the antiferromagnetic interaction between Mn(I) and Mn(II) atoms. The effect of spin-orbit coupling is found negligible. The identification of $K_2Mn_3S_4$ as an indirect band gap semiconductor is expected to open new doors for experimental research that could be used in the fabrication of new devices, including semiconductor lasers, solar cells, and light-emitting diodes.

5.2 Recommendations for Future Work

We further recommend applying our density functional theory calculation results to experimental work and then proceeding with the synthesis, characterization, and measurement of transport properties for $Cs_2Co_3S_4$ and $Li_2Fe_3S_4$. In the context of transport properties, our primary focus will be on anomalous Hall conductivity and Fermi arc surface states. Simultaneously, we will calculate the Berry curvature, anomalous Hall effect, and Fermi arc surface states of $Li_2Fe_3S_4$. For materials with a kagome lattice and a tunable band gap, such as $Rb_2Ni_3S_4$, $Cs_2Ni_3S_4$, $Rb_2Pd_3S_4$, and $Cs_2Pd_3S_4$, we will concentrate on calculations and measurements of thermoelectric properties.

CHAPTER 6

SUMMARY

To summarize, topological materials have attracted the attention of scientists in recent years due to their novel and intriguing physical properties. These materials are notable for having protected surface states with no energy gaps. This unique aspect stems from the peculiar arrangement of the material at its core. Topological materials could be used to create new and enhanced quantum information devices and applications. The kagome lattice is a form of crystal structure that exhibit promising option for investigation of topological Dirac, Weyl, and nodal line characteristics. A kagome lattice's electronic structure naturally comprises Dirac fermions, flat bands, and van Hove singularities. There has been much interest in the form of topological material known as Weyl semimetals over last thirteen years. Scientists have achieved precise theoretical predictions, developed these materials in labs, and developed advanced methods of studying them. Scientists have achieved precise theoretical predictions, developed these materials in labs, and developed advanced methods of studying them, such as utilizing specialized microscopy and measurements. We explore the number of compounds using a technique known as density functional theory simulations. First, we looked at the electronic, optical, magnetic, and topological properties of two materials with no energy gaps: $Cs_2Co_3S_4$ and $Li_2Fe_3S_4$. Their Weyl semimetal properties, such as Berry curvature, anomalous Hall conductivity, and Fermi arc surface states, piqued our curiosity. $Cs_2Co_3S_4$ was discovered to be a unique magnetic material with some intriguing properties. We found that materials with energy gaps, such as $Rb_2Ni_3S_4$, $Cs_2Ni_3S_4$, $Rb_2Pd_3S_4$, and $Cs_2Pd_3S_4$, have a nonmagnetic state. Some of these materials have a kagome lattice structure consisting of nickel Ni/Pd with S atoms existing in a semiconductor nature. We also looked at materials with magnetic properties but are still semiconductors, such as $K_2Mn_3S_4$ and $Rb_2Mn_3S_4$. We studied the optical properties of gapped $Rb_2Ni_3S_4$ and $Cs_2Ni_3S_4$ with kagome lattice structures, could be possible for optoelectronic devices application. We summarized our results in Tab. 17.

Table 17: Characteristics of $A_2T_3S_4$ materials within scalar relativistic case. “FIM” denotes the Ferimagnetic ground state, “NM” denotes the Nonmagnetic ground state, “WSM" denotes the Weyl semimetal and "SC" denotes the Semiconductor.

Material	**Structure type**	**Ground state**	**Electronic Nature**	**Gap(eV)**
$Cs_2Co_3S_4$	orthorhombic	FIM	WSM	0
$Li_2Fe_3S_4$	monoclinic	,,	,,	0
$Cs_2Ni_3S_4$	hexagonal (kagome)	NM	SC	0.80
$Rb_2Ni_3S_4$	orthorhombic (kagome)	,,	,,	0.67
$Rb_2Pd_3S_4$	monoclinic (kagome)	,,	,,	1.00
$Cs_2Pd_3S_4$	,,	,,	,,	1.20
$K_2Mn_3S_4$	monoclinic	FIM	,,	1.10
$Rb_2Mn_3S_4$	orthorhombic	,,	,,	0.75
$Cs_2Mn_3S_4$	orthorhombic	AFM	,,	1.50

REFERENCES

Ambrosch-Draxl, C., Majewski, J. A., Vogl, P., and Leising, G. (1995). First-principles studies of the structural and optical properties of crystalline poly(para-phenylene). *Phys. Rev. B*, 51(15):9668–9676.

Ando, Y. (2013). Topological insulator materials. *J. Phys. Soc. Jpn.*, 8(10):102001–102033.

Ando, Y. and Fu, L. (2015). Topological crystalline insulators and topological superconductors: From concepts to materials. *Annu. Rev. Condens. Matter Phys.*, 6(1):361–381.

Anisimov, V. I., Aryasetiawan, F., and Lichtenstein, A. I. (1997). First-principles calculations of the electronic structure and spectra of strongly correlated systems: the LDA+U method. *J. Condens. Matter Phys.*, 9(4):767–810.

Anisimov, V. I. and Gunnarsson, O. (1991). Density-functional calculation of effective coulomb interactions in metals. *Phys. Rev. B*, 43(10):7570–7574.

Armitage, N. P., Mele, E. J., and Vishwanath, A. (2018). Weyl and dirac semimetals in three-dimensional solids. *Rev. Mod. Phys.*, 90(1):015001.

Asaba, T., Thomas, S. M., Curtis, M., Thompson, J. D., Bauer, E. D., and Ronning, F. (2020). Anomalous Hall effect in the kagome ferrimagnet $GdMn_6Sn_6$. *Phys. Rev. B*, 101(17):174415–174419.

Austin, I. G. and Mott, N. F. (1970). Metallic and nonmetallic behavior in transition metal oxides. *Science*, 168(3927):71–77.

Avron, J. E., Osadchy, D., and Seiler, R. (2003). A Topological Look at the Quantum Hall Effect. *Phys. Today*, 56(8):38–42.

Becke, A. D. and Johnson, E. R. (2006). A simple effective potential for exchange. *J. Chem. Phys.*, 124(22):221101–221104.

Becke, A. D. and Roussel, M. R. (1989). Exchange holes in inhomogeneous systems: A coordinate-space model. *Phys. Rev. A*, 39(8):3761–3767.

Beenakker, C. (2013). Search for majorana fermions in superconductors. *Annu. Rev. Condens. Matter Phys.*, 4(1):113–136.

Belbase, B. P., Jaishi, D. R., Adhikari, R. P., and Ghimire, M. P. (2023). Electronic and optical properties of double perovskites $Ba_{2-x}Sr_xBiSbO_6$ (x = 0, 1). *Solid State Commun.*, 361(115085):1–6.

Bernevig, B. A. (2015). It's been a Weyl coming. *Nat. Phys.*, 11(9):698–699.

Bernevig, B. A. and Zhang, S.-C. (2006). Quantum spin Hall effect. *Phys. Rev. Lett.*, 96(10):106802–106806.

Berry, M. (1985). Aspects of degeneracy.

Bhardwaj, V. and Chatterjee, R. (2020). Topological materials: new quantum phases of matter. *Resonance*, 25(3):431–444.

Bian, G., Chang, T.-R., Sankar, R., Xu, S.-Y., Zheng, H., Neupert, T., Chiu, C.-K., Huang, S.-M., Chang, G., and Belopolski, I. (2016). Topological nodal-line fermions in spin-orbit metal $PbTaSe_2$. *Nat. Commun.*, 7(1):1–8.

Bilenky, S. (2005). The history of neutrino oscillations. *Phys. Scripta*, 121(3):1–18.

Borisenko, S., Evtushinsky, D., Gibson, Q., Yaresko, A., Koepernik, K., Kim, T., Ali, M., van den Brink, J., Hoesch, M., and Fedorov, A. (2019). Time-reversal symmetry breaking type-II weyl state in $YbMnBi_2$. *Nat. Commun.*, 10(1):1–7.

Boukhvalov, D. W. and Solovyev, I. V. (2010). Defects of the Crystal Structure and Jahn-Teller Distortion in $BiMnO_3$. *Phys. Rev. B*, 82(24):245101–245108.

Breunig, O. and Ando, Y. (2022). Opportunities in Topological Insulator Devices. *Nat. Rev. Phys.*, 4(3):184–193.

Bronger, W., Böhmer, M., and Schmitz, D. (2000). Synthese und Kristallstruktur von K_2Mn_3S4. *Z. fur Anorg. Allg. Chem.*, 626(1):6–8.

Bronger, W. and Böttcher, P. (1972). Über thiomanganate und-cobaltate der schweren alkalimetalle: $Rb_2Mn_3S_4$, $Cs_2Mn_3S_4$, $Rb_2Co_3S_4$, $Cs_2Co_3S_4$. *Z. fur Anorg. Allg. Chem.*, 390(1):1–12.

Bronger, W., Hendriks, U., and Müller, P. (1988a). Struktur und magnetische eigenschaften von $Cs_2Mn_3S_4$ und $Cs_2Co_3S_4$. *Z. fur Anorg. Allg. Chem.*, 559(1):95–105.

Bronger, W., Rennau, R., and Schmitz, D. (1988b). Die kristallstrukturen von $Cs_2Ni_3S_4$. *Z. fur Krist. - Cryst. Mater.*, 183(4):201–206.

Bronger, W., Rennau, R., and Schmitz, D. (1991). Schichtstrukturen ternärer chalkogenide $A_2M_3X_4$ (A=K, Rb, Cs; M=Ni, Pd, Pt; X=S, Se). *Z. fur Anorg. Allg. Chem.*, 597(1):27–32.

Burkov, A. and Balents, L. (2011). Weyl Semimetal in a Topological Insulator Multilayer. *Phys. Rev. Lett.*, 107(12):127205—127209.

Burkov, A., Hook, M., and Balents, L. (2011). Topological Nodal Semimetals. *Phys. Rev. B*, 84(23):235126–235140.

Bzdušek, T., Wu, Q., Rüegg, A., Sigrist, M., and Soluyanov, A. A. (2016). Nodal-chain metals. *Nature*, 538(7623):75–78.

Cao, W., Tang, P., Xu, Y., Wu, J., Gu, B.-L., and Duan, W. (2017). Dirac semimetal phase in hexagonal LiZnBi. *Phys. Rev. B*, 96(11):115203–115207.

Capelle, K. (2006). A Bird's-eye View of Density Functional Theory. *Braz. J. Phys.*, 36:1318–1343.

Ceperley, D. M. and Alder, B. J. (1980). Ground state of the electron gas by a stochastic method. *Phys. Rev. Lett.*, 45(7):566–569.

Chang, T.-R., Xu, S.-Y., Chang, G., Lee, C.-C., Huang, S.-M., Wang, B., Bian, G., Zheng, H., Sanchez, D. S., and Belopolski, I. (2016). Prediction of an arc-tunable weyl fermion metallic state in $Mo_xW_{1-x}Te_2$. *Nat. Commun.*, 7(1):1–9.

Chen, Y., Lu, Y.-M., and Kee, H.-Y. (2015). Topological crystalline metal in orthorhombic perovskite iridates. *Nat. Commun.*, 6(1):6593–65100.

Chiu, C.-K. and Schnyder, A. P. (2014). Classification of reflection-symmetry-protected topological semimetals and nodal superconductors. *Phys. Rev. B*, 90(20):205136–205162.

Cococcioni, M. (2012). Lecture notes of the autumn school correlated electrons 2012: The LDA+U approach: a simple hubbard correction for correlated ground states. *Correlated Electrons: From Models to Materials Modeling and Simulation.*

Deng, K., Wan, G., Deng, P., Zhang, K., Ding, S., Wang, E., Yan, M., Huang, H., Zhang, H., Xu, Z., *et al.* (2016). Experimental observation of topological fermi arcs in type-II Weyl semimetal $MoTe_2$. *Nat. Phys.*, 12(12):1105–1110.

Dirac, P. A. M. (1928). The quantum theory of the electron. *Proceedings of the Royal Society of London. Series A, Containing Papers of a Mathematical and Physical Character*, 117(778):610–624.

Dirac, P. A. M. (1930). Note on exchange phenomena in the thomas atom. In *Mathe-*

matical proceedings of the Cambridge philosophical society, volume 26, pages 376–385. Cambridge University Press.

Du, Y., Tang, F., Wang, D., Sheng, L., Kan, E.-j., Duan, C.-G., Savrasov, S. Y., and Wan, X. (2017). Cate: a new topological node-line and dirac semimetal. *npj Quantum Mater.*, 2(1):3–7.

Du, Y., Wan, B., Wang, D., Sheng, L., Duan, C.-G., and Wan, X. (2015). Dirac and Weyl semimetal in XYBi (X= Ba, Eu; Y= Cu, Ag and Au). *Sci. Rep.*, 5(1):14423–14431.

Ekahana, S. A., Wu, S.-C., Jiang, J., Okawa, K., Prabhakaran, D., Hwang, C.-C., Mo, S.-K., Sasagawa, T., Felser, C., Yan, B., *et al.* (2017). Observation of nodal line in non-symmorphic topological semimetal inbi. *New J. Phys.*, 19(6):065007–0650015.

Eschbach, M., Lanius, M., Niu, C., Młyńczak, E., Gospodarič, P., Kellner, J., Schüffelgen, P., Gehlmann, M., Döring, S., Neumann, E., *et al.* (2017). Bi1te1 is a dual topological insulator. *Nat. Commun.*, 8(1):14976–14985.

Eschrig, H., Sargolzaei, M., Koepernik, K., and Richter, M. (2005). Orbital polarization in the *s*Kohn-Sham-Dirac theory. *Europhys. Lett.*, 72(4):611.

Fang, Nagaosa, N., Takahashi, K. S., Asamitsu, A., Mathieu, R., Ogasawara, T., Yamada, H., Kawasaki, M., Tokura, Y., and Terakura, K. (2003). The anomalous Hall effect and magnetic monopoles in momentum space. *Science*, 302(5642):92–95.

Fang, Weng, H., Dai, X., and Fang, Z. (2016). Topological nodal line semimetals. *Chin. Phys. B*, 25(11):117106–1171012.

Fang, C., Gilbert, M. J., Dai, X., and Bernevig, B. A. (2012). Multi-weyl topological semimetals stabilized by point group symmetry. *Phys. Rev. Lett.*, 108(26):266802–266807.

Fermi, E. (1928). Eine statistische methode zur bestimmung einiger eigenschaften des atoms und ihre anwendung auf die theorie des periodischen systems der elemente. *Z. Phys.*, 48(1-2):73–79.

Fock, V. (1930). Näherungsmethode zur lösung des quantenmechanischen mehrkörperproblems. *Z. Phys.*, 61:126–148.

Freysoldt, C., Grabowski, B., Hickel, T., Neugebauer, J., Kresse, G., Janotti, A., and Van de Walle, C. G. (2014). First-principles calculations for point defects in solids. *Rev. Mod. Phys.*, 86(1):253–305.

Fu, L. and Berg, E. (2010). Odd-parity topological superconductors: Theory and application to $Cu_xBi_2Se_3$. *Phys. Rev. Lett.*, 105(9):097001–097005.

Fu, L., Kane, C. L., and Mele, E. J. (2007). Topological insulators in three dimensions. *Phys. Rev. Lett.*, 98(10):106803–106807.

Fukuda, Y., Hayakawa, T., Ichihara, E., Inoue, K., Ishihara, K., Ishino, H., Itow, Y., Kajita, T., Kameda, J., Kasuga, S., *et al.* (1998). Evidence for oscillation of atmospheric neutrinos. *Phys. Rev. Lett.*, 81(8):1562–1567.

Fukui, T., Hatsugai, Y., and Suzuki, H. (2005). Chern numbers in discretized brillouin zone: efficient method of computing (spin) Hall conductances. *J. Phys. Soc. Jpn.*, 74(6):1674–1677.

Gao, H., Kim, Y., Venderbos, J. W. F., Kane, C. L., Mele, E. J., Rappe, A. M., and Ren, W. (2018). Dirac-Weyl semimetal: Coexistence of Dirac and Weyl fermions in polar hexagonal ABC crystals. *Phys. Rev. Lett.*, 121(10):106404–106410.

Gao, H., Venderbos, J. W., Kim, Y., and Rappe, A. M. (2019). Topological semimetals from first principles. *Annu. Rev. Mater. Res.*, 49(8):153–183.

Ghimire, M. P., Facio, J. I., You, J.-S., Ye, L., Checkelsky, J. G., Fang, S., Kaxiras, E., Richter, M., and van den Brink, J. (2019). Creating Weyl nodes and controlling their energy by magnetization rotation. *Phys. Rev. Res.*, 1(3):032044–032051.

Ghimire, M. P. and Richter, M. (2017). Chemical gating of a weak topological insulator: $Bi_{14}Rh_3I_9$. *Nano Lett.*, 17(10):6303–6308.

Ghosh, A. and Thangavel, R. (2017). Electronic structure and optical properties of iron based chalcogenide FeX_2 (X= S, Se, Te) for photovoltaic applications: a first principle study. *Ind. J. Phys.*, 91:1339–1344.

Gibson, Q. D., Schoop, L. M., Muechler, L., Xie, L. S., Hirschberger, M., Ong, N. P., Car, R., and Cava, R. J. (2015). Three-dimensional Dirsac semimetals: Design principles and predictions of new materials. *Phys. Rev. B*, 91(20):205128–205139.

Goldhaber, M., Grodzins, L., and Sunyar, A. W. (1958). Helicity of neutrinos. *Phys. Rev.*, 109(3):1015–1017.

Gosálbez-Martínez, D., Souza, I., and Vanderbilt, D. (2015). Chiral degeneracies and Fermi-surface Chern numbers in bcc Fe. *Phys. Rev. B*, 92(8):085138–085160.

Gunnarsson, O. and Lundqvist, B. I. (1976). Exchange and correlation in atoms, molecules, and solids by the spin-density-functional formalism. *Phys. Rev. B*, 13(10):4274–4298.

Hartree, D. R. (1928). The wave mechanics of an atom with a non-coulomb central field, part I: Theory and methods. In *Mathematical Proceedings of the Cambridge Philosophical Society*, volume 24, pages 89–110. Cambridge university press.

Hasan, M. Z. and Kane, C. L. (2010). Colloquium: Topological insulators. *Rev. Mod. Phys.*, 82(4):3045–3067.

Haubold, E., Koepernik, K., Efremov, D., Khim, S., Fedorov, A., Kushnirenko, Y., Van Den Brink, J., Wurmehl, S., Büchner, B., Kim, T., *et al.* (2017). Experimental realization of type-II Weyl state in noncentrosymmetric $TaIrTe_4$. *Phys. Rev. B*, 95(24):241108–241115.

He, H., Orlando, R., Blanco, M. A., Pandey, R., Amzallag, E., Baraille, I., and Rérat, M. (2006). First-principles study of the structural, electronic, and optical properties of Ga_2O_3 in its monoclinic and hexagonal phases. *Phys. Rev. B*, 74(19):195123–195131.

Heikkilä, T. T., Kopnin, N. B., and Volovik, G. E. (2011). Flat bands in topological media. *JETP Lett.*, 94:233–239.

Heikkilä, T. T. and Volovik, G. E. (2011). Dimensional crossover in topological matter: Evolution of the multiple Dirac point in the layered system to the flat band on the surface. *JETP Lett.*, 93:59–65.

Herring, C. (1937). Accidental degeneracy in the energy bands of crystals. *Phys. Rev.*, 52(4):365–373.

Hirschberger, M., Kushwaha, S., Wang, Z., Gibson, Q., Liang, S., Belvin, C. A., Bernevig, B. A., Cava, R. J., and Ong, N. P. (2016). The chiral anomaly and thermopower of Weyl fermions in the half-heusler GdPtBi. *Nat. Mater.*, 15(11):1161–1165.

Hohenberg, P. and Kohn, W. (1964). Inhomogeneous electron gas. *Phys. Rev.*, 136(3B):B864–B871.

Hondou, K. and Chikazawa, S. (2007). Attempt to examine the origin of magnetism in water-immersed $Rb_2Ni_3S_4$. *J. Magn. Magn. Mater.*, 310(2):1815–1817.

Hondou, K., Fujiwara, Y., Kato, T., Iio, K., Saiki, A., Usuda, M., and Hamada, N. (2002). Reinvestigation of magnetism and electric transport in a ternary transition metal chalcogenide $Rb_2Ni_3S_4$. *J. Alloys Compd.*, 333(1-2):274–281.

Hosur, P. and Qi, X. (2013). Recent developments in transport phenomena in weyl semimetals. *Comptes Rendus Physique*, 14(9):857–870. Topological insulators / Isolants topologiques.

Hsieh, D., Xia, Y., Wray, L., Qian, D., Pal, A., Dil, J., Osterwalder, J., Meier, F., Bihlmayer, G., Kane, C., *et al.* (2009). Observation of unconventional quantum spin textures in topological insulators. *Science*, 323(5916):919–922.

Hu, J.-M., Huang, S.-P., Xie, Z., Hu, H., and Cheng, W.-D. (2007). First-principles study of the elastic and optical properties of the pseudocubic Si_3As_4, Ge_3As_4 and Sns_3As_4. *J. Condens. Matter Phys.*, 19(49):496215.

Hua, G., Nie, S., Song, Z., Yu, R., Xu, G., and Yao, K. (2018). Dirac semimetal in type-*IV* magnetic space groups. *Phys. Rev. B*, 98(20):201116–201121.

Hubbard, J. (1964). Electron correlations in narrow energy bands. the degenerate band case. *Proceedings of the Royal Society of London. Series A. Mathematical and Physical Sciences*, 277(1369):237–259.

Hubbard, J. (1965). Electron correlations in narrow energy bands-iv. the atomic representation. *Proceedings of the Royal Society of London. Series A. Mathematical and Physical Sciences*, 285(1403):542–560.

Ishida, K., Mukuda, H., Kitaoka, Y., Asayama, K., Mao, Z., Mori, Y., and Maeno, Y. (1998). Spin-triplet superconductivity in Sr_2RuO_4 identified by 17o knight shift. *Nature*, 396(6712):658–660.

Ivanov, V. (2021). Correlated topological materials (unpublished doctoral dissertation). University of California, Davis.

Kane, C. L. and Mele, E. J. (2005a). Quantum spin Hall effect in graphene. *Phys. Rev. Lett.*, 95(22):226801–226805.

Kane, C. L. and Mele, E. J. (2005b). Z2 topological order and the quantum spin Hall effect. *Phys. Rev. Lett.*, 95(14):146802.

Kang, M., Fang, S., Ye, L., Po, H. C., Denlinger, J., Jozwiak, C., Bostwick, A., Rotenberg, E., Kaxiras, E., Checkelsky, J. G., *et al.* (2020). Topological flat bands in frustrated kagome lattice CoSn. *Nat. Commun.*, 11(1):4004–4013.

Karki, B., Belbase, B. P., Acharya, G. B., Singh, S., and Ghimire, M. P. (2022). Pressure-induced creation and annihilation of weyl points in Td-$Mo_{0.5}W_{0.5}Te_2$ and 1T$''$-$Mo_{0.5}W_{0.5}Te_2$. *Phys. Rev. B*, 105(12):125138–125147.

Kim, Y., Wieder, B. J., Kane, C. L., and Rappe, A. M. (2015). Dirac line nodes in inversion-symmetric crystals. *Phys. Rev. Lett.*, 115(3):036806–036811.

Klitzing, K. v., Dorda, G., and Pepper, M. (1980). New method for high-accuracy determination of the fine-structure constant based on quantized Hall resistance. *Phys. Rev. Lett.*, 45(6):494.

Klitzing, K. v., Klaus, Chakraborty, T., Kim, P., Madhavan, V., Dai, X., McIver, J., Tokura, Y., Savary, L., Smirnova, D., and Rey, A. M. (2020). 40 years of the quantum Hall effect. *Nat. Rev. Phys.*, 2(8):397–401.

Koepernik, K. and Eschrig, H. (1999). Full-potential nonorthogonal local-orbital minimum-basis band-structure scheme. *Phys. Rev. B*, 59(3):1743–1757.

Koepernik, K., Kasinathan, D., Efremov, D. V., Khim, S., Borisenko, S., Büchner, B., and van den Brink, J. (2016). tairte$_4$: A ternary type-II Weyl semimetal. *Phys. Rev. B*, 93(20):201101–201106.

Kohn, W. (1999). Nobel lecture: Electronic structure of matter—wave functions and density functionals. *Rev. Mod. Phys.*, 71(5):1253–1266.

Kohn, W. and Sham, L. J. (1965). Self-consistent equations including exchange and correlation effects. *Phys. Rev.*, 140(4A):A1133–A1138.

Konig, M., Wiedmann, S., Brune, C., Roth, A., Buhmann, H., Molenkamp, L. W., Qi, X.-L., and Zhang, S.-C. (2007). Quantum spin Hall insulator state in HgTe quantum wells. *Science*, 318(5851):766–770.

Kübler, J. and Felser, C. (2014). Non-collinear antiferromagnets and the anomalous Hall effect. *Europhys. Lett.*, 108(6):67001.

Kübler, J. and Felser, C. (2016). Weyl points in the ferromagnetic heusler compound Co_2MnAl. *Europhys. Lett.*, 114(4):47005–47009.

Kumar, A. and Ahluwalia, P. (2012). A first principle comparative study of electronic and optical properties of 1h–MoS_2 and 2H–MoS_2. *Mater. Chem. Phys.*, 135(2-3):755–761.

Kumar, M., Raj, A., Kumar, A., Sharma, S., Bherwani, H., Gupta, A., and Anshul, A. (2021). Structural, electronic, magnetic and optical properties of double perovskite Nd_2CoMnO_6: first principle calculation. *Optik*, 242:166764–166775.

Kumar, N., Guin, S. N., Manna, K., Shekhar, C., and Felser, C. (2020). Topological quantum materials from the viewpoint of chemistry. *Chem. Rev.*, 121(5):2780–2815.

Kuroda, K., Tomita, T., Suzuki, M.-T., Bareille, C., Nugroho, A., Goswami, P., Ochi, M., Ikhlas, M., Nakayama, M., Akebi, S., *et al.* (2017). Evidence for magnetic Weyl fermions in a correlated metal. *Nat. Mater.*, 16(11):1090–1095.

Launay, M., Boucher, F., and Moreau, P. (2004). Evidence of a rutile-phase characteristic peak in low-energy loss spectra. *Phys. Rev. B*, 69(3):035101–035110.

Lee, S. H. (2017). *Dirac surface states of magnetic topological insulators (Unpublished doctoral dissertation).* Graduate School of the Missouri University of Science and Technology.

Levy, M. (1979). Universal variational functionals of electron densities, first-order density matrices, and natural spin-orbitals and solution of the v-representability problem. *Proceedings of the National Academy of Sciences*, 76(12):6062–6065.

Levy, M. (1982). Electron densities in search of hamiltonians. *Phys. Rev. A*, 26(3):1200–1208.

Li, Wang, Q., Wang, G., Yuan, Z., Song, W., Lou, R., Liu, Z., Huang, Y., Liu, Z., Lei, H., *et al.* (2021). Dirac cone, flat band and saddle point in kagome magnet YMn_6Sn_6. *Nat. Commun.*, 12(1):3129–3137.

Li, H., Zhu, Z., Ge, Z., Sun, A., and Tian, Y. (2020a). Ferrimagnetic semiconductor with a direct bandgap. *Appl. Phys. Lett.*, 116(12).

Li, P., Koo, J., Ning, W., Li, J., Miao, L., Min, L., Zhu, Y., Wang, Y., Alem, N., Liu, C.-X., *et al.* (2020b). Giant room temperature anomalous Hall effect and tunable topology in a ferromagnetic topological semimetal Co_2MnAl. *Nat. Commun.*, 11(1):3476–3484.

Li, Q., Wu, Y., Fan, X., Zhang, Y.-J., Zhu, X., Zhu, Z., Li, Y., and Wen, H.-H. (2022). Superconductivity arising from pressure-induced emergence of a Fermi surface in the kagome-lattice chalcogenide $Rb_2Pd_3Se_4$. *Phys. Rev. B*, 106(21):214501–214512.

Liang, Q.-F., Zhou, J., Yu, R., Wang, Z., and Weng, H. (2016). Node-surface and node-line fermions from nonsymmorphic lattice symmetries. *Phys. Rev. B*, 93(8):085427.

Lieb, E. H. (2002). Density functionals for Coulomb systems. *Inequalities: Selecta of Elliott H. Lieb*, pages 269–303.

Liu, Sun, Y., Kumar, N., Muechler, L., Sun, A., Jiao, L., Yang, S.-Y., Liu, D., Liang, A., Xu, Q., *et al.* (2018). Giant anomalous Hall effect in a ferromagnetic kagome-lattice semimetal. *Nat. Phys.*, 14(11):1125–1131.

Liu, C.-X., Zhang, S.-C., and Qi, X.-L. (2016). The quantum anomalous Hall effect: theory and experiment. *Annu. Rev. Condens. Matter Phys.*, 7:301–321.

Luke, G. M., Keren, A., Le, L. P., Wu, W. D., Uemura, Y. J., Bonn, D. A., Taillefer, L., and Garrett, J. D. (1993). Muon spin relaxation in UPt_3. *Phys. Rev. Lett.*, 71(9):1466–1469.

Lv, B. Q., Qian, T., and Ding, H. (2021). Experimental perspective on three-dimensional topological semimetals. *Rev. Mod. Phys.*, 93(2):025002–0250070.

Lv, B. Q., Weng, H. M., Fu, B. B., Wang, X. P., Miao, H., Ma, J., Richard, P., Huang, X. C., Zhao, L. X., Chen, G. F., Fang, Z., Dai, X., Qian, T., and Ding, H. (2015). Experimental discovery of Weyl semimetal TaAs. *Phys. Rev. X*, 5:031013.

Ma, W., Xu, X., Yin, J.-X., Yang, H., Zhou, H., Cheng, Z.-J., Huang, Y., Qu, Z., Wang, F., Hasan, M. Z., and Jia, S. (2021). Rare earth engineering in RMn_6Sn_6 (R= Gd, Tm, Lu) topological kagome magnets. *Phys. Rev. Lett.*, 126(24):246602–246607.

Majorana, E. (1937). Teoria simmetrica dell'elettrone e del positrone. *Il Nuovo Cimento (1924-1942)*, 14(4):171–184.

Manna, K., Muechler, L., Kao, T.-H., Stinshoff, R., Zhang, Y., Gooth, J., Kumar, N., Kreiner, G., Koepernik, K., Car, R., Kübler, J., Fecher, G. H., Shekhar, C., Sun, Y., and Felser, C. (2018). From colossal to zero: Controlling the anomalous Hall effect in magnetic heusler compounds via berry curvature design. *Phys. Rev. X*, 8:041045.

Martin, R. M. (2020). *Electronic structure: basic theory and practical methods*. Cambridge university press.

Materials, P. T. (2020). Materials data on $Li_2Fe_3S_4$ by materials project. *Materialproject*.

Mekata, M. (2003). Kagome: The story of the basketweave lattice. *Phys. Today*, 56(2):12–13.

Moore, J. E. and Balents, L. (2007). Topological invariants of time-reversal-invariant band structures. *Phys. Rev. B*, 75(12):121306–121310.

Morali, N., Batabyal, R., Nag, P. K., Liu, E., Xu, Q., Sun, Y., Yan, B., Felser, C., Avraham, N., and Beidenkopf, H. (2019). Fermi-arc diversity on surface terminations of the magnetic Weyl semimetal $Co_3Sn_2S_2$. *Science*, 365(6459):1286–1291.

Mourik, V., Zuo, K., Frolov, S. M., Plissard, S., Bakkers, E. P., and Kouwenhoven, L. P. (2012). Signatures of majorana fermions in hybrid superconductor-semiconductor nanowire devices. *Science*, 336(6084):1003–1007.

Murakami, S. (2007). Phase transition between the quantum spin hall and insulator phases in 3d: emergence of a topological gapless phase. *New J. Phys.*, 9(9):356–371.

Nagaosa, N., Sinova, J., Onoda, S., MacDonald, A. H., and Ong, N. P. (2010). Anomalous hall effect. *Rev. Mod. Phys.*, 82(2):1539–1592.

Nakatsuji, S., Kiyohara, N., and Higo, T. (2015). Large anomalous Hall effect in a non-collinear antiferromagnet at room temperature. *Nature*, 527(7577):212–215.

Nawai, S., Okazaki, K., Mizokawa, T., Fujimori, A., Hondou, K., Fujiwara, Y., Iio, K., Usuda, M., and Hamada, N. (2004). Electronic structure of the kagomé lattice compound $Rb_2Ni_3S_4$. *Phys. Rev. B*, 69:045103.

Nielsen, H. B. and Ninomiya, M. (1981). Absence of neutrinos on a lattice: (I) proof by homotopy theory. *Nucl. Phys. B*, 185(1):20–40.

Pak, C., Garlea, V. O., Yannello, V., Cao, H., Bangura, A. F., and Shatruk, M. (2019). $Na_2Mn_3Se_4$: strongly frustrated antiferromagnetic semiconductor with complex magnetic structure. *Inorg. Chem.*, 58(9):5799–5806.

Parr, R. G. and Weitao, Y. (1994). *Density-Functional Theory of Atoms and Molecules*. Oxford University Press, USA.

Pavarini, E., Koch, E., Anders, F., and Jarrell, M. (2012). *Correlated Electrons: From Models to Materials*. Forschungszentrum Jülich GmbH Institute for Advanced Simulation.

Penn, D. R. (1962). Wave-number-dependent dielectric function of semiconductors. *Phys. Rev.*, 128(5):2093–2097.

Perdew, J. P., Burke, K., and Ernzerhof, M. (1996). Generalized gradient approximation made simple. *Phys. Rev. Lett.*, 77(18):3865–3868.

Pontecorvo, B. (1957). Mesonium and anti-mesonium. *Sov. Phys. JETP*, 6(1957):429–431.

Quan, Y., Yin, Z. P., and Pickett, W. E. (2017). Single nodal loop of accidental degeneracies in minimal symmetry: Triclinic $CaAs_3$. *Phys. Rev. Lett.*, 118(17):176402–176408.

Ramamurthy, S. T. and Hughes, T. L. (2017). Quasitopological electromagnetic response of line-node semimetals. *Phys. Rev. B*, 95(7):075138–075147.

Rauch, T., Flieger, M., Henk, J., Mertig, I., and Ernst, A. (2014). Dual topological character of chalcogenides: theory for Bi_2Te_3. *Phys. Rev. Lett.*, 112(1):016802–016807.

Ray, R., Sadhukhan, B., Richter, M., Facio, J. I., and van den Brink, J. (2022). Tunable chirality of noncentrosymmetric magnetic Weyl semimetals in rare-earth carbides. *npj Quantum Mater.*, 7(1):19–28.

Read, N. and Green, D. (2000). Paired states of fermions in two dimensions with

breaking of parity and time-reversal symmetries and the fractional quantum Hall effect. *Phys. Rev. B*, 61(15):10267–10297.

Rhim, J.-W. and Kim, Y. B. (2015). Landau level quantization and almost flat modes in three-dimensional semimetals with nodal ring spectra. *Phys. Rev. B*, 92(4):045126–045134.

Roy, R. (2009). Topological phases and the quantum spin Hall effect in three dimensions. *Phys. Rev. B*, 79(19):195322–195327.

Sakhya, A. P., Huang, C.-Y., Dhakal, G., Gao, X.-J., Regmi, S., Wang, B., Wen, W., He, R.-H., Yao, X., Smith, R., Sprague, M., Gao, S., Singh, B., Lin, H., Xu, S.-Y., Tafti, F., Bansil, A., and Neupane, M. (2023). Observation of fermi arcs and Weyl nodes in a noncentrosymmetric magnetic weyl semimetal. *Phys. Rev. Mater.*, 7(5):L051202–L051208.

Sancho, M. L., Sancho, J. L., Sancho, J. L., and Rubio, J. (1985). Highly convergent schemes for the calculation of bulk and surface Green functions. *J. Phys. F*, 15(4):851–859.

Schnyder, A. P. (2020). Topological semimetals.

Schoop, L. M., Ali, M. N., Straßer, C., Topp, A., Varykhalov, A., Marchenko, D., Duppel, V., Parkin, S. S., Lotsch, B. V., and Ast, C. R. (2016). Dirac cone protected by non-symmorphic symmetry and three-dimensional Dirac line node in ZrSiS. *Nat. Commun.*, 7(1):11696–11703.

Schoop, L. M., Topp, A., Lippmann, J., Orlandi, F., Müchler, L., Vergniory, M. G., Sun, Y., Rost, A. W., Duppel, V., Krivenkov, M., *et al.* (2018). Tunable Weyl and Dirac states in the nonsymmorphic compound CeSbTe. *Sci. Adv.*, 4(2):eaar2317–eaar2325.

Shi, W., Muechler, L., Manna, K., Zhang, Y., Koepernik, K., Car, R., van den Brink, J., Felser, C., and Sun, Y. (2018). Prediction of a magnetic Weyl semimetal without spin-orbit coupling and strong anomalous Hall effect in the heusler compensated ferrimagnet Ti_2MnAl. *Phys. Rev. B*, 97(6):060406–060412.

Shore, A. (2019). Retraction: First-principle investigations of structural, electronic, magnetic and optical properties of bulk $BiVO_3$. *RSC Adv.*, 9(23):12813–12813.

Simon, B. (1983). Holonomy, the quantum adiabatic theorem, and Berry's phase. *Phys. Rev. Lett.*, 51(24):2167–2170.

Slater, J. C. (1929). The theory of complex spectra. *Phys. Rev.*, 34(10):1293–1322.

Soluyanov, A. A., Gresch, D., Wang, Z., Wu, Q., Troyer, M., Dai, X., and Bernevig, B. A. (2015). Type-II Weyl semimetals. *Nature*, 527(7579):495–498.

Steinberg, J. A., Young, S. M., Zaheer, S., Kane, C. L., Mele, E. J., and Rappe, A. M. (2014). Bulk Dirac points in distorted spinels. *Phys. Rev. Lett.*, 112(3):036403–036408.

Stepanjuga, A., Ray, R., Richter, M., Carrocci, S., Hampel, S., Galle, L., Grafe, H.-J., and Valldor, M. (2022). Metathesis as an alternative synthesis route to layered sulfides A(LiZn)S_2 (A= alkali-metal) with unexpected colors. *New J. Chem.*, 46(10):4900–4910.

Sun, Li, B., Zou, X., Li, R., Huang, B., Dai, Y., and Niu, C. (2023). Magnetic Weyl semimetal in Nd_2CoMnO_6 with long-distance distribution of Weyl points. *Adv. Sci.*, pages 2301474–2301479.

Sun, J., Zhou, X.-F., Fan, Y.-X., Chen, J., Wang, H.-T., Guo, X., He, J., and Tian, Y. (2006). First-principles study of electronic structure and optical properties of heterodiamond BC_2N. *Phys. Rev. B*, 73(4):045108–045118.

Sun, Y., Wu, S.-C., Ali, M. N., Felser, C., and Yan, B. (2015). Prediction of Weyl semimetal in orthorhombic $MoTe_2$. *Phys. Rev. B*, 92(16):161107–161114.

Taherinejad, M., Garrity, K. F., and Vanderbilt, D. (2014). Wannier center sheets in topological insulators. *Phys. Rev. B*, 89(11):115102–115116.

Tancogne-Dejean, N., Oliveira, M. J. T., and Rubio, A. (2017). Self-consistent DFT+U method for real-space time-dependent density functional theory calculations. *Phys. Rev. B*, 96(24):245133–245142.

Tang, P., Zhou, Q., Xu, G., and Zhang, S.-C. (2016). Dirac fermions in an antiferromagnetic semimetal. *Nat. Phys.*, 12(12):1100–1104.

Thomas, L. H. (1927). The calculation of atomic fields. In *Mathematical proceedings of the Cambridge philosophical society*, volume 23, pages 542–548. Cambridge University Press.

Thouless, D. J., Kohmoto, M., Nightingale, M. P., and den Nijs, M. (1982). Quantized Hall conductance in a two-dimensional periodic potential. *Phys. Rev. Lett.*, 49(6):405–408.

Tolba, S. A., Gameel, K. M., Ali, B. A., Almossalami, H. A., and Allam, N. K. (2018). The DFT+ U: Approaches, accuracy, and applications. *Density Functional Calculations-Recent Progresses of Theory and Application*, 1:5772.

Toll, J. S. (1956). Causality and the dispersion relation: Logical foundations. *Phys. Rev.*, 104(6):1760–1770.

Tong, D. (2016). The quantum Hall effect: Tifr infosys lectures. *arXiv preprint arXiv:1606.06687*.

Tran, F. and Blaha, P. (2009). Accurate band gaps of semiconductors and insulators with a semilocal exchange-correlation potential. *Phys. Rev. Lett.*, 102(22):226401–226405.

Tran, F., Blaha, P., and Schwarz, K. (2007). Band gap calculations with becke–johnson exchange potential. *J. Condens. Matter Phys.*, 19(19):196208–196217.

Tran, F., Blaha, P., Schwarz, K., and Novák, P. (2006). Hybrid exchange-correlation energy functionals for strongly correlated electrons: Applications to transition-metal monoxides. *Phys. Rev. B*, 74(15):155108–155118.

Tsuneda, T. (2014). *Density functional theory in quantum chemistry*. Springer Tokyo Heidelberg New York Dordrecht London.

Vanderbilt, D. (2018). *Berry Phases in Electronic Structure Theory: Electric Polarization, Orbital Magnetization and Topological Insulators*. Cambridge University Press, University Printing House, Cambridge CB2 8BS, United Kingdom.

von Barth, U. and Hedin, L. (1972). A local exchange-correlation potential for the spin polarized case. i. *J. Phys. C: Solid State Phys.*, 5(13):1629–1642.

Vosko, S. H., Wilk, L., and Nusair, M. (1980). Accurate spin-dependent electron liquid correlation energies for local spin density calculations: a critical analysis. *Can. J. Phys.*, 58(8):1200–1212.

Wan, X., Turner, A. M., Vishwanath, A., and Savrasov, S. Y. (2011). Topological semimetal and Fermi-arc surface states in the electronic structure of pyrochlore iridates. *Phys. Rev. B*, 83(20):205101–205110.

Wang, Neubauer, K. J., Duan, C., Yin, Q., Fujitsu, S., Hosono, H., Ye, F., Zhang, R., Chi, S., Krycka, K., Lei, H., and Dai, P. (2021). Field-induced topological Hall effect and double-fan spin structure with a c-axis component in the metallic kagome antiferromagnetic compound YMn_6Sn_6. *Phys. Rev. B*, 103(1):014416–014423.

Wang, Weng, H., Wu, Q., Dai, X., and Fang, Z. (2013a). Three-dimensional Dirac semimetal and quantum transport in Cd_3As_2. *Phys. Rev. B*, 88(12):125427–125433.

Wang, Xu, Y., Lou, R., Liu, Z., Li, M., Huang, Y., Shen, D., Weng, H., Wang, S., and Lei,

H. (2018). Large intrinsic anomalous Hall effect in half-metallic ferromagnet $Co_3Sn_2S_2$ with magnetic Weyl fermions. *Nat. Commun.*, 9(1):3681–3689.

Wang, Yates, J. R., Souza, I., and Vanderbilt, D. (2006). Ab initio calculation of the anomalous Hall conductivity by Wannier interpolation. *Phys. Rev. B*, 74(19):195118–195133.

Wang, C. S. and Klein, B. M. (1981). First-principles electronic structure of Si, Ge, GaP, GaAs, ZnS, and ZnSe. II. optical properties. *Phys. Rev. B*, 24(6):3417–3429.

Wang, W.-S., Li, Z.-Z., Xiang, Y.-Y., and Wang, Q.-H. (2013b). Competing electronic orders on kagome lattices at van Hove filling. *Phys. Rev. B*, 87(11):115135–115143.

Wang, Z., Gresch, D., Soluyanov, A. A., Xie, W., Kushwaha, S., Dai, X., Troyer, M., Cava, R. J., and Bernevig, B. A. (2016a). $MoTe_2$: A type-ii Weyl topological metal. *Phys. Rev. Lett.*, 117(5):056805–056810.

Wang, Z., Vergniory, M. G., Kushwaha, S., Hirschberger, M., Chulkov, E. V., Ernst, A., Ong, N. P., Cava, R. J., and Bernevig, B. A. (2016b). Time-reversal-breaking Weyl fermions in magnetic heusler alloys. *Phys. Rev. Lett.*, 117(23):236401–236407.

Waroquiers, D., Lherbier, A., Miglio, A., Stankovski, M., Ponc, S., and Oliveira, M. J. T. (2013). Band widths and gaps from the Tran-Blaha functional: Comparison with many-body perturbation theory. *Phys. Rev. B*, 87(7):075121–075136.

Weizsäcker, C. v. (1935). Zur theorie der kernmassen. *Zeitschrift für Physik*, 96(7-8):431–458.

Weng, Hongming, Liang, Y., Xu, Q., Yu, R., Fang, Z., Dai, X., and Kawazoe, Y. (2015a). Topological node-line semimetal in three-dimensional graphene networks. *Phys. Rev. B*, 92(4):045108–045116.

Weng, H., Fang, C., Fang, Z., Bernevig, B. A., and Dai, X. (2015b). Weyl semimetal phase in noncentrosymmetric transition-metal monophosphides. *Phys. Rev. X*, 5(1):011029–011039.

Weyl, H. (1929). Electron and gravitation. *z. Phys*, 56:330–352.

Wilczek, F. (2009). Majorana returns. *Nat. Phys.*, 5(9):614–618.

Wu, Ambler, E., Hayward, R. W., Hoppes, D. D., and Hudson, R. P. (1957). Experimental test of parity conservation in beta decay. *Phys. Rev.*, 105(4):1413–1415.

Wu, Wang, Q., Zhou, X., Wang, J., Dong, P., He, J., Ding, Y., Teng, B., Zhang, Y., and Li, Y. (2022). Nonreciprocal charge transport in topological kagome superconductor CsV_3Sb_5. *npj Quantum Mater.*, 7(1):105–112.

Xiao, D., Chang, M.-C., and Niu, Q. (2010). Berry phase effects on electronic properties. *Rev. Mod. Phys.*, 82(3):1959–2007.

Xie, L. S., Schoop, L. M., Seibel, E. M., Gibson, Q. D., Xie, W., and Cava, R. J. (2015). A new form of Ca_3P2 with a ring of Dirac nodes. *Apl Mater.*, 3(8).

Xu, G., Weng, H., Wang, Z., Dai, X., and Fang, Z. (2011). Chern semimetal and the quantized anomalous Hall effect in $HgCr_2Se_4$. *Phys. Rev. Lett.*, 107(18):186806–186811.

Yamakage, A., Yamakawa, Y., Tanaka, Y., and Okamoto, Y. (2016). Line-node dirac semimetal and topological insulating phase in noncentrosymmetric pnictides CaAgX (X= P, As). *J. Phys. Soc. Japan*, 85(1):013708.

Yan, Müchler, L., and Felser, C. (2012). Prediction of weak topological insulators in layered semiconductors. *Phys. Rev. Lett.*, 109(11):116406–116411.

Yan, B. and Felser, C. (2017). Topological materials:Weyl semimetals. *Annu. Rev. Condens. Matter Phys.*, 8:337–354.

Yan, Z., Huang, P.-W., and Wang, Z. (2016). Collective modes in nodal line semimetals. *Phys. Rev. B*, 93(8):085138–085147.

Yang, S.-Y., Yang, H., Derunova, E., Parkin, S. S., Yan, B., and Ali, M. N. (2018). Symmetry demanded topological nodal-line materials. *Adv. Phys. X.*, 3(1):1414631–1414665.

Ye, L., Kang, M., Liu, J., Von Cube, F., Wicker, C. R., Suzuki, T., Jozwiak, C., Bostwick, A., Rotenberg, E., Bell, D. C., *et al.* (2018). Massive dirac fermions in a ferromagnetic kagome metal. *Nature*, 555(7698):638–642.

Yin, J.-X., Ma, W., Cochran, T. A., Xu, X., Zhang, S. S., Tien, H.-J., Shumiya, N., Cheng, G., Jiang, K., Lian, B., *et al.* (2020). Quantum-limit Chern topological magnetism in $TbMn_6Sn_6$. *Nature*, 583(7817):533–536.

Young, S. M. and Kane, C. L. (2015). Dirac semimetals in two dimensions. *Phys. Rev. Lett.*, 115(12):126803–126808.

Young, S. M., Zaheer, S., Teo, J. C. Y., Kane, C. L., Mele, E. J., and Rappe, A. M. (2012). Dirac semimetal in three dimensions. *Phys. Rev. Lett.*, 108(14):140405–140410.

Yu, Weng, H., Fang, Z., Dai, X., and Hu, X. (2015). Topological node-line semimetal and

dirac semimetal state in antiperovskite Cu_3PdN. *Phys. Rev. Lett.*, 115(3):036807–0368012.

Yu, Wu, Q., Fang, Z., and Weng, H. (2017). From nodal chain semimetal to Weyl semimetal in HfC. *Phys. Rev. Lett.*, 119(3):036401–036406.

Yu, S.-L. and Li, J.-X. (2012). Chiral superconducting phase and chiral spin-density-wave phase in a hubbard model on the kagome lattice. *Phys. Rev. B*, 85(14):144402–144406.

Yupeng, L. and Xu, Z.-A. (2019). Exploring topological superconductivity in topological materials. *Adv. Quantum Technol.*, 2(9):1800112–1800128.

Zeng, M., Fang, C., Chang, G., Chen, Y.-A., Hsieh, T., Bansil, A., Lin, H., and Fu, L. (2015). Topological semimetals and topological insulators in rare earth monopnictides. *arXiv preprint arXiv:1504.03492*.

Zhang, Jin, L., Dai, X., and Liu, G. (2017). Topological type-II nodal line semimetal and dirac semimetal state in stable kagome compound Mg_3Bi_2. *J. Phys. Chem. Lett.*, 8(19):4814–4819.

Zhang, Tan, Y.-W., Stormer, H. L., and Kim, P. (2005). Experimental observation of the quantum Hall effect and Berry's phase in graphene. *Nature*, 438(7065):201.

Zhang, X., Chen, Z., Zhang, S., Liu, R., Zong, H., Jing, Q., Li, G., Ma, M., and Wang, W. (2007a). Electronic and optical properties of rock-salt aluminum nitride obtained from first principles. *J. Condens. Matter Phys.*, 19(42):425231–425237.

Zhang, Y., Talapatra, S., Kar, S., Vajtai, R., Nayak, S. K., and Ajayan, P. M. (2007b). First-principles study of defect-induced magnetism in carbon. *Phys. Rev. Lett.*, 99(10):107201.

Zheng, B., Xia, B., Wang, R., Zhao, J., Chen, Z., Zhao, Y., and Xu, H. (2019). Tunable ferromagnetic weyl fermions from a hybrid nodal ring. *npj Comput. Mater.*, 5(1):1–7.

APPENDIX

Academic Activities

A. Attended courses offered by IoST

In first semester:

PHS 911, Philosophy of Science (Cr. Hrs. 3)

PHS 912, Research Methodology (Cr. Hrs. 3)

PHS 913, Seminar (Cr. Hrs. 3)

In second semester:

PHS 951, Advanced Research Methodology (Cr. Hrs. 3)

PHS 957, Advanced Materials and Topology (Cr. Hrs. 3)

PHS 952, Seminar (Cr. Hrs. 3)

B. Paper publications

International

1) **Acharya, G. B.,** Kim, S. H., & Ghimire, M. P. (**2024**). Electronic and optical properties of ternary kagome $Rb_2Ni_3S_4$: A density functional study. *Modelling and Simulation in Materials Science and Engineering* 32, 065012.

2) **Acharya, G. B.,** Belbase, B. P., & Ghimire, M. P. **(2023)**. Electronic structure, optical properties and defect induced half-metallic ferromagnetism in kagome $Cs_2Ni_3S_4$. *Electronic Structure*, *5*(4), 045008.

3) Karki, B., Belbase, B. P., **Acharya, G. B.,** Singh, S., & Ghimire, M. P. **(2022)**. Pressure-induced creation and annihilation of Weyl points in *Td*-$Mo_{0.5}W_{0.5}Te_2$ and *1T′′*-$Mo_{0.5}W_{0.5}Te_2$. *Physical Review B*, *105*(12), 125138.

4) **Acharya, G. B.,** Richter, M., & Ghimire, M. P. (**2024**). Magnetic ground state, electronic structure, and anomalous Hall conductivity of $Cs_2Co_3S_4$: density-functional calculations. **(under review)**.

5) **Acharya, G. B.,** Neupane, M. B., Ghimire, R., & Ghimire, M. P. **(2022)**. Weyl Metal Phase in Delafossite Oxide $PtNiO_2$. *arXiv preprint arXiv:2212.00579* (**under review**).

6) Joshi P., **Acharya, G. B.,** , Ishwor Bahadur Khadka, I. B., Srinivasan, B.,Kim S. H., and Ghimire. M.P. (**2024**). Structural, Electronic, and Optical Properties of Kagome $Rb_2Pt_3S_4$. **(under review)**.

National

1) **Acharya, G. B.,** & Ghimire, M. P. (2022). Electronic and Magnetic Properties of $K_2Mn_3S_4$. *Journal of Nepal Physical Society*, *8*(3), 75.

2) **Acharya, G. B.,** & Ghimire, M. P. (2023). Electronic and magnetic properties of ternary sulfide $Rb_2Mn_3S_4$. *Himalayan Physics*, *10*(1), 33.

C. Participation and Presentation

1) Virtual Participation and presentation on the "first international e-conference on Recent Advancement in Physics and Material Science", held during 9-10 July, 2020, organized by Kurseong college, Darjeeling, West Bangal India in collaboration with St. Josepah's, college, Darjeeling, West Bangal, India.

2) Virtual poster presentation on "MANA International Symposium 2021 jointly with ICYS" held during 2-7 March, 2021, organized by National Institute for Materials Science (NIMS), Japan.

3) Participation on "Refresher Course on Material Science" held during 15-19 September, 2021, organized by central department of physics, Kirtipur, Nepal.

4) Participation on "International Workshop on Computational Materials Engineering (CME-2021)." held during 4-6 October, 2021, organized by central department of physics, Kirtipur, Nepal.

5) Virtual presentation on APS March Meeting 2022 on title "Engineering Weyl Nodes in Ferrimagnetic $Li_2Fe_3S_4$" held during March 14-18, 2022 Chicago & Online organized by American Physical Society, America.

6) Participation and poster presentation in the international scientific conference "Kathmandu Humboldt-Kolleg 2022", held during 16 -19 October, 2022, organized by Humboldt-Kolleg Nepal.

7) Participation in the "ACS WORKSHOP 2023", held 13 November, 2023, organized by IIT, Madras.

Modelling and Simulation in
Materials Science and Engineering

PAPER

Electronic and optical properties of ternary kagome $Rb_2Ni_3S_4$: a density functional study

To cite this article: Gang Bahadur Acharya *et al* 2024 *Modelling Simul. Mater. Sci. Eng.* **32** 065012

IOP Publishing Modelling and Simulation in Materials Science and Engineering

Modelling Simul. Mater. Sci. Eng. **32** (2024) 065012 (10pp) https://doi.org/10.1088/1361-651X/ad54e1

Electronic and optical properties of ternary kagome $Rb_2Ni_3S_4$: a density functional study

Gang Bahadur Acharya[1,2], **Se-Hun Kim**[3] and **Madhav Prasad Ghimire**[1,2,3,*]

[1] Central Department of Physics, Tribhuvan University, Kirtipur 44613 Kathmandu, Nepal
[2] Leibniz Institute for Solid State and Materials Research—IFW Dresden, Helmholtzstr. 20, 01069 Dresden, Germany
[3] Faculty of Science Education, Jeju National University, Jeju 63243, Republic of Korea

E-mail: madhav.ghimire@cdp.tu.edu.np

Received 12 November 2023; revised 10 May 2024
Accepted for publication 6 June 2024
Published 27 June 2024

Abstract

The application of semiconductors with optical properties has grown significantly in the development of semiconductor photovoltaics. Here, we explore the electronic and optical properties of ternary transition metal sulfide $Rb_2Ni_3S_4$ by means of density functional theory. From the structural perspective, Ni atoms are found to form a kagome-like lattice in a two-dimensional plane of $Rb_2Ni_3S_4$. From our calculations, $Rb_2Ni_3S_4$ is found to be a semiconductor with an indirect band gap of $\sim$0.67 eV. Strong hybridization was observed between the S-3p with the Ni-3d_{xz} and Ni-3d_{yz} orbitals. Interestingly, a flat band was noticed below the Fermi level demonstrating one significant feature of kagome lattice. From the optical calculations, $Rb_2Ni_3S_4$ is found to exhibit optical activity in both the visible and lower ultraviolet regions of the incident photon energies. The optical response suggests this material may be a potential candidate for opto-electronic device, given its ability to interact with light across a broad range of wavelengths. This work is expected to motivate the experimental group for transport measurements and may provide a new foundation in optics.

Keywords: density functional theory, kagome lattice, electronic structure, semiconductor, optoelectronic applications

* Author to whom any correspondence should be addressed.

1. Introduction

The family of ternary transition metal chalcogenides represented by the molecular formula $A_2M_3X_4$ (where A includes K, Rb, Cs; M includes Ni, Pd, Pt; and X includes S, Se) demonstrates diverse crystal symmetries [1]. These compounds possess unique properties, featuring a quasi-two dimensional (2D) layered structure, where the transition metal elements create kagome nets together with chalcogenide atoms. Kagome compounds are widely recognized as excellent platforms for exploring novel topological properties. The specific arrangement of atoms in a kagome pattern leads to remarkable transport characteristics, including negative magneto-resistance, anomalous Hall conductivity, and Fermi arc surface states [2–9]. They are also found to show interesting optical features which can give rise to optical device fabrication. The recently discovered kagome CsV_3Sb_5 was reported to exhibit efficient absorption of ultraviolet radiation and has a strong reflectivity for visible light [10]. Likewise, KV_3Sb_5 has been reported as a potential candidate for plasmon-mediated hot carrier applications in the infrared region [11]. Kagome Nb_3Cl_8 was reported to be a semiconductor which shows large optical anisotropy [12].

In the family of ternary chalcogenides $Rb_2Pd_3Se_4$, Li *et al*. predicted the superconductivity by applying pressure wherein Lifshitz transition was observed [13]. Elder *et al*. performed the magnetic and transport measurements in $K_2Ni_3S_4$ suggesting the possibility of co-existence of Ni^{1+} and Ni^{2+} in the crystal [14]. Likewise, we recently studied the electronic and optical properties of $Cs_2Ni_3S_4$ in addition to the effect of vacancy defects in the crystal. Our study suggests this material to be a suitable candidate for optoelectronic device [15]. While studies of $Rb_2Ni_3S_4$ are uncommon, the existing results suggest that the material could be interesting. For instance, Bronger *et al*. first synthesized and carried out the magnetic susceptibility measurements above 90 K to explore magnetism in $Rb_2Ni_3S_4$. They did not find any evidence of magnetism [16]. At 4.2 K, the magnetism of $Rb_2Ni_3S_4$ indicates that the ordered phase may represent the weak ferromagnetic phase [17]. Fukamachi *et al* reported the observation of weak ferromagnetism and semi-conducting characteristics in $Rb_2Ni_3S_4$. However, their findings, based on both nuclear magnetic resonance and magnetic measurements, led them to propose that $Rb_2Ni_3S_4$ is a band insulator. Consequently, they suggested that the intrinsic property of this system to be non-magnetic [18]. Later in 2002, Hondou *et al*. performed DFT calculations and find that the material is a semiconductor, featuring flat bands below the Fermi level (E_F) [19]. Additional investigations using photoemission spectroscopy have unveiled the moderate electron correlation and substantial hybridization between Ni-3*d* and S-3*p* orbitals, in agreement with the results from the band structure calculations [20]. Experiments have been performed in order to examine the origin of magnetism in water-immersed $Rb_2Ni_3S_4$. A possible ferromagnetic phase induced by the partial collapse of crystal structure was obtained. The intrinsic substance is non-magnetic semiconductor. The presence of a planar sulfur coordination around Ni^{2+} results in a low spin state with Ni in its $3d^8$ configuration [21]. Despite a number of studies, there are no reports on optical properties of $Rb_2Ni_3S_4$. With an aim to fill this gap and to show the interesting behavior of this material, we explore the detailed electronic structure and optical properties of $Rb_2Ni_3S_4$.

In this work, we report the electronic as well as optical properties of $Rb_2Ni_3S_4$. This material is found to be a non-magnetic semiconductor with an indirect band gap of $\sim$0.67 eV. The optical activity in this material is prominent within the visible and lower ultraviolet spectrum.

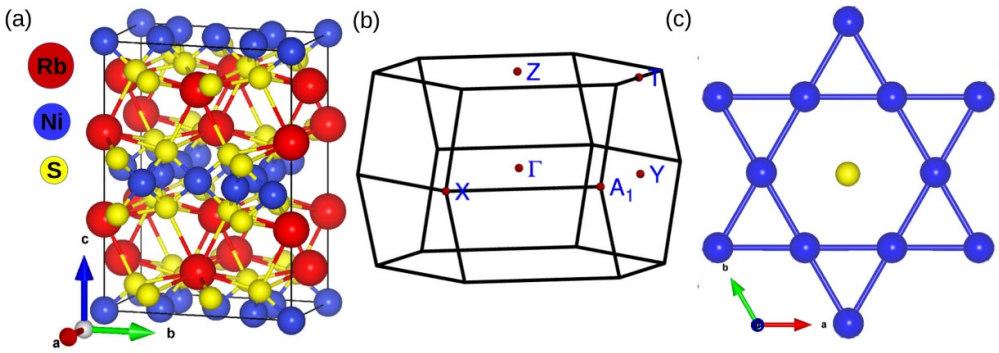

Figure 1. (a) Crystal structure of $Rb_2Ni_3S_4$. (b) Three dimensional Brillouin zone. Red dots are indicates the high symmetry points in momentum space. (c) Ni-ions constitute a kagome lattice in *ab* plane.

2. Structural and computational details

$Rb_2Ni_3S_4$ crystallizes in an orthorhombic crystal structure with space group *Fmmm* (no. 69) and belongs to the point group D_{2h}. The experimental lattice parameters used in this study are $a = 5.862$ Å, $b = 9.937$ Å and $c = 13.758$ Å [1]. The crystal system consists of four in-equivalent atoms labeled as Rb, Ni(I), Ni(II), and S, respectively. In $Rb_2Ni_3S_4$, Rb^{1+} ions are surrounded by eight equivalent S^{2-} ions in an 8-coordinate geometry. The Rb?S bond distances exhibit a range from 3.38 Å to 3.45 Å. All Ni^{2+} ions are coordinated by four equivalent S^{2-} ions, adopting a square co-planar arrangement (see figure 1(a)). At the first and second Ni^{2+} site, the Ni?S bond length measured are 2.22 Å. Furthermore, $Rb_2Ni_3S_4$ exhibits symmorphic crystal symmetry, and is centrosymmetric. Table 1 presents the fully relaxed atomic coordinates for $Rb_2Ni_3S_4$.

In order to investigate the electronic and optical characteristics of selected compound, we employed the DFT approach [22] using the full potential local orbital (FPLO) code [23], version 18.00. The standard generalized gradient approximation (GGA) within the parameterization of Perdew, Burke, and Ernzerhof (PBE-96) [24] was taken into account for the exchange and correlation energy. Self-consistent calculations were performed in the scalar relativistic and four component full relativistic modes of FPLO. In the full relativistic mode that includes spin–orbit coupling in all orders, the direction of magnetization was fixed by a global setting of the spin quantization axis. However, since the inclusion of spin–orbit coupling did not significantly impact the electronic properties, we focus our discussion only on the outcomes from the scalar-relativistic calculations. For the optical property calculations, we have used the FOPTICS module of FPLO which is based on random phase approximation. In the electronic structure calculations, a *k*-mesh subdivision of $12 \times 12 \times 12$ was used to cover the full Brillouin zone. As for the optical property calculations, a finer *k*-mesh subdivision of $32 \times 32 \times 32$ was employed. To ensure the accuracy of the energy, the convergence criteria for self-consistency as set to 10^{-8} Hartree. During the structural optimization, a force convergence of 10^{-3} eV Å^{-1} was applied.

Our Calculations done with FPLO are consistent with results performed using WIEN2k [25]. The accuracy of FPLO can be well compared with other electronic structure codes as reported by Lejaeghere *et al* [26].

Table 1. Total number of in-equivalent atoms and their Wyckoff positions in $Rb_2Ni_3S_4$.

Atom	Point location	x	y	z
Rb	8i	0	0	0.343
Ni(I)	8e	−1/4	−1/4	0
Ni(II)	4a	0	0	0
S	16 m	0	0.168	0.106

3. Results and discussion

3.1. Electronic properties

To understand the electronic properties, we initiated our calculations by searching for the stable ground state of $Rb_2Ni_3S_4$. To achieve this, we performed both nonmagnetic and ferromagnetic calculations in the scalar relativistic case (without spin–orbit coupling). The outcome was a nonmagnetic ground state, attributed to the square planar coordination of Ni^{2+} with S^{2-} ions. Our DFT ground state result agrees with the experimental nonmagnetic ground state [16, 27]. Additionally, we performed full-relativistic calculations, considering spin–orbit coupling. However, this consideration did not significantly affect the electronic structure of $Rb_2Ni_3S_4$. Consequently, we focus solely on the scalar relativistic results throughout our discussions.

Figures 2(a)–(c) illustrates the total, partial, and local density of states (DOS), respectively. In the total DOS, high peaks both above and below the E_F within a specific energy range result from the bonding and anti-bonding nature of the orbitals. Ni and S states are mainly dominate the DOS, while Rb has a minimal contribution (see figure 2(b)). This arises due to the presence of only one electron in the outermost 5 s orbital of Rb atom.

To precisely understand the contributions of the orbitals, we analyze the partial and local DOS. At around 1.3 eV in the DOS plot (see figure 2), antibonding states are observed which are contributed by Ni(I)-d_{xz} and S-3p states. This gives rise to peaks above E_F. While around -0.9 eV and -0.38 eV below E_F are contributed by Ni(I)-$d_{x^2-y^2}$ and d_{xy} orbitals giving rise to peaks due to the bonding states. The analysis of the local DOS projection (see figure 2(c)) reveals that the insulating behavior partially originates from the crystal field splitting of the energy bands [13]. It is well-established that each nickel (Ni) ion is surrounded by four S ions, forming a square planar coordination arrangement (see figure 1(a)). In this situation, the S^{2-} ions strongly bind with the central Ni^{2+} metal, causing a separation of energy levels known as crystal field splitting. As a result, metal ions with a d^8 configuration tend to adopt a square planar geometry when exposed to a strong field. This arrangement forms low spin complexes where the eight d electrons fill the lower-energy d_{xz}, d_{yz}, d_z^2 , and d_{xy} orbitals, while the high-energy $d_{x^2-y^2}$ orbital remains unoccupied. This also helps explain the origin of the nonmagnetic ground state even in the presence of a typically magnetic atom Ni. Above the E_F, the width and magnitude of the DOS of S-3p and Ni-3d (d_{xz} and d_{yz} orbitals) (see in figure 2(b)) are almost equal, suggesting strong hybridization within the energy range from 0.7 to 1.2 eV [19].

Based on the analysis of the electronic band structure, $Rb_2Ni_3S_4$ should exhibit semiconducting behavior with an energy band gap of ∼0.67 eV. These findings are consistent with the previously reported DFT value of 0.66 eV [20] and the experimental value of 0.80 eV deduced from a transport study [19]. The nature of the band gap is indirect. This is attributed to the occurrence of the VBM at the high symmetry point X and the CBM at the T–Z line in the

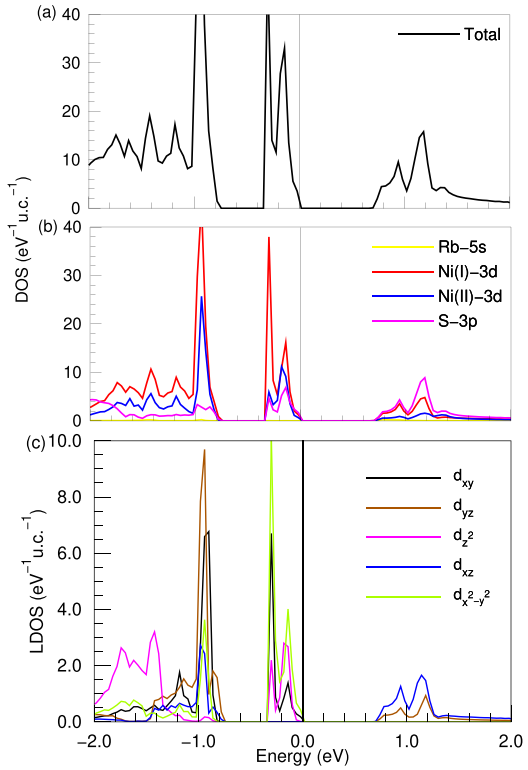

Figure 2. Total, partial and local DOS of $Rb_2Ni_3S_4$. (a) Total DOS. (b) partial DOS. (c) Projected local DOS for Ni(I)-3*d*. The vertical solid line at zero energy denotes E_F.

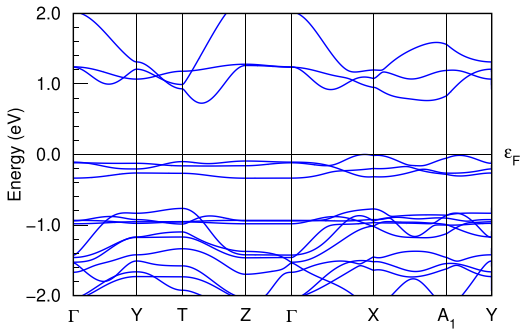

Figure 3. Electronic band structure of $Rb_2Ni_3S_4$. The horizontal solid line at zero energy denotes E_F.

momentum space (see figure 3). Additionally, the kagome lattice of Ni^{2+} leads to the formation of flat bands below E_F, which are largely comprised of the Ni-3*d* orbitals. Theoretical studies have suggested that such flat band systems in a kagome lattice can give rise to various exotic many-body phenomena when E_F is proximal to them [19, 28–30].

3.2. Optical properties

In order to understand the optical behavior of $Rb_2Ni_3S_4$, we perform the optical calculations. The linear response of the system to electromagnetic radiation is associated to the interaction of photons with electrons. This relation can be defined using the complex dielectric function, $\epsilon(\omega)$ as follows:

$$\epsilon(\omega) = \epsilon_1(\omega) + i\epsilon_2(\omega) \tag{1}$$

where, ϵ_1 and ϵ_2 are the real and imaginary part of the dielectric function, respectively [31, 32]. In accordance with the selection criteria, the momentum matrix elements between the occupied and unoccupied state are used to calculate the imaginary component of the dielectric function ϵ_2, given by

$$\epsilon_2(\omega) = \frac{4\pi^2 e^2}{m^2\omega^2 V}\sum_{g,g'} |< kg|p|kg' >|^2 \delta(E_{kg} - E_{kg'} - \hbar\omega) \tag{2}$$

where, V is the volume of the unit cell, and p is the momentum operator [33, 34]. Here, E_{kg} is the eigenvalue (approximated to the GGA eigenvalues) associated with eigenfunction $|kg>$. Likewise, the real part of dielectric function ϵ_1 is given by the Kramers–Kronig relation [35] as

$$\epsilon_1(\omega) = 1 + \frac{2}{\pi}\int \frac{\epsilon_2(\omega')\omega'}{(\omega')^2 - \omega^2} \mathrm{d}\omega'. \tag{3}$$

Additionally, the optical conductivity σ and electron loss function L are given by

$$\sigma(\omega) = \frac{-i\omega(\epsilon(\omega) - 1)}{4\pi} \tag{4}$$

$$L(\omega) = \frac{\epsilon_2}{\epsilon_1^2(\omega) + \epsilon_2^2(\omega)}. \tag{5}$$

We utilized these equations for the optical property calculations of $Rb_2Ni_3S_4$. As observed from the electronic band structure calculations, $Rb_2Ni_3S_4$ is found to be semiconductor with a band gap of ∼0.67 eV. Thus, when this material is exposed to an incident photons, transitions of electrons are expected. In such transitions, photon excites the electrons from an occupied states in the valence region to the unoccupied states in the conduction region (also called interband transition) [36]. To understand these phenomena, we consider the polarization components along x, y, and z directions as our material is orthorhombic in nature. We analyze the real part of the dielectric function $\epsilon_1(\omega)$ [37], as depicted in figure 4(a) which gives rise to electronic polarizability of the material under an applied electric field. $\epsilon_1(\omega)$ along x,y and z direction are denoted by ϵ_{1xx}, ϵ_{1yy}, and ϵ_{1zz}, respectively. The real part of the dielectric function $\epsilon_1(\omega)$ at zero frequency, which is connected to the material's band gap (also known as static dielectric constants $\epsilon_1(0)$), are found to be ∼7.5 along both the x and y directions, while the value along the z direction is ∼6.2. This corresponds to the refractive index which can be determined using the established Penn Relation $n(0) = \sqrt{\epsilon_1(0)}$ [38]. This give rise to the static refractive index value of 2.74 along x and y direction while 2.49 along z direction, respectively. The obtained value shows that the material has optical anisotropy. In the energy range 0 to 1.3 eV for the x, y direction, and 0 to 1 eV for the z direction, we observe a gradual increase in $\epsilon_1(\omega)$, which

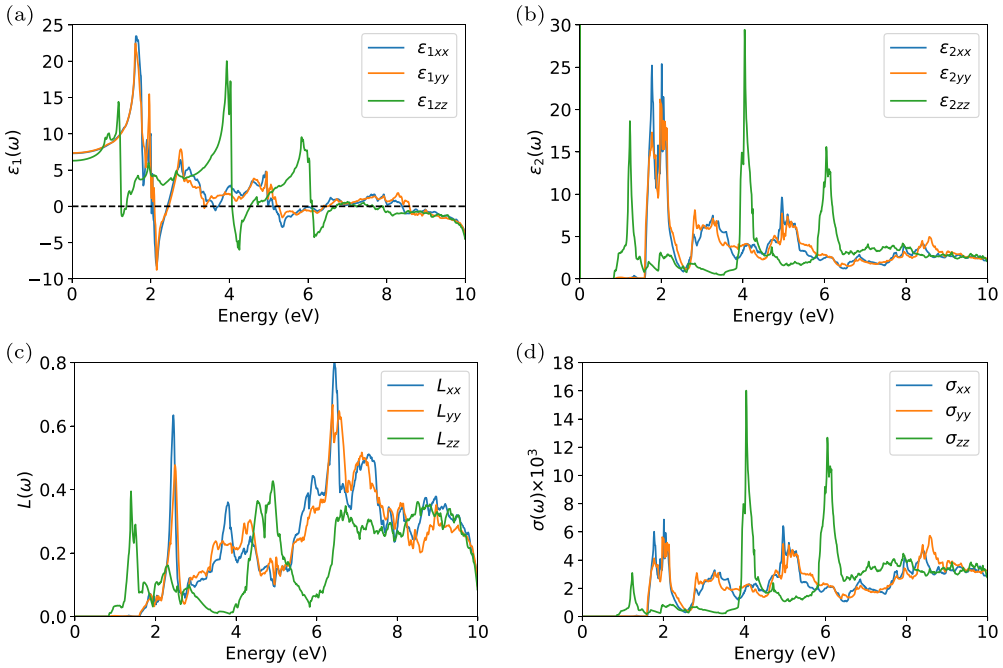

Figure 4. Optical properties of $Rb_2Ni_3S_4$. (a) real part of the dielectric function $\epsilon_1(\omega)$. (b) Imaginary part of the dielectric function $\epsilon_2(\omega)$. (c) Energy loss spectrum L(ω). (d) Optical conductivity $\sigma(\omega)$ [in Ohm^{-1}cm^{-1}].

indicates that the material interaction effectively with photons. Notably, at 1.63 eV, 1.60 eV, and 1.16 eV for ϵ_{1xx}, ϵ_{1yy}, and ϵ_{1zz}, respectively, sharp peaks are observed. These peaks correspond to the inter-band transition, indicating the photon-induced electron transitions from occupied valence bands to the unoccupied conduction bands. This means that the material can absorb light particularly well at that specific energy.

When the photon energy range exceeds 1.16 eV, the real part of the dielectric function $\epsilon_1(\omega)$ exhibits a remarkable characteristic: it adopts a negative value. This phenomenon is indicative of incident light being reflected by the medium. Consequently, the material demonstrates metallic attributes in this specific energy range [39, 40]. Furthermore, we also observe sharp peaks at approximately 2.01 eV, 1.96 eV, and 3.93 eV for x, y and z direction, respectively. $\epsilon_2(\omega)$, the imaginary part of the dielectric function, reveals details about optical absorption in crystal. The absorption begins at 0.84 eV for the imaginary part of the dielectric function, which acts as the threshold energy associated with the occurrence of an optical band gap (see figure 4(b)). Beyond the threshold point, the curve increases rapidly. Notably, sharp peaks are seen along the x, y, and z directions, respectively, at 2.02 eV, 1.97 eV, and 1.22 eV. These absorption peaks may clearly be associated with transitions from the Ni (3d) valence band to the S(3p) conduction band based on the predicted PDOS (see figure 2(b)). Additionally, within the energy range of 2.83 eV to 6.05 eV, various significant peaks are observed. These peaks correspond to inter-band transitions from the valence band to the conduction band [41, 42]. However, beyond the energy of 6.05 eV, the peaks begin to diminish, eventually disappearing at higher energy ranges.

Another important optical property calculated in this work is the electron energy loss function L(ω). Figure 4(c) shows the variation of L(ω) with photon energy. The L(ω) provides the information about the energy loss of a fast-moving electron traversing in the material, and is reciprocal of the imaginary part of the complex dielectric function [43, 44]. The visible area of the loss spectrum exhibits a slight energy loss, which rises as photon energy increases. The identified peaks in the L(ω) spectra provide information about the material's plasma frequency. Whether a material exhibits metallic properties or dielectric behavior is described by the plasma frequency. Materials exhibit metallic [$\epsilon_1(\omega) < 0$] behavior below the plasma resonance frequency and dielectric [$\epsilon_1(\omega) > 0$] behavior above this frequency [40, 45–47]. The maxima in L_{xx}, L_{yy}, and L_{zz} are clearly visible in the energy loss spectra at approximately 6.44 eV, 6.41 eV, and 4.91 eV, respectively. The resonant energy loss is seen at 6.44 eV along x direction with a maximum value of 0.8. After these peaks, the spectrum starts to decline. Figure 4(d) shows the optical conductivity which depends on photon energy. This indicates that the $Rb_2Ni_3S_4$ exhibits optical activity in the range from 1.25 eV to 8.60 eV. The $\sigma(\omega)$ edge starts 0.84 eV, which corresponds to the calculated optical band gap of the material, and numerous peaks are observed in the spectrum. The maximum optical conductivity, σ_{xx}, σ_{yy} and σ_{zz} was found to be 6.5×10^3 Ohm^{-1}cm^{-1}, 16×10^3 Ohm^{-1}cm^{-1} and 5.9×10^3 Ohm^{-1}cm^{-1}, respectively, at a photon energy of 2.02 eV to 4.05 eV. These findings are consistent with the imaginary part of the dielectric function (figure 4(b)).

4. Conclusions

We have investigated the electronic structure and optical properties of $Rb_2Ni_3S_4$ by means of density functional theory approach. The studied material is found to be a non-magnetic semiconductor with an indirect band gap of $\sim$0.67 eV. The Ni atoms form a kagome lattice in a two-dimensional plane resulting in a flat band located below the Fermi energy. From the optical properties calculations, the dielectric function including its real and imaginary parts, the loss function, and the optical conductivity has been obtained. We found that the material is optically active in the visible and lower ultraviolet region. We thus predict that $Rb_2Ni_3S_4$ could be a possible candidate for optoelectronics similar to some reported materials [48, 49].

Data availability statement

All data that support the findings of this study are included within the article (and any supplementary files).

Acknowledgments

This work was supported by a grant from UNESCO-TWAS and the Swedish International Development Cooperation Agency (SIDA) (award no. 21-377 RG/PHYS/AS G). The views expressed herein do not necessarily represent those of UNESCO-TWAS, SIDA or its Board of Governors. This work is supported also by the Brain Pool program (No. RS-2023-00304344), "Regional Innovation Strategy (RIS)" (No. 2023RIS-009) and the National Research Foundation of Korea (NRF-2023K2A9A1A01098919). M P G thanks the University Grants Commission, Nepal for the Collaborative Research Grants (Award No. CRG-78/79 S&T-03), and acknowledges IFW-Dresden for providing the large-scale compute nodes to Tribhuvan University for scientific computations. G B A thanks Nepal Academy of Science

and Technology (NAST) for the PhD fellowship. The author thanks Manuel Richter, IFW-Dresden for careful reading of the manuscripts and suggestions. M P G and G B A thanks Ulrike Nitzsche for the technical assistance.

ORCID iDs

Se-Hun Kim https://orcid.org/0000-0002-1695-7259
Madhav Prasad Ghimire https://orcid.org/0000-0003-2783-4008

References

[1] Bronger W, Rennau R and Schmitz D 1991 *Z. Anorg. Allg. Chem.* **597** 27–32
[2] Kang M *et al* 2020 *Nat. Mater.* **19** 163–9
[3] Chen D, Le C, Fu C, Lin H, Schnelle W, Sun Y and Felser C 2021 *Phys. Rev.* B **103** 144410
[4] Liu E *et al* 2018 *Nat. Phys.* **14** 1125–31
[5] Ghimire M P, Facio J I, You J S, Ye L, Checkelsky J G, Fang S, Kaxiras E, Richter M and van den Brink J 2019 *Phys. Rev. Res.* **1** 032044
[6] Yang H, Sun Y, Zhang Y, Shi W J, Parkin S S and Yan B 2017 *New J. Phys.* **19** 015008
[7] Kübler J and Felser C 2018 *Europhys. Lett.* **120** 47002
[8] Liu J and Balents L 2017 *Phys. Rev. Lett.* **119** 087202
[9] Ren Z *et al* 2022 *npj Quantum Mater.* **7** 109
[10] Naher M, Ali M A, Hossain M, Uddin M and Naqib S 2023 arXiv:2304.07669
[11] He W, Ma X, Jiang J, Wu X and Zhang J 2022 *J. Mater. Chem.* **10** 18393–403
[12] Bouhmouche A, Jabar A, Rhrissi I and Moubah R 2024 *Mater. Sci. Semicond. Process.* **175** 108238
[13] Li Q, Wu Y, Fan X, Zhang Y J, Zhu X, Zhu Z, Li Y and Wen H H 2022 *Phys. Rev.* B **106** 214501
[14] Elder S H, Jobic S, Brec R, Gelabert M and DiSalvo F J 1996 *J. Alloys Compd.* **235** 135–42
[15] Acharya G B, Belbase B P and Ghimire M P 2023 *Electr. Struct.* **5** 045008
[16] Bronger W, Eyck J, Rüdorff W and Stöussel A 1970 *Z. Anorg. Allg. Chem.* **375** 1–7
[17] Kato T, Hondou K and Iio K 1998 *J. Mag. Mag. Mater.* **177–181** 591–2
[18] Fukamachi T, Kobayashi Y, Nakamura A, Harashina H and Sato M 1999 *J. Phys. Soc. Japan* **68** 3668–72
[19] Hondou K, Fujiwara Y, Kato T, Iio K, Saiki A, Usuda M and Hamada N 2002 *J. Alloys Compd.* **333** 274–81
[20] Nawai S, Okazaki K, Mizokawa T, Fujimori A, Hondou K, Fujiwara Y, Iio K, Usuda M and Hamada N 2004 *Phys. Rev.* B **69** 045103
[21] Hondou K and Chikazawa S 2007 *J. Magn. Magn. Mater.* **310** 1815–7
[22] Kohn W and Sham L J 1965 *Phys. Rev.* **140** A1133
[23] Koepernik K and Eschrig H 1999 *Phys. Rev.* B **59** 1743
[24] Perdew J P, Burke K and Ernzerhof M 1996 *Phys. Rev. Lett.* **77** 3865
[25] Blaha P *et al* 2001 *WIEN2k: An Augmented Plane Wave Plus Local Orbitals Program for Calculating Crystal Properties*vol 60 (Universitat Wien, Institut fur Physikalische und Theoretische Chemie)
[26] Lejaeghere K *et al* 2016 *Science* **351** aad3000
[27] Dehnicke K and Kniep R 2003 *Zeit. Anorg. Allgem. Chem.* **629** 727–8
[28] Kang M *et al* 2020 *Nat. Commun.* **11** 1–9
[29] Wang W S, Li Z Z, Xiang Y Y and Wang Q H 2013 *Phys. Rev.* B **87** 115135
[30] Yu S L and Li J X 2012 *Phys. Rev.* B **85** 144402
[31] He H, Orlando R, Blanco M A, Pandey R, Amzallag E, Baraille I and Rérat M 2006 *Phys. Rev.* B **74** 195123
[32] Ghosh A and Thangavel R 2017 *Ind. J. Phys.* **91** 1339–44
[33] Ambrosch-Draxl C and Sofo J O 2006 *Comput. Phys. Commun.* **175** 1–14
[34] Launay M, Boucher F and Moreau P 2004 *Phys. Rev.* B **69** 035101–10
[35] Toll J S 1956 *Phys. Rev.* **104** 1760
[36] Stepanjuga A, Ray R, Richter M, Carrocci S, Hampel S, Galle L, Grafe H J and Valldor M 2022 *New J. Chem.* **46** 4900–10
[37] Hoat D, Silva J R and Blas A M 2019 *J. Solid Stat. Chem.* **270** 85–91

[38] Penn D R 1962 *Phys. Rev.* **128** 2093
[39] Shore A 2019 *RSC Adv.* **9** 12813
[40] Kumar M, Raj A, Kumar A, Sharma S, Bherwani H, Gupta A and Anshul A 2021 *Optik* **242** 166764
[41] Kumar A and Ahluwalia P 2012 *Mater. Chem. Phys.* **135** 755–61
[42] Belbase B P, Jaishi D R, Adhikari R P and Ghimire M P 2023 *Sol. Stat. Commun.* **361** 115085
[43] Wang C and Klein B 1981 *Phys. Rev.* B **24** 3417
[44] Zhang X, Chen Z, Zhang S, Liu R, Zong H, Jing Q, Li G, Ma M and Wang W 2007 *J. Phys.: Condens. Matter* **19** 425231
[45] Hu J M, Huang S P, Xie Z, Hu H and Cheng W D 2007 *J. Phys.: Condens. Matter* **19** 496215
[46] Kumar P, Soni A, Bhamu K and Sahariya J 2017 *Mater. Res. Bull.* **86** 131–8
[47] Sun J, Zhou X F, Fan Y X, Chen J, Wang H T, Guo X, He J and Tian Y 2006 *Phys. Rev.* B **73** 045108
[48] Celep G *et al* 2004 *Phys. Rev.* B **70** 165409
[49] Adachi S, Kimura T and Suzuki N 1993 *J. Appl. Phys.* **74** 3435–41

Electronic structure, optical properties and defect induced half-metallic ferromagnetism in kagome $Cs_2Ni_3S_4$

IOP Publishing Electron. Struct. 5 (2023) 045008 https://doi.org/10.1088/2516-1075/ad0951

Electronic Structure

PAPER

Electronic structure, optical properties and defect induced half-metallic ferromagnetism in kagome $Cs_2Ni_3S_4$

RECEIVED
3 July 2023

REVISED
13 October 2023

ACCEPTED FOR PUBLICATION
2 November 2023

PUBLISHED
16 November 2023

Gang Bahadur Acharya[1,2], **Bishnu Prasad Belbase**[3] **and Madhav Prasad Ghimire**[1,2,*]

[1] Central Department of Physics, Tribhuvan University, Kirtipur, 44613 Kathmandu, Nepal
[2] Leibniz Institute for Solid State and Materials Research—IFW Dresden, Helmholtzstr. 20, 01069 Dresden, Germany
[3] Department of Physics and Astronomy, Purdue University, West Lafayette, IN 47907, United States of America
[*] Author to whom any correspondence should be addressed.

E-mail: madhav.ghimire@cdp.tu.edu.np

Keywords: density functional theory, electronic structure, semiconductor, optical properties, optoelectronic applications

Abstract

Recent research focuses on electronic structure of kagome materials due to their fascinating properties such as topological insulators, Dirac semimetals, and topological superconductors. Materials with sizable electronic band gap are found to play vital role in device applications. Here, by means of density functional theory calculations, we study the electronic and optical properties of ternary transition metal sulphide $Cs_2Ni_3S_4$ by using the full potential local orbital code. Standard generalized gradient approximation (GGA) has been employed to consider the electron exchange and correlation effect, and modified Becke–Johnson (mBJ) potential has been used to obtain the accurate band gap of the material. From our electronic structure calculations $Cs_2Ni_3S_4$ is found to be nonmagnetic semiconductor with an indirect band gap of $\sim$1.4 eV within GGA + mBJ calculations. The structural analysis demonstrates that Ni atoms form a kagome lattice in a two-dimensional plane, resulting in the presence of a dispersionless flat band located below the Fermi energy. From the optical calculations, analyzing the dielectric function, loss function, and optical conductivity, $Cs_2Ni_3S_4$ is found to be optically active in the visible as well as lower ultraviolet energy ranges. This suggests that $Cs_2Ni_3S_4$ may be a suitable candidate for the opto-electronic devices. Additionally, this work may provides a foundation for the development of opto-electronic device and a framework for experimental work. We additionally investigated the effect of vacancy defects in $Cs_2Ni_3S_4$ to see it's influence on the electronic and magnetic properties. Interestingly, the Cs-vacancy defect give rise to half-metallic ferromagnetism with an effective magnetic moment of $1\mu_B$ per unit cell.

1. Introduction

In condensed matter physics, the structure with kagome lattice refers to a 2D arrangement consisting of interconnected triangles [1]. This lattice is constructed by utilizing the vertices and edges of a tri-hexagonal tiling, where each hexagon is surrounding by triangles [2]. Mineral jarosite is the first kagome compound which has been experimentally found [3]. The kagome lattice exhibits interesting electronic properties due to its unique geometric arrangement [4–19]. The family of ternary transition metal chalcogenides, represented by the formula $A_2M_3X_4$ (where A are K, Rb, Cs; M are Ni, Pd, Pt; and X are S, Se), is commonly found to exhibit various crystal symmetries [20]. These include orthorhombic symmetry with space groups *Fmmm* (SG No. 69), *Fddd* (SG No. 70) [20], hexagonal $P6_3/mmc$ (SG No. 194) [21], and monoclinic *C/2m* (SG No. 12) [22]. These compounds possess a quasi-2D layered structure, wherein the transition metal elements form kagome nets alongside chalcogenide atoms. Despite the potential of this family, only a few compounds have been studied for their electronic properties. For example, on the basis of density functional theory (DFT) calculations $Rb_2Ni_3S_4$ is predicted to be a band insulator, featuring flat bands just below the Fermi level (E_F) [23, 24]. Photemission spectroscopy investigations have revealed moderate electron correlation and strong hybridization between Ni-3d and S-3p orbitals, consistent with the band structure calculations [25].

Magnetic and electric transport measurements have confirmed that $Rb_2Ni_3S_4$ is a non-magnetic insulator [26].

In one notable study, Li *et al* [27] recently reported the observation of superconductivity in kagome $Rb_2Pd_3Se_4$ by pressure-induced Lifshitz transition. Recently, by means of DFT calculations, $Rb_2Mn_3S_4$ and $K_2Mn_3S_4$ found magnetic semiconducting materials [28, 29]. This finding suggests that the $A_2M_3X_4$ family has potential for exploring superconducting properties, but further investigations are needed to deepen our understanding in this family. Till date, very less kagome compounds in this family are explored as a semiconductors. Additionally, regarding the investigation of optical characteristics in a kagome lattice, a three-dimensional (3D) elemental carbon kagome lattice was examined. This lattice demonstrates a transition from a metallic state to a direct-gap semiconductor in the visible blue range and comparable to those of other direct-gap semiconductors such as GaN and ZnO [30]. Through the use of DFT calculations, it was predicted recently that the optical properties of kagome CsV_3Sb_5 make it a efficient absorber of ultraviolet radiation. Furthermore, this compound exhibits strong reflectivity for visible light [31].

Optical properties in a band gap semiconductor play a significant role in the development of diverse applications, including display devices, lasers, sensors, photo-electrodes, photonics, photo-detectors, and solar cells. Considering the significance of optical anisotropy in the design of optical devices such as LCD screens, 3D movie screens, polarizers, and wave plates, it becomes essential to study and understand this phenomenon [32]. Our study thus focuses on exploring the electronic and optical properties of $Cs_2Ni_3S_4$ which was synthesized [21]. But its electronic and optical properties are not reported till date. On the basis of DFT calculations, we have systematically investigated the electronic and optical properties of $Cs_2Ni_3S_4$ and predict that it is a nonmagnetic semiconductor with an indirect band gap.

Moreover, due to the strong localization of electrons the flat band is observed below the E_F. From the optical properties calculation, our system is found to be optically active in the visible and lower ultraviolet region.

2. Computational and structural details

We have performed the DFT calculation with a localized atomic basis and a full potential treatment using the full potential local orbital (FPLO) code [33]. We utilized the Perdew, Burke, and Ernzerhof's generalized gradient approximation (GGA) functional known as (PBE-96) [34], as well as the mBJ potential developed by Tran and Blaha [35], which provides improved treatment of energy band gaps compared to standard semi-local GGA functional that tend to underestimate them. For the GGA and GGA + mBJ calculations, we use FPLO version 18.00-52 and 22.00-64, respectively. In the Brillouin zone, we consider k-mesh subdivision of $20 \times 20 \times 20$ for electronic properties and $36 \times 36 \times 36$ for optical properties calculation. We calculate dielectric function, loss function and optical conductivity by using FOPTICS module of the FPLO [33]. A total of twenty two empty bands were included in the dielectric calculations for up to 10 eV photon energy. We set the energy and force convergence criteria to be 10^{-8} Hartree and 10^{-3} eV Å^{-1}, respectively. To construct the crystal structure, we utilized the VESTA software [36].

$Cs_2Ni_3S_4$ crystallizes in the hexagonal structure with space group $P6_3/mmc$ (no. 194) and the point group D_{6h}. A total of four in-equivalent atoms such as Cs, Ni, S(I) and S(II) are present with the charge state of Cs^{1+} ions bonded to seven S^{2-} atoms, forming distorted edge-sharing CsS_7 hexagonal pyramids. Among these bonds, there are six shorter Cs–S bond lengths measuring 3.53 Å, while one bond is longer, measuring 3.74 Å. The Ni^{2+} ions are bonded in a square co-planar arrangement to four S^{2-} atoms. Two of the Ni–S bond lengths are shorter, measuring 2.20 Å, while the other two bonds are longer, measuring 2.21 Å. The crystal structure contains two distinct S^{2-} sites denoted by S(I) and S(II). The experimental lattice parameters used in this study are $a = b = 5.841$ Å, and $c = 15.109$ Å, with lattice angles $\alpha = \beta = 90°$ and $\gamma = 120°$ [21]. Table 1 illustrates their fully relaxed atomic cordinates. Because fractional Bravais lattice vector translation and point group symmetry are combined, $Cs_2Ni_3S_4$ has a nonsymmorphic crystal symmetry. Due to the center of inversion, it is also a centrosymmetric crystal material.

3. Results and discussion

3.1. Electronic properties

We start with the calculation of the total energy to determine the ground state of $Cs_2Ni_3S_4$. We performed the total energy calculations for non-magnetic and ferromagnetic configuration. The total energy is found to be lowest for nonmagnetic dictating the ground state of the material. With a charge state of Cs^{1+}, Ni^{2+}, and S^{2-} the valence electronic states are Cs-$6s^1$, Ni-$3d^8 4s^2$, and S-$3s^2 3p^4$, respectively.

Table 1. Total number of inequivalent atoms and their Wyckoff positions in a $Cs_2Ni_3S_4$.

Atom	Point location	x	y	z
Cs	4f	1/3	−1/3	−0.409
Ni	6h	1/6	1/3	1/4
S(I)	4e	0	0	0.154
S(II)	4f	1/3	−1/3	0.154

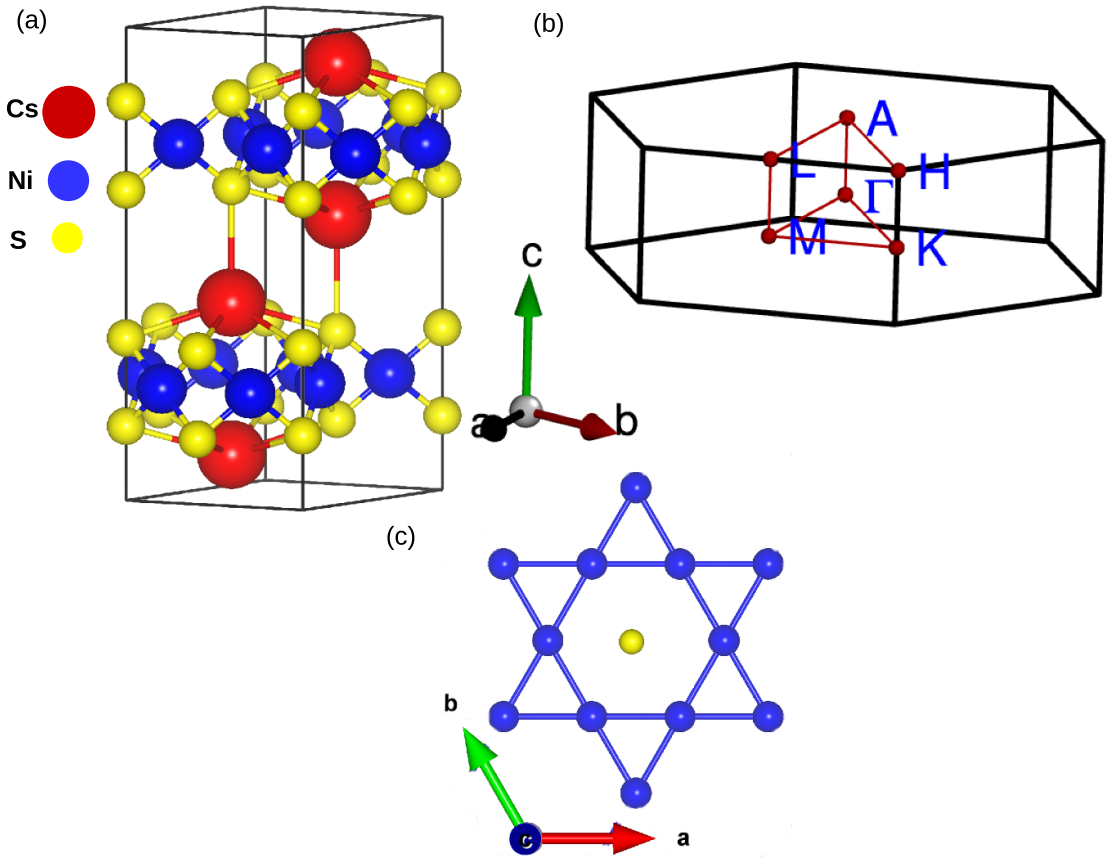

Figure 1. (a) Crystal structure of $Cs_2Ni_3S_4$. (b) 3D bulk Brillouin zone, the red dots and red lines indicate the high-symmetry point and high-symmetry line, respectively. (c) Ni-ions constitute a kagome lattice in *ab* plane.

In $Cs_2Ni_3S_4$, each Ni atom is surrounded by four S atoms, forming a square planar coordination geometry. The presence of sulfur as a strong field ligand influences the electronic structure of the system, resulting in the compound adopting a low spin state [24].

From the total density of states (DOS) and partial DOS shown in figure 2, $Cs_2Ni_3S_4$ is found to be semiconducting with a band gap of ∼0.8 eV (∼1.4 eV) between the top of the valence band and bottom of the conduction band within GGA (GGA + mBJ). As mBJ functional is reported to appropriately describe the semiconducting behaviour of non-magnetic systems [35], we will thus focus discussing our results obtained with the mBJ. From the partial DOS contributions from Cs-6s, Ni-3d, and S-3p orbitals shown in figure 2(b), the Ni-3d states have a significant contribution in the valence and conduction region hybridizing with the S-3p states. Two in-equivalent S atoms is found to exhibit similar features overlapping with each other. For a detailed study on the electronic properties, the projection of local DOS has been considered which shows clearly depicts the hybridization between Ni-3d and S-3p states (see figure 3). The study of the projection of the local DOS for Ni-3d and S-3p states, reveals the insulating state to arise due to crystal field splitting. As discussed earlier, each Ni ion is surrounded by four S ions, constituting a tetrahedral square planar coordination (see figure 1(a)). In this situation S^{2-} acts as a strong ligand to central metal Ni^{2+}, resulting in the crystal field splitting. This leads to the occupancy of some of the t_{2g} orbitals (d_{xy}, d_{yz}, d_{xz}), having energy levels higher compared to Ni-e_g state(i.e. $d_{x^2-y^2}$, and d_z^2). Furthermore, a strong hybridization between the S-3p_x, S-3p_y, S-p_z is noticed with the Ni-d_{yz}, d_{xz} orbitals above E_F within an energy range of 1.4–1.8 eV, while below E_F, S-3p_x, S-3p_y hybridize with the Ni-3d_{xy}, $d_{x^2-y^2}$ and d_z^2 orbitals within 0–0.45 eV. Additionally, the kagome lattice of Ni^{2+} leads to the formation of flat bands below E_F, which is mainly contributed by the

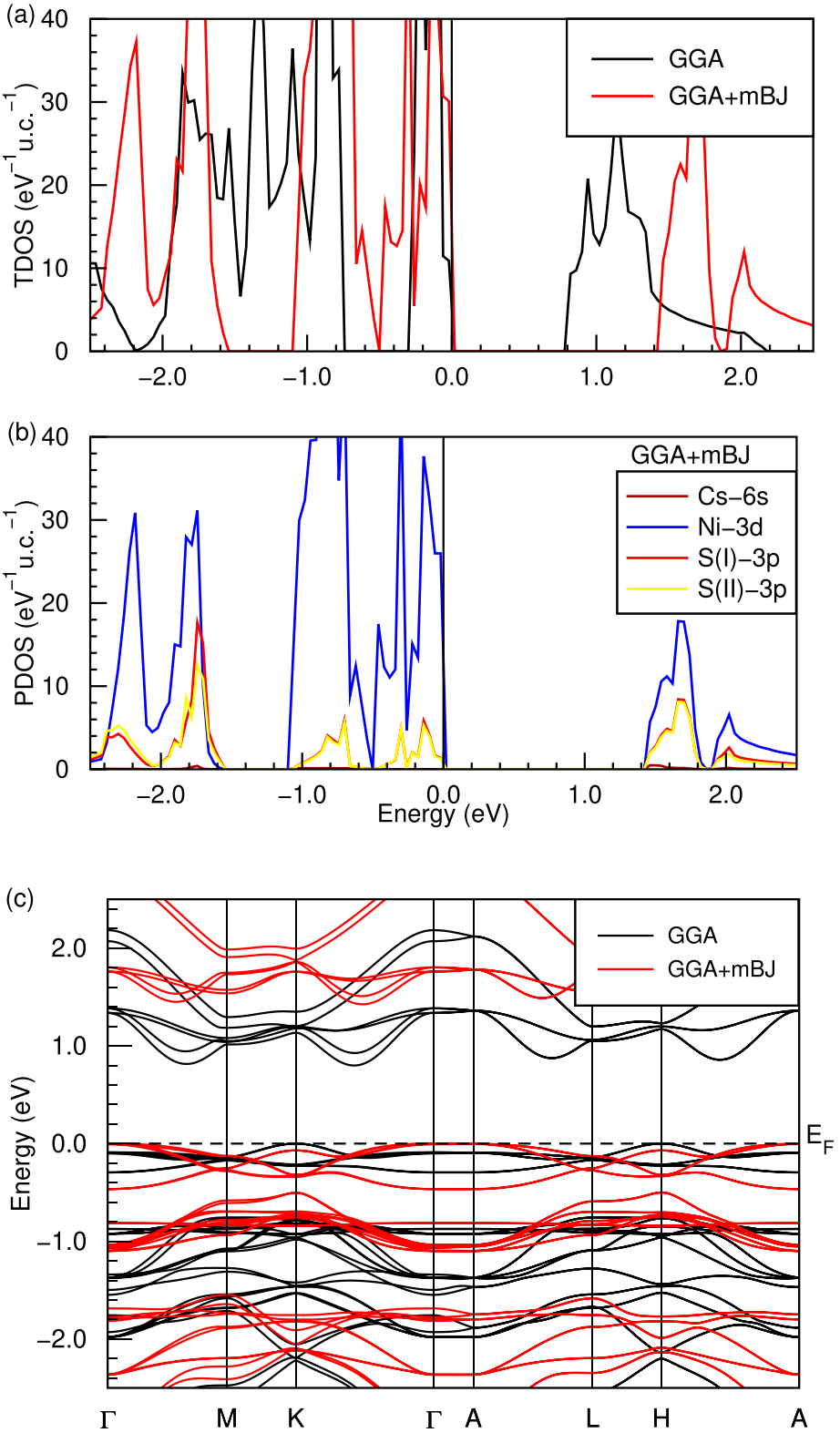

Figure 2. The DOS and electronic band structure of $Cs_2Ni_3S_4$: (a) total DOS within GGA and GGA + mBJ; (b) partial DOS within GGA + mBJ. The vertical solid line represents E_F; (c) electronic band structure in scalar relativistic mode within GGA and GGA + mBJ calculations. The horizontal dashed line at zero energy denotes E_F.

3d-orbitals of $d_{x^2-y^2}$ and d_{xy} of Ni atom. Theoretical studies have suggested that such flat band systems in a kagome lattice can give rise to various exotic many-body phenomena [7, 23, 24, 37–39].

From the electronic band structure calculation shown in figure 2(c), $Cs_2Ni_3S_4$ is found to be an indirect band gap semiconductor. The indirect band gap arises between the top of the valence band at the high symmetry point K, and the bottom of the conduction band along the K–Γ in the momentum space (see

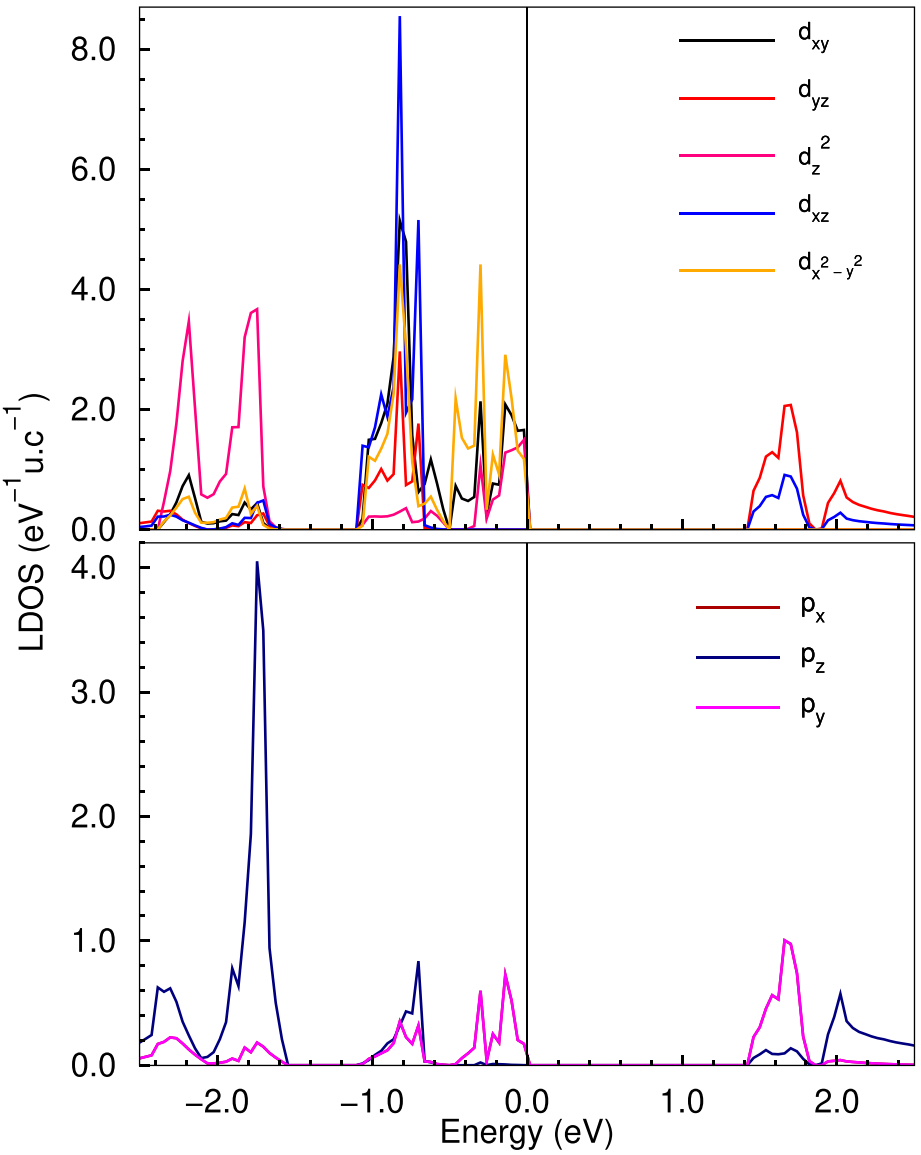

Figure 3. The projection of local DOS of Ni-3d and S-3p orbitals in $Cs_2Ni_3S_4$ within GGA + mBJ calculation.

figure 2(c)). With GGA + mBJ taken into account, the electronic band gap rises to ∼1.4 eV [35] Another important feature we observed is the presence of a dispersionless band (commonly referred to as a flat band) below E_F (see figure 2(c)) which exist usually in a kagome lattice layers [7, 23, 24]. Here, the flat band primarily consist of Ni-3d orbitals hybridizing with S-3p orbitals.

3.2. Effect of vacancy defect

Vacancy defects plays significant role in materials science. They provide a systematic approach to change the physical characteristics of materials, which significantly influence their ability for practical applications [40, 41]. We have considered vacancy defect in $Cs_2Ni_3S_4$ at the Cs-site. $Cs_2Ni_3S_4$ consists of two-formula unit with a total of 18 atoms in a unit cell. As shown in figure 4, there are four Cs atoms in the parent material. By removing one Cs atom from the Cs-site we create a vacancy defect in the system (see figures 4(c)–(f)). This corresponds to 25% vacancy at one of the Cs-site and 5.56% vacancy defect in $Cs_2Ni_3S_4$.

We performed DFT calculations for all the four defected structures (say D1, D2, D3, and D4) in nonmagnetic and ferromagnetic configurations. The total energy was found to be lowest for the optimized D4 structure with ferromagnetic ground state. The total energy of non-magnetic configuration was found to be 23.93 meV higher than the ferromagnetic state. Our calculation demonstrates that introducing a vacancy opens the possibility of adjusting magnetization leading to an effective magnetic moment of 1 μ_B per unit cell. From the electronic DOS and band structure calculation, as shown in figure 5, the vacancy defect

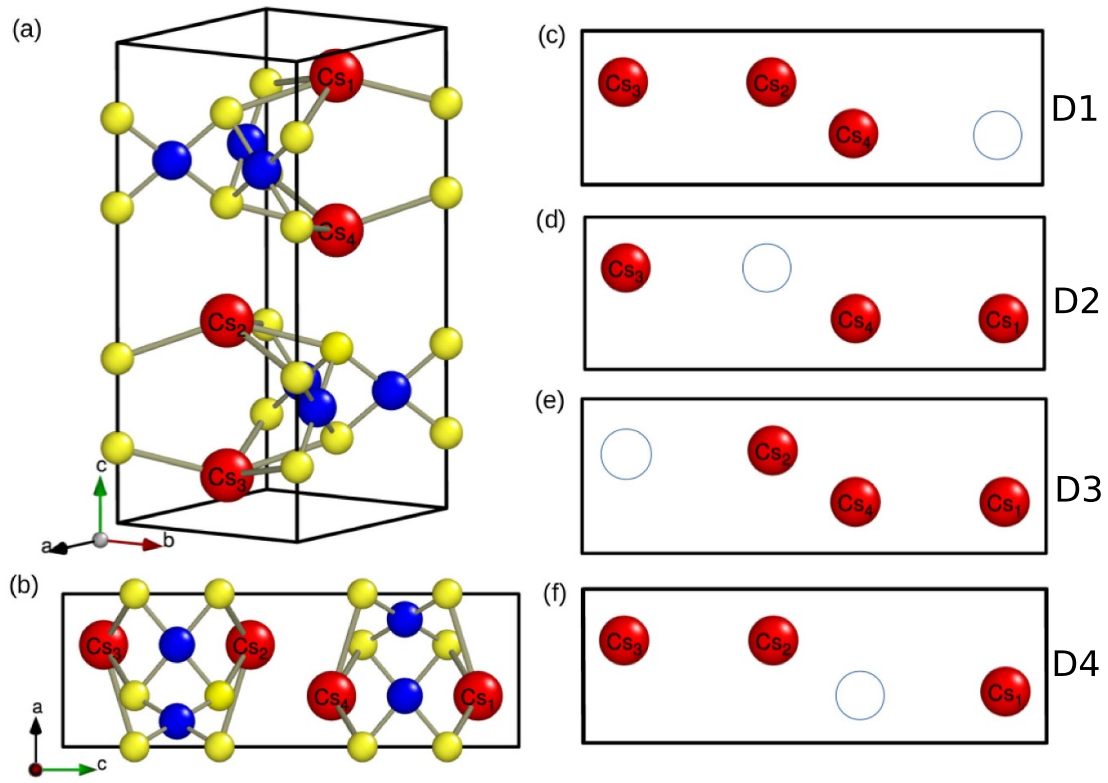

Figure 4. Crystal structure of $Cs_2Ni_3S_4$ in (a) 3D and (b) 2D view; (c)–(f) Vacancy defects at different sites by removing Cs atoms. Open circles represent the removal of Cs atom.

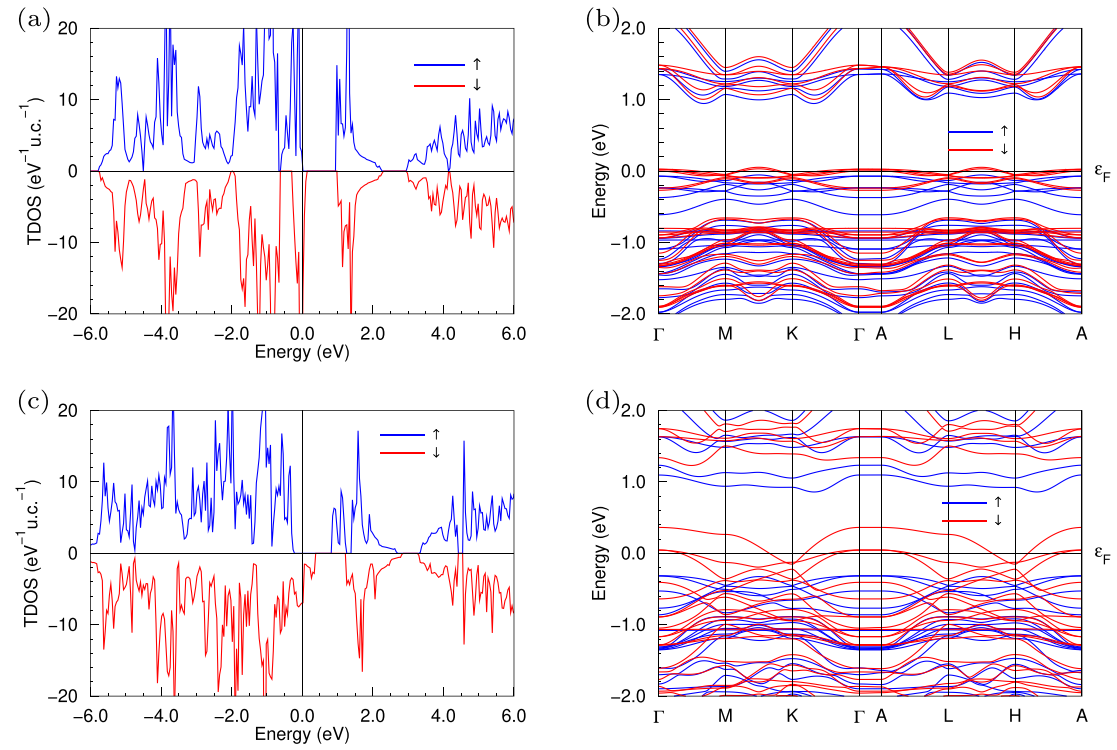

Figure 5. (a), (c) Total DOS and (b), (d) electronic band structure of defected $Cs_2Ni_3S_4$ within GGA and GGA + mBJ, respectively.

$Cs_2Ni_3S_4$ is found to exhibit half-metallic ferromagnetism. Spin-up channel shows insulating state (band gap of ∼0.9 (1.1) eV within GGA (GGA + mBJ) functionals) while spin-down channel is metallic in nature. The major contributions to the total DOS and band structure around E_F are from the Ni-3d and S-3p orbitals.

3.3. Optical properties

In this section, we discuss the optical properties of the material based on the previously discussed electronic properties of the system. The complex dielectric function provides a comprehensive description of the material's response to an electromagnetic field and is highly sensitive to the electronic band structure of the material. The dielectric function is composed of two parts, namely, the real ($\varepsilon_1(\omega)$) and imaginary ($\varepsilon_2(\omega)$) parts. These parts are associated with the interband transitions from the valence to the conduction band in semiconducting materials. The dielectric function is mathematically represented as follows:

$$\varepsilon(\omega) = \varepsilon_1(\omega) + i\varepsilon_2(\omega). \tag{3.1}$$

The imaginary component of the dielectric function is influenced by the electronic properties of the material, which can be described by the joint DOS and the momentum matrix elements connecting occupied and unoccupied states given by

$$\epsilon_2(\omega) = \frac{Ve^2}{2\pi hm^2\omega^2}\int d^3k \sum |\langle kg|p|kg'\rangle|^2 f(kg)\left[1 - f(kg')\right]\delta\left(E_{kg} - E_{kg'} - \hbar\omega\right) \tag{3.2}$$

where p denotes the momentum operator. The Fermi–Dirac distribution function is indicated by $f(kg)$, and E_{kg} is the energy eigenvalues of the states associated with the eigenfunction $|kg\rangle$.

On the other hand, the real part is obtained from the Kramer–Kronig dispersion relation [42] as

$$\varepsilon_1(\omega) = 1 + \frac{2}{\pi}\int \frac{\varepsilon_2(\omega')\,\omega'}{(\omega')^2 - \omega^2} d\omega'. \tag{3.3}$$

Dielectric function is closely related to optical conductivity $\sigma(\omega)$ and and loss function $L(\omega)$ as [43]

$$\sigma(\omega) = \frac{-i\omega(\varepsilon_2(\omega) - 1)}{4\pi} \tag{3.4}$$

$$L(\omega) = \frac{\varepsilon_2}{\varepsilon_1^2(\omega) + \varepsilon_2^2(\omega)}. \tag{3.5}$$

Since there is a significant change in the band gap after considering the mBJ potential, we discuss optical calculations within mBJ. Given the hexagonal symmetry of $Cs_2Ni_3S_4$, we limited our investigation of optical anisotropy to the x and z directions. Figure 6 illustrates the energy-dependent optical properties of the material, showing how these properties vary with direction within the energy range of 0–10 eV.

Figure 6(a) shows the real part of the dielectric function ($\varepsilon_1(\omega)$), which is related to the ability of the material to refract or transmit radiation. The x and z components are denoted by ε_{1xx} and ε_{1zz} respectively. The $\varepsilon_1(\omega)$ also plays an important role in determining the other optical properties of materials, such as refractive index, reflectivity, and transmission of light. The computed static dielectric functions, represented by $\varepsilon_{1xx}(0)$ and $\varepsilon_{1zz}(0)$, have respective values of 4.79 and 4.00, respectively. Correspondingly, $n(0) = \sqrt{\varepsilon_1(0)}$ gives static refractive index as 2.19 and 2.00 along x and z direction, indicating clear optical anisotropy. In the energy range of 0–1.8 eV and 0–1.4 eV, we observe a slow rise of $\varepsilon_1(\omega)$ in the x and z directions, respectively. Sharp peaks at ≈2.2 eV and 1.8 eV in $\varepsilon_{1xx}(\omega)$ and $\varepsilon_{1zz}(\omega)$, respectively, correspond to the first interband transition in the system. The features exhibited by the real part of the dielectric function (figure 6(a)), including the negative values, are the typical signatures of interband transitions that can be related to the maxima in the imaginary part and, to some extent, in the loss function. Additionally, we observe sharp peaks at ≈3.2 eV and 5.2 eV in $\varepsilon_{1xx}(\omega)$, and at ≈4.3 eV and 6.5 eV in $\varepsilon_{1zz}(\omega)$, which correspond to interband transitions.

In figure 6(b), the imaginary part of the dielectric function ($\varepsilon_2(\omega)$) is displayed, which characterizes the material's absorption or dissipation of radiation in response to an external electromagnetic field at a given frequency ω. It is a measure of the electronic transition strength and is closely linked to the band structure. The spectrum starts to emerge beyond 1.5 eV, resulting in an optical gap. We observe a sharp increase in $\varepsilon_2(\omega)$ at ≈2.4 eV and 1.8 eV along x and z directions, respectively, where optical response occurs and represents the energy of the initial inter-band transition between the valence band maximum and conduction band minimum. In the z direction, other significant peaks are observed at ≈4.5 eV and 6.6 eV,

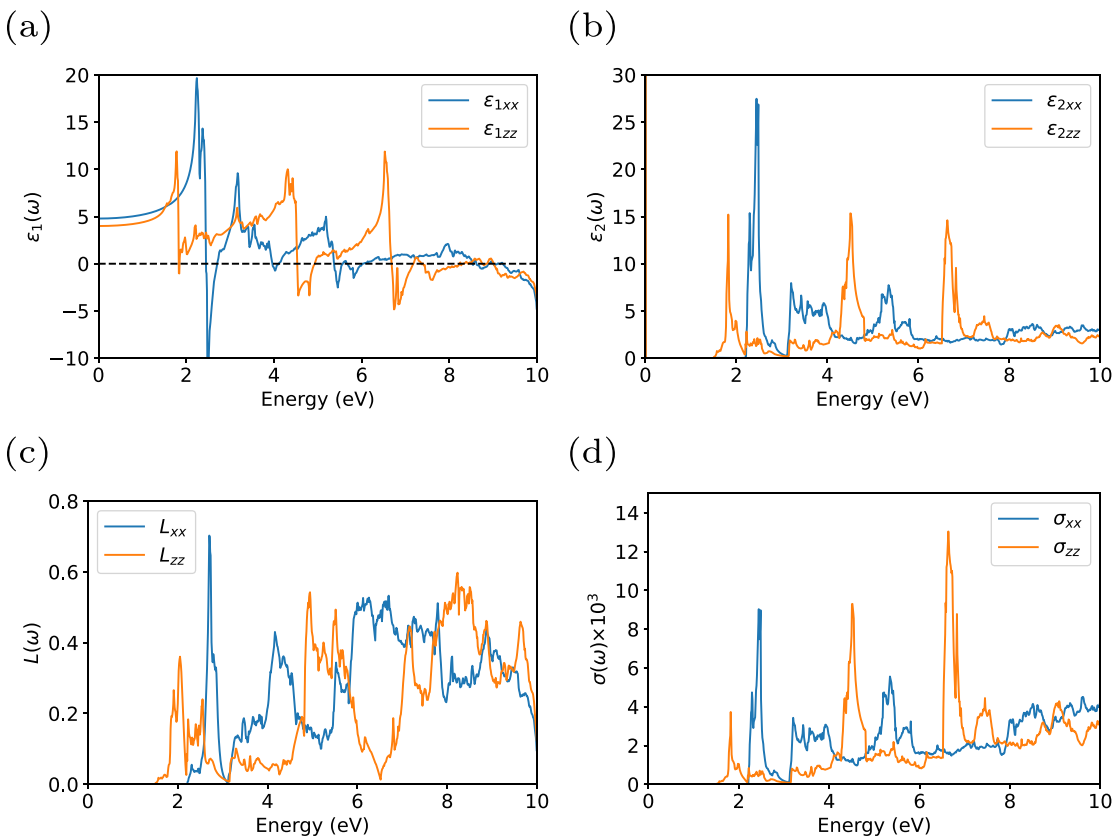

Figure 6. Optical properties of $Cs_2Ni_3S_4$ calculated within GGA + mBJ. (a) real part of the dielectric function $\epsilon_1(\omega)$. (b) Imaginary part of the dielectric function $\epsilon_2(\omega)$. (c) Energy loss spectrum L(ω). (d) Optical conductivity $\sigma(\omega)$ (in Ohm^{-1} cm^{-1}).

with smaller peaks appearing around 3.2 eV and 5.3 eV in *x* direction. These multiple peaks correspond to the interband transitions from the Ni-3d valence band to the S-3p conduction band and are consistent with the result obtained in figure 6(a). Beyond 6.6 eV, the peaks begin to decrease, eventually disappearing at higher energy ranges.

Figure 6(c) depicts the electron energy loss in correlation to photon energy. It characterizes the energy-dependent attenuation of the electric field of light as it passes through the material. Peaks begin to appear after approximately 2.2 eV and 1.8 eV along the *x* and *z* axes, respectively, suggesting photoelectron energy loss beyond that point. It is generally prominent around the plasmon energy. The most notable peak in the $L(\omega)$ spectra corresponds to the characteristic associated with the plasmon resonance, and such a peak is observed at 2.5 eV in the *x*-direction. Figure 6(d) displays the optical conductivity ($\sigma(\omega)$) as a function of energy. Peaks are noticeable around 2.5 eV, 3.2 eV, and 5.3 eV along the *x* direction, while sharp peaks can be seen around 1.8 eV, 4.5 eV, and 6.6 eV along the *z* direction. These outcomes are in agreement with the $\varepsilon_2(\omega)$ results we obtained in figure 6(b). In general, $Cs_2Ni_3S_4$ is optically active in the visible and lower ultraviolet energy ranges. Therefore, this material may be a promising candidate for optoelectronic applications. Nonetheless, it is crucial to note that precise predictions necessitate careful consideration of factors such as electron–phonon interactions, many-body effects, and disorder.

4. Summary

By means of DFT approach, we performed electronic and optical calculations on the kagome crystal $Cs_2Ni_3S_4$. From the electronic structure calculations the material is found to be an indirect band gap semiconductor. As the tuned band gap (∼1.4 eV) is found suitable for optical applications, we considered optical properties through the calculations of dielectric function, loss function, and optical conductivity. Our findings demonstrate that the material exhibits optical activity within the visible and lower ultraviolet energy range. These results suggest the potential of the $Cs_2Ni_3S_4$ system as a promising candidate for optoelectronic applications. In addition, we considered Cs-vacancy defect in $Cs_2Ni_3S_4$. The removal of one Cs atom from the system gives rise to half-metallic ferromagnetism making the material as a suitable candidate for spintronic device applications.

Data availability statement

All data that support the findings of this study are included within the article.

Acknowledgments

M P G was supported by a grant from UNESCO-TWAS and the Swedish International Development Cooperation Agency (SIDA). The views expressed herein do not necessarily represent those of UNESCO-TWAS, SIDA or its Board of Governors. M P G was also supported by University Grants Commission, Nepal with UGC grant number CRG-78/79 S&T-03. M P G acknowledges IFW-Dresden for providing the large-scale compute nodes to Tribhuvan University for scientific computations. G B A thanks Nepal Academy of Science and Technology (NAST) for the PhD fellowship. The author thanks Manuel Richter, IFW-Dresden for careful reading of the manuscripts and suggestions. M P G and G B A thanks Ulrike Nitzsche for the technical assistance.

ORCID iD

Madhav Prasad Ghimire https://orcid.org/0000-0003-2783-4008

References

[1] Ye L *et al* 2018 *Nature* **555** 638–42
[2] Ye L, Chan M K, McDonald R D, Graf D, Kang M, Liu J, Suzuki T, Comin R, Fu L and Checkelsky J G 2019 *Nat. Commun.* **10** 1–8
[3] Takano M, Shinjo T, Kiyama M and Takada T 1968 *J. Phys. Soc. Japan* **25** 902–902
[4] Fang S *et al* 2022 *Phys. Rev.* B **105** 035107
[5] Kang M *et al* 2020 *Nat. Mater.* **19** 163–9
[6] Han M *et al* 2021 *Nat. Commun.* **12** 1–10
[7] Kang M *et al* 2020 *Nat. Commun.* **11** 1–9
[8] Chen D, Le C, Fu C, Lin H, Schnelle W, Sun Y and Felser C 2021 *Phys. Rev.* B **103** 144410
[9] Liu E *et al* 2018 *Nat. Phys.* **14** 1125–31
[10] Ghimire M P, Facio J I, You J S, Ye L, Checkelsky J G, Fang S, Kaxiras E, Richter M and Van Den Brink J 2019 *Phys. Rev. Res.* **1** 032044
[11] Yang H, Sun Y, Zhang Y, Shi W J, Parkin S S and Yan B 2017 *New J. Phys.* **19** 015008
[12] Kübler J and Felser C 2018 *Europhys. Lett.* **120** 47002
[13] Liu J and Balents L 2017 *Phys. Rev. Lett.* **119** 087202
[14] Zhang X, Jin L, Dai X and Liu G 2017 *J. Phys. Chem.* **8** 4814–9
[15] Hao Z *et al* 2022 *Phys. Rev.* B **106** L081101
[16] Ren Z *et al* 2022 *npj Quantum Mater.* **7** 109
[17] Howlader S, Ramachandran R, Singh Y and Sheet G 2020 *J. Phys.: Condens. Matter* **33** 075801
[18] Chen P J and Jeng H T 2016 *Sci. Rep.* **6** 23151
[19] Siegfried P E, Bhandari H, Jones D C, Ghimire M P, Dally R L, Poudel L, Bleuel M, Lynn J W, Mazin I I and Ghimire N J 2022 *Commun. Phys.* **5** 58
[20] Bronger W, Rennau R and Schmitz D 1991 *Z. Anorg. Allg. Chem.* **597** 27–32
[21] Bronger W, Rennau R and Schmitz D 1988 *Z. Kristallogr. Cryst. Mater.* **183** 201–6
[22] Bronger W and Huster J 1971 *J. Less-Common Met.* **23** 67–72
[23] Hondou K, Fujiwara Y, Kato T, Iio K, Saiki A, Usuda M and Hamada N 2002 *J. Alloys Compd.* **333** 274–81
[24] Hondou K and Chikazawa S 2007 *J. Magn. Magn. Mater.* **310** 1815–7
[25] Nawai S, Okazaki K, Mizokawa T, Fujimori A, Hondou K, Fujiwara Y, Iio K, Usuda M and Hamada N 2004 *Phys. Rev.* B **69** 045103
[26] Bronger W, Eyck J, Rüdorff W and Stöussel A 1970 *Z. Anorg. Allg. Chem.* **375** 1–7
[27] Li Q, Wu Y, Fan X, Zhang Y J, Zhu X, Zhu Z, Li Y and Wen H H 2022 *Phys. Rev.* B **106** 214501
[28] Acharya G and Ghimire M 2022 *J. Nepal Phys. Soc.* **8** 75–78
[29] Acharya G B and Ghimire M P 2023 *Him. Phys.* **10** 33–39
[30] Chen Y, Sun Y Y, Wang H, West D, Xie Y, Zhong J, Meunier V, Cohen M L and Zhang S B 2014 *Phys. Rev. Lett.* **113** 085501
[31] Naher M, Ali M A, Hossain M, Uddin M and Naqib S 2023 arXiv:2304.07669
[32] Naher M and Naqib S 2022 *Results Phys.* **37** 105505
[33] Koepernik K and Eschrig H 1999 *Phys. Rev.* B **59** 1743
[34] Perdew J P, Burke K and Ernzerhof M 1996 *Phys. Rev. Lett.* **77** 3865
[35] Tran F and Blaha P 2009 *Phys. Rev. Lett.* **102** 226401
[36] Momma K and Izumi F 2011 *J. Appl. Crystallogr.* **44** 1272–6
[37] Li Q, Wu Y, Fan X, Zhang Y J, Zhu X, Zhu Z, Li Y and Wen H H 2022 arXiv:2203.00493
[38] Wang W S, Li Z Z, Xiang Y Y and Wang Q H 2013 *Phys. Rev.* B **87** 115135
[39] Yu S L and Li J X 2012 *Phys. Rev.* B **85** 144402
[40] Freysoldt C, Grabowski B, Hickel T, Neugebauer J, Kresse G, Janotti A and Van de Walle C G 2014 *Rev. Mod. Phys.* **86** 253
[41] Zhang Y, Talapatra S, Kar S, Vajtai R, Nayak S and Ajayan P 2007 *Phys. Rev. Lett.* **99** 107201
[42] Toll J S 1956 *Phys. Rev.* **104** 1760
[43] Hoat D, Silva J R and Blas A M 2019 *J. Solid State Chem.* **270** 85–91

Pressure-induced creation and annihilation of Weyl points in T_d-$Mo_{0.5}W_{0.5}Te_2$ and $1T''$-$Mo_{0.5}W_{0.5}Te_2$

Bishnu Karki,[1,*] Bishnu Prasad Belbase,[1,*] Gang Bahadur Acharya,[1,2] Sobhit Singh,[3,†] and Madhav Prasad Ghimire[1,2,‡]

[1]*Central Department of Physics, Tribhuvan University, Kirtipur, 44613 Kathmandu, Nepal*

[2]*Institute for Theoretical Solid State Physics, IFW Dresden, Helmholtzstrasse 20, 01069 Dresden, Germany*

[3]*Department of Physics and Astronomy, Rutgers University, Piscataway, New Jersey 08854, USA*

(Received 17 September 2021; revised 20 January 2022; accepted 10 March 2022; published 29 March 2022)

By means of first-principles density-functional theory calculations, we investigate the role of hydrostatic pressure in the electronic structure of the T_d ($Pmn2_1$) and $1T''$ (Pm) phases of the Weyl semimetal $Mo_{0.5}W_{0.5}Te_2$, which is a promising material for phase-change memory technology and superconductivity. We particularly focus on changes occurring in the distribution of the gapless Weyl points (WPs) within the 0 to 45 GPa pressure range. We further investigate the structural phase transition and lattice dynamics of the T_d and $1T''$ phases within the aforementioned pressure range. Our calculations suggest that both the T_d and $1T''$ phases of $Mo_{0.5}W_{0.5}Te_2$ host four WPs in their full Brillouin zone at zero pressure. The total number of WPs increases to 44 (36) with increasing pressure via pair creation up to 20 (15) GPa for the T_d ($1T''$) phase, and beyond this pressure pair annihilation of WPs starts occurring, leaving only 16 WPs at 45 GPa in both phases. The enthalpy versus pressure data reveal that the $1T''$ phase is more favorable below the critical pressure of 7.5 GPa; however, beyond this critical pressure the T_d phase becomes enthalpically favorable. We also provide the calculated x-ray diffraction spectra along with the calculated Raman- and infrared-active phonon frequencies to facilitate the experimental identification of the studied phases.

DOI: 10.1103/PhysRevB.105.125138

I. INTRODUCTION

The study of topological materials is of high interest at present due to their potential applications in emerging technology [1–9]. Weyl semimetals (WSMs), one class of topological materials, have attracted special attention since their experimental realization in 2015 [10–15]. Breaking of either time-reversal symmetry or spatial-inversion symmetry or both in WSMs results in a particular electronic band structure possessing crossings of the nondegenerate valance and conduction bands near the Fermi level E_F, forming gapless Weyl points (WPs) and Weyl cones [16]. The low-energy electronic excitations near these WPs behave as massless Weyl fermions [17–25]. WSMs are interesting due to their exotic properties such as WPs acting as the sources and sinks of the Berry curvature in momentum space, the existence of open Fermi-arc states connecting two opposite WPs, extremely large magnetoresistance [26–29], and various quantum Hall phenomena [30–37]. Moreover, based on the tilting of the band crossings near the Fermi level E_F, two types of WSMs are reported: (i) type-I WSMs that preserve the Lorentz invariance whose Fermi surface shrinks to zero when E_F is set at the energy of the WPs and (ii) type-II WSMs that violate the Lorentz invariance due to peculiar tilting of the Weyl cone such that WPs occur at the touching points of electron and hole pockets and whose Fermi surface never shrinks to absolute zero when E_F is set at the energy of the WPs [3,20,22,34,38,39].

WSMs belonging to the transition metal dichalcogenide (TMD) family are special, mainly because the s, p, and d orbitals in these systems hybridize to form bands near the Fermi level, which often yield various fascinating properties such as distinct quantum phase transitions between different structures, thermal and optical properties, topological domain walls, different kinds of Hall effects, and superconductivity [40–46]. Notably, dome-shaped superconducting behavior is observed in $MoTe_2$ with a transition temperature of 0.01 K that increase to 8.2 K at 11.7 GPa pressure [42,44,47–49]. $MoTe_2$ and WTe_2 are among the first reported WSMs with four WPs in their momentum space due to the broken inversion symmetry [22,50–61]. The application of external pressure and strain has been reported to play a vital role in tuning the WSM phase in $MoTe_2$ and WTe_2 [58,62–64].

Substitution of W by Mo in WTe_2, forming the polymorphic structure $Mo_xW_{1-x}Te_2$, is reported to control the structural phase transition, transport properties, thermal conductivity, Weyl phase, and superconductivity in this system [65–72]. Depending on the magnitude of the pressure applied to $Mo_xW_{1-x}Te_2$ ($x = 0.9$, 0.6, and 0.25), the superconducting transition temperature can be tuned [73]. Moreover, a tunable WSM phase and Fermi-arc states can be realized in $Mo_xW_{1-x}Te_2$ ($x \leqslant 0.5$) by varying x [74–76]. By means of the temperature-dependent elastic neutron scattering measurements, Schneeloch *et al.* [70] recently investigated the monoclinic $1T'$ to orthorhombic T_d structural phase

*These authors contributed equally to this work.

†sobhit.singh@rutgers.edu

‡madhav.ghimire@cdp.tu.edu.np

transition in $Mo_{1-x}W_xTe_2$ as a function of the W substitution and temperature. They observed that the $1T'$-T_d phase transition is accompanied by an intermediate pseudo-orthorhombic phase T_d^*, which was first reported by Tao *et al.* [72] for pure $MoTe_2$. Notably, the intermediate T_d^* phase exists only up to concentration $x = 0.34$ and vanishes for $x > 0.34$. Their results further suggest that at room temperature the $Mo_{0.5}W_{0.5}Te_2$ composition favors the T_d phase [70]. Marchenkov *et al.* [71] experimentally studied the transport and optical properties of single-crystal $Mo_{0.5}W_{0.5}Te_2$. Their temperature-dependent resistivity data revealed the metallic nature of the system. Li *et al.* recently performed dimensionality-dependent transport measurements on a special $Mo_{0.5}W_{0.5}Te_2$ sample having a thickness gradient across two- and three-dimensional regimes and reported strong evidence that this material is a type-II WSM [77].

The experimental observation of pressure-controlled superconductivity in $Mo_{0.5}W_{0.5}Te_2$ [73] calls for a systematic investigation of the pressure-induced changes occurring in the crystal structure, electronic structure, and WSM phase of this system. In this work, we theoretically study the structural, vibrational, and topological electronic properties of $Mo_{0.5}W_{0.5}Te_2$ as a function of the hydrostatic pressure within a 0 to 45 GPa pressure range. We explore the aforementioned properties of two candidate crystal phases of $Mo_{0.5}W_{0.5}Te_2$, T_d and $1T''$, as a function of the applied pressure. Our calculations indicate that both of these phases are dynamically stable within the studied pressure range and both of them host a number of WPs in their momentum-energy space. Interestingly, WPs in both phases can be created via pair creation, destroyed via pair annihilation, and shifted in the momentum-energy space by application of external pressure. Such tunability of the Weyl phase is desired to harness various transport and optical properties of WSMs [2–4,78–81], particularly those associated with the nonzero Berry-curvature dipole such as the nonlinear Hall effect [82,83], circular photogalvanic effect [84–86], and nonlinear optical responses [86–88]. Furthermore, creation (annihilation) of WPs near the Fermi level as well as their shifting in the momentum-energy space can enhance (suppress) electronic transport properties in WSMs. Our work implies that $Mo_{0.5}W_{0.5}Te_2$ exhibits a variety of interesting topological properties at higher pressures, and it may provide a novel platform for the realization of Weyltronics. Furthermore, our results suggest an increase in the superconducting transition temperature at higher pressures, which is in agreement with recent experimental observations [43,73].

II. COMPUTATIONAL DETAILS

The density-functional theory (DFT) calculations were performed using the projector augmented wave (PAW) method as implemented in the Vienna Ab initio Simulation Package (VASP) [89–91]. Six valence electrons were considered in the PAW pseudopotentials of Mo, W, and Te. The Perdew-Burke-Ernzerhof generalized gradient approximation (GGA) was used to compute the exchange-correlation functional [92]. The GGA-opt86b is more accurate exchange functional used for the van der Waals (vdW) density-functional corrections [93–95]. The reciprocal space was sampled using a Γ-centered k mesh with a size of $8 \times 12 \times 4$ together with a kinetic energy cutoff of 600 eV for plane waves. The energy and force convergence criteria were set to 10^{-8} eV and 10^{-4} eV/Å, respectively. The hydrostatic pressure was applied up to 45 GPa. The crystal structures were fully optimized in the inner coordinates as well in the cell parameters for each pressure considering spin-orbit coupling (SOC) and GGA-opt86b vdW corrections [93–95]. All the DFT calculations were carried out in a 12-atom unit cell of $Mo_{0.5}W_{0.5}Te_2$. The optimized lattice parameters for the T_d phase at zero pressure are $a = 6.301$, $b = 3.490$, and $c = 14.076$ Å, and cell angles are $\alpha = \beta = \gamma = 90^\circ$, which are in excellent agreement with the experimental data reported in Ref. [70].

The phonon calculations were performed using the finite-difference approach using $2 \times 3 \times 1$ supercells. SOC was considered in all phonon calculations. The PHONOPY [96] package was utilized to plot the phonon dispersions. The MECHELASTIC [97,98] package was used to perform the equation of states (EOS) analyses using the enthalpy versus pressure data. In order to understand the distribution of Weyl points in the momentum-energy space, we compute the real-space Wannier Hamiltonian using the full potential local orbital (FPLO) code, version 18 [99]. We employed the above-mentioned DFT convergence parameter in all the FPLO calculations. The Wannier fitting was done using the PYFPLO [99] module of the FPLO package considering Mo $4d$ and $5s$, W $5d$ and $6s$, and Te $5s$ and $5p$ as the local orbital basis. The PYPROCAR code [100] was used to investigate the DFT-calculated electronic band structures, and VESTA [101] software was used to draw the crystal structures.

III. RESULTS AND DISCUSSION

A. Crystal structures

In order to theoretically investigate the electronic structure of $Mo_{0.5}W_{0.5}Te_2$, we prepare two candidate crystal structures, as shown in Figs. 1(a) and 1(b), by taking the parent T_d phase (space group $Pmn2_1$) of WTe_2 and systematically substituting one W atom by one Mo atom in each vertically stacked layer. There are two possible ways to carry out such a substitution. First, we consider a scenario in which the ordering of Mo and W atoms is reversed in the adjacent vertically stacked layers, i.e., (Mo-W)$\cdots$(W-Mo)$\cdots$(Mo-W)$\cdots$. This results in a crystal structure belonging to space group $Pmn2_1$ (No. 31), similar to the parent T_d phase; hence, we call this structure the T_d phase. Note that this structure retains the vertical glide-mirror symmetry, as discussed in Ref. [37]. Also, this structure does not break the orthorhombic symmetry of the parent T_d structure after a free DFT relaxation.

Second, we consider a scenario in which ordering of the Mo and W atoms remains the same within the adjacent vertically -stacked layers, i.e., (Mo-W)$\cdots$(Mo-W)$\cdots$(Mo-W)$\cdots$. Such a configuration breaks the vertical glide-mirror symmetry [37] and results in space group Pm (No. 6) after a free DFT relaxation of the unit cell. Note that the optimized structure is slightly distorted from the parent orthorhombic cell to a distorted monoclinic cell with a monoclinic cell angle of $\beta \neq 90^\circ$, which varies as a function of the applied hydrostatic pressure, as we discuss below. Although this monoclinic structure is similar to the $1T'$ phase (space group $P2_1/m$) of

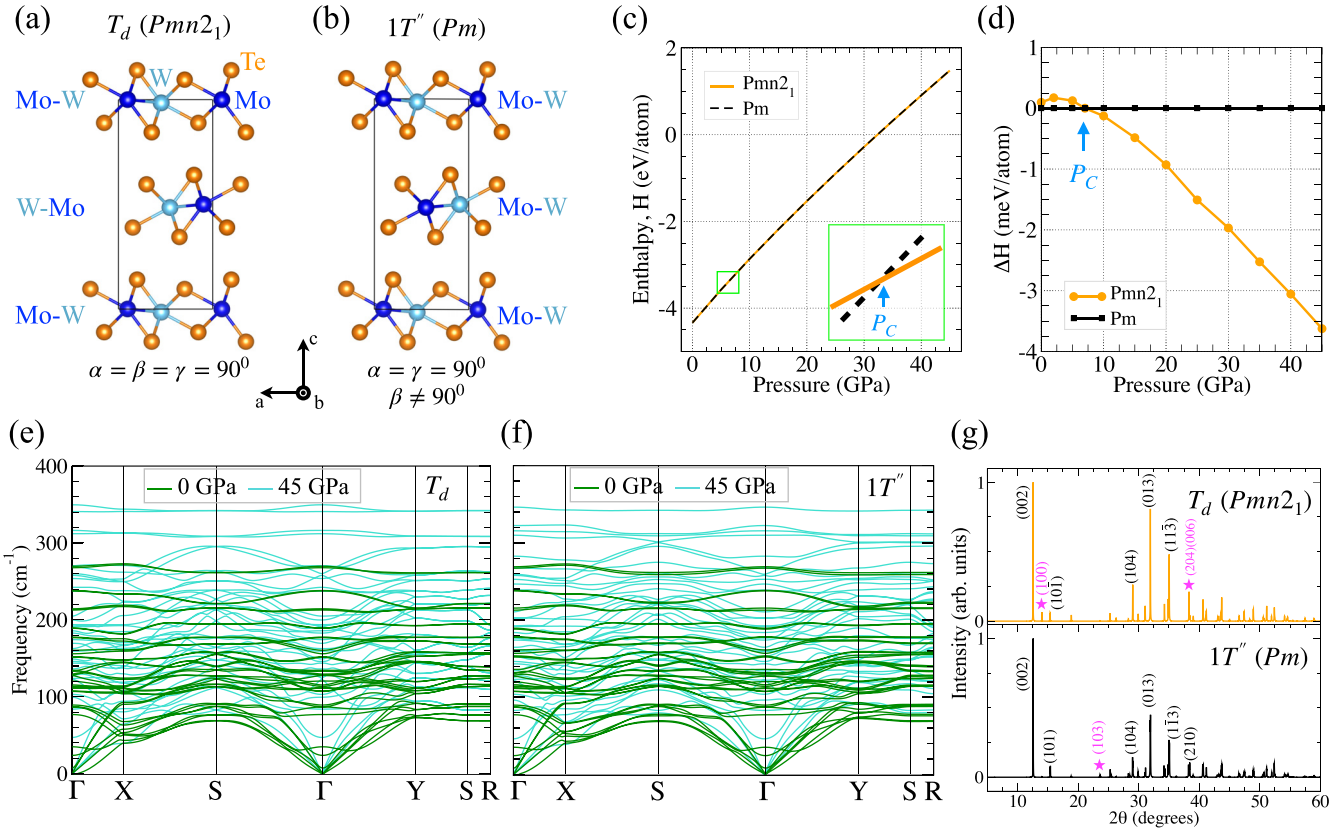

FIG. 1. (a) and (b) Crystal structures of the T_d and $1T''$ phases of $Mo_{0.5}W_{0.5}Te_2$. Note that $1T''$ has a subtle monoclinic distortion due to the cell angle $\beta \neq 90°$. (c) Enthalpy versus pressure phase diagram for the T_d and $1T''$ phases. The critical pressure P_C at which the structural phase transition occurs is predicted to be near 7.5 GPa. Inset: an enlarged view near the crossing point. (d) The enthalpy difference ΔH ($= H_{T_d} - H_{1T''}$) as a function of pressure. (e) and (f) Calculated phonon spectra (with SOC) at 0 and 45 GPa pressure for the T_d and $1T''$ phases. We would like to note that we decided to plot the phonon dispersion for the $1T''$ phase along the same high-symmetry k path as in the T_d phase for the sake of better comparison, although the $1T''$ phase has a subtle monoclinic distortion (see the SM [102] for details). (g) The calculated x-ray diffraction (XRD) patterns for the T_d and $1T''$ phases at 0 GPa pressure. The signature peaks in both phases are marked in magenta. More details about the crystal structures, calculated XRD patterns, phonon spectra calculated at higher pressures, and a comparison of the calculated Raman-active phonon frequencies with the available experimental data are provided in the SM [102].

TMDs, it is lower in symmetry due to the broken inversion and vertical glide-mirror symmetries [37]. Therefore, we decide to call this monoclinic phase the $1T''$ phase. We note both of the structures, T_d and $1T''$, have broken inversion symmetry, which is a fundamental requirement for nonmagnetic Weyl semimetals.

Before moving further, let us briefly discuss the possible reason behind the observed monoclinic distortion in the $1T''$ phase. One could imagine the presence of an in-plane polarity orientation determined by the peculiar ordering of Mo and W atoms with different electronegativities within each vertically stacked layer, as shown in Figs. 1(a) and 1(b). In Fig. 1(a), where the ordering of Mo-W pairs is reversed as we move in the vertical direction, the in-plane polarity would reverse its sign in the adjacent vertically stacked layers, i.e., $-+-+\cdots$ or $+-+-\cdots$ (antipolar order). Here, $+$ and $-$ signs denote the polarity orientation parallel or antiparallel to the a lattice vector. In such a configuration, a free relaxation of structure does not require any monoclinic distortion of the orthorhombic cell due to the perfect cancellation of dipolarlike interactions along the vertical direction (not strictly speaking because partial screening of electric dipoles may occur due to the semimetallic nature of this system). On the other hand, in Fig. 1(b), where the ordering of Mo-W pairs is the same in the adjacent vertical layers, the in-plane polarity would be parallel in the adjacent layers, i.e., $----\cdots$ or $++++\cdots$, similar to that of the $1T'$ phase [37,46]. Hence, in order to minimize the total free energy such structures tend to exhibit a monoclinic distortion due to the sliding of the adjacent polar layers along the in-plane direction, as discussed in Ref. [37].

B. Pressure-induced effects on the T_d and $1T''$ structures

Next, we test the relative stability of the T_d and $1T''$ phases as a function of pressure. Our calculations reveal that the enthalpy difference ΔH between these two phases is very small [Figs. 1(c) and 1(d)]. This implies the likelihood of the formation of a solid solution of the T_d and $1T''$ phases at finite temperatures. We find that below the critical pressure ($P_C =$ 7.5 GPa), the $1T''$ phase is more favorable, whereas above P_C the T_d phase is preferred. We further performed the EOS analyses using the Birch, Vinet, and Birch-Murnaghan models as implemented in the MECHELASTIC package [97,103,104].

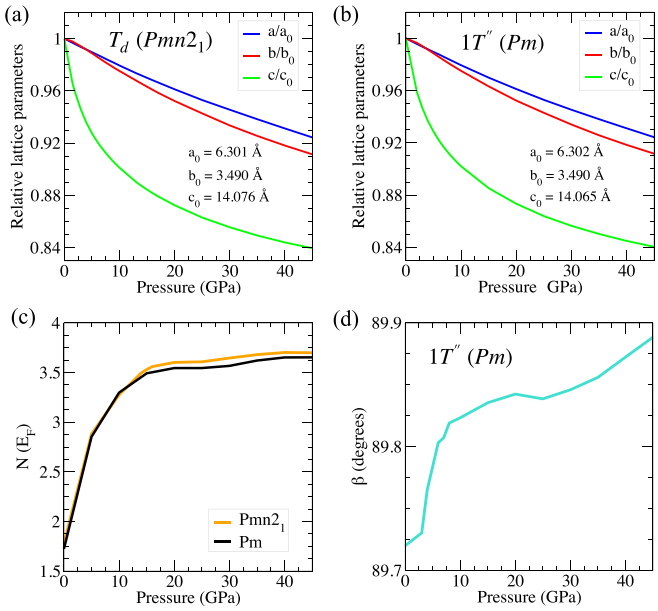

FIG. 2. (a) and (b) The optimized lattice parameters normalized to the lattice parameters obtained at zero pressure (a_0, b_0, c_0) and (c) the calculated density of states (states/eV) at the Fermi level $N(E_F)$ plotted as a function of pressure for both the T_d and $1T''$ phases. (d) Pressure-dependent variation in the monoclinic cell angle β for the $1T''$ phase. Note that $\beta = 90^\circ$ for the T_d phase.

The difference between the obtained EOS fitting parameters for the T_d and $1T''$ phases is minimal (see the Supplemental Material (SM) [102] for more details).

The phonon spectra calculated considering the SOC and vdW corrections for both the T_d [Fig. 1(e)] and $1T''$ [Fig. 1(f)] phases demonstrate the dynamical stability of these phases at zero pressure as well as at higher pressures (see the SM [102]). We notice an increase in the phonon frequencies with increasing pressure; that is, phonons harden at higher pressures. No dynamical instability was observed in either phase within the studied pressure range. A list of the infrared- and Raman-active phonon frequencies calculated at different pressures is provided in the SM [102]. We hope this can facilitate experimental identification of the T_d and $1T''$ phases.

Furthermore, we calculate the x-ray diffraction (XRD) patterns of the T_d and $1T''$ phases at various pressures using a Cu $K\alpha$ x ray with a wavelength of 1.5406 Å. Figure 1(g) shows the calculated XRD patterns at zero pressure (data at higher pressure are provided in the SM [102]). Although the calculated XRD spectra look quite similar for both phases, there are some signature peaks, marked using magenta stars, which are present in one phase but absent in the other. These peaks can be used to distinguish between the T_d and $1T''$ phases in real crystals. Notably, the calculated peak position for the (002) crystallographic peak and the Raman-active phonon frequencies (see the SM [102]) match remarkably well with the reported experimental data for $Mo_{0.5}W_{0.5}Te_2$ single crystals [65].

Figures 2(a) and 2(b) show the pressure dependence of the DFT optimized lattice parameters for the T_d and $1T''$ phases. We observe a very similar trend in the pressure-dependent structural parameters of both phases. To highlight the observed trend, we plot the normalized lattice parameters with respect to the lattice parameters obtained at zero pressure. We observe the maximum change in the c lattice parameter with varying pressure. At 45 GPa, the c lattice parameter decreases by ∼15% for both phases, whereas the relative change in the a and b lattice parameters is less than 10% within the studied pressure range. Such behavior is expected owing to the weak vdW interaction along the out-of-plane c axis. The optimized Mo-W bond length shows a pressure-dependent behavior similar to that of the in-plane lattice parameters. The Mo-W bond length decreases from a value of 2.85 Å at zero pressure to 2.70 Å at 45 GPa. This is an almost 5% decrease in the Mo-W bond length. On the other hand, the maximum compression in the Mo-Te and W-Te bond lengths is nearly 4% at 45 GPa.

Strikingly, the Te-Te interlayer distance undergoes the maximum change (∼24%) as a function of external pressure in both the T_d and $1T''$ phases; the optimized Te-Te interlayer distance decreases from 3.93 Å at zero pressure to 2.98 Å at 45 GPa. References [73,105] pointed out that such a softening of the Te-Te interlayer vibrational mode substantially contributes to the overall electron-phonon coupling, which could possibly be the origin of the emergence of superconductivity in this system.

Figure 2(d) shows the variation in the monoclinic angle β as a function of the pressure for the $1T''$ phase. With increasing pressure, the cell angle β tends to approach 90°, which implies a decrease in the monoclinic distortion and a preference for the orthorhombic T_d phase at higher pressures. This is consistent with the data shown in Fig. 1(d).

Since $Mo_{0.5}W_{0.5}Te_2$ is particularly interesting due to its superconducting properties [73], we calculate the density of states at the Fermi level $N(E_F)$ as a function of pressure for both the T_d and $1T''$ phases, as shown in Fig. 2(c). A systematic increase in $N(E_F)$ with increasing pressure was observed in both phases. We would like to note that phonons also harden with increasing pressure [see Figs. 1(e) and 1(f)]. Thus, an increased $N(E_F)$ together with the higher phonon frequencies implies an enhancement in the effective electron-phonon coupling at higher pressures, which could substantially increase the superconducting transition temperature in this system at higher pressures [47,105–107]. This is consistent with recent experimental observations [43,73].

C. Pressure-tunable Weyl semimetal phase

The band structure calculations of the T_d and $1T''$ phases for different pressures are presented in Figs. 3 and 4. The topmost valence band indicated in green forms the hole pocket, and the bottom of the conduction band indicated in red forms the electron pocket near E_F along the Γ-X, S-Γ-Y, and U-Z-T high-symmetry directions of the Brillouin zone (BZ) [108]. These electron and hole pockets touch each other at discrete points in the momentum space, forming type-II WPs [22]. The change in pressure affects the size of the electron and hole pockets in the momentum space. With increasing pressure, these pockets come close to each other, producing more band crossings, as implied in Figs. 3 and 4. A similar trend is found for the $1T''$ phase.

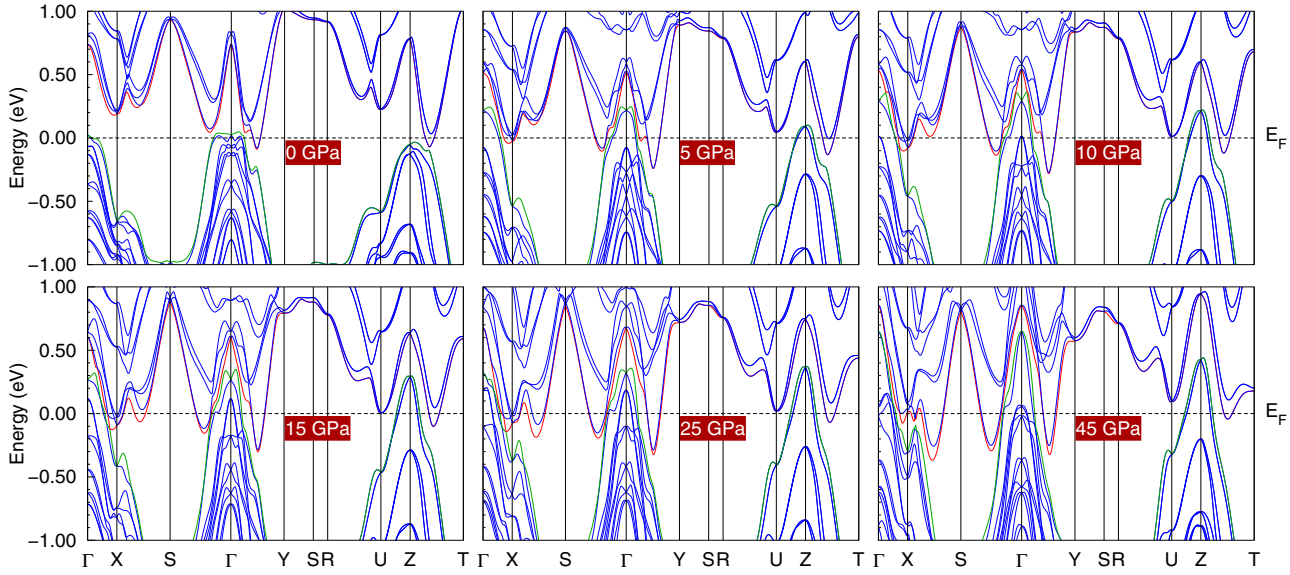

FIG. 3. Band structures of the T_d phase calculated at pressure values of 0, 5, 10, 15, 25, and 45 GPa with the inclusion of SOC. Red in the band structures represents the lowest conduction band, and green represents the highest valence band. The dashed horizontal line marks E_F ($E_F = 0$ eV).

TMDs are the first class of materials to host type-II WPs. Soluyanov *et al.* first reported type-II WPs in pure WTe_2 located between 0.052 and 0.058 eV above E_F [22]. Sixteen WPs are found in k space with eight WPs at the $k_z = 0$ plane and eight more WPs off the plane ($k_i \neq 0$, $i = x$, y, and z). With inclusion of SOC all the WPs at $k_i \neq 0$ are annihilated, leaving only 8 of the 16 WPs. Similarly, Sun *et al.* predicted the type-II WSMs in $MoTe_2$ [58]. Eight WPs are recorded at two different energies, 6 and 59 meV above E_F.

Here, in our study with 50% substitution of Mo on WTe_2 without the application of pressure, we report four WPs at an energy state 55 meV above E_F at the $k_z = 0$ plane for the T_d phase. In contrast, a similar number of WPs are recorded for the $1T''$ phase but at a different energy state, 93 meV below E_F at the $k_z \neq 0$ plane. The energy of the WPs obtained for the T_d phase is in agreement with the energy of WPs for $MoTe_2$ [58] and WTe_2 [22], whereas the $1T''$ phase hosts WPs below E_F. Moreover, the chemical effect is also found to play a significant role in the change in the total number of WPs in $Mo_{0.5}W_{0.5}Te_2$.

We obtain a total of four WPs (W_1) in the first BZ of the T_d and $1T''$ phases of $Mo_{0.5}W_{0.5}Te_2$ at zero pressure. The coordinates of the nonequivalent W_1 WPs are given in Table I; the other three WPs are the mirror reflections of W_1 at zero

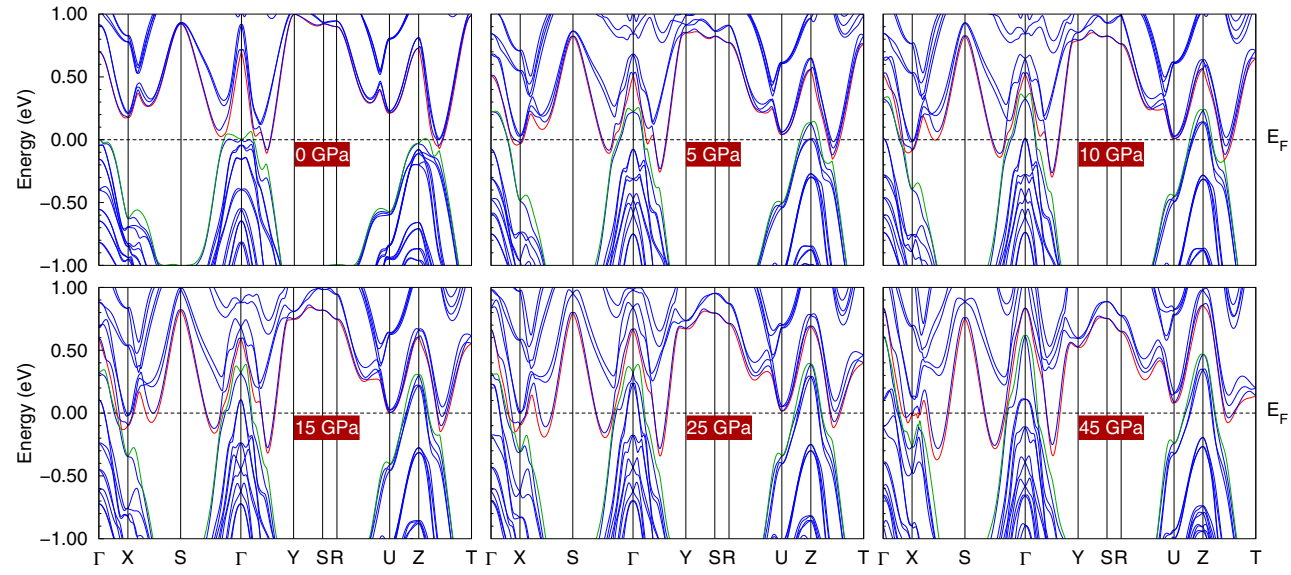

FIG. 4. Band structures of the $1T''$ phase calculated at pressure values of 0, 5, 10, 15, 25, and 45 GPa with the inclusion of SOC. Red in the band structures represents the lowest conduction band, and green represents the highest valence band. The dashed horizontal line marks E_F. For a better comparison the k paths of the $1T''$ phase are also chosen to be the same as in the T_d phase.

TABLE I. Location of W_1 WPs in the momentum space of the T_d and $1T''$ phases at zero pressure

WP	$k_x\left(\frac{2\pi}{a}\right)$	$k_y\left(\frac{2\pi}{b}\right)$	$k_z\left(\frac{2\pi}{c}\right)$	Chirality χ
$W_1(T_d)$	−0.132	−0.095	0.000	+1
$W_1(1T'')$	−0.004	−0.200	−0.416	+1

pressure. There is variation in the total number and locations of WPs due to the application of hydrostatic pressure. Below we discuss the role of the hydrostatic pressure in the Weyl phase of T_d- and $1T''$-$Mo_{0.5}W_{0.5}Te_2$.

1. Pressure effects on the T_d phase

The variation in the number of WPs and their energy states for the T_d phase is presented in the graphical plots in Figs. 5(a) and 5(b). On increasing the pressure value to 1.5 GPa new sets of WPs, W_2 and W_3, are generated along with the initial W_1, making the total number of WPs 20. Here, we notice that the pressure shifts the energy state of W_1 to $E_F + 75$ meV. The eight newly created copies of W_2 and W_3 are found in the energy states of $E_F + 8$ meV and $E_F - 7$ meV, respectively. No further creation of WPs up to a pressure of 8 GPa occurs; the position and energy states of the WPs simply vary with the pressure. The energy state of W_1 rises to the highest value of $E_F + 139$ meV at 8 GPa pressure and decreases on a further increase of the pressure, getting closest to the Fermi level (energy state $E_F + 1$ meV) at 35 GPa and shifting below the Fermi level above that pressure. The pair creation of W_4 and W_5, each with four WPs, occurs at 9 GPa and continues up to 10 GPa, getting annihilated above that pressure. The highest number of WPs is observed at 20 GPa, and a constant number of 16 WPs is observed at 30 to 45 GPa.

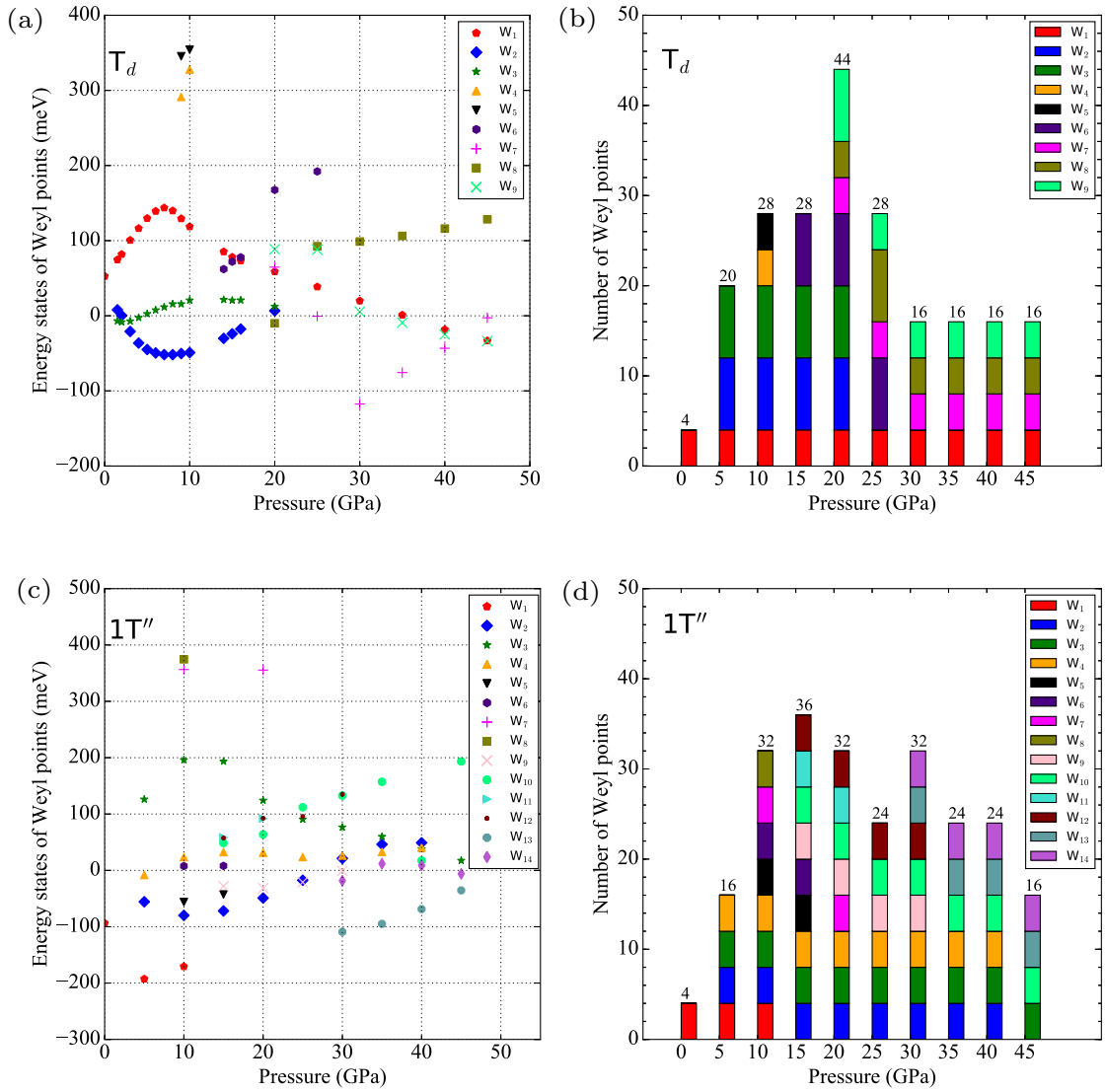

FIG. 5. (a) Energy states of WPs with respect to E_F calculated at different values of pressure for the T_d phase. (b) Stack-bar diagram showing the creation and annihilation of the WPs from 0 to 45 GPa for the T_d phase. (c) Energy states of WPs corresponding to different pressures for the $1T''$ phase. (d) Stack-bar diagram showing the creation and annihilation of the WPs from 0 to 45 GPa for the $1T''$ phase. The total number of WPs at each pressure is written at the top of each bar. See the SM [102] for more details regarding the number and location of WPs obtained at each pressure.

2. Pressure effects on the 1T″ phase

Pressure also has an impact on the dynamics of WPs in the $1T''$ phase. Pair creation and annihilation of WPs as a function of pressure are noticed in the momentum space of the $1T''$ phase. Here, the W_1 WPs continue to exist up to 10 GPa, getting annihilated with a further rise in pressure. Similarly, the W_2 WPs are created at 5 GPa pressure and exist up to 40 GPa and then get annihilated. A similar phenomenon of pair creation and annihilation is noticed for the other energy state of WPs as well, which is summarized in Figs. 5(c) and 5(d). More energy states of the WPs are observed in the $1T''$ phase compared to the T_d phase due to its lower symmetry. In terms of the total number of WPs, the highest number of 36 is observed at 15 GPa pressure, whereas a constant number of 16 WPs is noticed for pressures beyond 40 GPa.

IV. SUMMARY

In summary, we studied the structural, vibrational, electronic, and topological Weyl properties of $Mo_{0.5}W_{0.5}Te_2$ by means of first-principles DFT calculations. We found that there are two possible candidate structures, T_d and $1T''$, for 50:50 Mo:W substitution. We studied the aforementioned properties of these two phases in the 0–45 GPa pressure range. We found that both structures are energetically and dynamically stable in the studied pressure. The calculated x-ray diffraction spectra and the infrared- and Raman-active phonon frequencies indicate that these two phases can be identified in experiments, although they are likely to form solid solutions due to the subtle difference in their enthalpies at low pressures. The T_d ($1T''$) phase is theoretically more favorable at higher (lower) pressures, with the critical pressure being 7.5 GPa. Our calculations revealed that the density of states and phonon frequencies increase dramatically with increasing pressure in both phases, which is indicative of larger electron-phonon coupling at higher pressures, and it could substantially increase the superconducting transition temperature in this system at higher pressures.

Interestingly, we found that both the T_d and $1T''$ phases host a number of WPs in their momentum-energy space. The total number and location of WPs can be controlled by varying hydrostatic pressure. Four WPs were obtained in the T_d and $1T''$ phases at zero pressure. The total number of WPs increased to 44 (36) with increasing pressure, via pair creation, up to 20 (15) GPa for the T_d ($1T''$) phase, and beyond this pressure, pair annihilation of WPs started occurring, leaving only 16 WPs at 45 GPa in both phases. Therefore, we can conclude that pressure can tune WPs to the desired location, generate new WPs, and also annihilate them, thus providing an ideal platform for the realization of Weyltronics in $Mo_{0.5}W_{0.5}Te_2$.

ACKNOWLEDGMENTS

M.P.G. acknowledges the Alexander von Humboldt Foundation, Germany, for the equipment grants and IFW-Dresden for providing the large-scale computer nodes to the Advanced Materials Research Laboratory for scientific computations. S.S. acknowledges funding from Office of Naval Research (ONR) grant N00014-21-1-2107. This work was supported by the U.S. Department of Energy (DOE), Office of Science, Basic Energy Sciences under award DE-SC0020353 (S.S.). G.B.A. thanks the Nepal Academy of Science and Technology for the Ph.D. fellowship. M.P.G. and G.B.A. thank M. Richter for fruitful discussions and U. Nitzsche for technical assistance.

[1] M. Z. Hasan and C. L. Kane, Rev. Mod. Phys. **82**, 3045 (2010).
[2] N. P. Armitage, E. J. Mele, and A. Vishwanath, Rev. Mod. Phys. **90**, 015001 (2018).
[3] B. Yan and C. Felser, Annu. Rev. Condens. Matter Phys. **8**, 337 (2017).
[4] K. Manna, Y. Sun, L. Muechler, J. Kübler, and C. Felser, Nat. Rev. Mater. **3**, 244 (2018).
[5] H. Weng, X. Dai, and Z. Fang, J. Condens. Matter Phys. **28**, 303001 (2016).
[6] H. Gao, J. W. Venderbos, Y. Kim, and A. M. Rappe, Annu. Rev. Mater. **49**, 153 (2019).
[7] A. Burkov, Annu. Rev. Condens. Matter Phys. **9**, 359 (2018).
[8] M. Z. Hasan, S.-Y. Xu, I. Belopolski, and S.-M. Huang, Annu. Rev. Condens. Matter Phys. **8**, 289 (2017).
[9] M. Kang *et al.*, Nat. Mater. **19**, 163 (2020).
[10] B. Q. Lv, N. Xu, H. M. Weng, J. Z. Ma, P. Richard, X. C. Huang, L. X. Zhao, G. F. Chen, C. E. Matt, F. Bisti, V. N. Strocov, J. Mesot, Z. Fang, X. Dai, T. Qian, M. Shi, and H. Ding, Nat. Phys. **11**, 724 (2015).
[11] B. Q. Lv, H. M. Weng, B. B. Fu, X.P. Wang, H. Miao, J. Ma, P. Richard, X. C. Huang, L. X. Zhao, G. F. Chen, Z. Fang, X. Dai, T. Qian, and H. Ding, Phys. Rev. X **5**, 031013 (2015).
[12] S-M. Huang, S.-Y. Xu, I. Belopolski, C.-C. Lee, G. Chang, B. Wang, N. Alidoust, G. Bian, M. Neupane, C. Zhang, S. Jia, A. Bansil, H. Lin, and M. Z. Hasan, Nat. Commun. **6**, 7373 (2015).
[13] S.-Y. Xu, I. Belopolski, D. S. Sanchez, C. Zhang, G. Chang, C. Guo, G. Bian, Z. Yuan, H. Lu, T.-R. Chang *et al.*, Sci. Adv. **1**, e1501092 (2015).
[14] A. B. Sushkov, J. B. Hofmann, G. S. Jenkins, J. Ishikawa, S. Nakatsuji, S. Das Sarma, and H. D. Drew, Phys. Rev. B **92**, 241108(R) (2015).
[15] B. Q. Lv, S. Muff, T. Qian, Z. D. Song, S. M. Nie, N. Xu, P. Richard, C. E. Matt, N. C. Plumb, L. X. Zhao, G. F. Chen, Z. Fang, X. Dai, J. H. Dil, J. Mesot, M. Shi, H. M. Weng, and H. Ding, Phys. Rev. Lett. **115**, 217601 (2015).
[16] S. Murakami, New J. Phys. **9**, 356 (2007).
[17] S. Jia, S.-Y. Xu, and M. Z. Hasan, Nat. Mater. **15**, 1140 (2016).
[18] H. Weyl, Z. Phys. **56**, 330 (1929).
[19] X. Wan, A. M. Turner, A. Vishwanath, and S. Y. Savrasov, Phys. Rev. B **83**, 205101 (2011).
[20] D. Grassano, O. Pulci, A. M. Conte, and F. Bechstedt, Sci. Rep. **8**, 3534 (2018).
[21] J. Ruan, S.-K. Jian, H. Yao, H. Zhang, S.-C. Zhang, and D. Xing, Nat. Commun. **7**, 11136 (2016).
[22] A. A. Soluyanov, D. Gresch, Z. Wang, Q. Wu, M. Troyer, X. Dai, and B. A. Bernevig, Nature (London) **527**, 495 (2015).

[23] S. Singh, A. C. Garcia-Castro, I. Valencia-Jaime, F. Muñoz, and A. H. Romero, Phys. Rev. B **94**, 161116(R) (2016).

[24] S. Singh, Q. S. Wu, C. Yue, A. H. Romero, and A. A. Soluyanov, Phys. Rev. Material **2**, 114204 (2018).

[25] G. W. Winkler, S. Singh, and A. A. Soluyanov, Chin. Phys. B **28**, 077303 (2019).

[26] F. C. Chen, H. Y. Lv, X. Luo, W. J. Lu, Q. L. Pei, G. T. Lin, Y. Y. Han, X. B. Zhu, W. H. Song, and Y. P. Sun, Phys. Rev. B **94**, 235154 (2016).

[27] Q. L. Pei, W. J. Meng, X. Luo, H. Y. Lv, F. C. Chen, W. J. Lu, Y. Y. Han, P. Tong, W. H. Song, Y. B. Hou, Q. Y. Lu, and Y. P. Sun, Phys. Rev. B **96**, 075132(R) (2017).

[28] S. Thirupathaiah, R. Jha, B. Pal, J. S. Matias, P. K. Das, P. K. Sivakumar, I. Vobornik, N. C. Plumb, M. Shi, R. A. Ribeiro, and D. D. Sarma, Phys. Rev. B **95**, 241105 (2017).

[29] S. Lee, J. Jang, S.-I. Kim, S.-G. Jung, J. Kim, S. Cho, S. W. Kim, J. Y. Rhee, K.-S. Park, and T. Park, Sci. Rep. **8**, 13937 (2018).

[30] S.-Y. Xu, I. Belopolski, N. Alidoust, M. Neupane, G. Bian, C. Zhang, R. Sankar, G. Chang, Z. Yuan, C.-C. Lee *et al.*, Science **349**, 613 (2015).

[31] N. Xu, H. Weng, B. Lv, C. E. Matt, J. Park, F. Bisti, V. N. Strocov, D. Gawryluk, E. Pomjakushina, K. Conder *et al.*, Nat. Commun. **7**, 1 (2016).

[32] I. Belopolski, S.-Y. Xu, D. S. Sanchez, G. Chang, C. Guo, M. Neupane, H. Zheng, C.-C. Lee, S.-M. Huang, G. Bian, N. Alidoust, T.-R. Chang, B. K. Wang, X. Zhang, A. Bansil, H.-T. Jeng, H. Lin, S. Jia, and M. Z. Hasan, Phys. Rev. Lett. **116**, 066802 (2016).

[33] A. Tamai, Q. S. Wu, I. Cucchi, F. Y. Bruno, S. Riccò, T. K. Kim, M. Hoesch, C. Barreteau, E. Giannini, C. Besnard, A. A. Soluyanov, and F. Baumberger, Phys. Rev. X **6**, 031021 (2016).

[34] G. Autès, D. Gresch, M. Troyer, A. A. Soluyanov, and O. V. Yazyev, Phys. Rev. Lett. **117**, 066402 (2016).

[35] W. Zhang, Q. Wu, L. Zhang, S.-W. Cheong, A. A. Soluyanov, and W. Wu, Phys. Rev. B **96**, 165125 (2017).

[36] M. P. Ghimire, J. I. Facio, J.-S. You, L. Ye, J. G. Checkelsky, S. Fang, E. Kaxiras, M. Richter, and J. van den Brink, Phys. Rev. Research **1**, 032044(R) (2019).

[37] S. Singh, J. Kim, K. M. Rabe, and D. Vanderbilt, Phys. Rev. Lett. **125**, 046402 (2020).

[38] G. Chang, S.-Y. Xu, D. S. Sanchez, S.-M. Huang, C.-C. Lee, T.-R. Chang, G. Bian, H. Zheng, I. Belopolski, N. Alidoust *et al.*, Sci. Adv. **2**, e1600295 (2016).

[39] K. Koepernik, D. Kasinathan, D. V. Efremov, S. Khim, S. Borisenko, B. Büchner, and J. van den Brink, Phys. Rev. B **93**, 201101(R) (2016).

[40] B. Sipos, A. F. Kusmartseva, A. Akrap, H. Berger, L. Forró, and E. Tutiš, Nat. Mater. **7**, 960 (2008).

[41] X. Qian, J. Liu, L. Fu, and J. Li, Science **346**, 1344 (2014).

[42] R. Morris, R. Coleman, and R. Bhandari, Phys. Rev. B **5**, 895 (1972).

[43] H. Takahashi, T. Akiba, K. Imura, T. Shiino, K. Deguchi, N. K. Sato, H. Sakai, M. S. Bahramy, and S. Ishiwata, Phys. Rev. B **95**, 100501(R) (2017).

[44] Y. Qi, P. G. Naumov, M. N. Ali, C. R. Rajamathi, W. Schnelle, O. Barkalov, M. Hanfland, S.-C. Wu, C. Shekhar, Y. Sun *et al.*, Nat. Commun. **7**, 11038 (2016).

[45] F. C. Chen, X. Luo, J. Yan, Y. Sun, H. Y. Lv, W. J. Lu, C. Y. Xi, P. Tong, Z. G. Sheng, X. B. Zhu, W. H. Song, and Y. P. Sun, Phys. Rev. B **98**, 041114(R) (2018).

[46] F.-T. Huang, S. J. Lim, S. Singh, J. Kim, L. Zhang, J.-W. Kim, M.-W. Chu, K. M. Rabe, D. Vanderbilt, and S.-W. Cheong, Nat. Commun. **10**, 4211 (2019).

[47] C. Heikes, I.-L. Liu, T. Metz, C. Eckberg, P. Neves, Y. Wu, L. Hung, P. Piccoli, H. Cao, J. Leao, J. Paglione, T. Yildirim, N. P. Butch, and W. Ratcliff, Phys. Rev. Material **2**, 074202 (2018).

[48] H. Wei, S.-P. Chao, and V. Aji, Phys. Rev. B **89**, 014506 (2014).

[49] P. Hosur, X. Dai, Z. Fang, and X.-L. Qi, Phys. Rev. B **90**, 045130 (2014).

[50] P. Li, W. Wu, Y. Wen, C. Zhang, J. Zhang, S. Zhang, Z. Yu, S. A. Yang, A. Manchon, and X.-X. Zhang, Nat. Commun. **9**, 3990 (2018).

[51] F. Y. Bruno, A. Tamai, Q. S. Wu, I. Cucchi, C. Barreteau, A. de la Torre, S. McKeownWalker, S. Riccó, Z. Wang, T. K. Kim, M. Hoesch, M. Shi, N. C. Plumb, E. Giannini, A. A. Soluyanov, and F. Baumberger, Phys. Rev. B **94**, 121112 (2016).

[52] Y. Wu, D. Mou, N. H. Jo, K. Sun, L. Huang, S. L. Bud'ko, P. C. Canfield, and A. Kaminski, Phys. Rev. B **94**, 121113(R) (2016).

[53] P. Li, Y. Wen, X. He, Q. Zhang, C. Xia, Z.-M. Yu, S. A. Yang, Z. Zhu, H. N. Alshareef, and X.-X. Zhang, Nat. Commun. **8**, 2150 (2017).

[54] Y.-Y. Lv, X. Li, B.-B. Zhang, W. Y. Deng, S.-H. Yao, Y. B. Chen, J. Zhou, S.-T. Zhang, M.-H. Lu, L. Zhang, M. Tian, L. Sheng, and Y.-F. Chen, Phys. Rev. Lett. **118**, 096603 (2017).

[55] L. Huang, T. M. McCormick, M. Ochi, Z. Zhao, M.-T. Suzuki, R. Arita, Y. Wu, D. Mou, H. Cao, J. Yan *et al.*, Nat. Mater. **15**, 1155 (2016).

[56] K. Deng, G. Wan, P. Deng, K. Zhang, S. Ding, E. Wang, M. Yan, H. Huang, H. Zhang, Z. Xu *et al.*, Nat. Phys. **12**, 1105 (2016).

[57] M. Sakano, M. S. Bahramy, H. Tsuji, I. Araya, K. Ikeura, H. Sakai, S. Ishiwata, K. Yaji, K. Kuroda, A. Harasawa, S. Shin, and K. Ishizaka, Phys. Rev. B **95**, 121101(R) (2017).

[58] Y. Sun, S.-C. Wu, M. N. Ali, C. Felser, and B. Yan, Phys. Rev. B **92**, 161107 (2015).

[59] Z. Wang, D. Gresch, A. A. Soluyanov, W. Xie, S. Kushwaha, X. Dai, M. Troyer, R. J. Cava, and B. A. Bernevig, Phys. Rev. Lett. **117**, 056805 (2016).

[60] J. Jiang, Z. Liu, Y. Sun, H. Yang, C. Rajamathi, Y. Qi, L. Yang, C. Chen, H. Peng, C. Hwang *et al.*, Nat. Commun. **8**, 13973 (2017).

[61] A. Liang, J. Huang, S. Nie, Y. Ding, Q. Gao, C. Hu, S. He, Y. Zhang, C. Wang, B. Shen *et al.*, arXiv:1604.01706.

[62] S. Dissanayake, C. Duan, J. Yang, J. Liu, M. Matsuda, C. Yue, J. A. Schneeloch, J. C. Y. Teo, and D. Louca, npj Quantum Mater. **4**, 45 (2019).

[63] N. Aryal and E. Manousakis, Phys. Rev. B **99**, 035123 (2019).

[64] N. Xu, Z. W. Wang, A. Magrez, P. Bugnon, H. Berger, C. E. Matt, V. N. Strocov, N. C. Plumb, M. Radovic, E. Pomjakushina, K. Conder, J. H. Dil, J. Mesot, R. Yu, H. Ding, and M. Shi, Phys. Rev. Lett. **121**, 136401 (2018).

[65] Y.-Y. Lv, L. Cao, X. Li, B.-B. Zhang, K. Wang, B. Pang, L. Ma, D. Lin, S.-H. Yao, J. Zhou, Y. B. Chen, S.-T. Dong, W.

Liu, M.-H. Lu, Y. Chen, and Y.-F. Chen, Sci. Rep. **7**, 44587 (2017).
[66] X.-J. Yan, Y.-Y. Lv, L. Li, X. Li, S.-H. Yao, Y.-B. Chen, X.-P. Liu, H. Lu, M.-H. Lu, and Y.-F. Chen, Appl. Phys. Lett. **110**, 211904 (2017).
[67] S. M. Oliver, R. Beams, S. Krylyuk, I. Kalish, A. K. Singh, A. Bruma, F. Tavazza, J. Joshi, I. R. Stone, S. J. Stranick *et al.*, 2D Mater. **4**, 045008 (2017).
[68] D. Rhodes *et al.*, Nano Lett. **17**, 1616 (2017).
[69] O. B. Aslan, I. M. Datye, M. J. Mleczko, K. Sze Cheung, S. Krylyuk, A. Bruma, I. Kalish, A. V. Davydov, E. Pop, and T. F. Heinz, Nano Lett. **18**, 2485 (2018).
[70] J. A. Schneeloch, Y. Tao, C. Duan, M. Matsuda, A. A. Aczel, J. A. Fernandez-Baca, G. Xu, J. C. Neuefeind, J. Yang, and D. Louca, Phys. Rev. B **102**, 054105 (2020).
[71] V. Marchenkov, A. Domozhirova, A. Makhnev, E. Shreder, S. Naumov, V. Chistyakov, J. Huang, and M. Eisterer, Low Temp. Phys. **45**, 241 (2019).
[72] Y. Tao, J. A. Schneeloch, C. Duan, M. Matsuda, S. E. Dissanayake, A. A. Aczel, J. A. Fernandez-Baca, F. Ye, and D. Louca, Phys. Rev. B **100**, 100101(R) (2019).
[73] R. Dahal, L. Z. Deng, N. Poudel, M. Gooch, Z. Wu, H. C. Wu, H. D. Yang, C. K. Chang, and C. W. Chu, Phys. Rev. B **101**, 140505(R) (2020).
[74] I. Belopolski *et al.*, Phys. Rev. B **94**, 085127 (2016).
[75] T.-R. Chang, S.-Y. Xu, G. Chang, C.-C. Lee, S.-M. Huang, B. Wang, G. Bian, H. Zheng, D. S. Sanchez, I. Belopolski *et al.*, Nat. Commun. **7**, 1 (2016).
[76] I. Belopolski, D. S. Sanchez, Y. Ishida, X. Pan, P. Yu, S.-Y. Xu, G. Chang, T.-R. Chang, H. Zheng, N. Alidoust *et al.*, Nat. Commun. **7**, 13643 (2016).
[77] P. Li, Y. Deng, C.-H. Hsu, C. Zhu, J. Cui, X. Yang, J. Zhou, Y.-C. Hung, J. Fan, Z. Ji, F. Qu, J. Shen, C. Yang, X. Jing, H. Lin, Z. Liu, L. Lu, and G. Liu, Phys. Rev. B **104**, 085423 (2021).
[78] B. Ramshaw, K. A. Modic, A. Shekhter, Y. Zhang, E.-A. Kim, P. J. Moll, M. D. Bachmann, M. Chan, J. Betts, F. Balakirev *et al.*, Nat. Commun. **9**, 2217 (2018).
[79] E. V. Gorbar, V. A. Miransky, I. A. Shovkovy, and P. O. Sukhachov, Low Temp. Phys. **44**, 487 (2018).
[80] J. Hu, S.-Y. Xu, N. Ni, and Z. Mao, Annu. Rev. Mater. Res. **49**, 207 (2019).
[81] N. P. Ong and S. Liang, Nat. Rev. Phys. **3**, 394 (2021).
[82] I. Sodemann and L. Fu, Phys. Rev. Lett. **115**, 216806 (2015).
[83] Q. Ma *et al.*, Nature (London) **565**, 337 (2019).
[84] F. de Juan, A. G. Grushin, T. Morimoto, and J. E. Moore, Nat. Commun. **8**, 15995 (2017).
[85] E. J. König, H.-Y. Xie, D. A. Pesin, and A. Levchenko, Phys. Rev. B **96**, 075123 (2017).
[86] Y. Zhang, H. Ishizuka, J. van den Brink, C. Felser, B. Yan, and N. Nagaosa, Phys. Rev. B **97**, 241118(R) (2018).
[87] G. Liu, Nonlinear Optical Responses in Type-II Weyl Semimetals, Ph.D. Thesis, University of Pennsylvania, Philadelphia, 2019.
[88] Q. Xu, Y. Zhang, K. Koepernik, W. Shi, J. van den Brink, C. Felser, and Y. Sun, npj Comput. Mater. **6**, 32 (2020).
[89] G. Kresse and J. Furthmüller, Phys. Rev. B **54**, 11169 (1996).
[90] G. Kresse and J. Furthmüller, Comput. Mater. Sci. **6**, 15 (1996).
[91] G. Kresse and D. Joubert, Phys. Rev. B **59**, 1758 (1999).
[92] J. P. Perdew, A. Ruzsinszky, G. I. Csonka, O. A. Vydrov, G. E. Scuseria, L. A. Constantin, X. Zhou, and K. Burke, Phys. Rev. Lett. **100**, 136406 (2008).
[93] J. Klimeš, D. R. Bowler, and A. Michaelides, Phys. Rev. B **83**, 195131 (2011).
[94] T. Thonhauser, V. R. Cooper, S. Li, A. Puzder, P. Hyldgaard, and D. C. Langreth, Phys. Rev. B **76**, 125112 (2007).
[95] M. Dion, H. Rydberg, E. Schröder, D. C. Langreth, and B. I. Lundqvist, Phys. Rev. Lett. **92**, 246401 (2004).
[96] A. Togo and I. Tanaka, Scr. Mater. **108**, 1 (2015).
[97] S. Singh, L. Lang, V. Dovale-Farelo, U. Herath, P. Tavadze, F.-X. Coudert, and A. H. Romero, Comput. Phys. Commun. **267**, 108068 (2021).
[98] S. Singh, I. Valencia-Jaime, O. Pavlic, and A. H. Romero, Phys. Rev. B **97**, 054108 (2018).
[99] K. Koepernik and H. Eschrig, Phys. Rev. B **59**, 1743 (1999).
[100] U. Herath, P. Tavadze, X. He, E. Bousquet, S. Singh, F. Muñoz, and A. H. Romero, Comput. Phys. Commun. **251**, 107080 (2020).
[101] K. Momma and F. Izumi, J. Appl. Crystallogr. **44**, 1272 (2011).
[102] See Supplemental Material at http://link.aps.org/supplemental/10.1103/PhysRevB.105.125138 for detailed information about the XRD spectra, phonon spectra, Raman- and infrared-active phonon frequencies, DOS, and distribution of WPs calculated at higher pressures.
[103] P. Vinet, J. Ferrante, J. H. Rose, and J. R. Smith, J. Geophys. Res. **92**, 9319 (1987).
[104] P. Vinet, J. H. Rose, J. Ferrante, and J. R. Smith, J. Condens. Matter Phys. **1**, 1941 (1989).
[105] P. Lu, J.-S. Kim, J. Yang, H. Gao, J. Wu, D. Shao, B. Li, D. Zhou, J. Sun, D. Akinwande, D. Xing, and J.-F. Lin, Phys. Rev. B **94**, 224512 (2016).
[106] R. Dynes, Solid State Commun. **10**, 615 (1972).
[107] H. Paudyal, S. Poncé, F. Giustino, and E. R. Margine, Phys. Rev. B **101**, 214515 (2020).
[108] W. Setyawan and S. Curtarolo, Comput. Mater. Sci. **49**, 299 (2010).

Volume 10, Issue 1, June 2023 ISSN 2542-2545

The HIMALAYAN PHYSICS

A peer-reviewed Journal of Physics

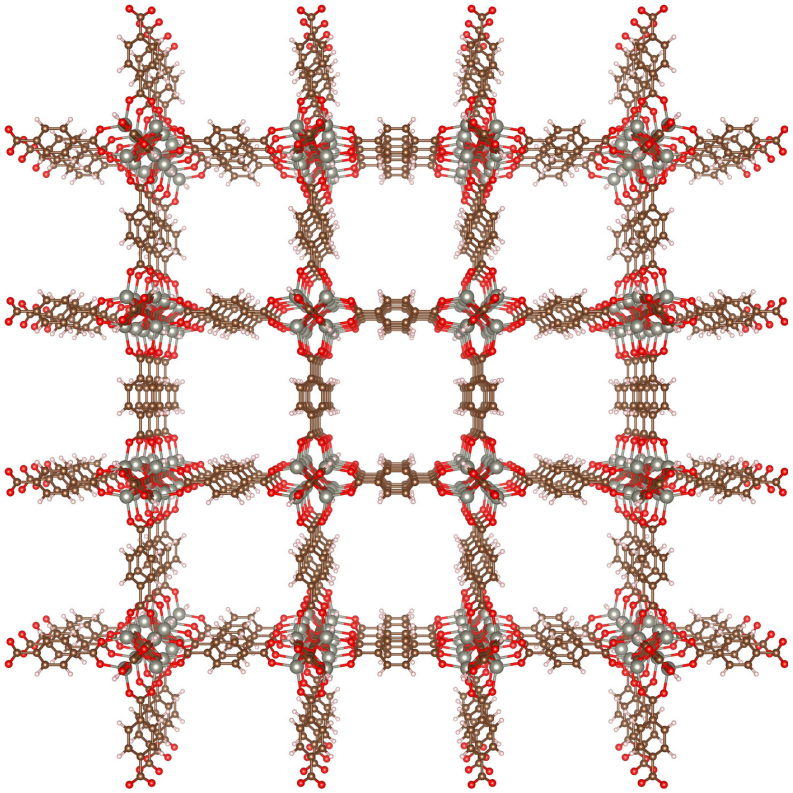

Department of Physics, Prithvi Narayan Campus, Pokhara
Nepal Physical Society, Gandaki Chapter, Pokhara

Publisher

Department of Physics, Prithvinarayan Campus, Pokhara
Nepal Physical Society, Gandaki Chapter, Pokhara

The Himalayan Physics

Volume 10, Issue 1, June 2023

ISSN 2542-2545

The Himalayan Physics (HimPhys) is an open access peer-reviewed journal that publishes quality articles which make innovative contributions in all areas of Physics. HimPhys is published annually by Nepal Physical Society (Gandaki Chapter), and Department of Physics, Prithvi Narayan Campus, Pokhara. The goal of this journal is to bring together researchers and practitioners from academia in Nepal and abroad to focus on advanced techniques and explore new avenues in all areas of physical sciences and establishing new collaborations with physics community in Nepal.

Chief Editor

Aabiskar Bhusal

Cover: Ball-and-stick model of MOF-5. © Roshani Sharma. Printed with permission.

Volume 10, Issue 1, June 2023 ISSN 2542-2545

The HIMALAYAN PHYSICS

A peer-reviewed Journal of Physics

Publisher

Department of Physics, Prithvi Narayan Campus, Pokhara
Nepal Physical Society, Gandaki Chapter, Pokhara

Nepal Physical Society

Gandaki Chapter

Pokhara, Nepal

Himalayan Physics Vol-10(1) (2023)

TABLE OF CONTENTS

****

Him. Phys. **10(1)** 33-39, (2023)

Himalayan Physics

Electronic and magnetic properties of ternary sulfide $Rb_2Mn_3S_4$

Research Article

Gang Bahadur Acharya[1,2] and Madhav Prasad Ghimire[1]*

1 Central Department of Physics, Tribhuvan University, Kirtipur-44613,Kathmandu, Nepal

2 Leibniz-IFW Dresden, Helmholtzstraβe 20, D-01069, Dresden, Germany.

Abstract: Semiconducting materials, especially with a direct band gap, are helpful for modern photovoltaic and optoelectronic device fabrication. Here, based on density functional theory calculations, we predict the electronic and magnetic properties of $Rb_2Mn_3S_4$ by using the full potential local orbital code. Considering different configurations such as nonmagnetic, ferromagnetic, ferrimagnetic, and antiferromagnetic, the magnetic ground state was found to be ferrimagnetic with the lowest total energy. The calculated effective magnetic moment is $10\mu_B$unit cell (two formula units) resulting from the opposite spin interaction between Mn (I) and Mn (II) atoms in $Rb_2Mn_3S_4$. From our calculations, $Rb_2Mn_3S_4$ is found to be a semiconductor with a direct energy band gap of 0.75 eV. With the inclusion of the Coulomb interaction (i.e., GGA+U), the band gap is found to rise to 2.34 eV for U = 4 eV.

Keywords: Density functional theory • Electronic structure • Semiconductor • Magnetism • Density of states • Magnetic moment

I. Introduction

The solid material whose conductivity lies between the insulator and metal is known as a semiconductor. Si and Ge are two well-known elemental semiconductors, whereas GaN GaP, GaSb, GaAs, InSb, GaAsSb, AlGaInP, etc. are some famous examples of compound semiconductors [1]. In compound semiconductors, nonmagnetic (NM), ferromagnetic (FM), antiferromagnetic (AFM) and ferrimagnetic (FIM) semiconductor are extensively studied theoretically as well as experimentally [2]. The magnetic semiconductor research is very attractive, due to its concurrent spontaneous magnetization and semiconducting properties [3–6]. Materials with these qualities are intriguing to microwave devices [7]. The FM semiconducting material La_2NiMnO_6 was reported to be near room temperature based material for spintronics applications. The application of a magnetic field can control the magnetic, electrical, and dielectric properties [8]. Other FM semiconductors which are predicted through the density functional theory (DFT) is $RbLnSe_2$ (Ln = Ce, Pr, Nd,Gd) [9]. Similar to the FM semiconductors, AFM semicondutors are also studied, for instance, S_2IrO_4. It was experimentally observed that Sr_2IrO_4 has anisotropic

* *Corresponding Author: madhav.ghimire@cdp.tu.edu.np*

magnetoresistance [10]. Additionally, a ternary selenide $Na_2Mn_3Se_4$ is a frustrated AFM semiconductor at 27 K. It was reported to have an indirect band gap semiconductor with gap size of 1.59 eV [11]. FIM semiconductors has also been found, such as $CaCu_3Fe_2Sb_2O_{12}$ [12], $CaCu_3Fe_2V_2O_{12}$, $CaCu_3Fe_2Ta_2O_{12}$ [13], and $CaCu_3Mn_4O_{12}$ [14], which has a direct band gap, and can utilized in practical applications for photoelectron materials. The widespread use of magnetic semiconductor can be a result of their excellent efficiency in terms of photocarrier life times. With the numerous number of possible application but less availability of magnetic semiconductor materials, we are motivated to explore magnetic materials with semiconducting character.

In this study, we have used the DFT approach to analyze the electronic and magnetic properties of experimentally synthesized $Rb_2Mn_3S_4$. We predict that the ferrimagnetic semiconductor $Rb_2Mn_3S_4$ can have a net magnetic moment of 10 μ_B per unit cell (two chemical formula unit). With a band gap of 0.75 eV, the material possesses a direct band gap.

II. Methods

We used the full-potential local orbital code (FPLO) [15], version 18.00-52, within the generalized gradient approximation (GGA) and with the inclusion of Coulomb interaction, GGA+U approach. A localized atomic basis and full potential treatment is applied to analyze the electronic band structure and associated characteristics of $Rb_2Mn_3S_4$ using DFT. The exchange-correlation energy functional employed is based on Perdew, Burke, and Ernzerhof's (PBE-96) [16] parameterization. While considering correlation effects, we have used U = 4 eV for our system. A 12 × 12 × 12 k-mesh grid has been used throughout the whole Brillouin zone. The energy convergence criterion was set to 10^{-8} eV for the self-consistent calculations.

III. Results and Discussion

Crystal structures

$Rb_2Mn_3S_4$ (Fig. 1) has been reported to be a body-centered orthorhombic structure with symmetry space group Ibam (space group no. 72). The structure has three dimensions. Eight equivalent S^{2-} atoms form a body-centered cubic geometry connection with Rb^{1+}. There exist two different sites of Mn^{2+}. Mn^{2+} is linked to four equivalent S^{2-} atoms in the initial Mn^{2+} site, creating a mixture of edge and corner-sharing MnS_4 tetrahedra. The experimental lattice parameter of $Rb_2Mn_3S_4$ are $a = 5.84$Å$, b = 11.21$Å$, c = 13.66$Å and angles $\alpha = \beta = \gamma = 90^\circ$, respectively. The atomic Wyckoff positions are [0.268, 0.119, 0.0] for Rb, [0.0, 0.276, 0.25] for Mn(I), [0.0, 0.0, 0.25] for Mn(II), [0.2183, 0.133, 0.344] for S [17].

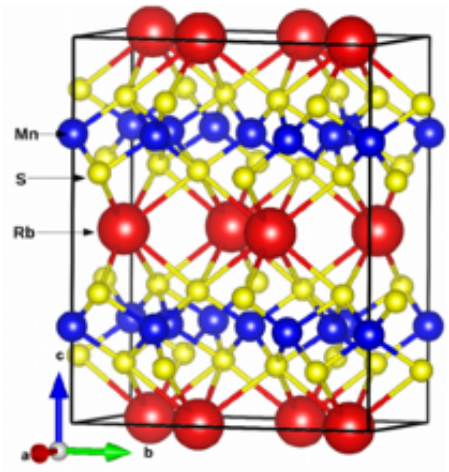

Figure 1. Crystal structure of $Rb_2Mn_3S_4$

Electronic structure

We start with studying the total and partial density of states (DOS) within GGA for the ferrimagnetic ground state, as shown in Fig. 2(a) and Fig. 2(b). A band gap of 0.75 eV is observed between the valence band and the conduction band. The main contributions to the total DOS are seen from the Mn(I)-3d, Mn(II)-3d and S-3p orbitals around E_F. In the conduction region, S-3p and Mn(II)-3d dominate above E_F in spin-up channels, while in spin-down, Mn(I)-3d has significant contributions. On the other hand, below E_F, Mn(I)-3d states significantly contribute to spin-up, while the spin-down channel is contributed by Mn(II)-3d hybridizing with the S-3p states. Generally, the DFT technique underestimates the size of the electronic band gap. To resolve this issue, we apply the Hubbard parameter (U), which plays a significant role in handling the delocalized d-bands resulting in the correct prediction of the experimental band gap. This was done following the literatures [11, 18–20] , which suggests that the appropriate value of U for Mn is between 3 and 4 eV in most cases. We thus report our result using 4 eV. The total and partial DOS within GGA+U is shown in Fig. 2(c) and Fig. 2(d). Interestingly, the Mn-3d states below E_F shift far below, with some minor states around E_F hybridizing significantly with the S-3p states. The band gap so formed is of charge-type between the Mn(I) and S-3p states. Focusing now on the electronic band structure of $Rb_2Mn_3S_4$ in scalar relativistic mode (see fig. 3(a,b)), both the valence band maximum (VBM) and the conduction band minimum (CBM) lies at the high-symmetry point Z in the momentum space dictating that the material $Rb_2Mn_3S_4$ is a direct band semiconductor. This suggests that electrons can transfer straight from the VBM to the CBM. In particular, the band gap makes $Rb_2Mn_3S_4$ an attractive choice for photovoltaic and optoelectronic devices due to the finite gap size within the visible range [13]. The calculated energy gap within GGA and GGA+U are 0.75 and 2.34 eV, respectively.

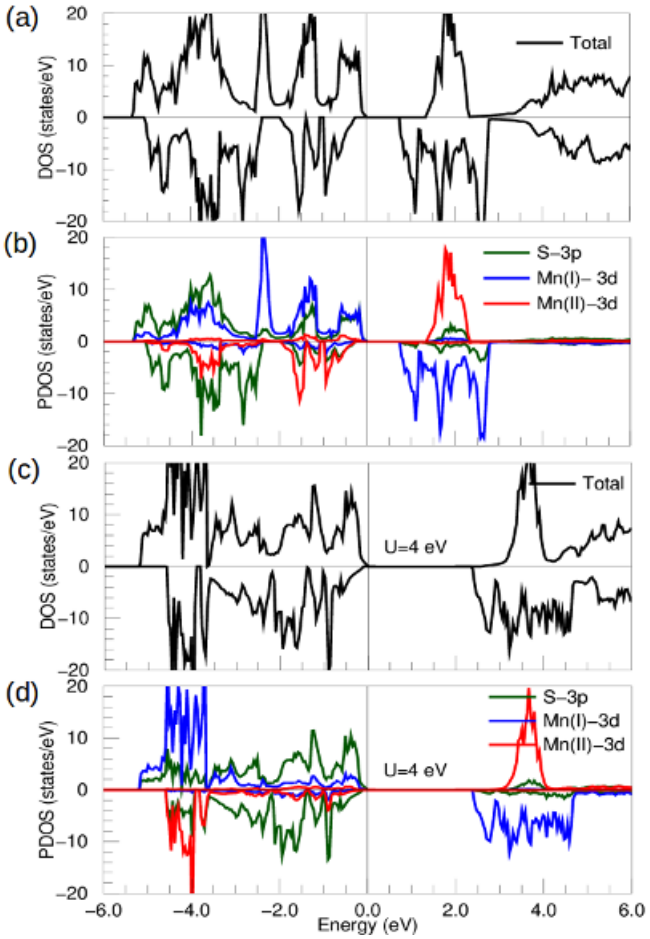

Figure 2. Total and partial DOS of $Rb_2Mn_3S_4$ in scalar relativistic mode within GGA and GGA+U (with U=4 eV for Mn).

We further calculate the band gap considering U (for Mn) ranging from 1 to 6 eV. Interestingly, with increased U, the electronic band gap is shown in Fig. 4. For U = 4 eV, we observed a direct band gap of 2.34 eV.

Magnetic properties

From the total energy calculations, the ferrimagnetic (FIM) configuration is the magnetic ground state with a total energy difference of 2.6 eV between the FM and FIM states. In the FIM configuration, two inequivalent Mn atoms MnI and Mn(II), align antiferromagnetically as Mn(I)↑-Mn(II)↓ interacting with each other via Sn-3p orbitals. The calculated effective magnetic moments is 10 μ_B/unit cell with an individual moment of 4.4 μ_B for Mn(I) and 4.1 μ_B for Mn(II), with polarized moment transfer to Sn (0.07 μ_B) atoms. However, the effective magnetic moment within GGA+U remains the same (10 μ_B/unit cell) as that of GGA; the individual moment rises slightly to 4.8 μ_B and 4.7 μ_B for Mn(I) and Mn(II), mainly due to correlation effects. We further consider the relativistic effect (spin-orbit coupling) to identify the magnetic easy axis along [001], [010], and [100] directions.

The magnetic easy axis was found along [010] while the hard axis is along [100] direction. The calculated magnetic anisotropic energy is ∼0.4 meV per unit cell, suggesting the minimal effect of spin-orbit coupling in $Rb_2Mn_3S_4$.

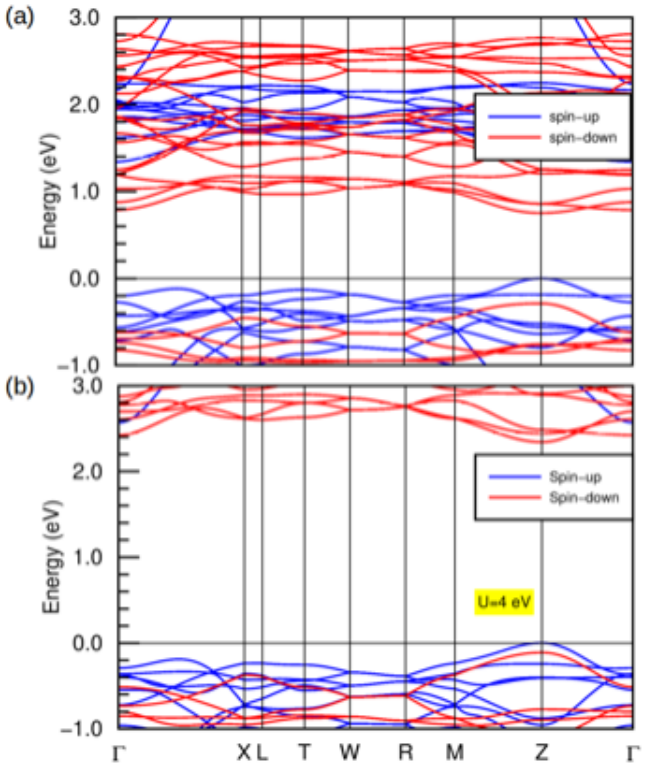

Figure 3. Electronic band structure of $Rb_2Mn_3S_4$ in scalar relativistic mode for GGA and GGA+U (with U=4 eV for Mn). The Fermi level is set to zero.

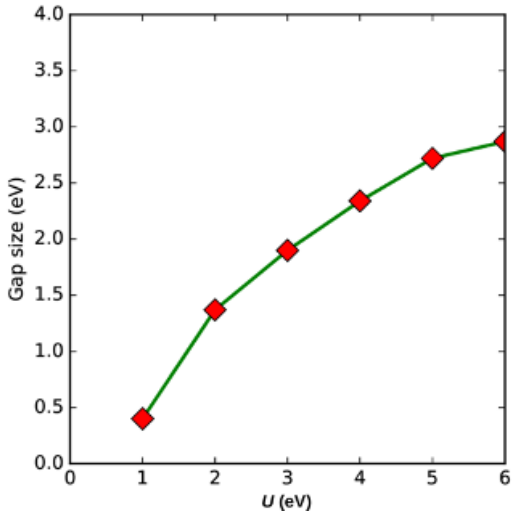

Figure 4. Calculated gap size with the changing value of U in $Rb_2Mn_3S_4$

IV. Conclusions

Using the density functional theory approach, we investigate the electronic structure and magnetic properties of $Rb_2Mn_3S_4$. The material is found to be a direct band gap magnetic semiconductor with a gap size of 0.75 eV within GGA. The ferrimagnetic $Rb_2Mn_3S_4$ has a total magnetic moment of $10\mu_B$/unit cell. Identifying new magnetic direct band gap semiconductors opens the door for additional experimental research for this group of materials that could be used to fabricate valuable devices, including semiconductor lasers, solar cells, and light-emitting diodes.

V. Acknowledgements

G.B.A. and M.P.G. thanks PD Dr. Manuel Richter, IFW-Dresden, for the fruitful discussion and suggestions. M.P.G. was supported by a grant from UNESCO-TWAS and the Swedish International Development Cooperation Agency (SIDA). The views expressed herein do not necessarily represent those of UNESCO-TWAS, SIDA, or its Board of Governors. G.B.A. thanks the Nepal Academy of Science and Technology for the Ph.D. fellowship. M.P.G. and G.B.A. thanks Ulrike Nitzsche for the technical assistance.

References

[1] Kasap SO, Capper P. Springer handbook of electronic and photonic materials. vol. 11. Springer; 2006.

[2] Hall KC, Lau WH, Gündoğdu K, Flatté ME, Boggess TF. Nonmagnetic semiconductor spin transistor. Applied Physics Letters. 2003;83(14):2937-9.

[3] Ohno H. Making nonmagnetic semiconductors ferromagnetic. science. 1998;281(5379):951-6.

[4] Dietl T. A ten-year perspective on dilute magnetic semiconductors and oxides. Nature materials. 2010;9(12):965-74.

[5] Matthias B, Bozorth R, Van Vleck J. Ferromagnetic interaction in EuO. Physical Review Letters. 1961;7(5):160.

[6] Baltzer P, Lehmann H, Robbins M. Insulating ferromagnetic spinels. Physical Review Letters. 1965;15(11):493.

[7] Shlyk L, Strobel S, Farmer B, De Long LE, Niewa R. Coexistence of ferromagnetism and unconventional spin-glass freezing in the site-disordered kagome ferrite SrS n 2 F e 4 O 11. Physical Review B. 2018;97(5):054426.

[8] Rogado NS, Li J, Sleight AW, Subramanian MA. Magnetocapacitance and magnetoresistance near room temperature in a ferromagnetic semiconductor: La2NiMnO6. Advanced Materials. 2005;17(18):2225-7.

[9] Azzouz L, Halit M, Charifi Z, Baaziz H, Rérat M, Denawi H, et al. Magnetic semiconductor properties of RbLnSe2 (Ln= Ce, Pr, Nd, Gd): a density functional study. Journal of Magnetism and Magnetic Materials.

2020;501:166448.

[10] Fina I, Marti X, Yi D, Liu J, Chu J, Rayan-Serrao C, et al. Anisotropic magnetoresistance in an antiferromagnetic semiconductor. Nature communications. 2014;5(1):4671.

[11] Pak C, Garlea VO, Yannello V, Cao H, Bangura AF, Shatruk M. Na2Mn3Se4: Strongly Frustrated Antiferromagnetic Semiconductor with Complex Magnetic Structure. Inorganic Chemistry. 2019;58(9):5799-806.

[12] Xiang H, Wang J, Meng J, Wu Z. Ferrimagnetic and semiconducting CaCu3Fe2Sb2O12 by first principles. Computational materials science. 2009;46(2):307-9.

[13] Li H, Ge Z, Sun A, Zhu Z, Tian Y, Lv S. Ferrimagnetic semiconductor of CaCu3Fe2V2O12 with direct bandgap. Chemical Physics Letters. 2020;759:137910.

[14] Weht R, Pickett WE. Magnetoelectronic properties of a ferrimagnetic semiconductor: The hybrid cupromanganite CaCu 3 Mn 4 O 12. Physical Review B. 2001;65(1):014415.

[15] Koepernik K, Eschrig H. Full-potential nonorthogonal local-orbital minimum-basis band-structure scheme. Physical Review B. 1999;59(3):1743.

[16] Perdew JP, Burke K, Ernzerhof M. Generalized gradient approximation made simple. Physical review letters. 1996;77(18):3865.

[17] Bronger W, Böttcher P. About thiomanganates and cobaltates of heavy alkali metals: Rb2Mn3S4Cs2Mn3S4Rb2Co3S4Cs2Co3S4. Journal of inorganic and general chemistry. 1972;390(1):1-12.

[18] Boukhvalov D, Solovyev I. Defects of the crystal structure and Jahn-Teller distortion in BiMnO 3. Physical Review B. 2010;82(24):245101.

[19] Tolba SA, Gameel KM, Ali BA, Almossalami HA, Allam NK. The DFT+ U: Approaches, accuracy, and applications. Density Functional Calculations-Recent Progresses of Theory and Application. 2018;1:5772.

[20] Tran F, Blaha P, Schwarz K, Novák P. Hybrid exchange-correlation energy functionals for strongly correlated electrons: Applications to transition-metal monoxides. Physical Review B. 2006;74(15):155108.

Electronic and Magnetic Properties of $K_2Mn_3S_4$

G. B. Acharya and M. P. Ghimire

Journal of Nepal Physical Society

Volume 8, Issue 3, December 2022

ISSN: 2392-473X (Print), 2738-9537 (Online)

JNPS, **8** (3): 75-78 (2022)

DOI: https://doi.org/10.3126/jnphyssoc.v8i3.50747

Published by:

Nepal Physical Society
P.O. Box: 2934
Tri-Chandra Campus
Kathmandu, Nepal
Email: nps.editor@gmail.com

JNPS 8 (3): 75-78 (2022)
ISSN: 2392-473X (Print), 2738-9537 (Online)

DOI: https://doi.org/10.3126/jnphyssoc.v8i3.50747

Electronic and Magnetic Properties of $K_2Mn_3S_4$

G. B. Acharya and M. P. Ghimire*
Central Department of Physics, Tribhuvan University, Kirtipur – 44613, Kathmandu, Nepal
*Corresponding Email: madhav.ghimire@cdp.tu.edu.np

Received: *14th Oct., 2022;* ***Revised:*** *14th Dec., 2022;* ***Accepted:*** *17th Dec., 2022*

ABSTRACT

Many opto-electronic and energy efficient devices depend on semiconductors' direct as well as indirect band gap. Using spin-polarized density functional theory approach, we calculate the electronic structure and magnetic properties of $K_2Mn_3S_4$. We found that this system has a ferrimagnetic ground state with a saturated magnetic moment of $10\mu_B$ per unit cell. This was mostly caused by the antiferromagnetic interaction between the Mn (I) and Mn (II) atoms, with individual magnetic moment of 4.2 μ_B and 4.1 μ_B, respectively. More significantly, from the density of states and band structure calculations, $K_2Mn_3S_4$ is noted as a semiconductor with an indirect band gap of 1.1 eV between the top of the valence band of spin up channel and bottom of the conduction bands of spin down channel, indicating the material as a promising candidate for photovoltaic and opto-electronic devices.

Keywords: Density functional theory, Electronic structure, Semiconductor, Density of states, Magnetic moment.

INTRODUCTION

A semiconductor has an electrical conductivity values that falls between a conductor (say Cu) and an insulator (glass). Si and Ge are two well-known semiconductor elements. Semiconductors have a number of significant properties, including resistivity that is lower than that of an insulator but higher than that of a conductor, a negative temperature coefficient of resistance, the ability to behave as an insulator at absolute zero Kelvin, and the potential to controllably increase conductivity through the semiconductor [1]**.** Well known semiconductors are GaN GaP, GaSb, GaAs, InSb, GaAsSb, AlGaInP, etc. are a few examples [2]. Compound semiconductor offers a significant advantage over element semiconductor in comparison. GaAs, as an example, has the following benefit over Si: (i) A six times increase in electron mobility that enables quicker functioning; (ii) A wider band gap, which enables power devices to operate more faster at higher temperatures and produces less thermal noise at ambient temperatures; (iii) Its optoelectronic properties are more advantageous than those of indirect band gap Si because it has a direct band gap; (iv) For alloying, ternary and quaternary compositions are recommended. In compound semiconductors, nonmagnetic (NM), ferromagnetic (FM), antiferromag-netic (AFM) and ferrimagnetic (FIM) semiconductor are extensively studied theoretically as well as experimentally [3-6]. As a NM semiconductor transistor, bulk inversion asymmetry in (110) InAs/GaSb/AlSb heterostructures was proposed [7]. The magnetic semiconductor research is very attractive, due to its concurrent spontaneous magnetization and semiconducting properties. Furthermore, the doping of magnetic atoms in nonmagnetic materials gives magnetic semiconductors [8-11]. For instance, $SrSn_2Fe_4O_{11}$ is a FM semiconductor having a long range ferromagnetic order, finite remanence, and conductivity that falls exponentially with temperature. Materials with these qualities are intriguing for microwave devices fabrication [12] and also for optoelectronic and photovoltic applications [13, 14]. The FM semiconducting material La_2NiMnO_6 was reported to be very near to room temperature for spintronics applications. The application of a magnetic field can control the magnetic, electrical, and dielectric properties of these magnetic material [15]. Other FM semiconductors which are predicted through the

density functional theory (DFT) is $RbLnSe_2$ (Ln = Ce, Pr, Nd, Gd) [16]. Sr_2IrO_4 is an AFM semiconductor, reported experimentally having anisotropic magnetoresistance [17]. A ternary selenide $Na_2Mn_3Se_4$ is an indirect band gap semiconductor with a 1.59 eV gap size that exhibits severely frustrated AFM ordering at 27 K [18]. Though magnetic semiconductors have numerous applications, there are very few materials available. This motivated us to explore several magnetic semiconductor materials**.** The theoretical electronic structure of $K_2Mn_3S_4$ has not been reported yet. In this study, we used the DFT to analyze the electronic structure and magnetic characteristics of experimentally synthesized $K_2Mn_3S_4$. Till date, their electronic structure and magnetic properties has not been fully explored. Based on our findings, we predict that the FIM semiconductor $K_2Mn_3S_4$ can have a net magnetic moment of 10 μ_B per unit cell. This was mainly driven by antiferromagnetic coupling between the Mn (I) and Mn (II) sites. $K_2Mn_3S_4$ also possesses an indirect band gap of 1.1 eV.

METHODS

To perform the DFT calculation, we used the full-potential local orbital code (FPLO) [19], version 18.00-52, within the generalized gradient approximation (GGA). A localized atomic basis and full potential treatment is applied to analyze the electronic band structure and associated characteristics of $K_2Mn_3S_4$ using DFT. The exchange-correlation energy functional employed is based on Perdew, Burke, and Ernzerhof's (PBE-96) [20] parameterization. We used the experimentally synthesized material crystal information such as unit cell dimension and atomic Wyckoff positions with full relaxation. A 12 × 12 × 12 k-mesh grid sample is used for the Brillouin zone. The energy and force convergence criteria were set to be 10^{-8} eV and 10^{-3} eV/ Å respectively.

RESULTS AND DISCUSSION

a. Crystal structures

$K_2Mn_3S_4$ has been reported to be a monoclinic structure with symmetry space group P2/c (space group no. 13). By fusing potassium carbonate and manganese in a stream of hydrogen sulfide at 900 °C, $K_2Mn_3S_4$ has been synthesized [21]. The structure has three dimensions. There are two inequivalent K^{1+} sites, Mn^{2+} sites and S^{2-} sites denoted by K (I), K (II), Mn (I), Mn (II), S (I) and S (II) respectively. Eight S^{2-} atoms are connected to both K^{1+} sites via a cubic bond with a body-centered shape. In order to create a mixture of corner and edge-sharing MnS_4 tetrahedra, Mn^{2+} is bound to four S^{2-} atoms at both Mn^{2+} sites. S^{2-} is linked to four K^{1+} and three Mn^{2+} atoms in the first S^{2-} site in a 3-coordinate geometry. S^{2-} is linked to four K^{1+} and three Mn^{2+} atoms in the second S^{2-} site in a 7-coordinate geometry as shown in figure 1(a). The respective Brillouin zone (BZ) for the crystal is shown in figure 1(b). $K_2Mn_3S_4$ has a non-symmorphic symmetry and is a centrosymmetric crystal system. The experimental lattice parameter that we used for our calculations are a = 7.244 Å, b = 5.822 Å, c = 11.018 Å and angles $\alpha = 90^o$, $\gamma = 90^o$ and $\beta = 112.33^o$ [21].

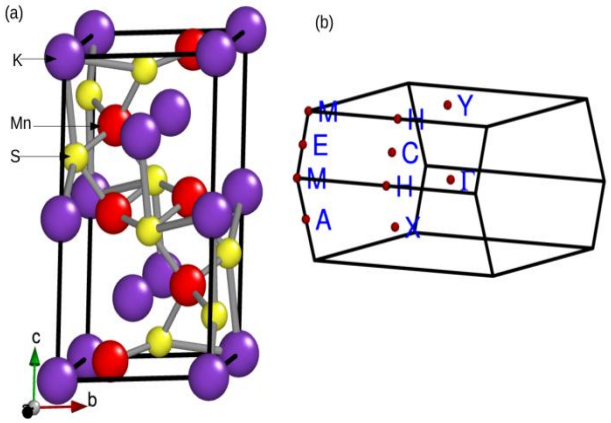

Fig. 1: (a) Crystal structure of $K_2Mn_3S_4$; (b) 3-D Brillouin zone of $K_2Mn_3S_4$. The red dot indicates the high symmetry point in the momentum space.

b. Electronic and magnetic properties

We start interpreting our results of $K_2Mn_3S_4$ by confirming that the material has a FIM ground state. To understand the electronic properties we analyze the total and partial density of states (DOS) within GGA calculation **as** shown in figure 2, wherein the main contributions above the Fermi level (E_F) in spin-up channels are from Mn (II)-3d and spin-down channels from Mn (I)-3d orbitals. Below E_F, the contributions are from Mn (I)-3d in spin-up channel and in spin-down channel contributions are from Mn (II)-3d states hybridizing with the S-3p states. Exchange coupling between the spin-up and spin-down DOS close to E_F are prominently contributed by Mn (II)-3d with an exchange energy of ~2 eV, while for Mn (I) the exchange energy is found to be approximately 3 eV, respectively.

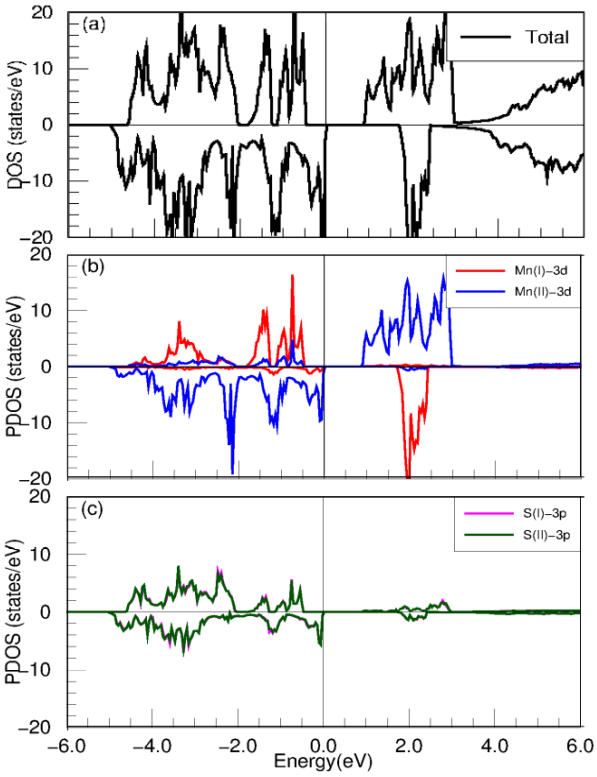

Fig. 2: (a) Total DOS of $K_2Mn_3S_4$ and (b & c) partial DOS for for both inequivalent S and Mn atoms without SOC. The Fermi level is set to zero.

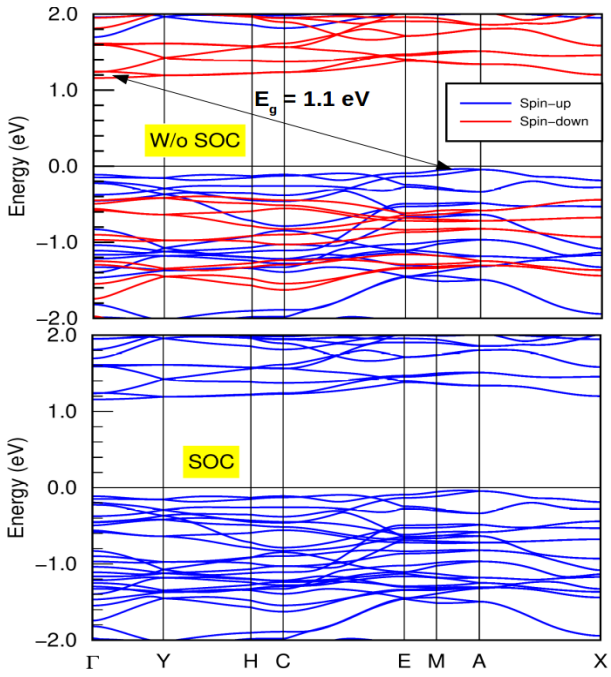

Fig. 3: Electronic band structure of $K_2Mn_3S_4$ in scalar (top) and full-relativistic (bottom). Horizontal solid line indicates the Fermi level. Arrow denotes the indirect band gap between the high symmetry point that lies in the different energy of the momentum space.

The electronic band structure of $K_2Mn_3S_4$ in scalar and full-relativistic (with spin orbit coupling (SOC)) are shown in figure 3. In scalar-relativistic case, the valence band maximum (VBM) lies in MA while the conduction band minimum (CBM) lies at ΓY line in the momentum space resulting in an indirect band gap between VBM and CBM [see figure 3(a)]. $K_2Mn_3S_4$ is thus a semiconductor with an indirect band gap of 1.1 eV.

The effect of SOC is minimal and retains the similar size of band gap within full-relativistic mode. In particular, the band gap value of 1.1 eV which falls in the infrared spectrum is an attractive choice for photovoltaic and optoelectronic devices. From our total energy calculations considering three magnetic configurations: namely FM, AFM, and FIM, the magnetic ground state is found to be FIM. The magnetic easy axis is found to be [001] with hard axis along [010] direction. The computed effective magnetic moments are found to be 10 μ_B per unit cell while the individual moments calculated is 4.2 μ_B for Mn (I), and 4.1 μ_B for Mn (II), respectively. This demonstrates that Mn (I)-Mn (II) couples antiferromagnetically in the ferrimagnetic compound $K_2Mn_3S_4$.

CONCLUSIONS

In conclusion, we perform the density functional theory calculations of K2Mn3S4 which has not been explored so far after the material was synthesized. $K_2Mn_3S_4$ is found to be a semiconductor with an indirect band gap of ~1.1 eV. The ferrimagnetic ground state of $K_2Mn_3S_4$ has a total magnetic moment of 10μ_B per unit cell. This magnetic moment was mostly created by the antiferromagnetic interaction between Mn (I) and Mn (II) atoms. The effect of spin orbit coupling is found negligible. The identification of $K_2Mn_3S_4$ as an indirect band gap magnetic semiconductor is expected to open new door for experimental research that could be used in the fabrication of new devices including semiconductor lasers, solar cells, and light-emitting diodes.

ACKNOWLEDGMENTS

G. B. A. and M. P. G. thanks PD Dr. Manuel Richter, IFW-Dresden for the fruitful discussion and suggestions. M.P.G. was supported by a grant from UNESCO-TWAS and the Swedish International Development Cooperation Agency (SIDA). The views expressed herein do not necessarily represent those of UNESCO-TWAS,

SIDA or its Board of Governors. G.B.A. thanks Nepal Academy of Science and Technology for the PhD fellowship. M.P.G. and G.B.A. thanks Ulrike Nitzsche for the technical assistance.

REFERENCES

[1] Braun, D.; Heeger, A. J.; & Kroemer, H. Improved efficiency in semiconducting polymer light-emitting diodes. *Journal of electronic materials*, **20**(11): 945-948 (1991).

[2] Kasap, S. O.; & Capper, P. (Eds.). *Springer handbook of electronic and photonic materials*, New York: Springer, **11**: (2006).

[3] Bhandari, S. R.; Yadav, D. K.; Belbase, B. P.; Zeeshan, M.; Sadhukhan, B.; Rai et al. Electronic, magnetic, optical and thermoelectric properties of $Ca_2Cr_{1-x}Ni_xOsO_6$ double perovskites. *RSC advances*, **10**(27): 16179-16186 (2020).

[4] Bhandari, S. R.; KC, S.; Lawaju, S.; Thapa, R. K.; Kaphle, G. C., & Ghimire, M. P. Electronic structure and estimation of Curie temperature in Ca_2BIrO_6 (B = Cr, Fe) double perovskites. *Journal of Applied Physics*, **130**(17): 173902 (2021).

[5] Mali, B.; Nair, H. S.; Heitmann, T. W.; Nhalil, H.; Antonio, D. et al. Re-entrant spin reorientation transition and Griffiths-like phase in antiferromagnetic $TbFe_{0.5}Cr_{0.5}O_3$. *Physical Review B*, **102**(1): 014418 (2020).

[6] Joshi, R. K.; Bhandari, S. R.; & Ghimire, M. P. Structural stability, electronic, optical, and thermo-electric properties of layered perovskite Bi_2LaO_4I. *RSC advances*, **12**(37), 24156-24162 (2022).

[7] Hall, K. C.; Lau, W. H.; Gündoğdu, K.; Flatté, M. E.; & Boggess, T. F. Nonmagnetic semiconductor spin transistor. *Applied Physics Letters*, **83**(14): 2937-2939 (2003).

[8] Ohno, H. Making nonmagnetic semiconductors ferromagnetic. *Science*, **281**(5379): 951-956 (1998).

[9] Dietl, T. A ten-year perspective on dilute magnetic semiconductors and oxides. *Nature Materials*, **9**(12): 965-974 (2010).

[10] Matthias, B. T.; Bozorth, R. M.; & Van Vleck, J. H. Ferromagnetic interaction in EuO. *Physical Review Letters*, **7**(5): 160 (1961).

[11] Baltzer, P. K.; Lehmann, H. W.; & Robbins, M. Insulating ferromagnetic spinels. *Physical Review Letters*, **15**(11): 493 (1965).

[12] Donchev, V. Surface photovoltage spectroscopy of semiconductor materials for optoelectronic applications. *Materials Research Express*, **6**(10): 103001 (2019).

[13] Mali, B.; Nair, H. S.; Heitmann, T. W.; Nhalil, H.; Antonio, D. et al. Re-entrant spin reorientation transition and Griffiths-like phase in antiferromagnetic $TbFe_{0.5}Cr_{0.5}O_3$. *Physical Review B*, **102**(1): 014418 (2020).

[14] Shlyk, L.; Strobel, S.; Farmer, B.; De Long, L. E.; & Niewa, R. Coexistence of ferromagnetism and unconventional spin-glass freezing in the site-disordered kagome ferrite $SrSn_2Fe_4O_{11}$. *Physical Review B*, **97**(5): 054426 (2018).

[15] Rogado, N. S.; Li, J.; Sleight, A. W.; & Subramanian, M. A. Magnetocapacitance and magnetoresistance near room temperature in a ferromagnetic semiconductor: La_2NiMnO_6. *Advanced Materials*, **17**(18): 2225-2227 (2005).

[16] Azzouz, L.; Halit, M.; Charifi, Z.; Baaziz, H.; Rérat, M.; et al. Magnetic Semiconductor Properties of $RbLnSe_2$ (Ln= Ce, Pr, Nd, Gd): A Density Functional Study. *Journal of Magnetism and Magnetic Materials*, **501**: 166448 (2020).

[17] Fina, I.; Marti, X.; Yi, D.; Liu, J.; Chu, J. H. Anisotropic magnetoresistance in anantiferromagnetic semiconductor. *Nature communications*, **5**(1): 1-7 (2014).

[18] Pak, C.; Garlea, V. O.; Yannello, V.; Cao, H.; Bangura, A. F.; & Shatruk, M. $Na_2Mn_3Se_4$: strongly frustrated antiferromagnetic semiconductor with complex magnetic structure. *Inorganic Chemistry* (2019).

[19] Koepernik, K.; & Eschrig, H. Full-potential nonorthogonal local-orbital minimum-basis band-structure scheme. *Physical Review B*, **59**(3): 1743 (1999).

[20] Perdew, J. P.; Burke, K.; & Ernzerhof, M. Generalized gradient approximation made simple. *Physical Review Letters*, **77**(18): 3865 (1996).

[21] Bronger, W.; Böhmer, M.; & Schmitz, D. Synthese und Kristallstruktur von $K_2Mn_3S_4$. *Zeitschrift für anorganische und allgemeine Chemie*, **626**(1): 6-8 (2000).

WPI-Center for Materials NanoArchitectonics (WPI-MANA)
National Institute for Materials Science (NIMS)
1-1 Namiki, Tsukuba 305-0044, Japan. Tel: +81 29 860 4709. Fax: +81 29 860 4706

March 10th, 2021

To whom it May Concern

This is certify that a poster presentation below was accepted and distributed in the online poster session from March 2nd to 7th, 2021, at the "MANA International Symposium 2021 jointly with ICYS" which is organized by the International Center for Materials Nanoarchitectonics (WPI-MANA), National Institute for Materials Science (NIMS) .

Name of Presenter registered; Mr. Gang Bahadur Acharya

Affiliation; Tribhuvan University

Contact e-mail address; gang.765711@cdp.tu.edu.np

Registration Number; MANA2021-U0215

Poster number; Category 6. Interactions of Experiment, Theory and Computing -6

Presentation Title; “Identification of Half Metallicity and Flat Bands in Co-Doped $Rb_2Ni_3S_4$”

Abstract submission and a presentation by video streaming.

Sincerely,

Tomo Nakayama

Tomonobu Nakayama

Committee Chair of MANA International Symposium 2021 jointly with ICYS
Deputy Director
WPI Center for Materials Nanoarchitectonics (WPI-MANA)
National Institute for Materials Science (NIMS)

1st International e-Conference on
Recent Advances in Physics & Materials Science-2020
(IC-RAPMS-2020)

Organized by

Kurseong College, Darjeeling, West Bengal, India-734203

In collaboration with

St. Joseph's College, Darjeeling, West Bengal, India-734104

Certificate

This is to certify that **Mr. Gang Bahadur Acharya**

of

Tribhuvan University

has participated in the 1st International e-Conference on Recent Advances in Physics & Materials Science (IC-RAPMS-2020) held during 9 & 10 July, 2020 and presented a paper entitled

Identification of half metallicity in Co-doped Rb 2 Ni 3 S 4

Samir Bal

Dr. Samir Bal
Principal
Kurseong College

Amit Shankar

Dr. Amit Shankar
Convener

Fr. Dr. Donatus Kujur S.J.
Principal
St. Joseph's College

Certificate of Attendance

American Physical Society
March Meeting 2022
March 14–18, 2022 | Chicago & Online

THIS IS TO CERTIFY THAT

Mr. Gang Bahadur Acharya

attended the American Physical Society's March Meeting.
Pre-meeting tutorials and short courses were held on March 12 and 13.

APS physics MARCH MEETING 2022

Don Wise, Senior Meetings Registrar
March 18, 2022

काठमाडौं हुम्बोल्ड सम्मेलन

KATHMANDU HUMBOLDT-KOLLEG 2022

Interdisciplinary Collaboration for Strengthening Science and Culture

October 16-19, 2022, Kathmandu, Nepal

Unterstützt von / Supported by

Alexander von Humboldt
Stiftung / Foundation

Certificate of Appreciation

is hereby awarded to Dr. / Mr. / Ms.

Gang Bahadur Acharya

for **Poster Presentation** in the international scientific conference "**Kathmandu Humboldt-Kolleg 2022**" organized by **Humboldt Club Nepal** generously supported by **Alexander von Humboldt Foundation, Germany.**

PROF. DR. RAMESHWAR ADHIKARI

Coordinator
Kathmandu Humboldt-Kolleg 2022
Humboldt Club Nepal

DR. JUDITH SCHILDT

Sponsorship and Network Department,
Alexander von Humboldt Foundation,
Germany

ACS WORKSHOP

ACS Chemistry for Life®

Certificate of Participation

VERIFYING THAT

Gang Acharya

ATTENDED THE FULL AGENDA OF THE ACS WORKSHOP:
IIT MADRAS
NOVEMBER 13, 2023

DR. JAMES MILNE
President, Publications Division
American Chemical Society